Institut für Geodäsie und Geoinformation der Universität Bonn

Professur für Astronomische, Physikalische und Mathematische Geodäsie

Large-scale mass redistribution in the Earth system from synergistic use of Swarm data

Dissertation

zur Erlangung des akademischen Grades

Doktorin der Ingenieurwissenschaften (Dr.-Ing.)

der

Landwirtschaftlichen Fakultät

der

Rheinischen Friedrich-Wilhelms-Universität Bonn

vorgelegt von

Christina Lück

aus Neuwied

Bonn 2022

Referent: Prof. Dr.-Ing. Jürgen Kusche
Korreferent: Prof. Dr.-Ing. Torsten Mayer-Gürr
Korreferent: Prof. Dipl.-Ing. Dr. techn. Wolf-Dieter Schuh

Tag der mündlichen Prüfung: 10. Dezember 2021
Angefertigt mit Genehmigung der Landwirtschaftlichen Fakultät der Universität Bonn.

Large-scale mass redistribution in the Earth system from synergistic use of Swarm data

Summary

Long and consistent time series of large-scale mass redistribution in the Earth system are important in many scientific research areas. The dedicated **G**ravity **R**ecovery **A**nd **C**limate **E**xperiment (GRACE) and **G**ravity **R**ecovery **A**nd **C**limate **E**xperiment **F**ollow-**O**n (GRACE-FO) satellite missions provide time-variable gravity fields with an unprecedented accuracy and thus contribute significantly to a better understanding of mass fluctuations within the Earth. However, it is important to find alternatives, because the GRACE(-FO) record is interrupted by an 11-months data gap and several (bi-)monthly gaps. Alternative approaches could help to fill the gaps and to extend the time series into the past and future.

In this thesis, time-variable gravity fields and large-scale mass redistribution are derived from the magnetic field mission Swarm, which is not specifically designed to measure the Earth's gravity field. The integral equation approach with short arcs is used to derive **S**pherical **H**armonic (SH) coefficients from kinematic orbits of the three satellites. As accelerometer measurements are corrupted by a variety of errors, non-gravitational accelerations are modeled, which improves the gravity field solutions. Different parameterizations are tested and the quality of the results is validated by comparing them to the more accurate GRACE(-FO) solutions during the overlap period. The analysis reveals that the Swarm solution derived in this thesis provides better results than the official **E**uropean **S**pace **A**gency (ESA) EGF_SHA_2_ product from July 2015 to December 2019 and similar results in the remaining months. Swarm is able to resolve mass change trends and seasonal signals from basin averages when either a large basin (e.g., ocean) or a region with a high signal content (e.g., Danube river basin) is investigated. Swarm can be used to fill the gap between GRACE and GRACE-FO and should be preferred to common GRACE(-FO) data interpolation methods. First results reveal that time-variable gravity fields from Swarm can be integrated in a sea level inversion framework with the aim to partition altimetric sea level change into its individual components.

Großskalige Massenumverteilungen im Erdsystem aus synergistisch genutzten Swarm Daten

Zusammenfassung

Lange und konsistente Zeitreihen von großskaligen Massentransporten im System Erde spielen in vielen wissenschaftlichen Bereichen eine wichtige Rolle. Die Satellitenmissionen **G**ravity **R**ecovery **A**nd **C**limate **E**xperiment (GRACE) und **G**ravity **R**ecovery **A**nd **C**limate **E**xperiment **F**ollow-**O**n (GRACE-FO) liefern zeitvariable Schwerefelder hoher Genauigkeit und tragen so zu einem besseren Verständnis von Massenbewegungen in und auf der Erde bei. Allerdings ist es wichtig, alternative Möglichkeiten zu finden, da die GRACE(-FO) Zeitreihe durch eine elfmonatige Lücke, sowie mehrere ein- und zweimonatige Lücken unterbrochen ist. Alternative Ansätze können helfen, die Lücke zu füllen und die Zeitreihe in die Vergangenheit und Zukunft zu verlängern.
In dieser Arbeit werden zeitvariable Schwerefelder sowie großskalige Massenänderungen mithilfe der Daten der Magnetfeldmission Swarm hergeleitet, obwohl diese nicht speziell für die Messung des Erdschwerefelds konzipiert wurde. Der Integralgleichungsansatz wird verwendet um Kugelfunktionskoeffizienten aus den kinematischen Orbits der drei Satelliten abzuleiten. Da die Akzelerometerbeobachtungen eine Vielzahl von Fehlern aufweisen, werden die nichtgravitativen Beschleunigungen modelliert, was die Schwerefeldlösungen verbessert. Verschiedene Parametrisierungen werden getestet und die Qualität wird durch einen Vergleich mit den genaueren GRACE(-FO) Lösungen während der Überschneidungszeit beurteilt. Die Untersuchungen zeigen, dass die Swarm Lösungen dieser Arbeit von Juli 2015 bis Dezember 2019 eine bessere Genauigkeit als das offizielle EGF_SHA_2_ Produkt der Europäischen Weltraumorganisation (**E**uropean **S**pace **A**gency, ESA) haben und eine vergleichbare Genauigkeit in den restlichen Monaten. Swarm kann Trends und saisonale Signale der Massenänderung aus Regionen herleiten, wenn sie entweder eine ausreichende Größe (z.B. Ozean) oder einen hohen Signalgehalt (z.B. Einzugsgebiet der Donau) haben. Zum Schließen der Lücke zwischen GRACE und GRACE-FO sollte Swarm den üblichen GRACE(-FO) Dateninterpolationsmethoden vorgezogen werden. Erste Ergebnisse zeigen, dass Swarm in das Inversionsprogramm integriert werden kann, um gemessene Meeresspiegeländerungen in einzelne Anteile zu partitionieren.

Acknowledgments

Now that I am about to finish this thesis, I realize that this would not have been possible without the support and guidance of so many people.

First of all, I would like thank my supervisor Jürgen Kusche, who gave me the opportunity to be a part of the Astronomical, Physical and Mathematical Geodesy (APMG) group at the Institute of Geodesy and Geoinformation of the University of Bonn. Thank you for letting me undertake this PhD journey and for always providing me with your help and advice. I appreciate that I could develop and pursue my own ideas, while always knowing that you would be there to help me when I get stuck. You encouraged me to discuss and present my results at scientific conferences, giving me the opportunity to meet new people and to discover the world of science.

Moreover, I want to thank Torsten Mayer-Gürr and Wolf-Dieter Schuh for being referees of this thesis and for your kind support. Thank you, Torsten, for helping me whenever I struggled or had questions concerning GROOPS.

A special thanks goes to all my colleagues of the SPP 1788. I always enjoyed our annual colloquia as well as the summer and winter schools. I am lucky to be part of such a great group. I want to thank my colleagues of the CONTIM project for fruitful discussions, especially Roelof Rietbroek, who once supervised my Bachelor's and Master's theses, which surely sparked my enthusiasm for astronomical and physical geodesy.

I want to thank my colleagues and former colleagues of the APMG, TG and GESS group of our institute for the wonderful time and the nice working environment. Thank you for all scientific and non-scientific discussions, for helping me, whenever I had any problems and for proof-reading parts of my thesis. You are not only my colleagues, but also became friends! I want to particularly thank you, Bernd, for being such a great office mate and for always being patient with me ;-)

I especially would like to thank my friends and family. Writing this thesis would not have been possible without the support of my parents, Manfred and Marlies, and my sister, Stefanie. Thank you for always believing in me. Last but not least, I want to thank Julian. Thank you for your patience (especially during these last few months!) and your unlimited support and encouragement.

Contents

Chapter 1

Introduction

1.1 Motivation

The determination of the Earth's gravity field is one of the central tasks in geodesy. A static gravity field model describes the mean distribution of mass within the Earth system. The geoid is an equipotential surface of the gravity field and important for many geodetic aspects, such as the definition of height systems. Physical heights are determined by leveling or gravity measurements and refer to the geoid. Geometric heights, as derived by **G**lobal **N**avigation **S**atellite **S**ystem (GNSS), on the other hand, refer to a reference ellipsoid. To bring these two kinds of heights together, an exact knowledge of the geoid is necessary. Another example would be the determination of the dynamic topography, i.e. the height of the sea surface above the geoid. Sea surface height is measured by altimetry satellites and refers to a reference ellipsoid. Only with a geoid model, the dynamic topography can be derived.

Our planet is a dynamic system and the Earth's gravity field changes over time. Thus, it is important to observe and monitor mass redistribution and mass variations. These can be induced by geophysical or anthropogenic processes. Ubiquitous examples are the melting of glaciers and ice sheets, ocean mass change, **G**lacial **I**sostatic **A**djustment (GIA), hydrological processes, and human ground-water retrieval. It is of great interest to measure these variations, as they are relevant for understanding Earth's system dynamics and provide insights to climate research. In Section 1.2 the importance of monitoring mass redistribution in the Earth system is discussed further.

The dedicated satellite missions **CHA**llenging **M**inisatellite **P**ayload (CHAMP) (Reigber et al., 2006), **G**ravity Field and Steady-State **O**cean **C**irculation **E**xplorer (GOCE) (Drinkwater et al., 2003), GRACE (Tapley et al., 2004), and GRACE-FO (Kornfeld et al., 2019) have been monitoring and continue to monitor our Earth's gravity during the last 20 years. The measurement technique of GRACE(-FO) is unique: range, range-rate, and range-acceleration between two satellites are precisely measured by a **K-B**and **R**anging (KBR) system, enabling the retrieval of time-variable gravity fields with a resolution of a few hundred km. Tapley et al. (2019) summarize the scientific highlights derived from GRACE data and provide an insight into the wide range of applications and their importance.

However, there is a gap of 11 months between GRACE and GRACE-FO. Furthermore, there are (bi-)monthly gaps starting in 2011 due to battery management and the data quality degraded during the end-of-life period of GRACE. In the time of these gaps, there is no dedicated gravity field mission. One option to bridge the gap would be to simply interpolate existing GRACE(-FO) data. With this approach, strong deviations from normal behavior would not be detectable. Such anomalies could for example originate from El Niño or La Niña events, which cannot be forecasted reliably. In 2011, a strong La Niña led to a drop of global mean sea level by 5 mm (Boening et al., 2012) and in 2016, the Amazon basin experienced a rainfall deficit due to an El Niño event (Jiménez-Muñoz et al., 2016). In this thesis, independent and unconstrained time-variable gravity fields are derived from kinematic orbits of ESA's three-satellite Swarm mission (Friis-Christensen et al., 2008).

The resolution of these gravity field models is lower compared to GRACE(-FO), because there are no inter-satellite measurements and one has to rely on **G**lobal **P**ositioning **S**ystem (GPS)-based **h**igh-**l**ow **S**atellite-to-**S**atellite **T**racking (hl-SST). The processing challenges are addressed in this work and the reliability of Swarm time-variable gravity fields is assessed. These analyses pave the way for experiments regarding the time after GRACE-FO, in case there will be no direct follow-up mission. The principle can be applied to any **L**ow **E**arth **O**rbit (LEO) satellite mission whose orbit is tracked with GNSS.

1.2 The Importance of Monitoring Mass Redistribution in the Earth System

Mass variations in the Earth system are closely linked to climate change. Satellite measurements enable global observations and help us to understand and monitor ongoing processes. Tapley et al. (2019) give an overview of important studies, which highlight the contributions of GRACE to better understanding the global climate system. In the following, three major aspects are introduced in more detail: (mass-related) sea level change, melting of glaciers and ice sheets, and land water redistribution.

1.2.1 Sea Level Change

Sea level rise affects many regions along the world's coastlines with severe consequences for coastal ecosystems and habitats (Nicholls and Cazenave, 2010). It is an important indicator for climate change and is not only of interest for the scientific community, but also for policy makers and the general public. Monitoring and understanding current and past sea level change will help to better predict future developments. Generally, sea level change can either be steric (i.e. volumetric), due to temperature or salinity variations or mass-related, e.g. from melting glaciers and ice sheets or hydrological water redistribution.

Total sea level change has been observed with satellite altimetry since the launch of Topex/Poseidon in 1993. According to the fifth assessment report of the **I**ntergovernmental **P**anel on **C**limate **C**hange (IPCC), the observed total global mean sea level rise amounts to 3.2 ± 0.4 mm/yr in the time from 1993 to 2010 (Church et al., 2013). A more recent estimate by Ablain et al. (2019) shows an increased trend of 3.35 ± 0.4 mm/yr between October 1992 and December 2017. To better understand the causes of sea level rise, it is inevitable to observe steric and mass-related contributions separately.

Steric variations are measured by Argo floats (Gould et al., 2004), which freely drift in the ocean to record temperature and salinity profiles. First measurements date back to 2000 and since then the number of buoys steadily increased and reached almost 4000 by July 2021. Due to the large number, the coverage is quasi-global. However, some regions are over-sampled, while others are under-sampled. Additionally, Argo floats collect their data only in the upper 2000 m of the ocean. According to Llovel et al. (2014), deeper ocean areas contribute only marginally to steric sea level change, but those estimates cannot be inferred from Argo data.

Mass-induced sea level variations are mainly caused by the melting of land glaciers, the Greenland and Antarctic ice sheets, and land water storage redistribution. Ocean mass variations are commonly observed by the GRACE(-FO) mission. WCRP (2018) compare different solutions and specify an ensemble mean ocean mass trend of 2.3 mm/yr from January 2005 to December 2016 (with the individual solutions ranging from 1.76 to 2.61 mm/yr). Uebbing et al. (2019) find a trend of mass-related sea level rise of 1.75 mm/yr from August 2002 to July 2016.

For the closure of the sea level budget it is important to determine all components as precisely as possible, which has been the aim of many studies (e.g., Rietbroek et al., 2016; Cazenave et al., 2017; Chambers et al., 2017). The **W**orld **C**limate **R**esearch **P**rogramme (WCRP) Global Sea Level Budget Group is an initiative of about 50 institutions and research teams with the goal of

assessing the global and regional sea level budget from 1993 to present (WCRP, 2018). They have been able to close the budget within 0.3 mm/yr and uncertainties remain in the processes of the deep ocean and the land water storage component. The exact knowledge of mass redistributions within the Earth system helps to determine the mass-related part of sea level change and thus also the steric component can be derived more reliably in sea level budget studies.

1.2.2 Melting of Glaciers and Ice Sheets

Glaciers and ice sheets play a key role in climate change studies. Due to the high albedo of snow and ice, most of the incoming solar radiation is reflected back into space. In simple words: glaciers and ice sheets help to keep our planet cool. During the last decades, an increased warming of the atmosphere and oceans has been causing ice sheets and glaciers to melt. This affects weather patterns, ocean currents, and sea level rise worldwide.

Shepherd et al. (2020) investigated the mass balance of the Greenland ice sheet and found a loss of 3902 ± 342 billion tonnes between 1992 and 2018. According to the fifth assessment report of the IPCC, the melting of glaciers and ice sheets in Greenland contributes 0.43 mm/yr to global mean sea level rise from 1993 to 2010 (Church et al., 2013). The Antarctic ice sheet and glaciers except for those in Greenland and Antarctica amount to 0.27 mm/yr and 0.76 mm/yr, respectively. More recent studies suggest increased rates; e.g. Sasgen et al. (2020) find that the Greenland ice sheet contributes 0.76 mm/yr to global mean sea level rise from 2005 to 2017.

Altimetry satellites measure the elevation of ice sheets by laser (**I**ce, **C**loud and Land **E**levation **Sat**ellite (ICESat)) or radar (e.g., CryoSat). However, a conversion to mass change requires assumptions of firn and snow density, which introduces large uncertainties. GRACE and GRACE-FO provide direct mass change estimates, but they observe the combined effect of ice mass loss and GIA. Hence, GIA models are needed to separate the effect of post-glacial rebound from actual ice mass change.

1.2.3 Hydrological Mass Redistribution

The hydrological cycle impacts freshwater supplies and agricultural productivity as well as ecosystems and habitats for humans and animals. Therefore, it is of utmost importance to observe, monitor, and understand hydrological processes. Measurements from space, especially from the GRACE(-FO) mission, enable global insights in water distribution on Earth. Rodell et al. (2018) find that freshwater is accumulating in low and high latitudes while it is decreasing in mid-latitudes (based on measurements from April 2002 to March 2016), which is also confirmed by IPCC reports (Church et al., 2013).

Anthropogenic impact is evident in many regions of the world where groundwater is withdrawn to support irrigation of agricultural areas (Döll et al., 2014). In combination with in situ measurements and climate models, GRACE(-FO) can help to quantify groundwater depletion and improve water management. Regarding the growing population accompanied by an increased need for food and freshwater, management decisions are more important than ever in times of global climate change.

Gouweleeuw et al. (2018) show how daily GRACE measurements can be used to track flooding events. Reager et al. (2014) reveal that the inclusion of GRACE-based **T**otal **W**ater **S**torage **A**nomaly (TWSA) into a river discharge model results in longer lead times in flood warnings. Furthermore, droughts can be identified with GRACE, such that e.g. Gerdener et al. (2020) developed a framework for deriving drought indicators. Boergens et al. (2020) used recent GRACE-FO data to quantify the European droughts in 2018 and 2019.

1.3 Objectives of the Thesis

The central question in this thesis is whether Swarm data can be used to derive large-scale mass redistribution in the Earth system, even though it is a magnetic field mission and not specifically dedicated to measuring the Earth's gravity field. As the 11-months gap between GRACE and GRACE-FO has shown, it is not always possible to implement successive satellite missions such that they seamlessly follow up on each other. This work provides an alternative, which becomes even more important in case no dedicated gravity field mission is available. Even though my research is tailored to the Swarm satellites, the approach can easily be adapted to be used with any other LEO satellite that is tracked by GNSS, as e.g. CHAMP, TerraSAR-X, or TanDEM-X. In this way, the thesis' results can help to extend the GRACE(-FO) time series into the past and into the future.

Due to the missing ultra-precise inter-satellite link, time-variable gravity fields from Swarm have a lower resolution than those from GRACE(-FO). In the scientific community, it is indisputable that gravity fields derived only from **P**recise **O**rbit **D**etermination (POD) also have a lower accuracy than those from a dedicated gravity field mission. I investigate the quality of the Swarm time-variable gravity fields and mass redistributions regarding different aspects. A common way to describe the accuracy of time-variable gravity fields is to compute formal errors. However, these are often inaccurate themselves because they cannot account for the quality of the background models and the kinematic orbits. Hence, in addition to investigating the formal errors, I provide alternatives by comparisons to GRACE(-FO) during the overlapping period with Swarm.

An important question that will be answered in this thesis is whether the gap between GRACE and GRACE-FO can be closed with the help of Swarm. One simple and widely accepted way to close data gaps is to use interpolation methods. This approach might deliver good results, when there are no deviations from the "normal" behavior during the gaps. Yet, interpolation strategies will not be able to reconstruct any unexpected mass changes, as for example during **E**l **N**iño **S**outhern **O**scillation (ENSO) events. Swarm offers valuable, independent data that can be used to fill the gaps, albeit with a lower resolution. I will investigate the question if it is more reliable to bridge gaps by interpolating between existing GRACE(-FO) data or by using Swarm time-variable gravity fields.

Accelerometer measurements from Swarm are corrupted by systematic and random errors. Usually, one would introduce the accelerometer observations in the gravity field processing to account for non-gravitational accelerations. Yet, only calibrated along-track data of Swarm C exists. A widely accepted method is to simply co-estimate non-gravitational accelerations when retrieving gravity fields. If non-gravitational accelerations are modeled, it is common to utilize standard techniques, which are often obsolete. De Teixeira da Encarnação et al. (2020) give an overview of the approaches used in Swarm gravity field retrieval. In this thesis, I utilize the most recent **N**aval **R**esearch **L**aboratory **M**ass **S**pectrometer **I**ncoherent **S**catter radar (NRLMSIS) 2.0 model (Emmert et al., 2021) to account for aerodynamic forces. Radiation pressure is modeled with advanced techniques as presented in Vielberg and Kusche (2020). The benefits when introducing non-gravitational accelerations in the gravity field processing are presented. Besides, future studies regarding the thermospheric density could also profit from the modeling approach.

A further objective is to include Swarm in the sea level inversion framework, which was developed originally by Rietbroek et al. (e.g., Rietbroek et al., 2012; Rietbroek, 2014) at the Institute of Geodesy and Geoinformation (IGG, **I**nstitut für **G**eodäsie und **G**eoinformation) of the University of Bonn. With the inversion approach, sea level change can be split into its individual components, such as the melting of glaciers and ice sheets, land water redistributions, and steric changes. Spatial patterns, characterizing the influence of individual contributors, are predefined. Their time-variability is expressed through monthly scaling factors, which are estimated in a least-squares adjustment. Until now, the approach utilized altimetry to observe total sea level change and GRACE and GRACE-FO, which are sensitive to mass-related changes. Hence, so far, it is only

possible to obtain results when GRACE(-FO) data is available. The challenge of including Swarm is its lower spatial resolution. The predefined patterns contain smaller features than Swarm is able to resolve. This thesis provides the first approach to extending the sea level inversion framework in a way that Swarm data can be used to close the sea level budget.

In this work, I provide an unprecedented analysis of time-variable gravity field and large-scale mass redistribution from Swarm for the time span 2014 to 2021. I present the challenges, the gravity field retrieval process, including different parameterizations, and an assessment of the results. Summarized, the main objectives of this work are:

1. Using Swarm to derive time-variable gravity fields and large-scale mass redistribution in the Earth system, even though it is a magnetic field mission.
2. Assessing the quality of Swarm time-variable gravity fields and mass change.
3. Bridging the gap between GRACE and GRACE-FO with Swarm.
4. Modeling non-gravitational accelerations to help during the gravity field retrieval process.
5. Including Swarm in the sea level inversion framework to help close the sea level budget.

1.4 Outline of the Thesis

The thesis is organized as follows: In Chapter 2, I give an overview of all satellite missions that appear throughout this work. These include GRACE, GRACE-FO, Swarm, and various **S**atellite **L**aser **R**anging (SLR) and radar altimetry satellites. I describe the aim of the missions, give facts about their orbits, explain the measurement principle and point out why and where they will be relevant in this work.

As one of the main objectives of the thesis is to derive time-variable gravity fields, mass change, and mass redistribution from Swarm data, I give a detailed presentation of Swarm in Chapter 3. It is important to understand the implications of the fact that Swarm is not a dedicated gravity field mission, hence the main objectives are described, which focus on the retrieval of the geomagnetic field. I furthermore explain the constellation of the three satellites and give an overview of the data products. Next, POD and non-gravitational acceleration modeling are documented, because their understanding is essential for gravity field retrieval. Finally, it is explained why Swarm is well suited to derive time-variable gravity fields and what kind of challenges it implicates.

Chapter 4 provides an overview of the gravity field recovery. First, the methodology, including the theory of SHs, the integral equation approach and the parameterization for the Swarm mission, are described. This is followed by an explanation of the implementation steps. Time-variable gravity field results from Swarm are presented in the last section of Chapter 4. They are analyzed with respect to their reliability by deriving degree amplitudes and comparing them to GRACE(-FO) gravity fields.

In Chapter 5, the time-variable gravity fields are converted to mass change. First, the theory is explained: several corrections need to be applied to the SH coefficients before converting to **E**quivalent **W**ater **H**eight (EWH) and computing regional basin averages. Results from Swarm are discussed and compared to GRACE(-FO) on global and regional scales. An important question under discussion is whether Swarm can reliably be used as a gap-filler in times when GRACE(-FO) is not available.

Chapter 6 shows the ongoing work of incorporating Swarm into IGG's sea level inversion framework. The joint inversion combines satellite gravimetry and altimetry to split sea level change into its individual components, such as the melting of glaciers and ice sheets, land water redistribution, and steric contributions. When including comparatively low-resolution Swarm models into the inversion framework, the challenge is to adapt predefined patterns such that they fit the spatial resolution

of Swarm.

Finally, the main findings of this thesis are summarized in Chapter 7. An outlook demonstrates further research possibilities.

Chapter 2

Satellite Missions

In the following chapter, I will introduce different types of satellite missions that will appear numerous times throughout this thesis. Figure 2.1 gives an overview of the missions and their lifetimes. CHAMP (Reigber et al., 2006) and GOCE (Drinkwater et al., 2003; Rummel et al., 2011) data will not be utilized in this thesis, but the two missions paved the way for many of today's common approaches for gravity field retrieval. CHAMP was the first dedicated mission to carry a GPS receiver and an accelerometer for gravity field retrieval and GOCE was the first gravitational gradiometry satellite. Both missions served as prototypes for the two-step approach: kinematic orbits are derived in a first step, which are then used to compute a gravity field.

In this thesis, the focus is on deriving time-variable gravity fields and mass changes (Chapters 4 and 5). The most prominent satellite mission in this field is of course the GRACE mission and its successor GRACE-FO. I will use kinematic orbits of the Swarm mission to derive time-variable gravity fields, even when GRACE(-FO) data is not available. In addition to GRACE(-FO), CHAMP and SLR data can also be used as a reference when comparing different solutions to each other. In Chapter 6, satellite radar altimetry is one of the main input quantities and provides information about total sea level changes. The mass change observed by GRACE(-FO) serves as the main input for mass-related sea level variations, while Swarm is used as an additional source, which will be most important in times of GRACE(-FO) gaps.

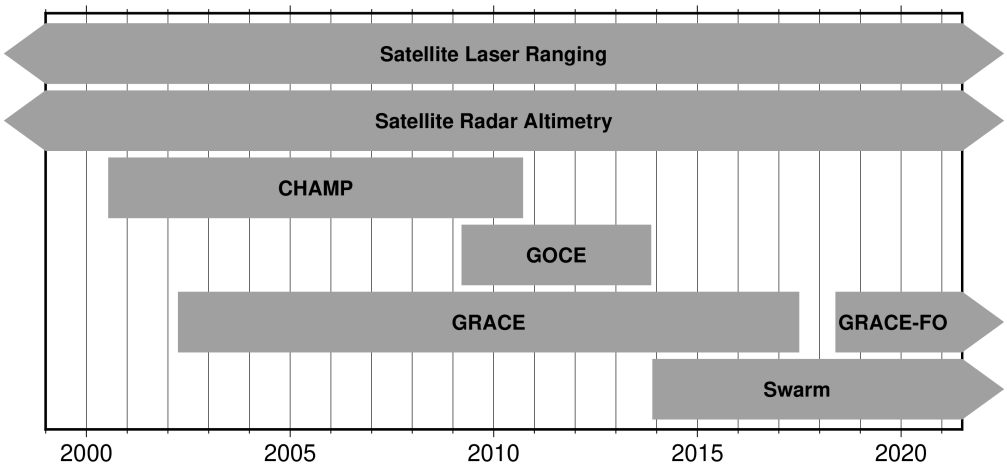

Figure 2.1: Overview of the satellite missions that are relevant for this thesis.

2.1 GRACE and GRACE-FO

GRACE was a joint satellite mission of **N**ational **A**eronautics and **S**pace **A**dministration (NASA) and German Aerospace Center (DLR, **D**eutsches Zentrum für **L**uft- und **R**aumfahrt e.V.) with the

primary objective of measuring the Earth's gravity field and its variations in time with unprecedented accuracy (Tapley et al., 2004). In 1996, the mission was proposed by **U**niversity of **T**exas at Austin, **C**enter for **S**pace **R**esearch (UTCSR), German Research Centre for Geosciences (GFZ, Deutsches **G**eo**F**orschungs**Z**entrum), **J**et **P**ropulsion **L**aboratory (JPL), DLR, **S**pace **S**ystems **L**oral (SSL), and Astrium GmbH. It was selected as the second mission under the NASA **E**arth **S**ystem **S**cience **P**athfinder (ESSP) Program in 1997 and finally launched on March 17, 2002 from Plesetsk Cosmodrome in Russia.

For over 15 years, GRACE has collected more than 160 monthly snapshots of the Earth's gravity field and thus contributed to a better understanding of mass fluctuations within the Earth. Some examples of mass redistribution processes monitored by GRACE include mass loss from ice sheets (Wouters et al., 2008; Shepherd et al., 2018) and glaciers (Gardner et al., 2013), seasonal fluctuations in water storage (Scanlon et al., 2019), anthropogenic groundwater storage changes (Rodell et al., 2018) as well as ocean mass changes (Chambers and Bonin, 2012; Johnson and Chambers, 2013; J. Chen et al., 2018). Ocean mass variations are essential for partitioning total sea level change, as measured by satellite altimeters, into mass-related and steric parts. Uebbing et al. (2019) show that different approaches of deriving ocean mass change from GRACE agree within less than 0.1 mm/yr on global scales (after applying several corrections), resulting in a trend of 1.75 mm/yr from August 2002 to July 2016. Tapley et al. (2019) highlight more representative studies based on GRACE observations with contributions to understanding climate change.

On October 12, 2017 the GRACE mission came to an end, due to battery failure. About seven months later, on May 22, 2018 the GRACE-FO satellite mission was successfully launched from Vandenberg Air Force Base in California, USA. It shares many similarities with its predecessor mission GRACE. The primary aim of GRACE-FO is to continue the record of high-resolution gravitational variations from GRACE (Kornfeld et al., 2019). Furthermore, the performance of a new kind of **L**aser **R**anging **I**nterferometer (LRI) is tested to improve the **S**atellite-to-**S**atellite **T**racking (SST) performance (Abich et al., 2015). GRACE-FO also continues radio occultation measurements in order to get new insights of the Earth's atmosphere. Landerer et al. (2020) show that GRACE-FO continues the GRACE record at an equivalent spatial and temporal sampling and precision.

2.1.1 GRACE Orbit Design

GRACE was a constellation of two identical satellites - GRACE-A and GRACE-B. The spacecraft were placed in the same near-polar ($i = 89.0°$), near-circular ($e < 0.005$) orbit with an along-track separation of 220 ± 50 km. The initial altitude of the satellites was approximately 500 km. Figure 2.2 shows that the satellites spent a large part of their lifetime at an altitude of 470 to 490 km. Starting in about 2010, when the sunspot activity of Solar cycle 24 got larger, the atmospheric drag acting on the spacecraft became stronger and the orbit decayed down to 335 km until the end of the mission. The relatively low orbit, in combination with the high inclination allowed a detailed mapping of gravity field anomalies, down to spatial scales of a few hundred kilometers after one month of collecting data.

GRACE-FO consists of the two identical satellites GRACE-C and GRACE-D with an along-track separation of 220 ± 50 km. The orbital parameters are very similar to the predecessor mission ($i = 89.0°$ and $e < 0.005$). The launch altitude was approximately 490 km and so far, the orbit does not show any unexpected signs of decay (see Figure 2.2).

2.1.2 GRACE Measurement Principle and Payload

Figure 2.3 illustrates the measurement principle of GRACE. Due to the inhomogeneous mass distribution within the Earth system, the two satellites experienced gravitational perturbations. These acted slightly differently on the leading and the trailing satellite, because they were separated by 220 ± 50 km in along-track direction. Thus, accurately measuring the relative motion

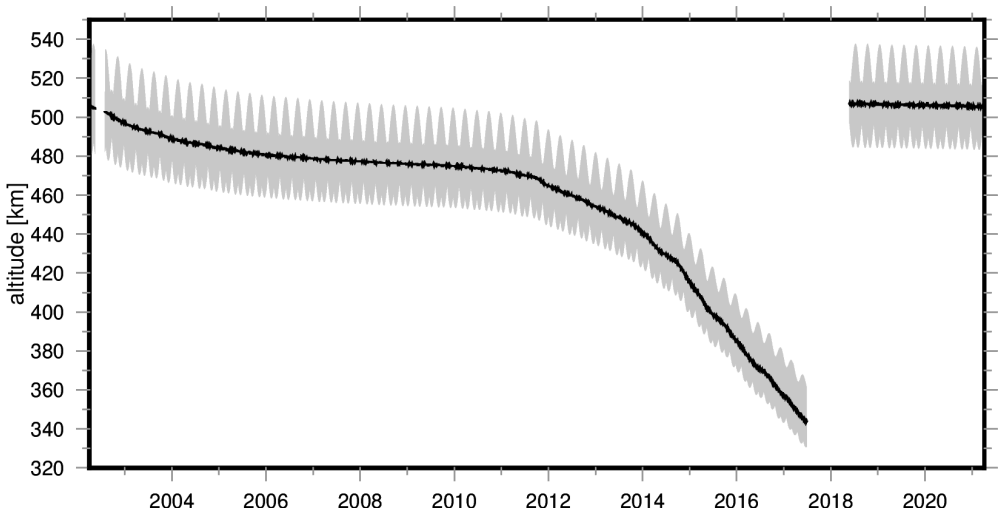

Figure 2.2: Evolution of the GRACE and GRACE-FO orbit altitude. The daily average height above the **G**eodetic **R**eference **S**ystem 1980 (GRS80) ellipsoid is indicated by the solid black line, while the daily minimum and maximum values are represented in gray.

(i.e. range, range-rate, and range-acceleration) between the satellites enabled the retrieval of the Earth's gravity field.

GRACE combined the two concepts of hl-SST and **l**ow-**l**ow **S**atellite-to-**S**atellite **T**racking (ll-SST) (see Section 4.1). To enable hl-SST, both satellites were equipped with a GPS receiver, as can be seen in Figure 2.4. The most obvious purpose of the GPS receivers was to determine the orbit with cm-accuracy. Furthermore, they assigned time tags to all payload data, enabled coarse positioning for real-time usage and could be used for atmospheric and ionospheric profiling. The key instrument for ll-SST - and the whole GRACE mission - was the dual one-way KBR system, developed by JPL. The horn, mounted on the front panel, transmitted and received the carrier phase signals between the satellites. These microwave signals consisted of two frequencies, 24 Hz and 32 Hz, and were generated by an ultra-stable oscillator. Ionospheric effects could be eliminated by a combination of the two frequencies. Eventually, the phase measurements allowed the determination of the range between the satellites with micrometer-accuracy.

Each satellite carried a SuperSTAR accelerometer in its **C**enter **o**f **G**ravity (CoG), built by French national aerospace research centre (ONERA, **O**ffice **N**ational d'**É**tudes et de **R**echerches **A**érospatiales) (Touboul et al., 1999). The accelerometer was needed to measure the sum of all non-gravitational accelerations, such as atmospheric drag, **S**olar **R**adiation **P**ressure (SRP), and **E**arth **R**adiation **P**ressure (ERP). These measurements were (and still are) important for gravity field recovery (to separate the non-gravitational accelerations from the gravitational ones) or for deriving atmospheric density variations. Moreover, a star camera assembly was mounted on each satellite. It was developed by Technical University of Denmark (DTU, **D**anmarks **T**ekniske **U**niversitet) and consisted of two star camera heads, which provided the attitude of the satellite with respect to an inertial reference frame. A **L**aser **R**etro-**R**eflector (LRR) was developed at GFZ and was used for orbit verification in connection with GPS. Figure 2.4 shows the physical layout of the instruments in the spacecraft. More information on the GRACE payload can be found on the GRACE mission pages of GFZ[1], NASA[2], and **C**enter for **S**pace **R**esearch (CSR)[3].

GRACE-FO carries enhanced versions of the GRACE payload, with up-to-date hardware and software. The United States and Germany jointly developed a LRI as an additional instrument onboard GRACE-FO, which offers the opportunity to improve the SST measurements (Abich

[1] https://www.gfz-potsdam.de/en/grace/grace-payload/ (last access: June 29, 2021)
[2] https://www.nasa.gov/mission_pages/Grace/spacecraft/index.html (last access: June 29, 2021)
[3] http://www2.csr.utexas.edu/grace/spacecraft/sis.html (last access: June 29, 2021)

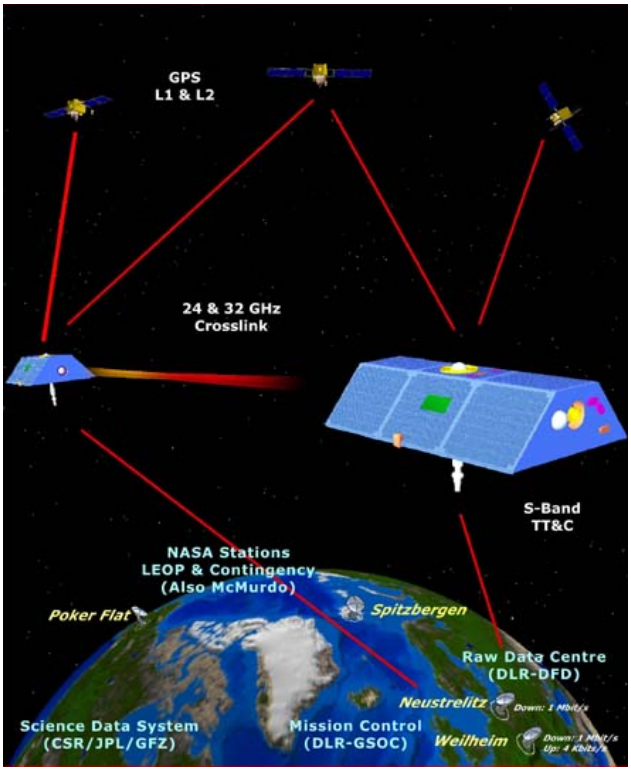

Figure 2.3: Measurement principle of the GRACE satellite mission (Source: http://www2.csr.utexas.edu/grace/mission/flight_config.html, last access: June 29, 2021).

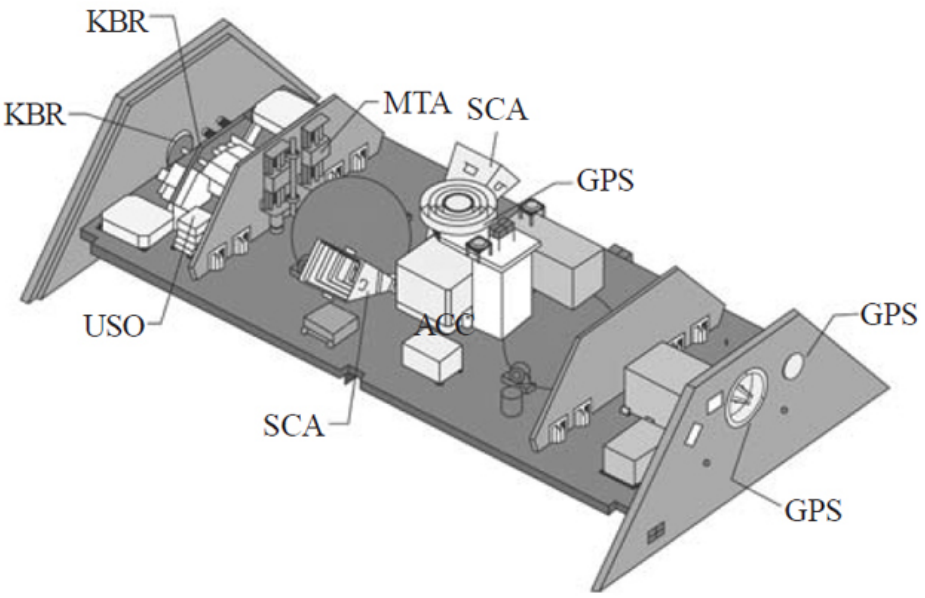

Figure 2.4: Instruments of the GRACE satellite mission (Source: https://www.nasa.gov/mission_pages/Grace/spacecraft/index.html, last access: June 29, 2021).

et al., 2015). The LRI is the first implementation of laser interferometry in space and provides the inter-satellite range changes with less noise than the KBR system (Abich et al., 2019). The instrument serves as a pathfinder for future gravity missions (Kornfeld et al., 2019).

2.1.3 GRACE Data Levels and Processing Centers

The GRACE and GRACE-FO **S**cience **D**ata **S**ystem (SDS) is responsible for science data processing, archiving and distribution. The tasks are shared between JPL, CSR, and GFZ for both the GRACE and the GRACE-FO mission. Data products are officially divided into different processing stages, from **L**evel-**0** (L0) to **L**evel-**3** (L3) data (Bettadpur, 2012).

Level-0
The raw measurements are stored in the L0 data. They are transmitted via telemetry to the GRACE **R**aw **D**ata **C**enter (RDC) at DLR in Neustrelitz at every pass of the satellites.

Level-1A
Once a non-destructive processing has been applied to the L0 data, they are referred to as **L**evel-**1A** (L1A) data. The processing includes sensor calibration, conversion from binary to engineering units, time tagging to the satellite receiver clock time, adding of quality control flags, and reformatting.

Level-1B
While L0 and L1A data is not publicly available, **L**evel-**1B** (L1B) and subsequent products are accessible to the public and contain the science instrument and housekeeping data products. The sampling rate is reduced and the data is transformed to a common reference frame. User handbooks for GRACE (Case et al., 2010) and GRACE-FO (Wen et al., 2019) contain all necessary information for a proper handling of the data.

Level-2
Level-**2** (L2) data contain the monthly time-variable gravity fields, stored as SH potential coefficients. Furthermore, ancillary data sets, such as mean atmospheric and oceanic mass variations are provided for a correct interpretation of the gravity field solutions. Detailed descriptions of the products can be found in the user handbooks for GRACE (Bettadpur, 2018) and GRACE-FO (Yuan, 2019b).

Level-3
The monthly SH potential coefficients are converted to L3 data, which can be described as gridded maps of EWH (Cooley and Landerer, 2020). The processing includes corrections to the potential coefficients (e.g., replacing lower degrees, GIA correction, and filtering, see Section 5.1). For ocean-related studies, additional steps have to be applied, as explained in Section 5.3.

As the processing chain from L1B to L2 data contains many different steps, a variety of gravity field solutions exist. Amongst them are the solutions of the three official processing centers: GFZ (Dahle et al., 2019a; Dahle et al., 2019b), JPL (Yuan, 2019a), and CSR (Save, 2019). Additional processing centers produce monthly GRACE and GRACE-FO gravity field solutions: e.g., Institute of Geodesy (IfG, **I**nstitut **f**ür **G**eodäsie) of the Graz University of Technology (Kvas et al., 2019a), Astronomical Institute of the University of Bern (AIUB, **A**stronomisches **I**nstitut der **U**niversität **B**ern) (Meyer et al., 2016; Meyer et al., 2019), Tongji University (Q. Chen et al., 2018; Q. Chen et al., 2019), and others. In this thesis, I work with the **I**nstitute of **T**heoretical Geodesy and **S**atellite **G**eodesy (ITSG)-Grace2018 data from IfG Graz, as they provide not only SH solutions but also the monthly normal equations, which will be needed in Chapter 6. Moreover, the solutions are unconstrained and are available for the whole GRACE(-FO) time period.

2.1.4 ITSG-Grace2018 Solutions

ITSG-Grace2018 gravity field solutions are generated at IfG of the Graz University of Technology and are based on **Re**l**e**ase (RL)06 processing standards (Mayer-Gürr et al., 2018; Kvas et al., 2019a). They are recovered using variational equations with an arc length of 24 hours up to maximum **d**egree and **o**rder (d/o) 60, 96, and 120, corresponding to wavelengths of about 330 km, 210 km and 170 km, respectively. In addition to the monthly gravity fields, the monthly means of the background models as well as the normal equations are provided online[4].

ITSG-Grace2018 gravity field solutions are continuously updated and improved. Klinger and Mayer-Gürr (2016) investigated the role of accelerometer data calibration within the gravity field recovery. They found a temperature-dependent behavior and the presence of off-diagonal elements in the accelerometer scale factor matrix. With their new calibration method, they considerably improved estimates of the c_{20} SH coefficient. Behzadpour et al. (2019) identified error sources in the GRACE range-rate residuals with the help of a multiresolution analysis using discrete wavelet transform. In 2019, Kvas and Mayer-Gürr (2019) further improved the gravity field solutions by incorporating background model uncertainties into the gravity field recovery process. Recently, Behzadpour et al. (2021) presented a novel approach to recover missing GRACE-D accelerometer data by using non-gravitational force models. Their results show an improvement of c_{20} and c_{30} SH coefficients as well as a generally reduced noise.

Figure 2.5 shows an overview of all available monthly ITSG-Grace2018 solutions. May 2015 is the only month that is not available in ITSG-Grace2018 while JPL, CSR, and GFZ provide a solution. However, a significant amount of L1B data is missing and the solutions of the official processing centers span April 12, 2015 to May 11, 2015. Other than that, the four processing centers provide the time-variable gravity fields for the same months. One can see monthly gaps due to missing L1B data. These occur, starting in 2011, because the KBR and accelerometer instruments were shut down systematically for 40-50 days of each β' cycle[5] in order to save battery capacity (Tapley et al., 2015). Furthermore, there is a gap of 11 months between GRACE and GRACE-FO. Months with inferior quality of the gravity field models are highlighted and should be interpreted with caution. These include (1) months with a groundtrack pattern close to a repeat orbit, which is unfavorable for gravity field determination and (2) the end-of-life period of GRACE, starting in November 2016 when the accelerometer of GRACE-B was shut down due to battery problems. For example, Save et al. (2006) developed a method to transplant accelerometer measurements from one GRACE satellite to the other. The approach was improved by e.g. Bandikova et al. (2019) and became part of JPL's RL06 processing strategy. However, the quality of the gravity field models is still inferior compared to earlier months. Due to unknown reasons, accelerometer measurements of GRACE-D exhibit a large noise level, such that they also need to be replaced by transplant data from GRACE-C. The current calibration approach to retrieve GRACE-FO L1B ACT accelerometer data is explained in McCullough et al. (2019), with the transplant procedure based on Save et al. (2006). Behzadpour et al. (2021) present an approach to further improve the data by incorporating non-gravitational force models.

In this thesis, ITSG-Grace2018 solutions are used as the "ground-truth" when evaluating time-variable gravity fields and mass changes from Swarm. In principle, solutions of any other processing center, such as JPL, CSR, or GFZ, could have been used as ground-truth because the quality of GRACE(-FO) is much higher than that of Swarm and differences between the GRACE(-FO) solutions would not be significant. ITSG-Grace2018 monthly **N**ormal **EQ**uations (NEQs) serve as the main input for mass-related sea level changes in Chapter 6.

[4] http://ftp.tugraz.at/outgoing/ITSG/GRACE/ITSG-Grace2018/monthly/ (last access: June 29, 2021)

[5] One β' cycle lasts 161 days and the β' angle is defined as the angle between the Earth-Sun-line and the orbital plane (Klinger, 2018).

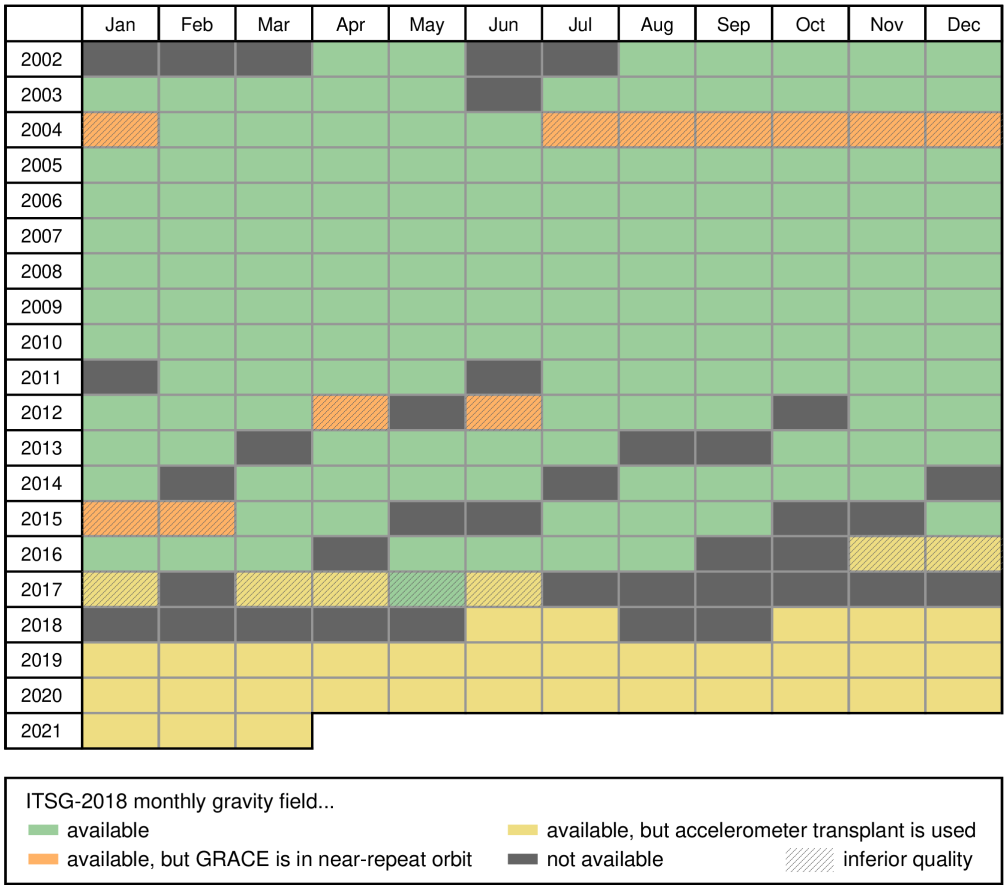

Figure 2.5: Availability of ITSG-Grace2018 monthly gravity fields up to March 2021.

2.2 Swarm

Swarm is a three-satellite ESA mission designed to provide the best survey of the Earth's geomagnetic field and its temporal variations (Friis-Christensen et al., 2008). The spacecraft were launched on November 22, 2013 from Plesetsk Cosmodrome in Russia. Figure 2.6 illustrates the orbit design: All three satellites are situated in a near-polar, near-circular orbit. Swarm A and C fly side-by-side at an initial altitude (after the orbit commissioning phase) of approximately 480 km, while Swarm B flies slightly higher at 530 km initial altitude.

In this thesis, Swarm plays a major role. The kinematic orbits of the satellites are used to derive fluctuations in the Earth's time-variable gravity field. This is possible even though Swarm is a magnetic field mission, but one should keep in mind that the resolution of the gravity fields is lower than the resolution of those derived from the dedicated gravity field mission GRACE(-FO). Swarm is needed to derive time-variable gravity fields (Chapter 4) and mass change (Chapter 5) and as an additional input in the sea level inversion (Chapter 6). Chapter 3 is dedicated to describe the Swarm mission in more detail, to ease the understanding of the results of this thesis.

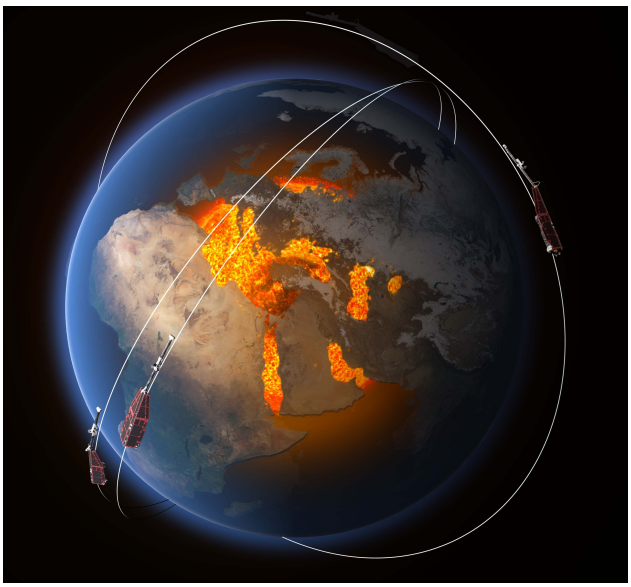

Figure 2.6: Illustration of the Swarm satellites in orbit (Source: https://earth.esa.int/eogateway/missions/swarm, last access: January 19, 2021).

2.3 Satellite Laser Ranging

The era of SLR began with the launch of NASA's Beacon-B satellite in 1964. SLR is used to measure the distance between a ground station and a satellite, which can be used to solve different geophysical tasks. The basic principle of SLR is relatively simple: A telescope on Earth transmits short laser pulses towards a satellite. A part of these pulses is reflected by a LRR, which is mounted on the spacecraft, and thus sent back to the telescope. Once the pulse is received, the distance can be computed from the two-way travel time (Tapley et al., 1985a). Figure 2.7 shows the current **I**nternational **L**aser **R**anging **S**ervice (ILRS) network of ground stations.

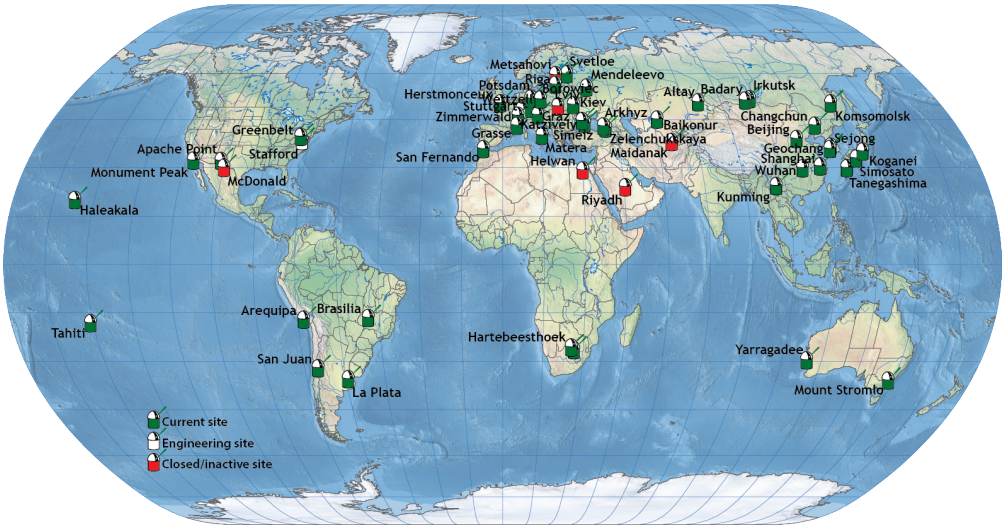

Figure 2.7: Network of ILRS stations (Source: https://ilrs.gsfc.nasa.gov/network/stations/index.html, last access: June 29, 2021).

Nowadays, LRR are usually part of any geodetic satellite mission. They serve as an independent tool for orbit validation within cm-accuracy. Furthermore, a group of dedicated SLR satellites exists, which are usually spheres with a diameter of several dm and completely covered with LRRs. This promises a long lifetime, because the need for spacecraft stabilization is reduced and only a rather small area is opposed to atmospheric drag.

Pearlman et al. (2019) summarize geophysical tasks that can commonly be solved with SLR. One well-known application is the retrieval of the long-wavelength part of the Earth's gravity field, where SLR is still supportively used today (e.g., Lerch et al., 1985; Reigber et al., 1985; Biancale et al., 2000; Meyer et al., 2019). Further examples of SLR applications are the determination of Earth rotation parameters (e.g., He et al., 1982; Tapley et al., 1985b), contribution to the definition of the **I**nternational **T**errestrial **R**eference **F**rame (ITRF) (e.g., Altamimi et al., 2016; Appleby et al., 2016), observing post-glacial rebound (e.g., Rubincam, 1984), determining ocean and solid Earth tides (e.g., Cazenave and Daillet, 1981; Williamson and Marsh, 1985), and many more. SLR measurements can be used to derive the low degrees of time-variable gravity fields, as was e.g. shown in Cheng et al. (1997) or Bianco et al. (1998). Recently, Löcher and Kusche (2021) presented a hybrid approach for recovering high-resolution time-variable gravity fields from SLR. They use the leading GRACE-derived spatial patterns and adjust the respective scaling factors within the dynamic orbit computation, while they estimate the lower SH degrees separately.

In this thesis, the five dedicated SLR satellites, **LA**ser **GEO**dynamics **S**atellite (LAGEOS)-1/2, Ajisai, Starlette, and Stella, will be relevant, as their orbital parameters are suitable for gravity field determination (see Figure 2.8 for an illustration of the satellites). Table 2.1 summarizes their most important characteristics, like the year of launch and their orbital parameters. Both LAGEOS satellites fly in an altitude of more than 5500 km and are thus the highest of those considered in this work. Ajisai, also referred to as **E**xperimental **G**eodetic **S**atellite (EGS), orbits the Earth in an altitude of 1500 km and is rather large and heavy, compared to other SLR satellites (215 cm in diameter and 685 kg). The special characteristic of Starlette's orbit is its high eccentricity of 0.021, resulting in different altitudes of 790 km and 1100 km in apogee and perigee, respectively. Stella is identical in construction, as compared to Starlette. However, Stella's orbit is almost circular with an altitude of 810 km.

(a) Lageos 1 and Lageos 2 (b) Ajisai (c) Stella and Starlette

Figure 2.8: Illustration of SLR satellites from Pearlman et al. (2019).

	LAGEOS-1	LAGEOS-2	Ajisai	Starlette	Stella
Year of Launch	1976	1992	1986	1975	1993
Agency	NASA	ASI	JAXA	CNES	CNES
Diameter [cm]	60.0	60.0	215.0	24.0	24.0
Mass [kg]	411	411	685	47.3	48.0
Altitude [km]	5860	5620	1500	790-1100	810
Eccentricity [-]	0.004	0.014	0.002	0.021	0.001
Inclination [°]	109.9	52.7	50.0	49.8	98.6

Table 2.1: Characteristics of SLR satellites used in this thesis (modified from Pearlman et al., 2019).

SLR will be used in this work (1) as a comparison to Swarm time-variable gravity fields (Section 4.3)

and (2) to correct low-degree SH potential coefficients in the gravity fields (Section 5.1). If not mentioned otherwise, the IGG-SLR-HYBRID_S5+4E[6] solution is used (Löcher and Kusche, 2021). In this solution, degrees 2-5 are estimated directly and degrees 6-60 are obtained from SLR while using GRACE-derived **E**mpirical **O**rthogonal **F**unctions (EOFs) as base functions. In Richter et al. (2021), we computed post-fit SLR range residuals to validate the Swarm time-variable gravity field solutions.

2.4 Satellite Radar Altimetry

All previously illustrated satellite missions can be used to derive the gravitational field of the Earth. Satellite radar altimetry differs from those missions in that its primary aim is to measure global and regional sea level variations. With altimetry, the topography of the ocean surface and the total sea level change can be determined, i.e. the sum of steric and mass-related variations. The first satellite altimetry measurements date back to the 1970s and were carried out by the Skylab (1973), **G**eodynamics **E**xperimental **O**cean **S**atellite **3** (GEOS-3) (1975), and Seasat (1978) missions. However, it took until the early 1990s that satellite altimetry achieved its breakthrough. Dedicated missions, like the **E**uropean **R**emote **S**ensing 1 (ERS-1) satellite (1991) and TOPEX/-Poseidon (1992), were equipped with more accurate instruments, which for example allowed for an improved POD.

Figure 2.9 illustrates the basic measurement principle, which is described by Chelton et al. (1989). A radar pulse is emitted in nadir direction by the altimeter, reflected at the sea surface and again received by the antenna. From the two-way travel time, the distance R between the satellite and the sea surface can be derived. The spacecraft's orbit is precisely tracked by GPS satellites, resulting in the altitude above the ellipsoid S. The sea surface height can be computed with the difference $S - R$.

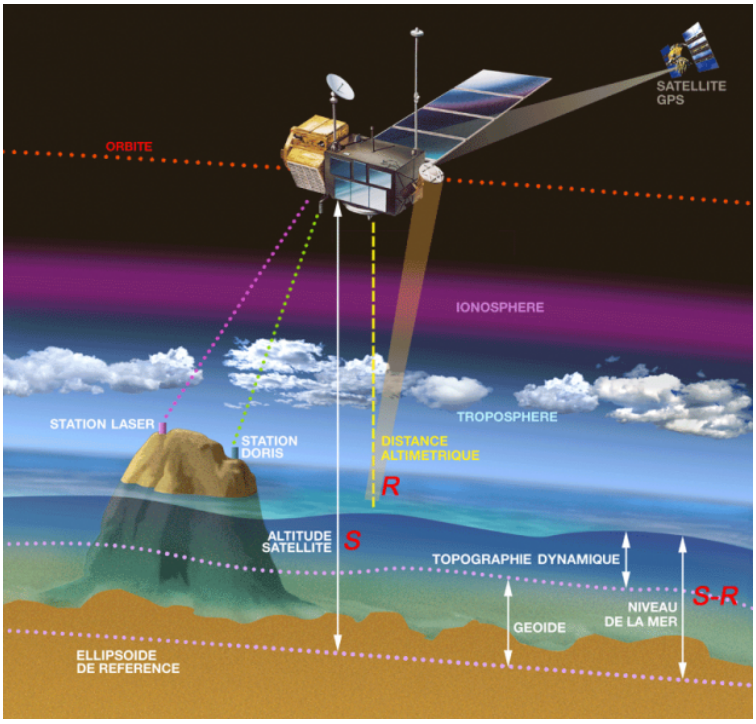

Figure 2.9: Measurement principle of satellite altimetry (Source: https://cnes.fr/en/how-altimetry-works, last access: June 29, 2021).

The usual orbit altitude of altimetry missions is 800 to 1300 km. Altimeter satellites usually fly

[6] http://icgem.gfz-potsdam.de/series/04_SLR/IGG_SLR_HYBRID/IGG-SLR-HYBRID_S5+4E (last access: August 8, 2021)

in a repeat orbit, which means that they observe the same location after a fixed time or, in other words, the groundtrack repeats after a certain number of days. Here, a compromise between a good spatial resolution (i.e. the track separation) and the temporal resolution (i.e. the repeat period) needs to be found.

Several corrections have to be applied to altimetry measurements. These include the ionospheric correction, the wet and dry tropospheric corrections, a sea state bias correction as well as geophysical and instrumental corrections (Andersen and Scharroo, 2011). Furthermore, retracking algorithms should be applied to obtain accurate water heights from the radar waveform (e.g., Uebbing et al., 2015).

The most obvious application of satellite radar altimetry is to measure sea level changes. Ablain et al. (2019) suggest the global mean total sea level rise to be 3.35 ± 0.4 mm/yr between October 1992 and December 2017. A special challenge is the processing of measurements in coastal zones, as evaluated e.g. by Benveniste et al. (2019). Moreover, satellite altimetry can be used to detect the thickness of ice sheets (e.g., Tilling et al., 2018) or the water level of rivers and lakes (e.g., Crétaux et al., 2017).

In this thesis, along-track sea surface heights derived from radar altimetry data will be used in Chapter 6 as input data for the sea level inversion. Table 2.2 gives an overview of the Jason missions, which are relevant in this work.

	Jason-1	Jason-2	Jason-3
Nominal mission orbit	2001-2009	2008-2016	2016-
Agency	NASA, CNES	NASA, CNES, NOAA, EUMETSAT	NASA, CNES, NOAA, EUMETSAT
Repeat cycle [days]	10	10	10
Spatial coverage [°]	± 66	± 66	± 66
Altitude [km]	1336	1336	1336
Track separation [km]	315	315	315

Table 2.2: Characteristics of radar altimetry satellites used in this thesis (information is taken from the respective mission pages[7]).

[7] https://jason.cnes.fr/en/JASON2/index.htm (last access: June 29, 2021)
https://www.aviso.altimetry.fr/en/missions/future-missions/jason-3.html?id=601&L=0 (last access: June 29, 2021)

Chapter 3

The Swarm Satellite Mission

ESA's three-satellite Swarm mission was launched on November 22, 2013 from Plesetsk (Russia) with the primary aim of studying the Earth's geomagnetic field and its temporal evolution (Friis-Christensen et al., 2008). Figure 2.6 shows an illustration of the satellites in orbit. Swarm is part of a series of Earth Explorer missions from ESA's **L**iving **P**lanet (LP) Programme (O. M. Johannessen et al., 1998). LP is a user-driven program, which addresses global environmental issues with Earth observation from space. LP missions have three main characteristics: (1) the missions are rather single-targeted than multi-purpose, (2) the missions should address a large community in order to get through the selection process, (3) there is a cost cap. Hence, LP missions are often a compromise, such that low-priced variants of secondary instruments are chosen in some cases (e.g., the accelerometers of the Swarm mission).

ESA's Earth Explorer missions investigate changes and interactions of the atmosphere, biosphere, hydrosphere, cryosphere, and the Earth's interior. CryoSat (later renamed as CryoSat-1) should have been the first Earth Explorer Mission, but its launch ended in a failure on October 8, 2005[1]. After CryoSat-1, five missions have been launched successfully, five further missions have been selected and proposals for Earth Explorer 11 were recently submitted (see Table 3.1). The GOCE satellite (Drinkwater et al. (2003), March 17, 2009 - November 11, 2013) measured the Earth's static gravity field with unprecedented accuracy and spatial resolution. GOCE has been part of many studies (e.g., J. Johannessen et al., 2003; Ebbing et al., 2018) and its scientific data is still utilized for today's gravity field models, for example the **E**uropean **I**mproved **G**ravity model of the **E**arth by **N**ew techniques (EIGEN) (e.g., Foerste et al., 2014), the **GRACE** **G**ravity **M**odels (GGMs) (which also include GOCE data, see e.g., Ries et al., 2016), or the **G**ravity **O**bservation **CO**mbination (GOCO) models (e.g., Kvas et al., 2019b).

Currently, four Earth Explorer missions are in orbit and collecting data. **S**oil **M**oisture and **O**cean **S**alinity (SMOS) (Barre et al., 2008) was launched on November 2, 2009 to measure the surface soil moisture and ocean salinity. It was followed by CryoSat-2 on April 9, 2010 (Wingham et al., 2006), which measures changes in the continental and marine ice sheets. Swarm was selected to be part of the Earth Explorer Programme in 2004 (Friis-Christensen et al., 2008) and has been collecting valuable data about the Earth's magnetic field since its launch in 2013. The Aeolus mission was launched on August 22, 2018 and measures horizontal wind profiles to improve weather forecasts (Stoffelen et al., 2005).

Five further missions have already been chosen to be part of the Earth Explorer Programme[2]: **Earth** **C**louds **A**erosols and **R**adiation **E**xplorer (EarthCARE) will study clouds, aerosols, and radiation, Biomass will investigate how much carbon is stored in the world's forests, **FL**uorescence **EX**plorer (FLEX) will measure vegetation fluorescence for photosynthetic activity studies, and **F**ar-infrared **O**utgoing **R**adiation **U**nderstanding and **M**onitoring (FORUM) will quantify the Earth's

[1] http://www.esa.int/Applications/Observing_the_Earth/CryoSat/CryoSat_Mission_lost_due_to_launch_failure (last access: July 8, 2021)

[2] https://www.esa.int/Applications/Observing_the_Earth/The_Living_Planet_Programme/Earth_Explorers/About_Earth_Explorers2 (last access: July 8, 2021)

radiation budget. The Harmony mission is currently in Phase-A (including feasibility studies) and will deliver new insights of the shape of the Earth's surface by using **S**ynthetic **A**perture **R**adar (SAR) measurements.

Satellite	Research Area	Start	Comment
(CryoSat-1	Ice	October 8, 2005	Launch failure)
GOCE	Gravity field	March 17, 2009	End: November 11, 2013
SMOS	Water	November 2, 2009	
CryoSat-2	Ice	April 8, 2010	
Swarm	Magnetic field	November 22, 2013	
Aeolus	Wind	August 22, 2018	
EarthCARE	Clouds and aerosols	2023 (planned)	
Biomass	Forests	2023 (planned)	
FLEX	Photosynthesis	2023 (planned)	
FORUM	Radiation	2026 (planned)	
Harmony	Shape of the Earth	Unknown	Currently in Phase A
Earth Explorer 11	Not yet decided	2031/2032	Proposals received in Dec. 2020

Table 3.1: ESA's Earth Explorer Missions.

As this thesis uses Swarm data to retrieve time-variable gravity fields and ocean mass changes, the following sections describe the mission in more detail. Swarm consists of three identical satellites Swarm Alpha, Swarm Beta, and Swarm Charlie. They are often referred to as Swarm A, B, and C, which is also adapted in this thesis for reasons of simplicity. After launch, orbit maneuvers were conducted during the commissioning phase, until the satellites reached their selected near-polar orbit in April 2014 (van den IJssel et al., 2015). Swarm A and C fly side-by-side and were placed in an initial altitude of about 480 km, while Swarm B flies in a higher orbit of an initial altitude of about 530 km (see Figure 2.6). The nominal mission duration (starting after the commissioning phase) was initially defined as four years. In November 2017, the Earth Observation Programme Board approved an extension until the end of 2021.

In February 2018, ESA introduced **E**nhanced **P**olar **O**utflow **P**robe (e-POP) as the fourth element of the Swarm mission[3]. e-POP is now called Swarm Echo or simply Swarm E and is part of the payload on **C**anadian **S**pace **A**gency (CSA)'s **CA**scade **S**mall**S**at and **IO**nospheric **P**olar **E**xplorer (CASSIOPE) satellite mission (Yau and James, 2015). It collects space weather data and provides an improved understanding of magnetosphere-ionosphere coupling. However, CASSIOPE's orbit is not well suited for the use of gravity field retrieval. Montenbruck et al. (2019) mention three unfavorable characteristics: (1) The orbit is highly elliptical (325 km to 1500 km) and high altitudes are less useful for gravity field determination, (2) POD achieves a decimeter-level accuracy, which is inferior to Swarm A-C's accuracy of a few cm (van den IJssel et al., 2015), and (3) the typical data availability is less than 50 % with regular long-duration gaps. For these reasons, I only consider Swarm A, B, and C's orbits in this thesis.

3.1 Objectives of the Swarm Mission

The magnetic field varies in strength and direction. It is of utmost importance to observe these quantities, as the magnetic field acts as a protecting shield against solar radiation. The Swarm satellite mission was designed to provide the best ever survey of the Earth's geomagnetic field and its temporal evolution (Friis-Christensen et al., 2006; Friis-Christensen et al., 2008). In this section, the primary research objectives, as they were defined by Friis-Christensen et al. (2006) before launch, are described:

[3] https://www.esa.int/Applications/Observing_the_Earth/Swarm/Swarm_trio_becomes_a_quartet (last access: July 8, 2021)

Core Dynamics, Geodynamo Processes, and Core-Mantle Interaction

One of the main goals of the Swarm mission is to improve models of the core field dynamics. This will be accomplished by ensuring long-term space observations with a better spatial and temporal resolution than former magnetic field missions, such as Ørsted, CHAMP, and Scientific Application Satellite-C (SAC-C, **S**atélite de **A**plicaciones **C**ientíficas-**C**) (Olsen et al., 2006; Sabaka and Olsen, 2006; Lesur et al., 2006). The temporal resolution of core surface flow models will also be improved, opening the possibility of further investigating torsional oscillations (Zatman and Bloxham, 1997; Pais and Hulot, 2000), core-mantle interactions (Holme, 2000; Jault, 2003), geomagnetic jerks (Mandea et al., 2000) as well as the connections between them (Le Huy et al., 2000; Bloxham et al., 2002; Holme and de Viron, 2005). By combining Ørsted, CHAMP, and Swarm observations, it will furthermore be possible to investigate magnetohydrodynamic phenomena that potentially affect the core on sub-annual to decadal scales, down to wavelengths of about 2000 km. Finally, Swarm will contribute to understanding the role of magnetic diffusion in the core and to predicting the future development of the Earth's magnetic field.

Lithospheric Magnetisation and its Geological Interpretation

Before the launch of the Swarm mission, Maus et al. (2006) resolved the lithospheric crustal field up to spherical harmonic d/o 90 (corresponding to ≈450 km) from CHAMP data. Lower wavelengths, starting at d/o 150 (corresponding to ≈270 km), can be obtained from aeromagnetic surveys. The launch of Swarm offers the opportunity to close the spectral gap in the middle crust. Maus et al. (2006) and Olsen et al. (2006) demonstrate that combining Swarm with aeromagnetic surveys will provide a global coverage of lithospheric fields from 5 to 3000 km. Before Swarm, the understanding of plate tectonics in the oceanic lithosphere was limited due to the sparse data coverage in the southern oceans. For the first time, the identification of oceanic magnetic stripes from satellite altitude will be possible with Swarm. Artifacts in along-track direction will be limited due to the unique constellation of the three Swarm satellites (Maus et al., 2006a).

3-D Electrical Conductivity of the Mantle

Knowledge about the electrical conductivity of the mantle also sheds light on its physical and chemical properties. Mantle conductivity can be measured by geomagnetic observatories, but their distribution is sparse and inhomogeneous, especially in oceanic regions. Hence, observations from space are necessary to obtain global coverage of the 3-D electrical mantle conductivity structure of the deep Earth. Kuvshinov et al. (2006) show that the Swarm mission is well suited for this aim, since the constellation of three magnetic field satellites provides simultaneous observations over different regions, as opposed to a single satellite.

Currents Flowing in the Magnetosphere and Ionosphere

Currents in the ionosphere and magnetosphere affect magnetic field models and thus limit the understanding of the Earth's interior. Sabaka et al. (2004) developed a joint inversion approach that allows to model the Earth's core field and its secular variations together with ionospheric and magnetospheric contributions. As shown in Olsen et al. (2006), the Swarm mission will be able to separate internal and external sources even better, and thus improve geomagnetic field models, by simultaneously measuring at different altitudes and local times. Moreover, Swarm will be the first mission to determine the near-Earth field-aligned currents, which connect the magnetosphere with the ionosphere, and will thus significantly improve the understanding of the upper atmosphere dynamics (Ritter and Lühr, 2006; Moretto et al., 2006; Vennerstrom et al., 2006).

In addition, Friis-Christensen et al. (2006) defined two secondary research objectives:

Identification of Ocean Circulation by its Magnetic Signature

Ocean circulations produce a magnetic field that affects the magnetic field at satellite altitude. Hence, by observing the magnetic field from space, it will be possible to identify ocean flows.

Lithospheric field models will be improved by correcting magnetic data for ocean tidal signals. Manoj et al. (2006) demonstrate, based on ocean circulation and conductivity models, that the expected field amplitudes are within the resolution of the Swarm satellites.

Quantification of Magnetic Forcing of the Upper Atmosphere
The geomagnetic field has a direct impact on the dynamics of ionized and neutral particles in the upper atmosphere. Swarm will help to understand the system by providing high-resolution and simultaneous in-situ measurements of the interacting fields and particles. Furthermore, Swarm's plasma density measurements allow a detailed mapping of the structure of the ionospheric phenomena.

Swarm's research objectives have already been addressed in many studies: Swarm data has, for example, contributed to models of the core magnetic field (Finlay et al., 2016), the lithospheric magnetic field (Thébault et al., 2016), to a better understanding of magnetospheric and ionospheric currents (Laundal et al., 2018) and magnetic storms (Vichare et al., 2019). More research highlights of the Swarm mission are summarized in Olsen et al. (2016).

Regarding the aims outlined above, it is obvious that Swarm was designed to contribute new insights to the scientific field of geomagnetism. In this thesis, however, Swarm will be used for a totally different purpose: I will use Swarm data to derive time-variable gravity fields and large-scale mass redistribution in the Earth system. One should keep in mind that Swarm is not a dedicated gravity field mission and will not provide gravity fields with GRACE(-FO) resolution. Yet, it is extremely important to find alternatives for GRACE(-FO) as the gap between the missions, as well as the monthly GRACE gaps, reveal.

3.2 Constellation of the Swarm Mission

The Swarm mission consists of three LEO satellites in a near-polar orbit. Swarm A and C fly side-by-side while Swarm B's orbit is slightly higher. All three satellites were launched into the same orbital planes. The orbital planes precess westwards; but the rate of precession is different for Swarm A/C and B, leading to a relative drift of the plane (Figure 3.1). At the beginning of 2018, the orbital plane of Swarm A/C was perpendicular to that of Swarm C. Provided that the drift will proceed as during the previous years, Swarm B will be counter-rotating the lower pair in late 2021.

Figure 3.2 shows the evolution of the satellites' altitudes. Right after launch, the altitude of all three spacecraft was approximately 508 km. During the commissioning phase, which lasted until April 2014, the satellites were placed in their selected orbits of approximately 480 km (Swarm A and C) and 530 km (Swarm B) altitude. Non-gravitational accelerations, with the air drag being the most prominent one, lead to a natural orbit decay. This effect depends on the thermospheric density and is larger for the lower pair. In the beginning of 2021, after seven years in orbit, the altitude decreased to about 443 km (Swarm A and C) and 512 km (Swarm B). The orbital period of the satellites is between 93 minutes and 95 minutes, depending on the semi-major axis and thus on the orbit decay.

The Swarm satellites fly in a near-polar orbit, with an inclination i between 87° and 88°. Figure 3.3 shows the evolution of the inclination since launch. During the nominal mission phase, Swarm A's and C's inclination varies between 87.24° and 87.45°, with a period of approximately 2 years and 8 months. One can see that Swarm A's inclination was slightly changed in October 2019. Swarm B's orbital plane is generally more tilted with respect to the equatorial plane, with values between 87.65° and 87.86° and a period of about 3 years and 1 month.

The longitude of the ascending node Ω, also called the **R**ight **A**scension of the **A**scending **N**ode (RAAN) is defined as the angle, measured in the equatorial plane, between the two lines "center of the Earth to the vernal equinox" and "center of the Earth to the upward crossing of the orbit on the equatorial plane". Figure 3.4 shows the evolution of the RAAN of the Swarm orbits. As the

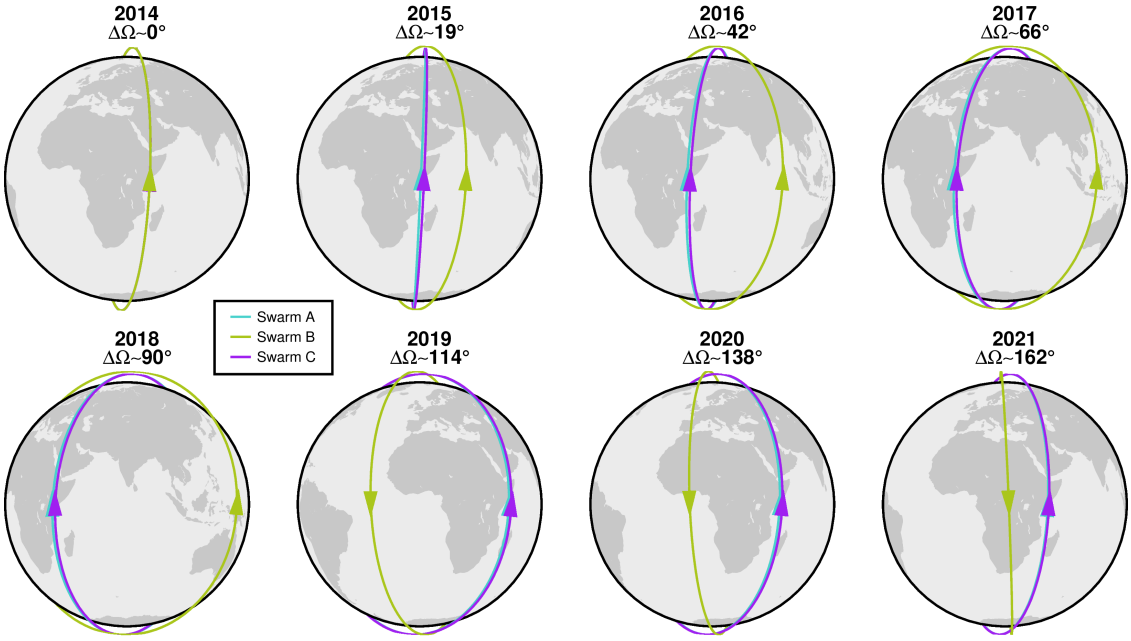

Figure 3.1: Constellation of the Swarm satellite mission. The orbit is shown for the beginning of each year and the world map is plotted as a reference only (fixed to Swarm A's equator crossing). All satellites were launched into the same orbital plane. At the beginning of 2018, the orbital planes of Swarm A/C and B are perpendicular. Starting from 2019, the view is modified, such that the descending orbit of Swarm B is shown.

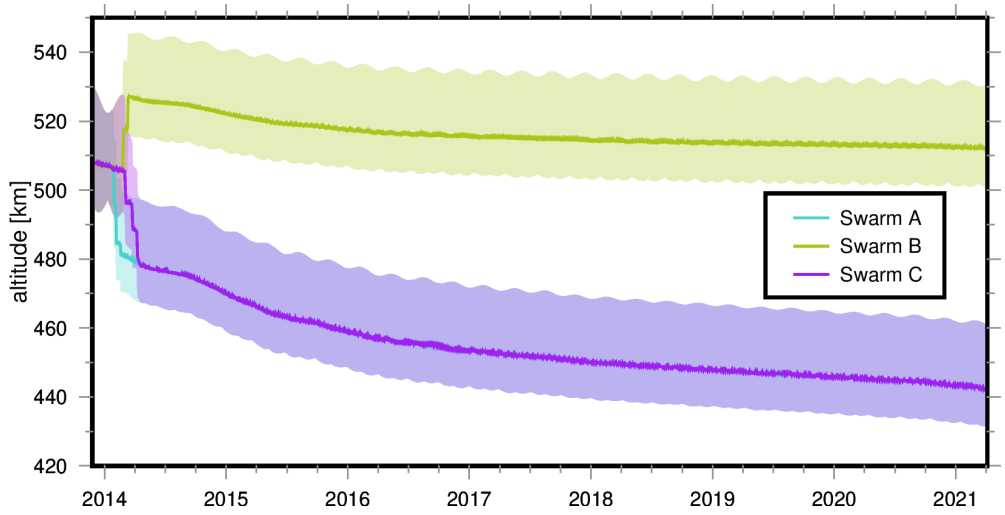

Figure 3.2: Evolution of the Swarm orbit altitude. The daily average height above the GRS80 ellipsoid is indicated by the solid line, while the daily minimum and maximum values are represented by the shaded areas.

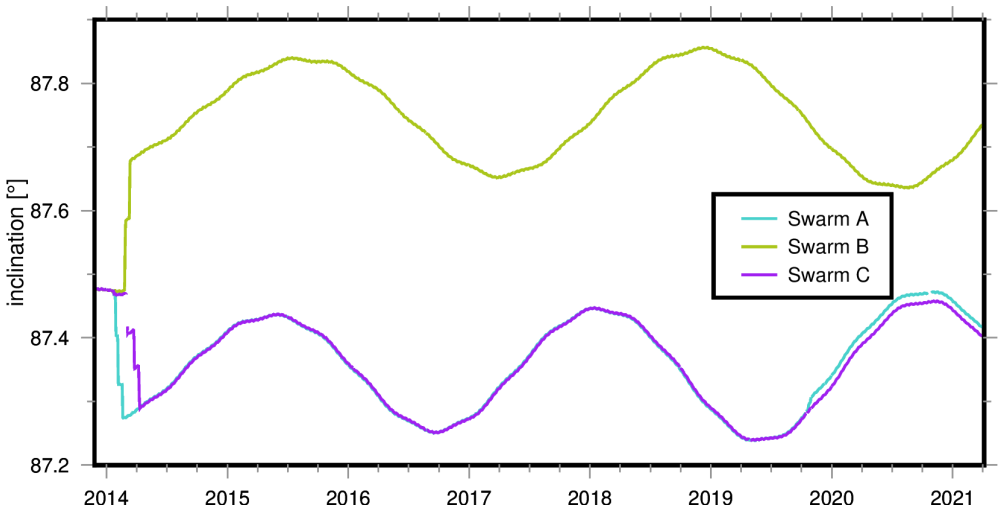

Figure 3.3: Evolution of the Swarm orbit inclination.

three satellites were initially placed into the same orbit, they all had the same RAAN. Naturally, the RAAN changes as a function of essentially the semi-major axis a and the inclination i. During the commissioning phase, Swarm A and C were lowered, while Swarm B was raised to a higher orbit. As a result, a and i changed and the orbital planes started to precess at a different rate. Swarm A's and C's plane precess westward with approximately 133 °/yr and Swarm B's rate is 109 °/yr. Consequently, the orbital plane of Swarm B drifts with respect to A and C with 24 °/yr. This peculiarity of Swarm's constellation could already be seen in Figure 3.1 and is also visible in Figure 3.4, where the temporal evolution of the RAANs is plotted in detail. At the beginning of 2018, the orbital planes are perpendicular. As Swarm A and C fly side-by-side, they precess almost equally. Their RAANs differ by approximately 1.4°, resulting in a distance between the spacecraft of less than 200 km, with a decrease in the second half of 2019, when the inclination of Swarm A was changed.

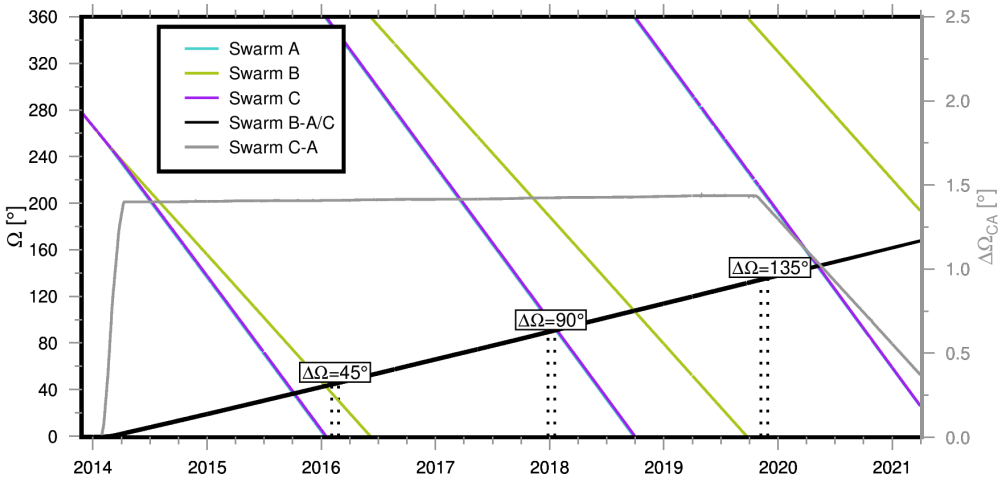

Figure 3.4: Evolution of the RAAN of the Swarm orbits. The black and gray lines indicate the difference between the RAAN of the satellites. Notice that the right y-axis is only valid for $\Delta\Omega_{CA}$, i.e. the difference of the RAAN of Swarm A and C. In the beginning of the mission, the orbital planes were the same. Perpendicular orbital planes result in a difference of 90° ($\Delta\Omega_{BA}$ and $\Delta\Omega_{BC}$ in January 2018).

3.3 Instruments of the Swarm Mission

Swarm A, B, and C are identical in construction. On the one hand, the payload of each satellite consists of the common instruments for Earth observation satellites: a **S**tar **TR**acker (STR), a

Global Positioning System Receiver (GPSR), and an accelerometer. On the other hand, there are three further instruments that are related to the goals of the mission: an Absolute Scalar Magnetometer (ASM), a Vector Field Magnetometer (VFM), and an electrical field instrument Electric Field Instrument (EFI). Figure 3.5 shows a sketch of the spacecraft with the positions of its instruments. If not stated otherwise, the following description of the individual instruments is based on ESA's earth observation information discovery platform[4].

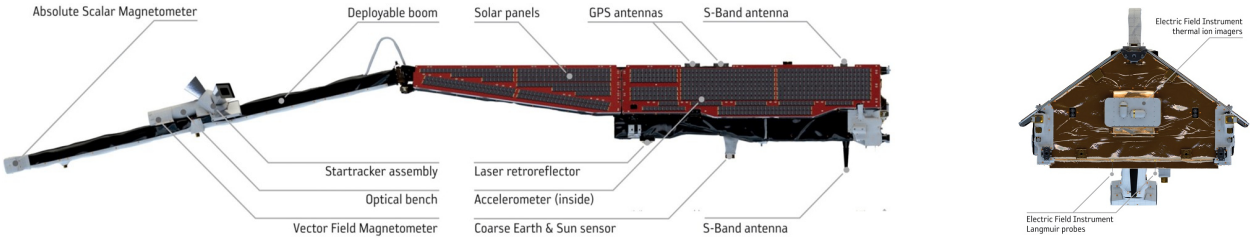

(a) Side view. (b) Front view.

Figure 3.5: Instruments of the Swarm satellite mission (Source: https://earth.esa.int/eogateway/missions/swarm, last access: July 8, 2021).

Vector Field Magnetometer (VFM)

The high-precision VFM, developed by DTU Space is the core instrument of the Swarm mission. It measures the magnitude and direction of the magnetic field, which is one of the prime research objectives (Section 3.1 and Friis-Christensen et al., 2006).

The VFM shares an optical bench, which is situated halfway along the satellite's boom, together with the star trackers. It consists of a Compact Spherical Coil (CSC), creating a homogeneous magnetic field, and a Compact Detector Coil (CDC). The CSC currents are adjusted in order to maintain a null field at the CDC. The currents are observed and provide the raw measurements of the Earth's magnetic field. Tøffner-Clausen et al. (2016) developed a model for the calibration of magnetic field measurements.

Absolute Scalar Magnetometer (ASM)

The ASM provides absolute measurements of the intensity of the Earth's magnetic field with a sampling of 1 Hz. It was designed by Alternative Energies and Atomic Energy Commission - Research Institute for Electronics and Information Technologies (CEA-LETI, Commissariat à l'Énergie Atomique et aux énergies alternatives - Laboratoire d'Électronique et de Technologie de l'Information) and developed in collaboration with National Centre for Space Studies (CNES, Centre National d'Études Spatiales) (Hulot et al., 2015).

Since ASM measurements of the strength of the magnetic field are of a higher accuracy than those of any other magnetometer, the ASM is used for the in-flight calibration of the VFM. Hulot et al. (2015) and Leger et al. (2015) investigate the performance of the instrument's independent vector readings of the magnetic field.

The ASM is situated at the end of the satellite's boom and makes use of the Electron Spin Resonance principle and the Zeeman effect. More details on the operating mode can be found in the aforementioned studies.

Star Tracker (STR)

The STR aboard each Swarm spacecraft measures the orientation and attitude of the satellite in space. It was developed by DTU Space.

[4] https://earth.esa.int/eogateway/missions/swarm (last access: July 8, 2021)

The basic principle of STRs is described in Liebe (2002). Swarm uses three **C**amera **H**ead **U**nits (CHUs), fixed to the optical bench, to take pictures of the stars in its **F**ield **o**f **V**iew (FoV). The inter-boresight angles between the CHUs are approximately 90°, such that not more than one camera is blinded by big objects, like Sun or Moon, at a time (Herceg et al., 2017). Hence, usually two or three pictures are taken simultaneously. By localizing and identifying the stars on the pictures, the attitude of the satellite is determined and provided in terms of quaternions.

In October (Swarm B) and December (Swarm A and C) 2018, the rate of the L1B data product was changed from 1 to 2 Hz. STRs can be considered as an essential part of the payload, as without the attitude information, measurements from other instruments could become worthless (Klinger, 2018). The STR data product is e.g. needed to transform accelerometer measurements from the satellite reference frame (x-direction is roughly along-track, y-direction is roughly cross-track, z-direction is roughly radial) into a global reference frame. In this thesis, star camera measurements are also utilized in order to model the non-gravitational accelerations and to compute covariance functions of the POD in the satellite reference frame.

Electric Field Instrument (EFI)

The Swarm satellites carry an EFI to characterize the electric field around the Earth. The instrument was funded by the Canadian Space Agency and developed by COM DEV in Canada. It provides high-resolution measurements of the electron density, electron temperature as well as plasma density, drift, velocity, and acceleration.

The EFI consists of **S**uprathermal **I**on **I**mager (SII) sensors, the **L**angmuir **P**robe (LP) sensors, and the electronics Assembly. It is attached to the front side of the spacecraft, with the LPs pointing in nadir direction (see Figure 3.5 (b)). Knudsen et al. (2017) describe the EFI, its in-flight performance, and possible applications in more detail.

Global Positioning System Receiver (GPSR)

Each Swarm spacecraft is equipped with two high-quality eight-channel dual-frequency GPSRs, which were developed by Joint Stock Defense Company (RUAG, **R**üstungs**U**nternehmen-**A**ktien-**G**esellschaft) Space (Zangerl et al., 2014). The most obvious application of GPS observations is to geotag data of all other instruments. Furthermore, the satellites' orbits can be precisely determined (see Chapter 3.5), which allows the retrieval of time-variable gravity fields of the Earth.

The GPSRs are composed of an antenna and a receiver electronics unit. Only the main receiver of each satellite is operating in nominal mode, while the redundant one will be used in case of a failure of the main receiver (van den IJssel et al., 2016).

Schreiter et al. (2019) evaluate how ionospheric disturbances affect the Swarm GPSRs and thus also map into the time-variable gravity fields. Several receiver updates, such as tracking loop modifications or changes in the antenna FoV, have been carried out to improve the performance of the GPSRs (Dahle et al., 2017). Moreover, the sampling rate was increased from 0.1 to 1 Hz on July 15, 2014.

Laser Retro-Reflector (LRR)

The Swarm spacecraft carry a LRR, manufactured at GFZ, for supporting, externally validating and calibrating data from the GPSR. The LRR consists of four prisms, arranged on a 45° pyramid on the bottom side of each satellite. The instrument's size is 10 cm×10 cm×4.8 cm and it weighs 400 g.

A ground station sends laser pulses to the LRR, which then reflects the pulses back to the station (i.e. the LRR is a passive payload). From the measured runtime of the pulses, the distance between the ground station and the LRR can be derived. SLR stations all over the world track the satellites with high accuracy (see Section 2.3). As opposed to GPS, the measurement principle

of SLR directly links the satellite's position to the terrestrial reference frame, without introducing ambiguities. However, the temporal and spatial coverage is inferior to that of GPS.

Accelerometer (ACC)

The Swarm accelerometers were developed and manufactured by the Czech Aerospace Research Centre (VZLU, **V**ýzkumný a **Z**kušební **L**etecký **Ú**stav) (Fedosov and Peřestý, 2011). An accelerometer measures the sum of all non-gravitational accelerations that act on a satellite. For LEO satellites, the non-gravitational forces are dominated by atmospheric drag, followed by SRP and ERP. Apart from the accelerations that act on a satellite's surface, accelerometers also observe satellite-induced accelerations. These include, amongst others, thruster firings, which are occasionally needed to maintain the nominal altitude, as well as heater switches and accelerations induced by a magnetic torquer (Flury et al., 2008; Peterseim et al., 2012).

Each Swarm satellite carries one accelerometer of 17.7 cm×20.4 cm×36 cm and 6.06 kg. The center of the sensor is located in the spacecraft's CoG. The sensor is composed of a cubic proof-mass, which levitates in a cubic cavity. Control voltages ensure that the proof mass is able to flow freely in the cavity. Gravitational forces, such as the central term of the Earth's gravity field or perturbations thereof, act on both, the satellite and the proof mass in the same way. This means that the position of the proof mass with respect to the cavity does not change. Non-gravitational forces, on the other hand, only act on the surface of the satellite. The control voltage, which is needed to keep the proof mass levitating, is related to the magnitude of the non-gravitational accelerations.

However, the Swarm accelerometers suffer from a variety of errors and noise, such that the data quality is much reduced as compared to the ONERA accelerometers flown on GRACE(-FO) and GOCE. Thus, the possible use of the Swarm accelerometer data is limited. Siemes et al. (2016) evaluate how sudden bias changes ("steps"), temperature-induced bias changes, thruster spikes, and **E**rror **D**etection **A**nd **C**orrection (EDAC) failure events degrade the quality of accelerometer data. They clean and calibrate the along-track accelerations of Swarm C in order to derive thermospheric neutral densities. As it is beneficial for the retrieval of time-variable gravity fields to include all three components of the three satellites (Lück et al., 2018), it is shown in Chapter 3.6 how non-gravitational accelerations can be modeled.

3.4 Swarm Data Products

Swarm data products are classified into different categories, depending on their processing state. The Swarm **P**ayload **D**ata **G**round **S**egment (PDGS), managed by ESA's **E**uropean **S**pace **R**esearch **IN**stitute (ESRIN), processes the raw instrument data to Level-1 data, while the Swarm **S**cientific **P**rocessing **C**entres (SPCs) produce the majority of Level-2 data. The PDGS is responsible for making Level-1b and Level-2 products publicly available. The product identifier always consists of 10 characters of the form AAAxBBBBLL, where

AAA ... file category (instrument-specific),
x ... "A", "B" or "C", for Swarm A, Swarm B or Swarm C,
BBBB ... description of the product,
LL ... product level, e.g. "1B" or "2_".

A short description of each processing step, including examples of the products relevant for this thesis, can be found below.

3.4.1 Level-0 Data Products

Swarm measurements are initially received as Level-0 data. These raw and uncalibrated products are time-ordered and free from duplicates. PDGS makes the Level-0 data available to all SPCs.

3.4.2 Level-1a Data Products

Level-0 products are decoded and reformatted to obtain the Level-1a products. Nielsen (2019) describes the conversion from Swarm Level-0 data to Level-1a data in detail. Level-1a products consist of housekeeping, instrument, and auxiliary data that are needed for further processing and calibrations. The data are grouped into blocks containing coherent sets of observations and converted to either engineering units or physical units. Level-1a products are not available to the public, but they are (as the Level-0 products) distributed to all SPCs for further processing.

3.4.3 Level-1b Data Products

Level-1b data are corrected and calibrated time series of relevant quantities along the satellites' orbits (PDGS Team, 2018). Each data set consists of three files: a data file, a header file, and a data quality report (Siemes, 2019). The products are freely available via anonymous **F**ile **T**ransfer **P**rotocol (FTP)[5] with a latency of a few days. Nielsen (2019) explains the contents of all Swarm Level-1b products. Attitude, GPS RINEX observation data, and preprocessed accelerometer data are described in the following (based on Nielsen, 2019b), as they are relevant for this thesis.

STRxATT_1B

The STRxATT_1B data product provides information on the spacecraft's attitude, measured by the on-board star cameras. The time stamp refers to **C**oordinated **U**niversal **T**ime (UTC) and the attitude is represented in terms of quaternions. These quaternions describe the rotation from the spacecraft reference frame to the ITRF2008. Furthermore, quality flags characterize the attitude information and a maneuver ID specifies if a satellite maneuver was carried out. The STRxATT_1B product is stored in daily .cdf files. Initially, the sampling rate was 1 Hz. This was changed to 2 Hz in October (Swarm B) and December (Swarm A and C) 2018. It is important to know that the STRxATT_1B data product refers to the transformation between the satellite reference frame and the ITRF, while it is more common to specify the attitude with respect to the inertial reference frame.

GPSx_RO_1B

The GPSx_RO_1B data product stores the GPSR data as daily files in the **R**eceiver **IN**dependent **EX**change Format (RINEX) 3.00 format (Gurtner and Estey, 2007). The time stamp refers to GPS time and the files contain GPS RINEX observation data with a sampling of 0.1 Hz until July 15, 2014 and 1 Hz afterwards.

ACCx_PR_1B

The ACCx_PR_1B data product provides preprocessed acceleration data. The time stamp refers to UTC and linear and angular accelerations are given in the spacecraft reference frame. Furthermore, the position of the proof mass within the accelerometer cavity and the temperature of the instrument are provided. Quality flags assess the performance of the accelerometer. Swarm accelerometer measurements suffer from a variety of errors (Siemes et al., 2016) and it was consequently decided to not distribute the ACCx_PR_1B to the regular users. Instead, they can find data that is further processed in the Level-2 products. In Section 3.6, the approach to obtain modeled non-gravitational accelerations that is pursued in this thesis is explained.

SC_xDYN_1B

The SC_xDYN_1B data product provides auxiliary data for precise orbit determination and non-gravitational acceleration modeling. The time stamp is specified as UTC and the product contains

[5] ftp://swarm-diss.eo.esa.int/Level1b/Latest_baselines/ (last access: July 8, 2021)

information such as the mass of the spacecraft, temperature and pressure of the gas tanks or the position of the CoG in the spacecraft reference frame.

3.4.4 Level-2 Data Products

Swarm Level-2 products contain data and models derived from Level-1b, such as magnetic field models, thermosphere neutral density, and POD products. Level-2 data are either publicly available[6] (indicated by "_2" in the product type) or intermediate (indicated by "i2" in the product type), which means that they are only available to SPC and PDGS (Siemes, 2019). Publicly accessible data is validated prior to release, while the validation of intermediate products is not yet completed.

Level-2 data is characterized by the categories CAT-1 and CAT-2. SPC produces the CAT-1 products, which cannot be automated and needs supervision. CAT-2 products are automatically generated by the Swarm PDGS, including a quality report. Kervalishvili (2019) specifies all Swarm Level-2 data and the following explanations are taken from there. Due to their relevance for this thesis, orbit products, calibrated accelerometer data, and monthly gravity fields are presented below.

SP3xCOM_2_

The SP3xCOM_2_ data product provides a time series of position and velocity of the **C**enter **o**f **M**ass (CoM) of each satellite from reduced-dynamic POD. Position and velocity are represented in the ITRF2008 in km and dm/s, respectively, and the time reference is GPS time. Data is stored in daily files with a sampling of 10 s. The following Level-1B input data is required for generating the SP3xCOM_2_ data product: GPSx_RO_1B, STRxATT_1B, MODx_SC_1B (which contains position and velocity from a preliminary medium-accuracy orbit determination), and SC_xDYN_1B. Moreover, external data from **I**nternational **G**NSS **S**ervice (IGS), **I**nternational **E**arth **R**otation **S**ervice (IERS) and **C**enter for **O**rbit **D**etermination in **E**urope (CODE) is used as input. For more information on reduced-dynamic orbits, please have a look at Section 3.5, van den IJssel et al. (2015), van den IJssel et al. (2016), and Montenbruck et al. (2018).

SP3xKIN_2_

The SP3xKIN_2_ data product contains a time series of the position of the CoM of each satellite from kinematic POD. The position is represented in the ITRF2008 and is given in units of km. The time reference is GPS time. SP3xKIN_2_ is stored in daily files, with the same sampling as the GPSx_RO_1B input data. This means that the sampling rate is 10 s until July 15, 2014 and 1 s afterwards, with possible data gaps. Apart from the GPSx_RO_1B data product, STRxATT_1B, MODx_SC_1B, SC_xDYN_1B, and external data from IGS, IERS, and CODE is used as input. More details on Swarm kinematic orbits can be found in Section 3.5, van den IJssel et al. (2015), van den IJssel et al. (2016), and Montenbruck et al. (2018). Apart from this official product, several kinematic orbit products are provided by other groups (Section 3.5).

ACCxPOD_2_

The ACCxPOD_2_ data product contains a time series of non-gravitational accelerations obtained from POD in units of m/s^2. The time reference is UTC and the data is stored in daily files with time steps of 30 s. The non-gravitational accelerations are computed from GPS data using a Kalman filter approach. The SP3xCOM_2_ product is used as a priori reference orbit.

[6] ftp://swarm-diss.eo.esa.int/Level2daily/Latest_baselines/ (last access: July 8, 2021)

ACCxCAL_2_

The ACCxCAL_2_ data product provides corrected and calibrated accelerometer observations including all correction and calibration parameters (Siemes et al., 2016). Calibration is performed against the ACCxPOD_2_ product. The time stamp refers to UTC and accelerations are represented in m/s^2. The sampling rate is 1 Hz and the output time span is 1 day. All accelerations are provided in the spacecraft reference frame. Several flags indicate if the data is valid, which corrections are applied and if there were thruster activations. So far, this product is only available for Swarm C, because the accelerometers of Swarm A and B contain too many disturbances. In this thesis, the ACCxCAL_2_ product is compared to modeled non-gravitational accelerations.

EGF_SHA_2_

The EGF_SHA_2_ product contains monthly Earth gravity field models stored as SH coefficients in **I**nternational **C**entre for **G**lobal **E**arth **M**odels (ICGEM) format (de Teixeira da Encarnação et al., 2020). The product is derived from a combination of four solutions of different analysis centers. All centers use different kinematic orbit products (with GPSx_RO_1B as original input) and STRxATT_1B star camera data to compute combined monthly gravity fields from the three spacecraft. The EGF_SHA_2_ provides SH coefficients up to d/o 40, but it is recommended to only use d/o up to 12. Information on variances and covariances is not provided with the product. In this thesis, the EGF_SHA_2_ product is compared to the IGG-Swarm time-variable gravity fields.

3.5 Precise Orbit Determination

The task of determining the trajectory of an artificial satellite with high accuracy is commonly called **P**recise **O**rbit **D**etermination (POD), nowadays. POD has been revolutionized with the development of high-precision GNSS receivers in the 1990s. They enable the tracking of LEO satellites independently of the ground station coverage, with a precision of a few cm. In this thesis, I will focus on orbits determined with GPS, as this is part of the payload of the Swarm satellites. Examples for other GNSSs would be the European Galileo navigation system, the Russian **GLO**bal **NA**vigation **S**atellite **S**ystem (GLONASS, **GLO**balnaja **NA**wigazionnaja **S**putnikowaja **S**istema) or the Chinese BeiDou.

The main purpose of GPSRs on board a spacecraft is to precisely determine its orbit. Each measurement epoch is assigned a position with cm-accuracy, such that data of all instruments can be geolocated. GPS measurements are also used for studies of the ionosphere: Zakharenkova et al. (2019) and Cherniak et al. (2019) investigate ionospheric plasma irregularities during geomagnetic storms from GPS observations. Many studies have used Swarm GPS data to derive thermospheric densities (e.g., Visser et al., 2013; Siemes et al., 2016; van den IJssel et al., 2020). Density models are important for a wide range of scientific investigations (e.g., long-term cooling of the thermosphere due to climate change, thermospheric gravity waves, or thermosphere-ionosphere coupling) and operational activities (e.g., re-entry predictions, lifetime analysis of satellites, or ground-track maintenance).

In this work, POD will be used to derive time-variable gravity fields (Lück et al., 2018). These are important to monitor mass redistribution processes within the Earth system, such as the melting of ice sheets and glaciers, water storage changes, and mass-related sea level changes. In Section 3.7, the special characteristics for retrieving Swarm time-variable gravity fields are described.

For the determination of gravity fields, the CoM of a LEO satellite in an inertial reference frame needs to be known precisely. GPS measurements generally refer to the antenna phase center of a LEO satellite, which is usually not located in the CoM. In order to obtain the CoM in an inertial reference frame, one needs to know the location of the antenna phase center in a satellite-fixed reference system on the one hand and the attitude of the spacecraft on the other hand. There are

different methods for POD of a LEO satellite (see Figure 3.6 and Jäggi and Arnold, 2017), which will be explained in the following.

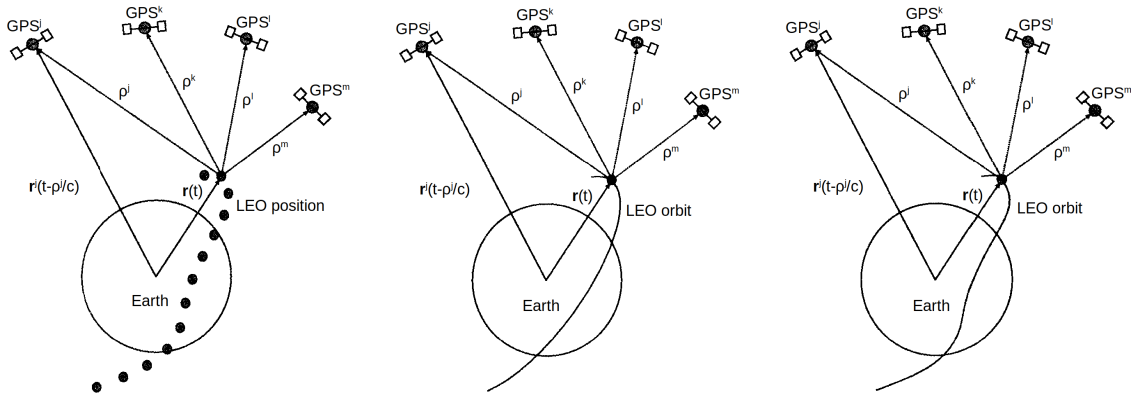

Figure 3.6: Illustration of three ways of precisely determining the position of a LEO satellite: kinematic (left), dynamic (middle), and reduced-dynamic (right) representation. ρ denotes the geometric distance between the LEO position and the GPS satellite and $\mathbf{r}$ is the inertial position with respect to the center of the Earth. The figure is taken from Jäggi and Arnold (2017) with a slightly modified labeling.

Kinematic Orbits

Figure 3.6 (left) shows the principle of a kinematic orbit. The LEO satellite is equipped with a GPS antenna and its position is tracked by GPS satellites. Kinematic orbits do not contain any information on velocities or accelerations, instead the trajectory is represented as a series of three coordinates. Furthermore, there are no values for any positions in between the measurements or in data gaps. The positions are derived purely from geometric GPS observations at the measurement epochs. No information on the force field or orbit dynamics is employed in the processing. For this reason, kinematic positions can be used in gravity field recovery, as has been shown earlier (Gerlach et al., 2003) and will be utilized in this thesis. Usually, kinematic positions are referred to as "pseudo-observations", as they are not measured directly. Instead, they are derived from GPS carrier phase data. Švehla and Rothacher (2003) present various approaches for deriving kinematic orbits: the zero-difference kinematic POD and the double-difference kinematic POD with and without ambiguity resolution.

Dynamic Orbits

In a dynamic orbit representation (see Figure 3.6, middle), the satellite's trajectory is based on the integration of the equation of motion (Beutler, 2005). The orbit is modeled by considering all known forces, such as the Earth's gravity field, tides, and non-gravitational accelerations. Using state-of the art models and accelerometer measurements, the goal is to reproduce all acting forces of the real world. During the computation, the trajectory is divided into orbit arcs. For each arc, at least six initial conditions are determined, which can be represented as Keplerian elements. Dynamic positions and velocities can be derived for any epoch within an arc.

Reduced-Dynamic Orbits

The quality of the force models employed in the processing of dynamic orbits might not be sufficient to derive the orbit with the desired precision. Therefore, the GPS tracking data is used to estimate empirical parameters along with the dynamic orbit parameters (Beutler et al., 2006; Swatschina, 2012). These additional parameters compensate for unmodeled forces or deficient force models. The combination of actual measurements and the best possible modeling of all acting forces on a satellite is suited to provide trajectories of highest accuracy. Figure 3.6 (right) illustrates a reduced-dynamic orbit, which does not completely rely on the force models, but allows for deviations due to the actual measurements and additional

parameters. Positions and velocities can be determined for any epoch of the arc. Even though the reduced-dynamic orbit is often considered as the most accurate one, it should not be used for gravity field determination, as it heavily relies on the employed force models. In this thesis, the reduced-dynamic orbit is utilized for georeferencing when modeling the non-gravitational accelerations. Therefore, the computation only needs to be performed once and the result can be interpolated to different kinematic orbit products. This is reasonable, because the non-gravitational accelerations only change on larger spatial scales and the influence of the different orbit products is not significant. Moreover, the plots of Section 3.2 are generated using the reduced-dynamic orbits.

As outlined above, kinematic orbits are used in this thesis to derive time-variable gravity fields. Hence, the quality of the orbits is directly related to the quality of the gravity fields. The Swarm spacecraft are equipped with two eight-channel dual-frequency GPSRs (one main receiver and one redundant receiver). An early study of van den IJssel et al. (2015) explains the Swarm GPS data characteristics and shows first precise science orbit results, revealing an accuracy of 4 to 5 cm of the kinematic orbit.

One drawback of the Swarm GPSRs is that they can only receive POD signals from not more than eight GPS satellites at a time, which is a rather small number, compared to many other missions (e.g., 12 for GRACE and 16 for GRACE-FO). In addition, it turned out that the GPSRs are sensitive to ionospheric disturbances, which occurred especially in the beginning of the mission, when solar activity was high. These effects are predominantly visible around the geomagnetic equator and the geomagnetic poles, leading to systematic errors in the gravity fields. Schreiter et al. (2019) mitigate ionospheric signatures in the AIUB orbit solutions by applying weighting schemes to the GPS observations.

Over time, the quality of the kinematic orbits improved, on the one hand due to the naturally decreasing ionospheric activity, and on the other hand due to receiver updates and modified tracking loop settings (van den IJssel et al., 2016; Dahle et al., 2017). According to Montenbruck et al. (2018) a 50 % improvement of the kinematic orbits is achieved, which contributes to improving the time-variable gravity fields (as will later be shown in Figure 4.12 (d)).

The official L2 kinematic orbit product SP3xKIN_2_ is provided by ESA and produced at Delft University of Technology (TUD, **T**echnische **U**niversiteit **D**elft) (van den IJssel et al., 2015; van den IJssel et al., 2016). Since there are many processing choices when computing kinematic orbits from GPS observations, various other groups additionally produce and provide their science orbits. These include IfG of the Graz University of Technology (Zehentner and Mayer-Gürr, 2016)[7], Institute of Geodesy (IfE, **I**nstitut **f**ür **E**rdmessung) of the University of Hannover (Ren and Schön, 2018), and AIUB (Jäggi et al., 2016; Schreiter et al., 2019)[8].

In this thesis, I use the kinematic orbits provided by IfG as they (1) deliver the best gravity field results, (2) include 3x3 covariance matrices for each epoch, (3) are continuously available since the update of the sampling rate on July 15, 2014, and (4) are regularly updated. In Section 4.3, I also show gravity field results that I computed from AIUB orbits for comparison.

3.6 Non-Gravitational Accelerations

For the recovery of time-variable gravity fields from satellite measurements, one needs to separate the non-gravitational forces from the gravitational forces. In satellite gravimetry, the non-gravitational forces are usually introduced in the processing as measured by on-board accelerometers. The actual accelerometer measurement is a voltage that needs to be converted to non-gravitational accelerations. Nominal calibration values for this conversion are specified for each

[7] http://ftp.tugraz.at/outgoing/ITSG/satelliteOrbitProducts/operational/Swarm-1/kinematicOrbit/ (last access: July 8, 2021)

[8] http://ftp.aiub.unibe.ch/LEO_ORBITS/SWARM/SWARMA/RL03/ (last access: July 8, 2021)

accelerometer (Fedosov and Peřestý, 2011). However, the real calibration values cannot be determined on ground, as gravity on Earth complicates the calibration of instruments, which should perform well in space. For this reason, many studies deal with the calibration of accelerometer measurements in order to obtain reliable values for non-gravitational accelerations.

Gruber et al. (2005) and Weigelt and Sneeuw (2005) investigate calibration methods for the accelerometer of the CHAMP satellite mission. Information on the calibration of GRACE's accelerometer can be found in e.g. Bettadpur (2009), Bezděk (2010), or Vielberg et al. (2018). Klinger and Mayer-Gürr (2016) show the advantages of an elaborate calibration for the recovery of time-variable gravity fields from GRACE. Towards the end of its lifetime, GRACE-B's accelerometer failed, such that efforts were made to use information from the operating instrument of GRACE-A and transplant it to GRACE-B (e.g., Save et al., 2006; Bandikova et al., 2019). The scientific community is confronted with similar challenges for GRACE-FO, as the accelerometer of one satellite delivers data of degraded quality.

The above-mentioned studies give a small insight into the complexity of using accelerometer measurements for gravity field recovery. For Swarm one is confronted with an even bigger challenge: The accelerometers on-board Swarm suffer from various anomalies, leading to a limited applicability of their data. Siemes et al. (2016) give an overview of the disturbances and their consequences, which are summarized in the following.

Sudden changes in the accelerometer bias are called steps. They usually occur simultaneously in all three axes-directions and might be related to a stress release inside the sensor structure. Furthermore, the Swarm accelerometers are heavily sensitive to temperature changes. To a certain limit, this is already known from previous satellite missions, but for Swarm, the sensitivity turned out to be 10 to 100 times stronger than expected before launch. Furthermore, the accelerometers need to be rebooted occasionally (in case the implemented so-called EDAC fails). During the reboot, the proof-mass is not controlled and might touch the walls of the cavity. Therefore, after such EDAC failure events, the data must be interpreted with caution, until the proof mass recovers and flows freely in the cavity again. Another source of disturbance are the thruster spikes. The attitude of the satellite is usually maintained by torques from magnetic torquers. Thrusters are activated when this control torque is insufficient for maintaining the attitude. The thrusters are designed to only exert a torque on the satellite, but observations showed that they also generate a small linear force, which leads to acceleration spikes in the measurements. In gravity field determination, accelerometer observations during thruster events should consequently be removed.

The above-mentioned disturbances lead to a serious degradation of the Swarm accelerometer data quality. Therefore, ESA has decided to make the L1B ACCx_PR_1B data product not available to the public. Siemes et al. (2016) present an approach to process the accelerometer data in several steps. They first manually remove the steps. Then they calibrate the observations against non-gravitational accelerations derived from POD, while also considering the temperature-dependency. In a last step, both types of non-gravitational accelerations are merged using frequency slicing in the spectral domain. To this day, only along-track data of Swarm C has been cleaned and calibrated in this way, as this is least affected by the various disturbances.

Over time, non-gravitational forces as measured by e.g. CHAMP, GRACE(-FO), and Swarm gained more attention, because they would be useful for thermospheric density studies and gravity field retrieval. Bezděk et al. (2017) compare the Swarm measurements to modeled data to obtain a better understanding of the disturbances. A GPS-based calibration procedure, which also incorporates the temperature-dependency is presented by Bezděk et al. (2018). Van den IJssel et al. (2020) use Swarm GPS observations to derive non-gravitational accelerations and thermospheric densities. However, non-gravitational accelerations derived from POD are not suitable for the retrieval of time-variable gravity fields, as knowledge about gravitational forces is required. In Lück et al. (2018), we showed that it is beneficial for gravity field recovery to introduce non-gravitational forces in the processing, therefore I model them in this thesis.

IGG has a long experience in studies of the thermosphere. I could profit from a software for determining non-gravitational accelerations along a satellite's orbit, which was developed originally by my colleague Ehsan Forootan. I implemented the computation of accelerations due to atmospheric drag and lift after Sentman (1961) and modified by K. Moe and M. M. Moe (2005), as explained in Doornbos (2012). Furthermore, I conducted all tasks related to the Swarm mission, such as the implementation of the satellite's macro model, tests, and validations. My colleague Kristin Vielberg refined the modeling of SRP and ERP, as is explained in Vielberg and Kusche (2020). Armin Corbin took care of the integration of the new NRLMSIS 2.0 empirical atmospheric model into the software (Emmert et al., 2021). In the following, I describe the main steps of modeling non-gravitational accelerations.

For LEO satellite missions, the non-gravitational accelerations are dominated by aerodynamic accelerations (due to drag and lift forces), SRP, and ERP. Hence, the non-gravitational accelerations are commonly modeled by summing up the aforementioned effects

$$\mathbf{a}_{model} = \mathbf{a}_{aero} + \mathbf{a}_{SRP} + \mathbf{a}_{ERP}. \tag{3.6.1}$$

The aerodynamic acceleration is the largest of the three terms of Equation (3.6.1) for LEO satellites and can be computed by

$$\mathbf{a}_{aero} = C_{aero} \frac{A_{ref}}{2m} \rho \, |\mathbf{v}_r| \, \mathbf{v}_r, \tag{3.6.2}$$

where m is the spacecraft's mass, $\mathbf{v}_r$ is its velocity relative to the atmosphere, and ρ depicts the thermospheric density. In this thesis, I use the recent NRLMSIS 2.0 empirical atmospheric model to derive the density (Emmert et al., 2021). A_{ref} is a reference area, which should be an agreed value for the entire spacecraft. It cancels out in further computations of C_{aero} and was originally introduced to provide the correct dimensions of each quantity. C_{aero} is a coefficient accounting for drag and lift forces acting on the satellite. Aerodynamic accelerations strongly depend on C_{aero}, which is evaluated for each panel of the satellite separately

$$C_{aero} = \left[\sum_{i=1}^{N} \sum_{j=1}^{M} \frac{\rho_j}{\rho} \left(C_{D,i,j} \hat{\mathbf{u}}_D + C_{L,i,j} \hat{\mathbf{u}}_{L,i} \right) \right] \cdot \hat{\mathbf{v}}_r. \tag{3.6.3}$$

In the above equation, N depicts the number of spacecraft panels, as defined by the macro model ($N = 15$ for Swarm). The index j considers the different components of the atmosphere. The NRLMSIS 2.0 model incorporates $M = 8$ so-called species: Helium (He), Oxygen (O & O_2), Nitrogen (N & N_2), Argon (Ar), Hydrogen (H), and anomalous oxygen (O^+). For each species, the inner part of Equation (3.6.3) is evaluated separately and finally summed up. $\hat{\mathbf{u}}_D$ is the unit vector in drag direction and $\hat{\mathbf{u}}_{L,i}$ is the unit vector in lift direction. $\hat{\mathbf{u}}_{L,i}$ is perpendicular to $\hat{\mathbf{u}}_D$ and depends additionally on the normal unit vector for each plane. The computation of the drag and lift coefficients $C_{D,i,j}$ and $C_{L,i,j}$ is implemented as explained by Doornbos (2012), who follows Sentman (1961) with modifications from K. Moe and M. M. Moe (2005).

Accelerations due to SRP and ERP are implemented as explained in detail in Vielberg and Kusche (2020). $\mathbf{a}_{SRP}$ is modeled by

$$\mathbf{a}_{SRP,N} = \frac{A}{m} \cos(\gamma) \, \nu \frac{1}{2} \left(\mathbf{c}^{\odot}_{R_{SW}} + \mathbf{c}^{\odot}_{R_{LW}} \right) \left(\frac{1AU}{r_{\odot,sat}} \right)^2 P_{1AU}(\lambda, t). \tag{3.6.4}$$

The above equation is evaluated for each panel N and summed up to obtain the acceleration due to SRP that acts on the entire spacecraft. A is the area of a satellite panel and γ is the angle between the normal vector of a panel and the incoming radiation. ν is the shadow function, which indicates if the satellite is in full sunlight (ν=1), fully eclipsed (ν=0) or in penumbra. $r_{\odot,sat}$ denotes the distance between the Sun and the satellite and $P_{1AU}(\lambda, t)$ accounts for solar radiation pressure at the distance of 1 **A**stronomical **U**nit (AU). The absorption and reflection of incoming photons of

the Sun at the spacecraft's panel are modeled by the radiation pressure coefficients $\mathbf{c}^{\odot}_{R_{SW}}$ and $\mathbf{c}^{\odot}_{R_{LW}}$ for shortwave and longwave fluxes, respectively. Accelerations due to ERP are usually quite small compared to aerodynamic accelerations and SRP. ERP decreases with increasing distance from the Earth and it acts mainly in radial direction of the spacecraft. For each panel N, the ERP is derived by

$$\mathbf{a}_{ERP,N} = \frac{A}{m} \sum_{k=1}^{K} \cos(\gamma) \left(\mathbf{c}^{\oplus}_{R_{SW,k}} F_{SW,k} R_{SW,k} + \mathbf{c}^{\oplus}_{R_{LW,k}} F_{LW,k} R_{LW,k} \right) \frac{\cos(\alpha_k)\, \Delta\omega_k}{\pi c r^2_{sat,k}}, \tag{3.6.5}$$

and summed up for the entire spacecraft. The index $\oplus$ now denotes the radiation pressure coefficient related to the Earth. For the computation of ERP accelerations the outgoing radiation of the Earth's surface in the spacecraft's FoV needs to be considered. In our implementation, the FoV consists of K $\Delta\omega_k$ surface elements of a regular $1° \times 1°$ grid. $r_{sat,k}$ denotes the distance from the center of a specific grid cell to the satellite, α_k is the angle between the surface element's normal and the connection line to the satellite and c is the speed of light. **C**louds and the **E**arth's **R**adiant **E**nergy **S**ystem (CERES) observations provide outgoing **T**op **O**f the **A**tmosphere (TOA) longwave flux $F_{LW,k}$ and shortwave flux $F_{SW,k}$ data (Doelling et al., 2016; Loeb et al., 2018). In this thesis, the hourly *CERES_SYN1deg_Ed4.1*[9] data is used. $R_{LW,k}$ and $R_{SW,k}$ are factors considering the angular dependency of the Earth's radiation. These factors furthermore depend on the land cover type and cloud coverage, which are also delivered with the CERES data.

For a more detailed explanation of the individual terms in the computation of radiation pressure accelerations, see Vielberg and Kusche (2020). All three terms of Equation (3.6.1) are evaluated per satellite panel and depend on its size and orientation. Additionally, the radiation pressure depends on the optical properties of the panel surface. I use the Swarm macro model as described by Montenbruck et al. (2018). Figure 3.7 shows an illustration of the model and Table 3.2 describes the properties (area, normal vector, and optical properties) of each panel.

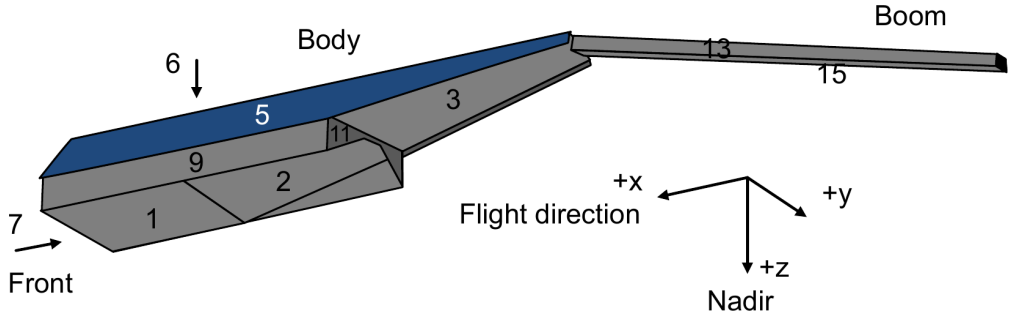

Figure 3.7: Illustration of the Swarm macro model (taken from Montenbruck et al., 2018). Area, normal vector, and optical properties of each panel are listed in Table 3.2.

In the following, the aerodynamic acceleration (drag+lift) will simply be denoted as "drag", as this is the main contributor. Figure 3.8 shows modeled and calibrated non-gravitational accelerations for Swarm C. In the left column (Figure 3.8 a-c), the effects of drag, SRP, and ERP are compared in along-track, cross-track, and radial directions. In the along-track direction, drag makes by far the biggest contribution in the order of $10^{-7}\,\mathrm{m/s^2}$, while ERP is smallest. The orbital period of about 94 minutes is reflected in the accelerations. In the cross-track direction, SRP has the largest magnitude, while drag shows strong variations. In the radial direction, SRP and ERP act in opposite directions, as the radiation is emitted from above and below the spacecraft, respectively. In general, non-gravitational accelerations are largest in along-track direction and smallest in radial direction. One should keep in mind that Figure 3.8 (a-c) shows the results for April 1, 2015, which is a day with medium solar activity. The magnitude of the individual contributions depends on the solar activity. But nevertheless, drag in the along-track direction is always the largest contributor

[9] https://ceres-tool.larc.nasa.gov/ord-tool/jsp/SYN1degEd41Selection.jsp (last access: July 8, 2021)

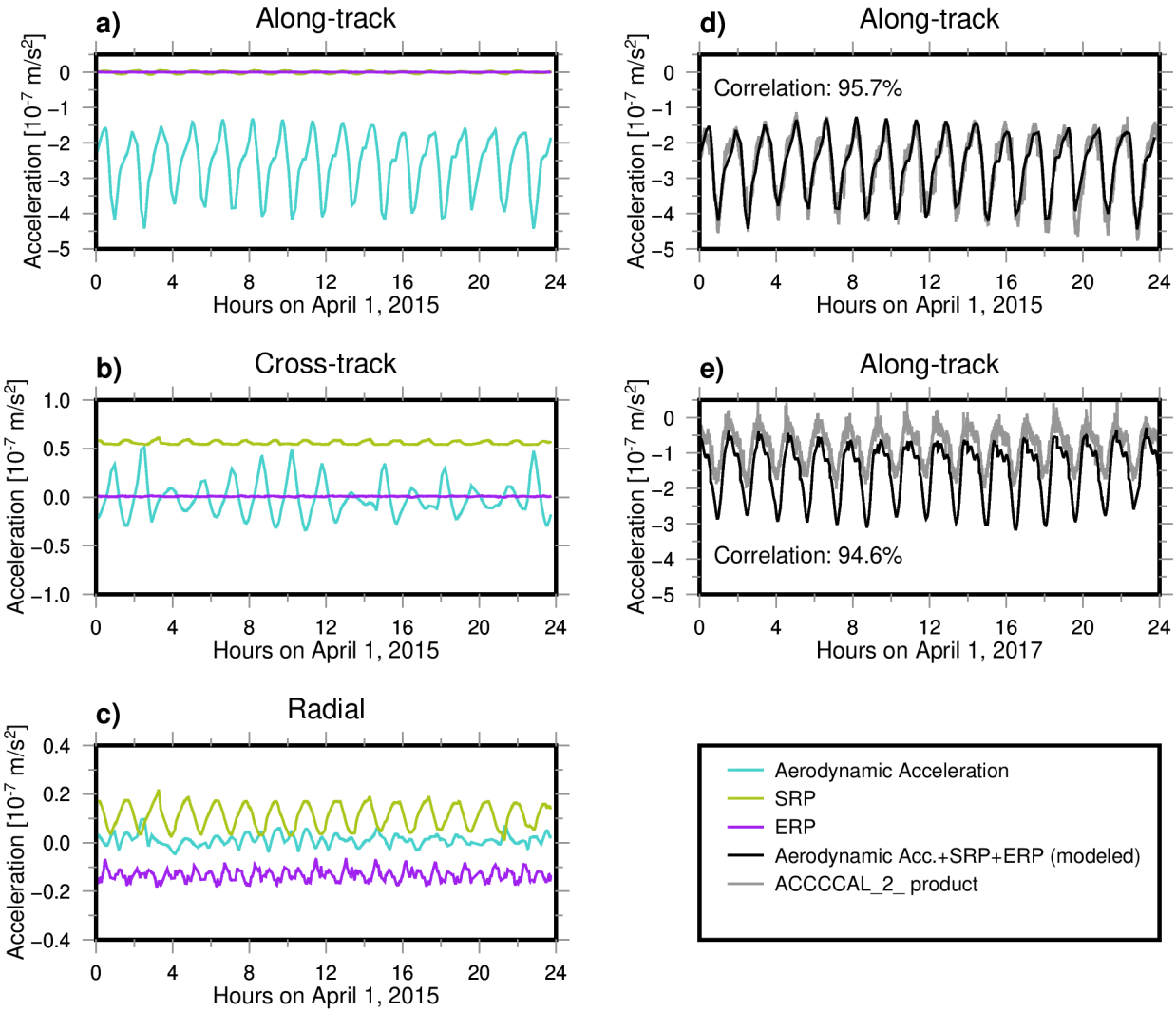

Figure 3.8: Investigation of non-gravitational accelerations acting on Swarm C. a)-c) show the three individual components (i.e. aerodynamic acceleration, SRP, and ERP) in along-track, cross-track and radial directions on April 1, 2015. d) and e) show the comparison of modeled non-gravitational accelerations with the ACCCCAL_2_ product (Siemes et al., 2016) on April 1 of 2015 and 2017, respectively. Correlation values are computed disregarding a bias and scale factor.

#	Panel	Normal vector			Area [m^2]	δ_{vis}	ρ_{vis}	δ_{ir}	ρ_{ir}
1	Bottom 1	+0.000	+0.000	+0.000	1.54	0.79	0.03	0.31	0.01
2	Bottom 2	−0.198	+0.000	+0.098	1.40	0.17	0.06	0.20	0.02
3	Bottom 3	−0.138	+0.000	+0.990	1.60	0.14	0.00	0.22	0.00
4	Solar array right	+0.000	+0.588	−0.809	3.45	0.10	0.00	0.28	0.00
5	Solar array left	+0.000	−0.588	−0.809	3.45	0.10	0.00	0.28	0.00
6	Top	+0.000	+0.000	−1.000	0.50	0.07	0.00	0.22	0.00
7	Front	+1.000	+0.000	+0.000	0.56	0.80	0.00	0.83	0.00
8	Side wall +y	+0.000	+1.000	+0.000	0.75	0.07	0.03	0.21	0.01
9	Side wall −y	+0.000	−1.000	+0.000	0.75	0.07	0.03	0.21	0.01
10	Support front	+1.000	+0.000	+0.000	0.80	0.00	0.55	0.00	0.20
11	Support back	−1.000	+0.000	+0.000	0.80	0.07	0.00	0.22	0.00
12	Boom +y	+0.000	+1.000	+0.000	0.60	0.03	0.79	0.09	0.12
13	Boom −y	+0.000	−1.000	+0.000	0.60	0.03	0.33	0.09	0.12
14	Boom top	−0.239	+0.000	−0.971	0.60	0.06	0.11	0.18	0.04
15	Boom bottom	+0.228	+0.000	+0.974	0.60	0.00	0.55	0.00	0.20

Table 3.2: Properties of the Swarm macro model (taken from Montenbruck et al., 2018). For each panel, the normal vector, the area, and optical properties are specified. The optical properties comprise the effective fraction of diffusely (δ) and specularly (ρ) reflected photons in the visible (vis) and infrared (ir) spectral range. Optical properties related to absorption are not shown here, as they are not needed in this thesis. The numbers in the first column relate to Figure 3.7.

at Swarm altitude.

In Figure 3.8 (d) modeled non-gravitational accelerations are compared to the ACCCCAL_2_ product on April 1, 2015. The modeled values are the result of the sum of drag, SRP, and ERP of Figure 3.8 (a), whereas the ACCCCAL_2_ product contains calibrated accelerometer measurements (see Section 3.4 and Siemes et al., 2016). On this particular day, both time series agree very well with each other and are correlated by 95.7 %, while the correlation drops below 0 % for individual other days, as will be evaluated in the course of this section. This comparison is important, because I use the modeled non-gravitational accelerations in the determination of monthly Swarm gravity fields; the calibrated data is only available in along-track direction for Swarm C, which is not sufficient for gravity field retrieval, as other directions and data from Swarm A and B are completely missing.

However, both methods for deriving non-gravitational accelerations do not always match perfectly, as can be seen in Figure 3.8 (e) for April 1, 2017. The time series show an offset and a different amplitude. It is now hard to evaluate which result is closer to the true non-gravitational accelerations, as they are simply unknown. The differences might for example occur due to possible errors in the density model or the calibration process. When disregarding a bias and scaling factor, the time series still show a correlation of 94.6 %. A bias and scaling factor are usually co-estimated during the gravity-field processing anyway, such that they can be neglected when comparing modeled and calibrated data. Disregarding the bias and scaling factor, the modeled and calibrated non-gravitational accelerations largely agree with each other. An investigation of daily batches shows a correlation of more than 90 % (75 %) for 49 % (80 %) of the data (February 2014 to December 2020).

For further validation, Figure 3.9 shows the correlation between different non-gravitational acceleration products for the along-track direction of Swarm C. The investigated products are

- $\text{IGG}_{\text{advanced}}$: This is the version that I explained throughout this section (i.e. NRLMSIS 2.0 density model and advanced radiation pressure modeling as explained in Vielberg and Kusche, 2020),

- $IGG_{standard}$: This version is additionally computed at IGG, as it is still more common in the scientific community (i.e. NRLMSISE-00 density model and standard radiation pressure modeling, Vielberg and Kusche, 2020),
- IfG: Modeled non-gravitational accelerations from IfG[10],
- ACCCCAL_2_: calibrated L2 accelerometer data (Section 3.4).

Each point represents the linear correlation coefficient between two daily time series. One evident observation is that most correlations are higher than 75 % and that there are specific times when the correlations get lower and even drop to zero or below. The correlation between $IGG_{advanced}$ and $IGG_{standard}$ is always larger than 90 % and mostly even larger than 95 %. It is however interesting to see that the advanced modeling is generally stronger correlated, when compared to the calibrated ACCCCAL_2_ product than the standard version. This indicates an improvement of the non-gravitational acceleration modeling at IGG. The modeled products from IGG and IfG have a larger correlation than when each of them is compared to the ACCCCAL_2_ product. This suggests that there are no major errors in the modeling and the differences might occur due to slightly different modeling procedures. When compared to the calibrated ACCCCAL_2_ product, $IGG_{advanced}$ has a higher correlation than IfG, but both are in the same order of magnitude. Periods with lower correlations are similar for all products and are investigated in the following.

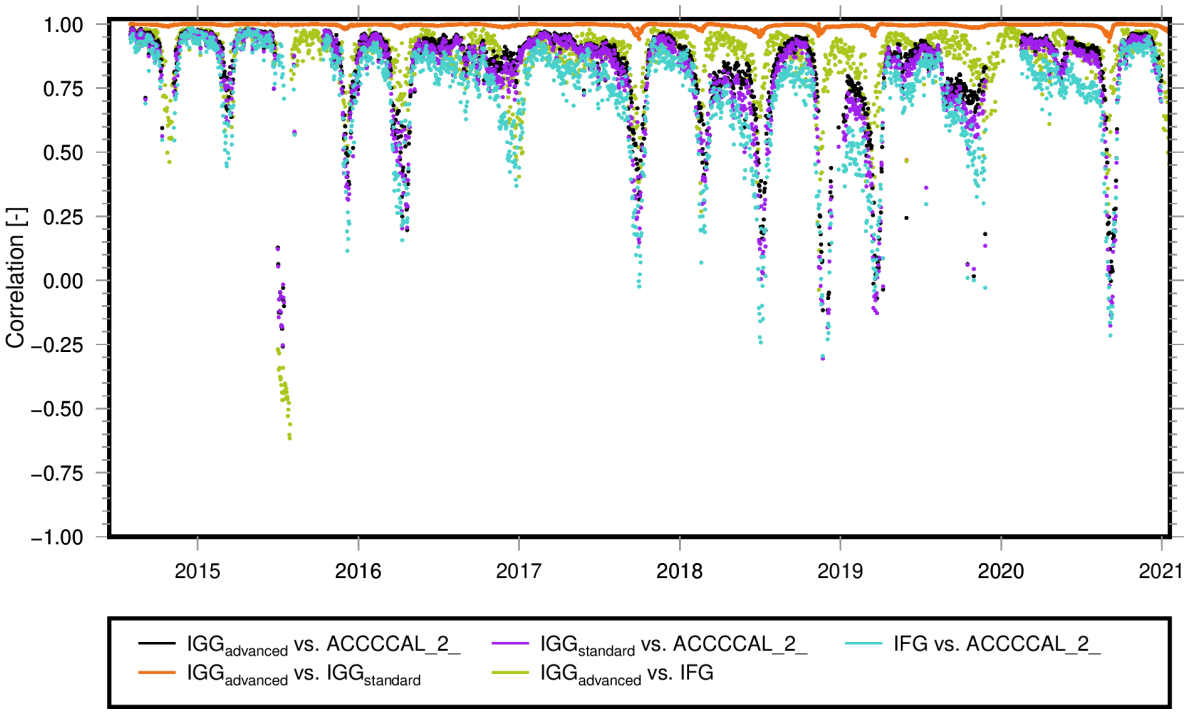

Figure 3.9: Correlation of different non-gravitational acceleration products for the along-track direction of Swarm C.

Figure 3.10 shows the relation between the **L**ocal **T**ime of the **A**scending **N**ode (LTAN) of Swarm C and the daily correlation between ACCCCAL_2_ and $IGG_{advanced}$. Hence, each black dot of Figure 3.9 is also present in Figure 3.10; they are only plotted against different x-axes. Low correlations are concentrated at local times of 6 to 9 h and 18 to 21 h. These times coincide with dawn and dusk, where ionospheric activity is generally high. One possible explanation for the lower correlations could be that density models (used for the modeling of non-gravitational accelerations) are less reliable during dusk and dawn. This assumption is supported by the fact that correlations between modeled accelerations at IGG and IfG are also low during the same times (Figure 3.9).

[10] http://ftp.tugraz.at/outgoing/ITSG/satelliteOrbitProducts/operational/Swarm-1/nonConservativeForces/ (last access: July 8, 2020)

Furthermore, Bruinsma et al. (2017) found low correlations between CHAMP-derived density and density models during dusk and dawn hours. At around 10 h and 20 h, an increased number of artifacts can be found in the accelerometer measurements (Christian Siemes, personal communication), which contributes additionally to the accumulation of lower correlations in Figure 3.10. Moreover, the correlations are larger during night- (85 to 100 %) than during daytime (65 to 100 %).

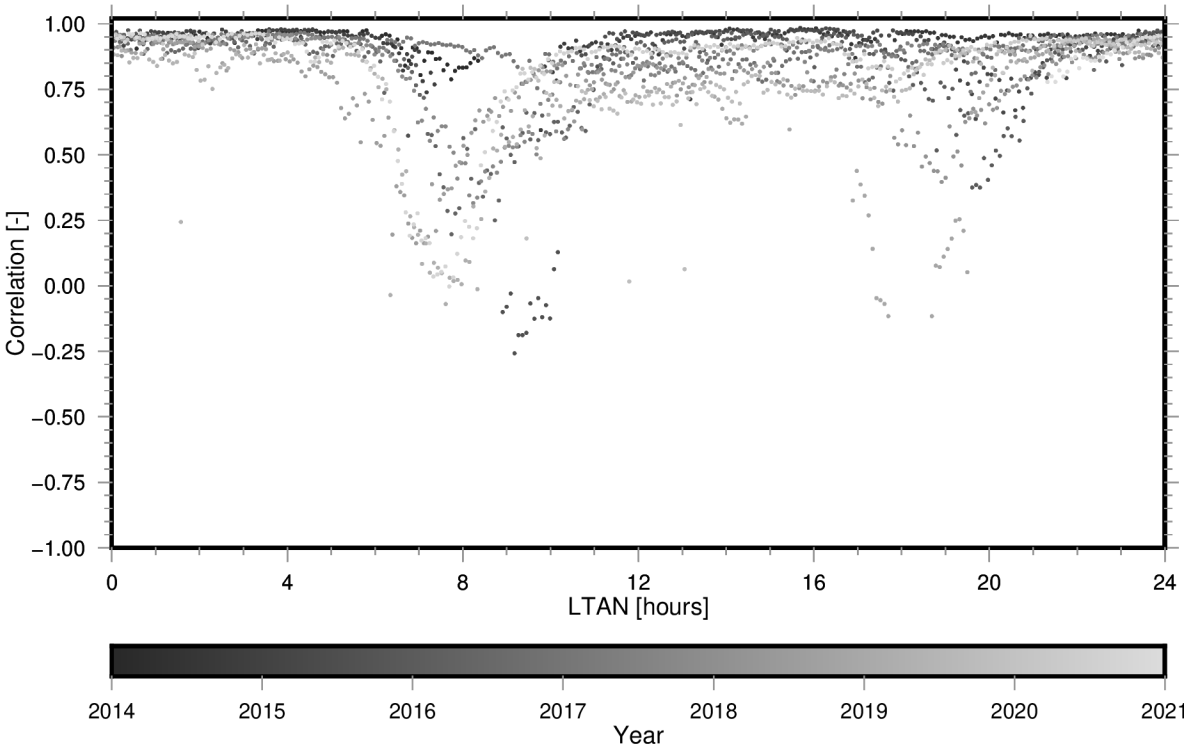

Figure 3.10: Relation between the LTAN and the correlation of modeled and calibrated non-gravitational accelerations for the along-track direction of Swarm C. The correlation is computed between $IGG_{advanced}$ and ACCCCAL__2__ on a daily basis. The color of each dot indicates the date between 2014 and 2021.

In summary, it can be stated that the use of non-gravitational accelerations from Swarm is more complicated than for other missions. Due to various disturbances, accelerometer data cannot be used as it is and calibrated data only exists for the along-track direction of Swarm C. However, by modeling the non-gravitational accelerations, they can be introduced into the gravity field recovery. Comparing modeled and calibrated data shows a good agreement. Only for LTANs during dusk and dawn times deviations are larger.

3.7 Time-Variable Gravity Fields from the Swarm Mission

A large part of this thesis will deal with gravity field recovery from the Swarm satellite mission. In Chapter 4, the theory of gravity field determination is explained and results from Swarm will be shown. Chapter 5 shows how the results can be used to derive mass changes globally and regionally and in Chapter 6, normal equations of monthly gravity fields will be used as input for the sea level inversion. Therefore, I would like to point out the characteristics and challenges when using Swarm for gravity field recovery in this section.

Usually, GRACE(-FO) is the first choice for obtaining high-quality time-variable gravity fields. The key instrument of GRACE(-FO) is the KBR system, which precisely measures the range, range-rate, and range-acceleration between the satellites. It allows for determining mass changes at spatial scales of down to a few hundred kilometers with unprecedented accuracy. However, there is an 11-months gap between the data from GRACE and GRACE-FO. Hence, in order to close this gap, the need for alternative time-variable gravity fields arises. Furthermore, additional data

always has the potential to improve existing solutions.

As changes in the Earth's gravity field induce changes of a spacecraft's orbit, it is also possible to use POD for gravity field recovery. LEO satellites are best suited for deriving time-variable gravity fields, because the signal is less attenuated compared to higher-flying satellites. The most important quantities to derive the Earth's gravity field from kinematic orbits are (1) high-precision orbit products, (2) information on the satellite's attitude, and (3) information on the non-gravitational forces acting on the satellite.

The Swarm mission is well suited to derive the Earth's time-variable gravity field. It was launched in November 2013 and is still in orbit. This means that it completely spans the GRACE-GRACE-FO gap and additionally offers the opportunity for comparisons with both missions. The altitude of the spacecraft is between 450 km and 530 km and is thus appropriate for gravity-field recovery. Higher altitudes would downgrade the resolution and lower altitudes would lead to a faster orbit decay and a shorter lifetime of the satellite. The combination of the three satellites offers a more stable solution and reduces noise in the gravity field.

There are a few challenges when deriving time-variable gravity fields from kinematic orbits of Swarm. One should always keep in mind that Swarm is not a dedicated gravity field mission and that the solutions will never reach the quality of those from GRACE(-FO), due to the lack of an inter-satellite ranging system. Moreover, the quality of the GPS measurements is not outstanding, as is explained in Section 3.5. Especially in the beginning of the mission, the orbits were heavily influenced by ionospheric activities, leading to systematic errors in regions of the geomagnetic equator and the geomagnetic poles. Figure 3.11 shows that the F10.7 index and the **V**ertical **T**otal **E**lectron **C**ontent (VTEC) (indicators of solar/ionospheric activity) are high in the early years and decrease continuously until they reach their minimum in 2017. GPSR updates led to improvements of the orbit quality (Dahle et al., 2017) and are additionally plotted in Figure 3.11. The first important update was the increase of the sampling rate from 0.1 Hz to 1 Hz on July 15, 2014. The following updates concern the increase of the antenna FoV from originally 80° to 88° until May 6, 2015. Then, until August 11, 2016, the tracking loop bandwidth was modified in order to achieve a higher robustness against ionospheric scintillation.

Swarm accelerometer measurements are corrupted by a variety of errors and, so far, calibrated data only exists for the along-track direction of Swarm C. In Lück et al. (2018), we showed that modeling the non-gravitational forces leads to better results than co-estimating them. In Section 3.6 the modeling procedure is explained.

In this thesis, I will cope with the above-mentioned challenges to derive the best-possible monthly gravity fields from the Swarm mission. During my research, I also looked into two additional variants of time-variable gravity field representation: In Lück et al. (2018), we fit a six-parameter model consisting of mean, trend, annual, and semiannual variability to each SH coefficient. In Richter et al. (2021) we developed a reconstruction method, which combines monthly Swarm gravity field models with the dominating spatial modes of mass change obtained from GRACE. Both approaches provide reliable results, which often outperform the monthly solutions, as assessed in these studies. However, the two approaches are not completely unconstrained, as they depend on the long-term mass change observed by Swarm or GRACE. In this thesis, the focus will be on unconstrained monthly gravity field solutions. Other groups provide their own gravity fields and de Teixeira da Encarnação et al. (2020) combine four different gravity fields, processed at AIUB (Jäggi et al., 2016), Astronomical Institute of the Czech Academy of Sciences (ASU, **AS**tronomický **U**stav) (Bezděk et al., 2016), IfG (Zehentner and Mayer-Gürr, 2016), and **O**hio **S**tate **U**niversity (OSU) (J.-Y. Guo et al., 2015). In Section 4.3 a comparison of my IGG results to other solutions is shown.

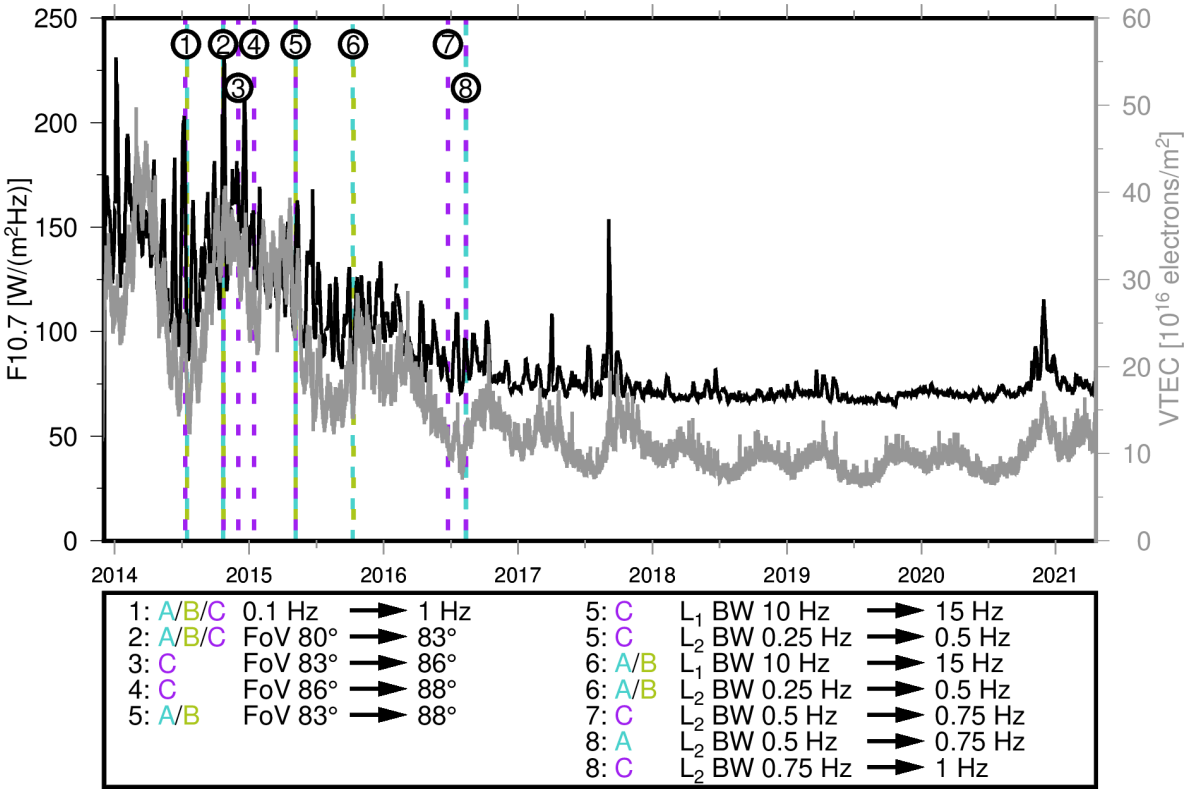

Figure 3.11: Evolution of the F10.7 index and the VTEC during the Swarm lifetime. GPSR receiver updates are indicated with vertical lines.

Chapter 4

Gravity Field Recovery

The determination of the Earth's gravity field and its temporal variations is one of the main challenges in geodesy. Starting with Sputnik 2 in 1957, observations of satellite orbits could be used to gain a better knowledge of the Earth's gravitational field than ever before (Merson and King-Hele, 1958). Measuring techniques have significantly improved since then - from optical observations, to laser ranging techniques, GNSS-based POD and concepts especially designed for gravity field retrieval. The dedicated gravity missions include CHAMP, GRACE(-FO), and GOCE (see Chapter 2).

One major task in space geodesy is the determination of a global *mean* or *static* gravitational field. A static gravity field is derived from data accumulated over several years. Usually, observations from different satellite missions are combined and sometimes terrestrial data is also included. The combination of different measurement techniques during a long timespan leads to high spatial resolutions with high accuracies. The knowledge of the Earth's static gravity field is important in many areas of geodesy or geophysics. A static gravity field is often used as a background model or as a reference in the determination and evaluation of time-variable gravity fields.

Another important aspect is the determination of *time-variable* gravity fields. Time-variable gravity fields represent mass redistributions within the Earth system, for example expressed in a monthly sampling. These mass redistributions are of great interest for a large community, as they are closely related to climate change. They include variations in the continental water cycle, mass change of glaciers and ice sheets, GIA, ocean mass change, atmospheric mass fluxes, and mass variations within the solid Earth, such as earthquakes. In general, there is always a trade-off between the spatial and temporal resolution of a gravity field. While static gravity fields have a high spatial resolution, time-variable gravity fields have a lower spatial resolution (the higher the temporal resolution, the lower the spatial resolution will be).

Since the start of the first satellite, the scientific interest in gravity field determination grew considerably, especially with the launch of the GRACE mission. A large number of different approaches to derive the Earth's gravity field exists. Therefore, in Section 4.1 the methodology is described in general and special characteristics for the Swarm mission are addressed. Section 4.2 shows how the gravity field determination is implemented in the **G**ravity **R**ecovery **O**bject **O**riented **P**rogramming **S**ystem (GROOPS) software and in Section 4.3 the results are presented and compared to existing GRACE(-FO) solutions.

4.1 Methodology

In general, the determination of the Earth's gravity field from space is closely linked to observing the position and movements of satellites. One group of approaches is based on SST: A satellite collects observations by tracking another satellite. There are two main concepts that need to be distinguished: hl-SST and ll-SST.

In the hl-SST mode, a higher flying satellite measures the position of a LEO satellite. Typically, this

means that the lower satellite is equipped with on-board GNSS receivers. The GNSS observations can be used to derive the Earth's gravitational field either directly or, more commonly, in a two-step approach: First, kinematic orbits (see Section 3.5) are derived from the GNSS positions, without introducing a priori information about the gravity field. In a second step, the gravitational field is derived from the kinematic orbits.

Ll-SST means that two satellites are flying in the same orbit behind each other, with a distance of a few hundred kilometers. An on-board ranging system measures the relative positions and velocities. The GRACE(-FO) satellites use a combination of ll-SST and hl-SST to infer information about the Earth's gravity field.

In this thesis, the concept of hl-SST is used to derive time-variable gravity fields from kinematic orbits of the Swarm mission. The two-step approach offers the possibility to investigate kinematic orbit products from several scientific groups. Löcher (2010) gives a detailed overview of different methods of using kinematic satellite orbits in gravity field recovery.

Amongst the most common and successful techniques are (1) the energy balance approach, (2) the classical variational equation approach, (3) the celestial mechanics approach, (4) the acceleration approach, and (5) the integral equation approach with short arcs .

The fundamental theory of the energy balance approach dates back to O'Keefe (1957). However, due to an insufficient data coverage at that time, the method was only a rather theoretical option for future satellite programs (e.g., Bjerhammar, 1969; Jekeli, 1999). The approach was revived with the advent of the CHAMP mission (e.g., Han et al., 2002; Gerlach et al., 2003; Kusche and Loon, 2005) and has also widely been used in GRACE studies (e.g., Han et al., 2006; Ramillien et al., 2011; Zeng et al., 2015). One outcome of the approach is the TUM-2Sp gravity field model (Földváry et al., 2005). The energy balance approach relies on the law of energy conservation and thus links position and velocity of a satellite to the unknown gravitational potential. Shang et al. (2015) developed the improved energy balance approach, which is now used at OSU. On the one hand, it preserves more information from the KBR range-rate data of the GRACE measurements and on the other hand, it reduces orbit errors by several adaptations.

The classical variational equation approach, also called dynamic approach, is based on the numerical solution of Newton's equation of motion, formulated as initial value problem. In order to get the best fit to the observations, the equation of motion is linearized and iteratively solved until convergence. The set of parameters updated in each iteration step includes the initial position and velocity but may be extended by any quantity which impacts the orbit, e.g., the gravity field parameters. The partial derivatives required for the computation of the parameter updates are obtained by solving another set of differential equations, the so-called variational equations. The dynamic approach is widely used in GRACE(-FO) gravity field estimation, e.g. by GFZ (Dahle et al., 2019a), JPL, CSR, and IfG Graz (Kvas et al., 2019a). More information on the mathematics of this approach can e.g. be found in Riley et al. (1967); Reigber (1989) or Bettadpur and McCullough (2017).

The celestial mechanics approach was developed at AIUB and is an extension of the classical variational equation approach (Beutler et al., 2010). The key difference compared to the classical approach is that additional pseudo-stochastic accelerations are estimated in order to compensate for deficiencies in the force models (Jäggi et al., 2006). Jäggi et al. (2011) apply the celestial mechanics approach to GOCE, CHAMP, and GRACE data, while Jäggi et al. (2016) investigate gravity fields recovered from kinematic orbits of Swarm. Meyer et al. (2019) combine SLR, GRACE, and Swarm data for gravity field determination.

Accelerations of a satellite can, e.g., be obtained by differentiating kinematic orbits twice. The acceleration approach uses Netwon's equation of motion to directly link a satellite's acceleration to gravity field parameters (Reubelt et al., 2003; Reubelt, 2009). In this way, there is no accumulation of integration errors. The modified acceleration approach is evaluated in Ditmar and van Eck van der Sluijs (2004) and Ditmar et al. (2006) and utilizes weighted average accelerations instead of point-wise ones. Weigelt (2017) presents a possibility to also include range-accelerations from

GRACE. However, the relative velocity of the two satellites (observed by GPS) would have to be known with the same accuracy as the range acceleration (observed by the KBR system) to fully take advantage of this approach. A variant, the so-called decorrelated acceleration approach, which decorrelates errors in the GPS observations, was implemented at ASU. Bezděk et al. (2016) use this extension to derive time-variable gravity fields from Swarm data.

The integral equation approach was developed for orbit determination by Schneider (1968). It was modified by Reigber (1969) in order to be used for gravity field determination. The approach is based on integrating Newton's equation of motion (Equation (4.1.12)) twice and then formulating the differential equation as a boundary value problem. The integral equation approach is used in this thesis and is described in more detail in Section 4.1.3.

In a mathematical sense, all of the above approaches, except for the energy balance approach, are equivalent as they are based on Newton's equation of motion. Baur et al. (2014) compare different approaches for deriving gravity fields from GOCE-GPS data. They conclude that the real-data results are in agreement with theoretical considerations when comparing the approaches. Only the energy balance approach shows systematic shortcomings and is inferior compared to the other approaches by a factor of $\sqrt{3}$. This is due to the fact that only the norm of the velocity vector is considered when transferring the velocity to energy. Hence, a 3-element vector is transformed into a scalar quantity, leading to a loss of redundancy. Differences in the results of other approaches arise mainly as a consequence of processing choices or the propagation of error characteristics.

4.1.1 Representing the Earth's Gravity Field with Spherical Harmonics

The gravity field of the Earth is determined by the distribution of masses. In this section, the mathematical context of gravity field theory is explained. If not stated otherwise, the description follows Hofmann-Wellenhof and Moritz (2006), who also provide further information for interested readers.

According to Newton's law of universal gravitation, two point masses, m_1 and m_2, attract each other with a force $\mathbf{F}_{12}$, which is directed along their line of connection

$$\mathbf{F}_{12} = Gm_1m_2\frac{\mathbf{r}_2 - \mathbf{r}_1}{|\mathbf{r}_2 - \mathbf{r}_1|^3}. \tag{4.1.1}$$

In the above equation, $\mathbf{r}_1$ and $\mathbf{r}_2$ denote the positions of the two point masses, while $G = 6.6742 \cdot 10^{-11}\,\mathrm{m}^3/\mathrm{kgs}^2$ is the gravitational constant. Usually one of the masses is called *attracting* mass (hereinafter denoted by the index Q) and the other one is called *attracted* mass (hereinafter referred to without any index). In this thesis, the Earth will in general be the attracting mass, while other bodies, such as satellites, will be the attracted mass. Instead of computing the force $\mathbf{F}_{12}$, one can also consider the gravitational field strength $\mathbf{g}$, which is created by the attracting mass. Considering the following relations,

$\mathbf{g} = \mathbf{g}_1 = \frac{\mathbf{F}_{12}}{m_2}$ ... gravitational field strength, created by the attracting mass,
$\mathbf{r}_Q = \mathbf{r}_1$ ... position of the attracting mass,
$\mathbf{r} = \mathbf{r}_2$ ... position of the attracted mass,
$M = m_Q = m_1$ ... attracting mass, i.e. mass of the Earth,
$l = |\mathbf{r} - \mathbf{r}_Q|$ ... distance between the two point masses,

Equation (4.1.1) simplifies to

$$\mathbf{g} = GM\frac{\mathbf{r} - \mathbf{r}_Q}{l^3}. \tag{4.1.2}$$

The right hand side can be replaced by the gradient of a scalar function V, which represents the gravitational potential

$$\mathbf{g} = \nabla V. \tag{4.1.3}$$

Evaluating Equations (4.1.2) and (4.1.3) leads to

$$V = \frac{GM}{l}. \tag{4.1.4}$$

The potential of a system can now be expressed as the sum of all individual contributions. Newton's integral Equation (4.1.5) describes a continuous distribution of mass elements dm over a volume v as

$$V = G \iiint_v \frac{dm}{l}, \tag{4.1.5}$$

with $dm = \rho dv$ and ρ denoting the volume of the mass element. There are two cases that have to be considered:

$$\Delta V = \begin{cases} -4\pi G\rho & \text{for any point } \mathbf{r} \text{ inside } v \quad \text{(Poisson)} \\ 0 & \text{for any point } \mathbf{r} \text{ outside } v \quad \text{(Laplace).} \end{cases} \tag{4.1.6}$$

1) $\mathbf{r}$ is inside the attracting masses: in this case, ΔV can be determined with Poisson's equation (see Equation (4.1.6)),

2) $\mathbf{r}$ is outside the attracting masses: in this case, ΔV equals zero and Laplace's equation is valid. The solutions of Laplace's equation are called *harmonic functions*. This case will be important in the further course of this work, as it allows the determination of the gravitational potential exterior of the Earth's mass.

Now, considering the Earth's gravitational potential outside the attracting masses, the solution of Laplace's equation can be formulated in terms of SH base functions Y_n

$$V(\lambda, \theta, r) = \frac{GM}{R} \sum_{n=0}^{\infty} \left(\frac{R}{r}\right)^{n+1} Y_n(\lambda, \theta), \tag{4.1.7}$$

with (λ, θ, r) denoting the geocentric position in spherical coordinates. λ and θ are the geographical longitude and colatitude, whereas r is the distance to the origin of an Earth-fixed coordinate system. R denotes the mean Earth's radius. The base functions Y_n are also called *surface spherical harmonics*. As they define a complete system of harmonic orthogonal functions on the surface of a sphere, each arbitrary function on a sphere can be expressed as a series of Y_n. The base functions are obtained by

$$Y_n(\lambda, \theta) = \sum_{m=0}^{n} \left[c_{nm} C_{nm}(\lambda, \theta) + s_{nm} S_{nm}(\lambda, \theta)\right], \tag{4.1.8}$$

where c_{nm} and s_{nm} denote the SH coefficients of degree n and order m, also called *Stokes' coefficients*. C_{nm} and S_{nm} are the corresponding surface spherical harmonics, which can be expressed as

$$\begin{aligned} C_{nm}(\lambda, \theta) &= P_{nm}(\cos(\theta)) \cos(m\lambda), \\ S_{nm}(\lambda, \theta) &= P_{nm}(\cos(\theta)) \sin(m\lambda). \end{aligned} \tag{4.1.9}$$

In the above equation, $P_{nm}(\cos(\theta))$ are the associated Legendre functions (also called Legendre polynomials) of degree n and order m. They are obtained from a stable recursion formula. Inserting Equation (4.1.8) into Equation (4.1.7) leads to a common representation of the gravitational potential

$$V(\lambda, \theta, r) = \frac{GM}{R} \sum_{n=0}^{\infty} \left(\frac{R}{r}\right)^{n+1} \sum_{m=0}^{n} \left[c_{nm} C_{nm}(\lambda, \theta) + s_{nm} S_{nm}(\lambda, \theta)\right]. \tag{4.1.10}$$

Background model	Product	Reference
Gravity Field Model	GOCO06s	Kvas et al., 2019b; Kvas et al., 2021
Moon, Sun, and Planets	JPL DE421	Folkner et al., 2009
Earth Tide	IERS2010	Petit and Luzum, 2010
Ocean Tide	FES2014b	Carrère et al., 2016
Solid Earth Pole Tide	IERS2010	Petit and Luzum, 2010
Ocean Pole Tide	Desai2002	Desai, 2002
Atmospheric Tide	AOD1B RL06	Dobslaw et al., 2017a
Atmosphere and Ocean Dealiasing	AOD1B RL06	Dobslaw et al., 2017a
Permanent Tidal Deformation	included (zero tide)	

Table 4.1: Background models used during the processing.

With Equation (4.1.10) every possible gravitational potential can be expressed. In reality, the summation is truncated at a degree n_{max} and a compromise between a high spatial resolution (i.e. a high n_{max}) and a high temporal resolution has to be found. The spatial resolution can be computed by

$$\psi = \frac{2\pi R}{n_{max}} \approx \frac{40\,000\,\text{km}}{n_{max}}, \tag{4.1.11}$$

where ψ denotes the full-wavelength of the smallest feature that can be represented with a maximum degree n_{max}. Static gravity fields usually have a maximum degree $n_{max} = 300$ or higher, leading to spatial resolutions of $\psi \approx 130\,\text{km}$ or better. Monthly GRACE(-FO) gravity fields are evaluated up to $n_{max} = 120$ and $\psi \approx 330\,\text{km}$, while the spatial resolution of monthly Swarm-only gravity fields is in the range of a few thousand km as will be discussed in this thesis.

4.1.2 Background Models

One major aspect of this thesis is to derive time-variable gravity field models from satellite observations. This means that all other forces that act on a satellite have to be reduced during the processing. Non-gravitational forces, such as air drag, SRP, and ERP, are usually measured by accelerometers or, as in this thesis, modeled (see Section 3.6). Other disturbing forces are taken into account by so-called background models. Table 4.1 gives an overview of the models that are applied during the processing within this thesis. The individual models are described in the following. Further explanations can be found in the *IERS Conventions (2010)* (Petit and Luzum, 2010).

Gravity Field Model

The GOCO06s is used as gravity background model in this work. It is computed by the **G**ravity **O**bservation **CO**mbination (GOCO) initiative and is one of the latest satellite-only global gravity field models (Kvas et al., 2019b; Kvas et al., 2021). More than 15 years of data from GOCE, GRACE, kinematic orbits of several LEO satellites and SLR observations have been combined using **V**ariance **C**omponent **E**stimation (VCE). The model consists of a static part up to degree and order 300 and an additional time-variable part, consisting of trend and annual variations, up to degree and order 200.

Direct Tides

In addition to the gravitational field of the Earth, other bodies induce a tidal potential on satellites. These include primarily the Sun and the Moon, but also planets and are called *third body perturbations*. The third bodies induce gravitational forces on the Earth, on the one hand, and on the satellite, on the other hand. The difference between these two are the *direct tides*. They depend

on the positions of the third bodies, which can be extracted from the JPL DE421 Ephemerides (Folkner et al., 2009).

Solid Earth Tides

The direct tides lead to a deformation of the solid Earth. The resulting mass displacements induce a secondary change in the gravitational field, denoted as the *solid Earth tides*. This effect can be modeled by employing Love numbers (Farrell, 1972). Here, I follow the specifications of the *IERS Conventions (2010)*.

Ocean Tides

The direct tides furthermore lead to a mass flux in the oceans, which, again, causes a change in the gravitational field. In this thesis, I use the ocean tide model FES2014b (Carrère et al., 2016) to account for this effect.

Atmospheric Tides

Atmospheric tides are another consequence of the direct tides. A redistribution of atmospheric masses leads to a change in the gravitational field. This can be accounted for using the atmospheric tide model that is additionally delivered with the **A**tmosphere and **O**cean **D**e-aliasing Level-**1B** (AOD1B) RL06 product (Dobslaw et al. (2017); Dobslaw et al. (2017), see *Atmosphere and Ocean De-aliasing*, below).

Solid Earth Pole Tides

Polar motion is defined as the movement of the Earth's rotational axis with respect to a crust-fixed reference frame. This motion induces centrifugal forces, which in turn cause deformations of the solid Earth. The resulting change in the gravitational potential is called pole tide. Here, the pole tides are implemented according to the *IERS Conventions (2010)*.

Ocean Pole Tides

Polar motion induces a centrifugal effect on the ocean, which in turn results in changes of the gravitational potential. These changes are called ocean pole tide. As suggested in the *IERS Conventions (2010)*, I use the self-consistent equilibrium model by Desai (2002) in this thesis.

Atmosphere and Ocean De-aliasing

Apart from tidal signals, there are also short-periodic non-tidal variations in the vicinity of the Earth's surface. These can for example be the result of heavy precipitation events or surface winds. In order to prevent aliasing of such high frequencies into the gravity field solutions, the AOD1B RL06 product is commonly applied (Dobslaw et al., 2017a). It models the short-periodic, non-tidal variations of the atmosphere as well as the oceans' reaction to it in intervals of three hours. The product is routinely provided by GFZ and a technical documentation can be found in Dobslaw et al. (2017).

Permanent Tidal Deformation

As explained above, the Earth's gravity field is influenced by direct and indirect tidal effects. Both contain a permanent and a periodic part. Depending on how the permanent part is treated, there are three different ways to define a gravity field solution. They essentially differ regarding their c_{20} SH coefficient.

In a *tide-free* system, the permanent effect of Sun and Moon (both direct and indirect) are reduced and not present anymore. This equals the assumption that Sun and Moon do not exist or are

moved to infinity.

In a *mean-tide* system, on the other hand, direct and indirect permanent effects of Sun and Moon are still included, which corresponds to a long-term average.

If only the indirect effects of Sun and Moon are retained, while the direct effect is reduced, the solution is referred to as *zero-tide*. As suggested in the International Association of Geodesy (IAG) (IAG, 1984), I use the zero-tide version in this thesis.

4.1.3 Integral Equation Approach

The integral equation approach relates satellite positions to parameters of the Earth's gravity field. It was developed by Schneider (1968) for orbit determination and modified by Reigber (1969), such that it can be used for gravity field determination. Mayer-Gürr (2006) successfully used the integral equation approach to derive global CHAMP and GRACE gravity field models. Eicker (2008) computed regional gravity fields from CHAMP and GRACE and Schall (2020) optimized the integral equation approach for regional analysis from GOCE data.

When applying the integral equation approach, the satellite orbit is typically divided into short orbit arcs (i.e. 30 to 90 minutes). For long arcs (i.e. daily arcs), matrices would need too much disc space. The advantages of short arcs are: (1) With each arc, new boundary parameters are estimated, which help to absorb mismodeling, comparable to pseudo-stochastic pulses. (2) Short arcs allow for an easy handling of data gaps. After each gap, a new arc will start. (3) Individual weights can be assigned to each arc by applying VCE. Therefore, arcs of poorer quality have a smaller influence on the final solution. (4) Correlations can be handled relatively easily: Within one arc, the observations are assumed to be correlated over time and individual arcs are assumed to be uncorrelated. Thus, observations of one arc can efficiently be decorrelated during the processing. (5) The program can easily be parallelized, such that arcs can be treated at the same time, as they are not correlated to each other. (6) Regional analyses can be conducted by selecting the appropriate arcs. The last point is not relevant for this thesis, but should be mentioned for completeness.

In the following, the integral equation approach is described based on Mayer-Gürr (2006), where one can also find more detailed information.

Newton's equation of motion formulates the relation between the satellite's movement along its orbit and the forces $\mathbf{F}$ acting on the satellite for a given time t

$$m\ddot{\mathbf{r}}\left(t\right) = \mathbf{F}\left(t, \mathbf{r}, \dot{\mathbf{r}}\right). \tag{4.1.12}$$

In the above equation, $\mathbf{r}$, $\dot{\mathbf{r}}$, and $\ddot{\mathbf{r}}$ describe the position, velocity, and acceleration of the satellite in an inertial reference frame, while m denotes the satellite's mass. In the following, the force will be described with respect to a unity mass element $\mathbf{F} := \frac{1}{m}\mathbf{f}$, leading to

$$\ddot{\mathbf{r}}\left(t\right) = \mathbf{f}\left(t, \mathbf{r}, \dot{\mathbf{r}}\right). \tag{4.1.13}$$

The solution of the differential equation can be obtained by integrating twice. This results in a Fredholm type integral equation of the second kind

$$\mathbf{r}\left(\tau\right) = \mathbf{r}_A\left(1-\tau\right) + \mathbf{r}_B\tau - T^2\int_0^1 K\left(\tau,\tau'\right)\mathbf{f}\left(\tau'\right)d\tau'. \tag{4.1.14}$$

The equation above represents the orbit as a solution of a boundary value problem (Schneider, 1968) with the boundary values

$$\mathbf{r}_A := \mathbf{r}\left(t_A\right) \text{ and } \mathbf{r}_B := \mathbf{r}\left(t_B\right) \tag{4.1.15}$$

for the first and last position of each orbit arc. The concept of an exemplary orbit arc is illustrated in Figure 4.1. The straight line between $\mathbf{r}_A$ and $\mathbf{r}_B$ can be expressed through $\mathbf{r}_A(1-\tau)+\mathbf{r}_B\tau$, which is the first part of Equation (4.1.14).

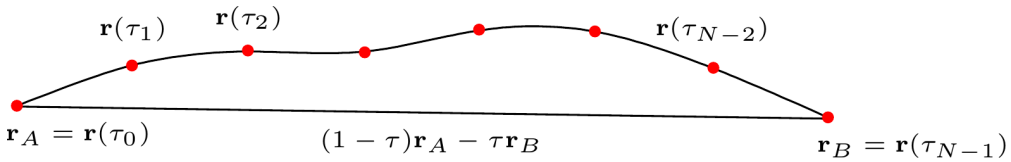

Figure 4.1: Representation of one orbit arc (taken from Mayer-Gürr, 2006).

The deviation from the straight line is described by the subsequent integral in which K denotes the integral kernel

$$K(\tau,\tau') = \begin{cases} \tau'(1-\tau) & \text{for } \tau' \le \tau \\ \tau(1-\tau') & \text{for } \tau' > \tau. \end{cases} \tag{4.1.16}$$

and τ represents the normalized time variable

$$\tau = \frac{t-t_A}{T}, \qquad \text{with } T = t - t_A. \tag{4.1.17}$$

In this thesis, the integral equation approach is used to derive time-variable gravity fields from kinematic orbits of the Swarm mission. The gravity field parameters are part of the specific force function $\mathbf{f}(\tau')$. Consequently, the unknowns in Equation (4.1.14) are $\mathbf{f}(\tau')$ and the boundary values $\mathbf{r}_A$ and $\mathbf{r}_B$. The satellite positions $\mathbf{r}$ serve as observations and are derived from GPS measurements in POD. Equation (4.1.14) is evaluated at every epoch of the orbit arc and can be formulated as a system of equations

$$\mathbf{l} = \mathbf{B}\mathbf{b} + \mathbf{h} + \mathbf{e}. \tag{4.1.18}$$

In this system, the observation equation is split into three parts. The first part ($\mathbf{Bb}$) contains the relation to the boundary values and the second part ($\mathbf{h}$) concerns the specific force that one is actually interested in. Furthermore, $\mathbf{e}$ represents the noise. The vector $\mathbf{l}$ contains the observed satellite positions at N equidistant times τ_i with $i = 1, ..., N$

$$\mathbf{l} = \begin{pmatrix} \mathbf{r}(\tau_1) \\ \vdots \\ \mathbf{r}(\tau_N) \end{pmatrix}. \tag{4.1.19}$$

$\mathbf{b}$ contains the boundary values and $\mathbf{B}$ are the associated factors from Equation (4.1.14).

$$\mathbf{B} = \begin{pmatrix} (1-\tau_1) & \tau_1 \\ (1-\tau_2) & \tau_2 \\ \vdots & \\ (1-\tau_N) & \tau_N \end{pmatrix}, \qquad \mathbf{b} = \begin{pmatrix} \mathbf{r}_A \\ \mathbf{r}_B \end{pmatrix}. \tag{4.1.20}$$

Vector $\mathbf{h}$ of Equation (4.1.18) represents the second part of Equation (4.1.14), which is the integral evaluated at N observation epochs

$$\mathbf{h} = \begin{pmatrix} \mathbf{h}(\tau_1) \\ \vdots \\ \mathbf{h}(\tau_N) \end{pmatrix} \qquad \text{with} \qquad \mathbf{h}(\tau_i) = -T^2 \int_0^1 K(\tau_i,\tau')\,\mathbf{f}(\tau')\,d\tau'. \tag{4.1.21}$$

$\mathbf{h}$ can now be split up into two parts: the first part ($\mathbf{h}_0$) is related to known reference forces, tides, and non-gravitational accelerations and the second part ($\mathbf{Ax}$) defines the relation to the unknown parameters $\mathbf{x}$, which are basically the SH coefficients. The design matrix $\mathbf{A}$ contains the partial derivatives of $\mathbf{h}$ with respect to $\mathbf{x}$

$$\mathbf{h} = \mathbf{h}_0 + \mathbf{Ax} \qquad \text{with} \qquad \mathbf{A}_{ij} = \frac{\partial \mathbf{h}\left(\tau_i\right)}{\partial x_j}. \tag{4.1.22}$$

By combining Equation (4.1.18) and Equation (4.1.22), a linear system of observation equations can be set up

$$\mathbf{l} - \mathbf{h}_0 = \mathbf{Bb} + \mathbf{Ax} + \mathbf{e}. \tag{4.1.23}$$

The above equation can be solved using a Gauß-Markoff model (Section 4.2.1). The unknown parameters are $\mathbf{b}$ and $\mathbf{x}$. For further information on the approach, such as the calculation of the design matrix $\mathbf{A}$, see Mayer-Gürr (2006).

4.1.4 Parameterization for the Swarm Mission

The integral equation approach with short arcs provides many opportunities for different parameterizations. Even if two gravity field models are computed with the integral equation approach from the same data base, they can differ considerably. In Lück et al. (2018), we investigated how different parameterizations affect the Swarm gravity field models. I expanded the investigations to the current time (until March 2021) and chose the following parameters

- arc length: 45 minutes,
- maximum d/o: 40,
- modeling of non-gravitational accelerations: aerodynamic accelerations (drag+lift), SRP, and ERP (Section 3.6),
- bias for non-gravitational accelerations: once per arc and direction,
- scale factor for drag: once per arc and direction,
- scale factor for (SRP+ERP): once per day and direction.

These have proven to deliver best results, when GRACE(-FO) is considered as the ground-truth. If not mentioned otherwise, the gravity field models presented in the following chapters are computed using the above parameterization and are referred to as "IGG-Swarm" or simply "Swarm solutions". The effect of other choices is analyzed in Section 4.3.4.

4.1.5 Visualizing and Comparing Potential Coefficients

A gravity field model is represented by the Stokes coefficients c_{nm} and s_{nm}. The number N of coefficients depends on the maximum degree n and can be determined by

$$N = (n+1)^2\,. \tag{4.1.24}$$

For time-variable GRACE gravity fields, it is not unusual to choose $n = 120$, which leads to $N = 14\,641$ SH coefficients. This number illustrates that special tools are needed to visualize and compare the Stokes' coefficients of gravity field models. In the following, the concept of degree amplitudes and spherical harmonic triangles is described.

Degree Amplitudes

Degree amplitudes σ_n are a tool for the visualization of the Earth's gravity field in the spectral domain (van Gelderen and Koop, 1997). The contribution of each SH degree n to the total gravity field model can be evaluated along with its formal error. In terms of geoid height, degree amplitudes can be computed with

$$\sigma_n = \sqrt{\sigma_n^2} = R\sqrt{\sum_{m=0}^{n}(c_{nm}^2 + s_{nm}^2)}. \tag{4.1.25}$$

Often, one is interested in comparing two gravity field models to each other. These could for example be a static gravity field and a time-variable (e.g., monthly) gravity field. Another possibility would be to compare two static models or two time-variable models to each other to assess their similarities or differences. This can be achieved by computing the difference degree amplitudes $\Delta\sigma_n$

$$\Delta\sigma_n = R\sqrt{\sum_{m=0}^{\Delta n}(\Delta c_{nm}^2 + \Delta s_{nm}^2)}, \tag{4.1.26}$$

where Δc_{nm} and Δs_{nm} simply denote the difference in the SH coefficients of the two models that are compared to each other. Similarly, the error degree amplitudes can be computed to evaluate the error content of the model

$$\widehat{\sigma}_n = R\sqrt{\sum_{m=0}^{n}\left(\widehat{\sigma}_{c_{nm}}^2 + \widehat{\sigma}_{s_{nm}}^2\right)}. \tag{4.1.27}$$

$\widehat{\sigma}_{c_{nm}}^2$ and $\widehat{\sigma}_{s_{nm}}^2$ denote the formal errors of the SH coefficients of the gravity field model. Figure 4.2 illustrates the concept of degree amplitudes σ_n, difference degree amplitudes $\Delta\sigma_n$ and error degree amplitudes $\widehat{\sigma}_n$ (Equations (4.1.25) to (4.1.27)) using the GOCO06s and ITSG-Grace2018 gravity field models.

Spherical Harmonic Triangles

SH triangles are a common tool to visualize a set of Stokes' coefficients. Each coefficient is represented by a color. Due to the large variety, one usually chooses a logarithmic color scale. The left side of the triangle represents the sine coefficients s_{nm}, while the right part illustrates the cosine coefficients c_{nm}. The SH order m is plotted on the x-axis, while the degree n is plotted on the y-axis. It is possible to either show the Stokes' coefficients themselves, or their respective uncertainties.

Figure 4.3 shows exemplarily SH triangles for the ITSG-Grace2018 gravity field from January 2016. In Figure 4.3 (a), the full signal of the monthly Stokes' coefficients is plotted. It is well visible that lower degrees have higher values, as they represent the coarse structure of the Earth. Finer structures, i.e. higher degrees, have smaller values. Figure 4.3 (b) shows the monthly coefficients from subplot (a) minus the static part of the GOCO06s with a different color scale. Again, the lower degrees are larger in general, because they contain more signal. Here, also orders $m > 70$ and degrees $n > 115$ have larger values. However, the quality of the coefficients in these areas is inferior as can be seen in the uncertainty plot of Figure 4.3 (c). Furthermore, degree c_{20} is not well determined (see Section 5.1) and uncertainties of sectoral coefficients are larger in general. Certain orders have a higher uncertainty than others, which is reflected in a vertical striping pattern and might be related to the resonance orders of GRACE, occurring at multiples of 15 (Cheng and Ries, 2017).

Throughout this thesis, SH triangles will be used to compare different gravity field models to each other.

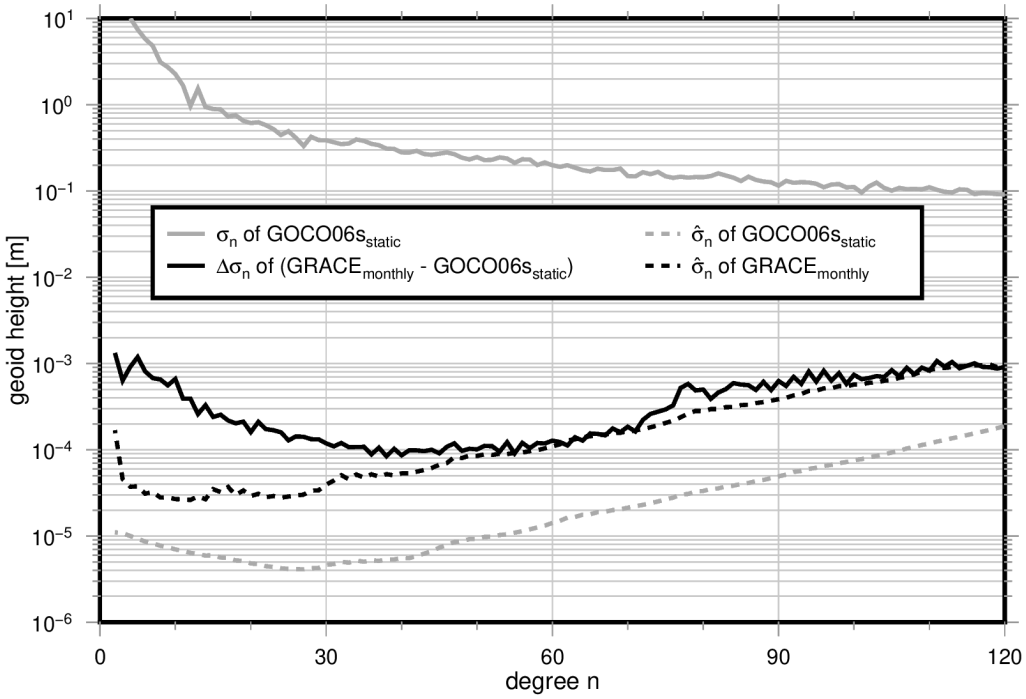

Figure 4.2: Concept of degree amplitudes σ_n, difference degree amplitudes $\Delta\sigma_n$, and error degree amplitudes $\widehat{\sigma}_n$. As a reference field, the static part of the GOCO06s is chosen and the monthly ITSG-Grace2018 gravity field model of January 2016 is used for comparison.

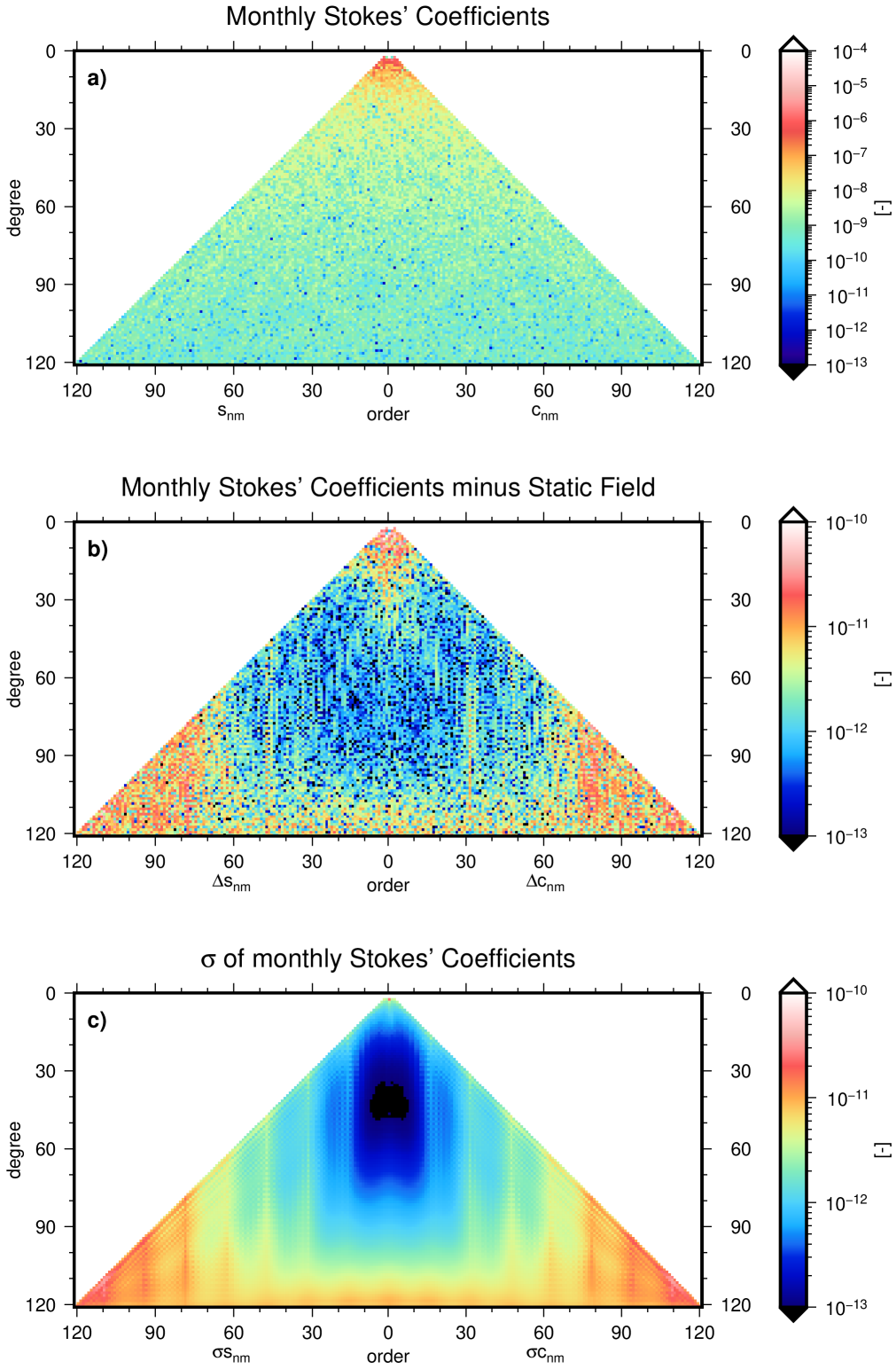

Figure 4.3: Representation of ITSG-Grace2018 SH coefficients from January 2016 in a triangle. a) Full signal of the monthly gravity field solution. b) Monthly gravity field with respect to the static part of the GOCO06s. c) Uncertainties of the monthly gravity field.

4.2 Implementation

The main software that is used in this thesis is **G**ravity **R**ecovery **O**bject **O**riented **P**rogramming **S**ystem (GROOPS) (Mayer-Gürr et al., 2021). GROOPS has been developed at IGG Bonn and is now maintained at both IGG and IfG Graz[1]. The software is written in C++ and was designed to solve geodetic tasks such as GNSS processing and gravity field recovery. Non-gravitational accelerations are modeled using MATLAB (Section 3.6) and plots in this thesis are generated with version 6.2.0 of the **G**eneric **M**apping **T**ools (GMT) software (Wessel et al., 2019).

NEQ systems for one month can become huge. Table 4.2 gives an overview of the number of observations and parameters for each month, with the parameterization of Section 4.1.4 taken as a basis. A sampling of 10 s leads to an average number of 2 343 615 observations for each month accumulated for the three satellites. This number varies due to data gaps and the number of days per month (standard deviation of 71 018). A gravity field of maximum d/o 40 contains 1677 parameters (degree 0 and 1 are not estimated). Furthermore, six parameters for the boundary values are estimated for each arc, which leads to almost 18 000 additional parameters. Bias and scale parameters for the non-gravitational accelerations amount to approximately 18 000 additional parameters. Hence, all in all there are more than 2 000 000 observations and 37 000 parameters for each month, which would result in a design matrix of 650 GB, a covariance matrix of 40 TB and a NEQ matrix of 10 GB. A straight-forward computation of a monthly gravity field model is not possible with matrices of such size. In the following sections, ways to reduce the computational costs are presented.

	Mean	± Std.
# Observations (A+B+C)	2 343 615	± 71 018
# Gravity field parameters	1677	± 0
# Boundary value parameters (A+B+C)	17 576	± 545
# Bias parameters (A+B+C)	8788	± 273
# Scale parameters (A+B+C)	9061	± 280

Table 4.2: Number of observations and parameters for the monthly gravity fields. Due to data gaps and the different number of days per month, the number of observations and parameters varies. A mean value and the corresponding standard deviation is given. Orbit arcs of 45 minutes are assumed and the bias is estimated for each direction per arc, while the scaling factors are estimated separately for drag and radiation pressure for each direction (drag: once per arc; radiation pressure: once per day).

4.2.1 General Least Squares Adjustment

A widely used approach to determine the parameters of an overdetermined system of observation equations is the **L**east **S**quares **A**djustment (LSA) (Koch, 1999). The basic principle is shortly described in this subsection, while all modifications are explained throughout the next paragraphs of this subsection.

A linear or linearized Gauß-Markoff model consists of a functional model

$$\mathbf{l} = \mathbf{A}\mathbf{x} + \mathbf{e}, \tag{4.2.1}$$

and a stochastic model

$$\boldsymbol{\Sigma}_{ll} = \sigma_0 \mathbf{P}^{-1}. \tag{4.2.2}$$

The functional model describes the relation between the observations $\mathbf{l}$ and the unknown parameters $\mathbf{x}$, with the design matrix $\mathbf{A}$ and observation residuals $\mathbf{e}$. The stochastic model describes the variances and covariances of the observations. $\boldsymbol{\Sigma}_{ll}$ denotes the variance-covariance matrix of the

[1] https://github.com/groops-devs/groops (last access: July 5, 2021)

observations and can alternatively be described using a general variance factor σ_0 and the weight matrix $\mathbf{P}$. The goal is to find the **B**est **L**inear **U**nbiased **E**stimator (BLUE), which can be achieved by minimizing the weighted sum of the squared residuals

$$\mathbf{e}^T\mathbf{P}\mathbf{e} \rightarrow \min. \tag{4.2.3}$$

The NEQ matrix $\mathbf{N}$ and NEQ vector $\mathbf{n}$ can be computed by

$$\mathbf{N} = \mathbf{A}^T{\boldsymbol{\Sigma}_{ll}}^{-1}\mathbf{A}, \quad \mathbf{n} = \mathbf{A}^T{\boldsymbol{\Sigma}_{ll}}^{-1}\mathbf{l}. \tag{4.2.4}$$

The estimated parameters $\hat{\mathbf{x}}$ are obtained by solving

$$\mathbf{N}\hat{\mathbf{x}} = \mathbf{n}. \tag{4.2.5}$$

4.2.2 Preparing the Data

Before starting with the actual computations for gravity field retrieval, the data has to be prepared. Swarm data that is used in this thesis is provided in daily files. Detailed information on the data can be found in Section 3.4. The following products are used for gravity field retrieval: kinematic orbits including 3×3 epoch-wise covariance matrices from IfG (see Section 3.5), the L1B star camera data STRxATT_1B and the mass of the satellites from the SC_xDYN_1B product for modeling the non-gravitational accelerations. Furthermore, the calibrated along-track accelerometer data of Swarm C ACCCCAL_2_ is prepared for comparison.

All products have to be stored in monthly files with an adequate sampling. After some tests regarding the computation time and the quality of the results, I reduced the data sampling to 10 s. A higher sampling would lead to considerably longer run-times without an improvement of the results, as successive observations would be highly correlated.

Times where a satellite maneuver was carried out (provided in the STRxATT_1B product) are excluded, as this data would distort the gravity field processing. A large number of maneuvers was performed during the commissioning phase in the first months of the Swarm mission in order to place the satellites into their selected orbits. Since then, mainly short maneuvers are carried out occasionally for orbit control.

Non-gravitational accelerations are modeled according to Section 3.6. In a next step, all data products are synchronized, i.e. only epochs that are available in all files are kept. While synchronizing, the monthly files are divided into short orbit arcs that are assumed to be uncorrelated and can thus be processed in parallel. One month contains for example around 1000 45-minute arcs, depending on the number and distribution of data gaps. Investigations on the length of the orbit arcs are conducted in Section 4.3.4.

4.2.3 Computing the Reference Forces

In order to derive a time-variable gravity field of the Earth, all known reference forces are reduced during the processing. These reference forces include an a priori background model, tidal disturbances, and non-gravitational accelerations. For a complete description of all models, see Section 4.1.2.

The reference forces can directly be included in the processing or their impact on the satellite's orbit can be computed beforehand. The prior determination has the advantage that it is possible to save the accelerations for each position along the satellite's orbit. If one wants to investigate different parameterizations (see Section 4.3.4), this step of reducing the reference forces only needs to be computed once, independent of later choices, and can be used for several following investigations, thus saving computing time.

4.2.4 Preprocessing the Kinematic Orbits

In a preprocessing step, an empirical covariance function is estimated to describe the temporal correlation of the kinematic orbit epochs. Furthermore, a variance factor for each arc is computed in order to downweight arcs with lower accuracy or outliers. The goal is to obtain a full covariance matrix $\boldsymbol{\Sigma}_{\boldsymbol{ll}arc}$ for each orbit arc with temporal as well as epoch-wise correlations

$$\boldsymbol{\Sigma}_{\boldsymbol{ll}arc} = \sigma_0^2 \sigma_{arc}^2 \mathbf{D}_{diag} \mathbf{S}_{x,y,z} \mathbf{D}_{diag}^T. \tag{4.2.6}$$

In the above equation, σ_0^2 is an overall variance factor, which is set to 1 in this thesis, as full 3×3 covariance matrices per epoch are provided with the kinematic orbits. $\mathbf{D}_{diag}$ is a block diagonal matrix and consists of 3×3 matrices which are placed on the main diagonal

$$\mathbf{D}_{diag} = \begin{pmatrix} \mathbf{D}\left(t_1\right) & 0 & \dots & 0 \\ 0 & \mathbf{D}\left(t_2\right) & \dots & 0 \\ \vdots & \vdots & \ddots & \vdots \\ 0 & 0 & \dots & \mathbf{D}\left(t_n\right) \end{pmatrix}, \tag{4.2.7}$$

where n is the number of epochs in the considered arc. The individual matrices $\mathbf{D}$ are obtained from an eigenvalue decomposition of the 3×3 epoch-wise covariance matrices

$$\boldsymbol{\Sigma}_{3x3}\left(t_i\right) = \mathbf{Q}\boldsymbol{\Lambda}\mathbf{Q}^T = \left(\mathbf{Q}\boldsymbol{\Lambda}^{1/2}\mathbf{Q}^T\right)\left(\mathbf{Q}\boldsymbol{\Lambda}^{1/2}\mathbf{Q}^T\right)^T = \mathbf{D}\left(t_i\right)\mathbf{D}^T\left(t_i\right). \tag{4.2.8}$$

Now only $\mathbf{S}_{x,y,z}$ and σ_{arc} are missing to assemble the full covariance matrix of Equation (4.2.6). They are both obtained using the residuals $\mathbf{e}_{arc}$ of a complete LSA. In a first step, the gravity field adjustment (see Section 4.2.5 for information on designing and solving the NEQs) is executed by considering $\boldsymbol{\Sigma}_{\boldsymbol{ll}arc}$ to only contain the available 3×3 epoch-wise covariance information on the main diagonal. The residuals are used to derive an empirical covariance function for each direction in the satellite reference frame. With Δt being the observation sampling, the covariances can be expressed for each direction by

$$\mathbf{S}_x = \begin{pmatrix} \sigma_{x(0\Delta t)}^2 \\ \sigma_{x(1\Delta t}^2) \\ \vdots \\ \sigma_{x(n\Delta t)}^2 \end{pmatrix}, \quad \mathbf{S}_y = \begin{pmatrix} \sigma_{y(0\Delta t)}^2 \\ \sigma_{y(1\Delta t}^2) \\ \vdots \\ \sigma_{y(n\Delta t)}^2 \end{pmatrix}, \quad \mathbf{S}_z = \begin{pmatrix} \sigma_{z(0\Delta t)}^2 \\ \sigma_{z(1\Delta t}^2) \\ \vdots \\ \sigma_{z(n\Delta t)}^2 \end{pmatrix}. \tag{4.2.9}$$

These components are sorted into matrix $\mathbf{S}_{x,y,z}$

$$\mathbf{S}_{x,y,z} = \begin{pmatrix} \sigma_{x(0\Delta t)}^2 & 0 & 0 & \sigma_{x(1\Delta t)}^2 & 0 & 0 & \dots & \sigma_{x(n\Delta t)}^2 & 0 & 0 \\ 0 & \sigma_{y(0\Delta t)}^2 & 0 & 0 & \sigma_{y(1\Delta t)}^2 & 0 & \dots & 0 & \sigma_{y(n\Delta t)}^2 & 0 \\ 0 & 0 & \sigma_{z(0\Delta t)}^2 & 0 & 0 & \sigma_{z(1\Delta t)}^2 & \dots & 0 & 0 & \sigma_{z(n\Delta t)}^2 \\ \sigma_{x(1\Delta t}^2) & 0 & 0 & \sigma_{x(0\Delta t)}^2 & 0 & 0 & \dots & \sigma_{x(1\Delta t)}^2 & 0 & 0 \\ 0 & \sigma_{y(1\Delta t}^2) & 0 & 0 & \sigma_{y(0\Delta t)}^2 & 0 & \dots & 0 & \sigma_{y(1\Delta t)}^2 & 0 \\ 0 & 0 & \sigma_{z(1\Delta t}^2) & 0 & 0 & \sigma_{z(0\Delta t)}^2 & \dots & 0 & 0 & \sigma_{z(1\Delta t)}^2 \\ \vdots & \vdots & \vdots & \vdots & \vdots & \vdots & \ddots & \vdots & \vdots & \vdots \\ \sigma_{x(n\Delta t)}^2 & 0 & 0 & \sigma_{x(1\Delta t)}^2 & 0 & 0 & \dots & \sigma_{x(0\Delta t)}^2 & 0 & 0 \\ 0 & \sigma_{y(n\Delta t)}^2 & 0 & 0 & \sigma_{y(1\Delta t)}^2 & 0 & \dots & 0 & \sigma_{y(0\Delta t)}^2 & 0 \\ 0 & 0 & \sigma_{z(n\Delta t)}^2 & 0 & 0 & \sigma_{z(1\Delta t)}^2 & \dots & 0 & 0 & \sigma_{z(0\Delta t)}^2 \end{pmatrix}. \tag{4.2.10}$$

The weight factors σ_{arc} for each arc are also derived from the residuals $\mathbf{e}_{arc}$ using a **V**ariance **C**omponent **E**stimation (VCE) (Koch and Kusche, 2002)

$$\sigma_{arc}^2 = \frac{\mathbf{e}_{arc}^T \boldsymbol{\Sigma}_{\boldsymbol{ll}arc}^{-1} \mathbf{e}_{arc}}{r_{arc}}, \tag{4.2.11}$$

where r_{arc} denotes the redundancy. Now, a refined $\boldsymbol{\Sigma}_{\boldsymbol{ll}arc}$, containing the full covariance information, is computed using Equation (4.2.6). The whole preprocessing step can be repeated iteratively until convergence.

4.2.5 Designing and Solving the Normal Equations for Each Satellite

As NEQ systems for one month can become huge, several steps are taken to reduce the computational efforts.

(1) The individual orbit arcs are assumed to be uncorrelated, such that one can set up the system of NEQs for each arc in parallel. Index i denotes the consideration of an individual arc.

(2) To design and solve the NEQs computationally efficiently, it is common to decorrelate the system of observation equations first by applying a Cholesky decomposition to the covariance matrix of the observations (Koch, 1999)

$$\boldsymbol{\Sigma}_{ll_i} = \mathbf{P}_i^{-1} = \mathbf{R}^T\mathbf{R}, \tag{4.2.12}$$

where $\mathbf{R}$ is a regular upper triangular matrix. The goal is to obtain an uncorrelated observation equation

$$\bar{\mathbf{l}}_i = \overline{\mathbf{A}}_i\mathbf{x} + \bar{\mathbf{e}}_i. \tag{4.2.13}$$

This is achieved by multiplying the transposed inverse transformation matrix $\mathbf{R}^{-T}$ with the design matrix $\mathbf{A}_i$ and the vector of observations $\mathbf{l}_i$

$$\overline{\mathbf{A}}_i = \mathbf{R}^{-T}\mathbf{A}_i, \quad \bar{\mathbf{l}}_i = \mathbf{R}^{-T}\mathbf{l}_i. \tag{4.2.14}$$

The NEQ matrix $\mathbf{N}_i$ and vector $\mathbf{n}_i$ can be computed using the transformed quantities

$$\mathbf{N}_i = \overline{\mathbf{A}}_i^T\overline{\mathbf{A}}_i = \mathbf{A}_i^T\mathbf{P}_i\mathbf{A}_i, \quad \mathbf{n}_i = \overline{\mathbf{A}}_i^T\bar{\mathbf{l}}_i = \mathbf{A}_i^T\mathbf{P}_i\mathbf{l}_i. \tag{4.2.15}$$

The decorrelation entails several advantages, such as the avoidance of the inversion of the covariance matrix, which is computationally intensive. The following explanations refer to decorrelated observation equations, without explicitly mentioning it (and omitting the bars for simplicity).

(3) The parameters are divided into "relevant" (i.e. gravity) parameters $\mathbf{x}$ and arc-related parameters $\mathbf{b}$ as is explained in Section 4.1.3. To recap, Equation (4.1.23) stated

$$\mathbf{l}_i - \mathbf{h}_{i,0} = \mathbf{B}_i\mathbf{b}_i + \mathbf{A}_i\mathbf{x} + \mathbf{e}_i. \tag{4.2.16}$$

The decorrelation of step (2) allows the reduction of the arc-related parameters from the system, which leads to a smaller NEQ and thus a shorter computing time. In order to reduce the parameters $\mathbf{b}$, one needs to build the submatrices

$$\begin{aligned} &\mathbf{N}_{i,11} = \mathbf{A}_i^T\mathbf{A}_i, \quad \mathbf{N}_{i,12} = \mathbf{A}_i^T\mathbf{B}_i, \quad \mathbf{N}_{i,22} = \mathbf{B}_i^T\mathbf{B}_i \\ &\mathbf{n}_{i,1} = \mathbf{A}_i^T\left(\mathbf{l}_i - \mathbf{h}_{i,0}\right), \quad \mathbf{n}_{i,2} = \mathbf{B}_i^T\left(\mathbf{l}_i - \mathbf{h}_{i,0}\right). \end{aligned} \tag{4.2.17}$$

The reduced NEQ matrix $\overline{\mathbf{N}_i}$ and NEQ vector $\overline{\mathbf{n}_i}$ are computed by

$$\overline{\mathbf{N}_i} = \mathbf{N}_{i,11} - \mathbf{N}_{i,12}\mathbf{N}_{i,22}^{-1}\mathbf{N}_{i,12}^T \quad \overline{\mathbf{n}}_i = \mathbf{n}_{i,1} - \mathbf{N}_{i,12}\mathbf{N}_{i,22}^{-1}\mathbf{n}_{i,2} \tag{4.2.18}$$

and lead to the reduced NEQ system (Niemeier, 2002)

$$\overline{\mathbf{N}}_i\hat{\mathbf{x}} = \overline{\mathbf{n}}_i. \tag{4.2.19}$$

(4) In the next step, the NEQ systems of all individual arcs need to be accumulated to obtain a solution for the whole month

$$\overline{\mathbf{N}} = \sum_{i=1}^{m}\overline{\mathbf{N}}_i, \quad \overline{\mathbf{n}} = \sum_{i=1}^{m}\overline{\mathbf{n}}_i, \tag{4.2.20}$$

where m is the total number of arcs in one month. The NEQ system

$$\overline{\mathbf{N}}\hat{\mathbf{x}} = \overline{\mathbf{n}} \tag{4.2.21}$$

can be solved to obtain the estimated parameters $\hat{\mathbf{x}}$ for the whole month.

4.2.6 Accumulating the Normal Equations from Swarm A, B, and C to Obtain a Combined Solution

In the previous steps, a full LSA has been performed for each Swarm satellite individually. This means that one obtains three systems of NEQs and three gravity field solutions that can be compared to each other. The goal is to derive one combined solution from all satellites. This is achieved by accumulating the NEQs of Swarm A, B, and C as explained in Equation (4.2.20) for the accumulation of individual arcs. It must be ensured that only gravity field parameters are included in the NEQs. In case that e.g. a global scaling factor for the modeled non-gravitational accelerations was estimated for the whole month, it should be reduced from the NEQs beforehand (see Equations (4.2.17) to (4.2.19)).

4.2.7 Reassembling the Monthly Gravity Field

One has to keep in mind that the obtained solution is residual with respect to the initial reference forces that were computed as explained in Section 4.2.3. In general, there are four quantities that are sensed by the satellite: (1) forces represented in the a priori model, (2) the residual force model (which is estimated by solving the NEQs), (3) tidal forces, and (4) non-gravitational accelerations. The common way to disseminate gravity field models in the scientific community (e.g., by the ICGEM) is to add the a priori reference model back to the solution. This means that tidal disturbances and non-gravitational accelerations are not part of the gravity field models. Furthermore, the corrections mentioned in Section 5.1 are also not yet included in the gravity fields, such that the user can decide him-/herself which corrections to apply. I also follow this convention and add the a priori reference gravity field model back to my solution (i.e. the monthly mean of the GOCO06s).

4.2.8 Time Period for Comparisons

When comparing GRACE(-FO) and Swarm gravity field models, one can usually assume GRACE(-FO) as the ground truth. Due to the ultra-precise KBR measurements, GRACE(-FO) achieves a higher resolution and a better quality. In this way, one can evaluate the error of Swarm by comparing to GRACE(-FO). This helps to assess the quality of Swarm time-variable gravity field models, even when GRACE(-FO) is not available.

Figure 4.4 gives an overview of the data availability. Swarm was launched on November 22, 2013. Kinematic orbits from IfG are produced starting on July 15, 2014 (which coincides with the update of the sampling rate, see Figure 3.11). However, the quality of the kinematic orbits and thus also of the time-variable gravity fields was inferior in the beginning. Due to the decreasing solar activity and several receiver updates, the orbit products became more reliable over time. As the results will show, the reliability of the Swarm gravity field models strongly increases in May 2015. The middle panel shows the data availability and quality of GRACE(-FO), for more details see Section 2.1.4.

When deriving metrics, such as trends, **R**oot **M**ean **S**quare (RMS) values, **R**oot **M**ean **S**quare **E**rrors (RMSEs) or correlations, it is important to use the same time period for both satellites. Otherwise, the results and metrics would not be comparable. I chose to only use those months which are available with good quality for both GRACE(-FO) and Swarm (see bottom panel of Figure 4.4). These include 11 months during the GRACE period (July to September and December 2015 as well as January to March and May to August 2016) and 32 months of GRACE-FO (June and July 2018 as well as October 2018 to March 2021).

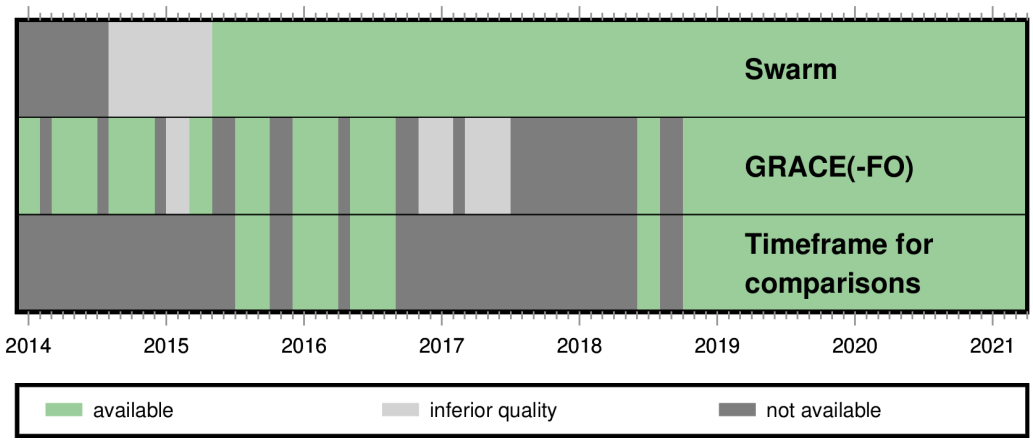

Figure 4.4: Availability of GRACE(-FO) and Swarm data and the base for comparison. Upper panel: Availability of IGG-Swarm gravity field models. Middle panel: Availability of ITSG-Grace2018 gravity field models. Bottom panel: Base for comparison when deriving metrics such as RMS, RMSE, trend, and correlation. Only months where both GRACE(-FO) and Swarm are of good quality are considered.

4.3 Results from Swarm and Comparison to GRACE(-FO)

Swarm and GRACE(-FO) gravity field models consist of a large number of SH coefficients for each month. As it would be out of the scope of this thesis to investigate the time series for each coefficient (e.g., 1677 coefficients for d/o 40), I show some representative examples of the lower degrees (Section 4.3.1). In order to still get the whole overview, different metrics (e.g., RMS, RMSE, correlation) for each coefficient are derived and illustrated as SH triangles (Section 4.3.2). Furthermore, I analyze degree amplitudes in order to assess the signal and error content for each degree (Section 4.3.3). Finally, the effect of different parameterization choices on the gravity field models is investigated (Section 4.3.4).

4.3.1 Comparing the Lower Degrees

Lower SH degrees are important to describe the long-wavelength part of the Earth's gravity field. c_{20} and c_{30} of the GRACE(-FO) solutions are commonly replaced with values from **T**echnical **N**ote (TN)-14 (Loomis et al., 2020), as will be explained in Section 5.1. The replacement values from TN-14 are computed at NASA's **G**oddard **S**pace **F**light **C**enter (GSFC) from up to seven SLR satellites. They estimate SH coefficients up to d/o 5 and additionally c_{61} and s_{61}, while considering higher degrees from background models. Figure 4.5 shows time series of selected low-degree SH coefficients from ITSG-Grace2018, Swarm, SLR, and TN-14. The solution that is referred to as SLR in this section is the IGG-SLR gravity field model.

The time series of c_{20} from TN-14 shows a clear annual signal and looks smoother as compared to GRACE(-FO) and Swarm. c_{20} from SLR and TN-14 are highly correlated by 94 % and the RMS of the difference is $0.39 \cdot 10^{-10}$. Swarm data is more noisy, but still shows a correlation of 47 %, while the RMS of the difference is $1.31 \cdot 10^{-10}$. GRACE(-FO) data seems to be completely noisy, with a correlation of 0 % and a RMS of $1.58 \cdot 10^{-10}$.

The c_{30} coefficient shows clear similarities between TN-14, GRACE(-FO), and Swarm. Correlations are 90 % (TN-14 vs. GRACE(-FO)) and 61 % (TN-14 vs. Swarm). RMS values are significantly lower than they are for c_{20}, they amount to $0.32 \cdot 10^{-10}$ (TN-14 minus GRACE(-FO)) and $0.68 \cdot 10^{-10}$ (TN-14 minus Swarm). The SLR time series and TN-14 are correlated by 75 %, but SLR starts to drift away from the other solutions in the second half of 2019 and therefore has a larger RMS of $1.04 \cdot 10^{-10}$, when compared to TN-14.

GRACE(-FO), Swarm, and IGG-SLR time series of s_{31} are similar. The correlation of SLR and GRACE(-FO) is slightly higher than that of Swarm and GRACE(-FO) (85 % vs. 83 %). Regarding

the RMS, on the other hand, Swarm shows less deviations to GRACE(-FO) (Swarm $0.24 \cdot 10^{-10}$, SLR: $0.27 \cdot 10^{-10}$).

Time series of the s_{33} coefficient are strongly correlated for GRACE(-FO) and Swarm (89 %) and GRACE(-FO) and IGG-SLR (78 %). However, the SLR time series is more noisy, which is reflected in the RMS with respect to GRACE(-FO) (Swarm: $0.25 \cdot 10^{-10}$ and SLR $0.58 \cdot 10^{-10}$).

In general, the lower degrees of GRACE(-FO) and Swarm show strong correlations and only small differences (except for c_{20}, which is replaced). While Figure 4.5 only shows four SH coefficients in detail, the next subsections give an overview of all coefficients and confirm this statement.

4.3.2 Spherical Harmonic Triangles

In this section, the individual SH coefficients are examined in terms of SH triangles (Section 4.1.5). Figure 4.6 highlights different aspects of GRACE(-FO) and Swarm SH coefficients. For the analysis, only months that are available in both GRACE(-FO) and Swarm are considered, as evaluated in Figure 4.4.

In Figure 4.6 (a) the variability of the GRACE(-FO) SH coefficients is depicted, which is, in a mathematical sense, the standard deviation of each coefficient. It is interpreted as signal in the following. As could be expected, the variability is high for low degrees. Furthermore, the edges of the triangle (in the following referred to as "sectoral and near-sectoral coefficients") have larger values than the interior.

The RMSE of Swarm with respect to GRACE(-FO) is presented in Figure 4.6 (b) for each coefficient. The RMSE can be interpreted as noise, because GRACE(-FO) is considered to be the ground-truth. Lower degrees as well as sectoral and near-sectoral coefficients have smaller RMSEs. Interestingly, zonal coefficients of the lower degrees show larger values than lower degrees in general. For degrees higher than ∼10-15, the RMSE is clearly larger than the variability of GRACE(-FO) of subfigure (a), which will be discussed in terms of the **S**ignal-to-**N**oise **R**atio (SNR) in subfigure (f).

Figure 4.6 (c) shows the RMS of formal GRACE(-FO) errors. The c_{20} coefficient has the largest RMS, but it is commonly replaced (Section 5.1). A general pattern related to the SH order is visible in the triangle. Orders lower than ∼15 have small RMS values, which decrease with increasing degree and they are generally lower than the variance of subfigure (a). The RMS of orders larger than ∼15 does not show a clear dependence on the degree (only sectoral coefficients are generally larger). With increasing order, the RMS gets higher. High orders of (c) are in the same magnitude as high orders of (a), which means that they should be handled with caution.

In Figure 4.6 (d) the RMS of formal Swarm errors is presented. The RMS is higher than that of GRACE(-FO), which could be expected due to different ways of gravity field retrieval. However, it is interesting that subfigures (b) and (d) look very similar. This means that formal Swarm errors are a realistic estimate of the real error.

Figure 4.6 (e) presents the correlation between GRACE(-FO) and Swarm SH coefficients. Lower degrees (except for c_{20}) have high correlations. This is a sign for a good reliability of the Swarm coefficients. For d/o up to ∼10, a large part of the coefficients has a correlation of 70 % or higher. The correlation is further analyzed in Figure 4.7.

The SNR is analyzed in Figure 4.6 (f). It is computed by dividing the values of subfigure (a) by those of subfigure (d). Blue values indicate that the signal is larger than the noise. As expected, lower degrees show SNR values larger than 1 and with increasing degree, the SNR decreases. Starting from degree 11, all coefficients have a smaller SNR than 1. Yet, they can still provide information on mass changes (by applying a smoothing filter and spatial averaging), as will be shown in Chapter 5.

In Figure 4.7 the correlation of Swarm with respect to GRACE(-FO) (Figure 4.6 f) is analyzed in more detail. In subfigure (a) the mean and RMS correlation per degree is shown. They generally

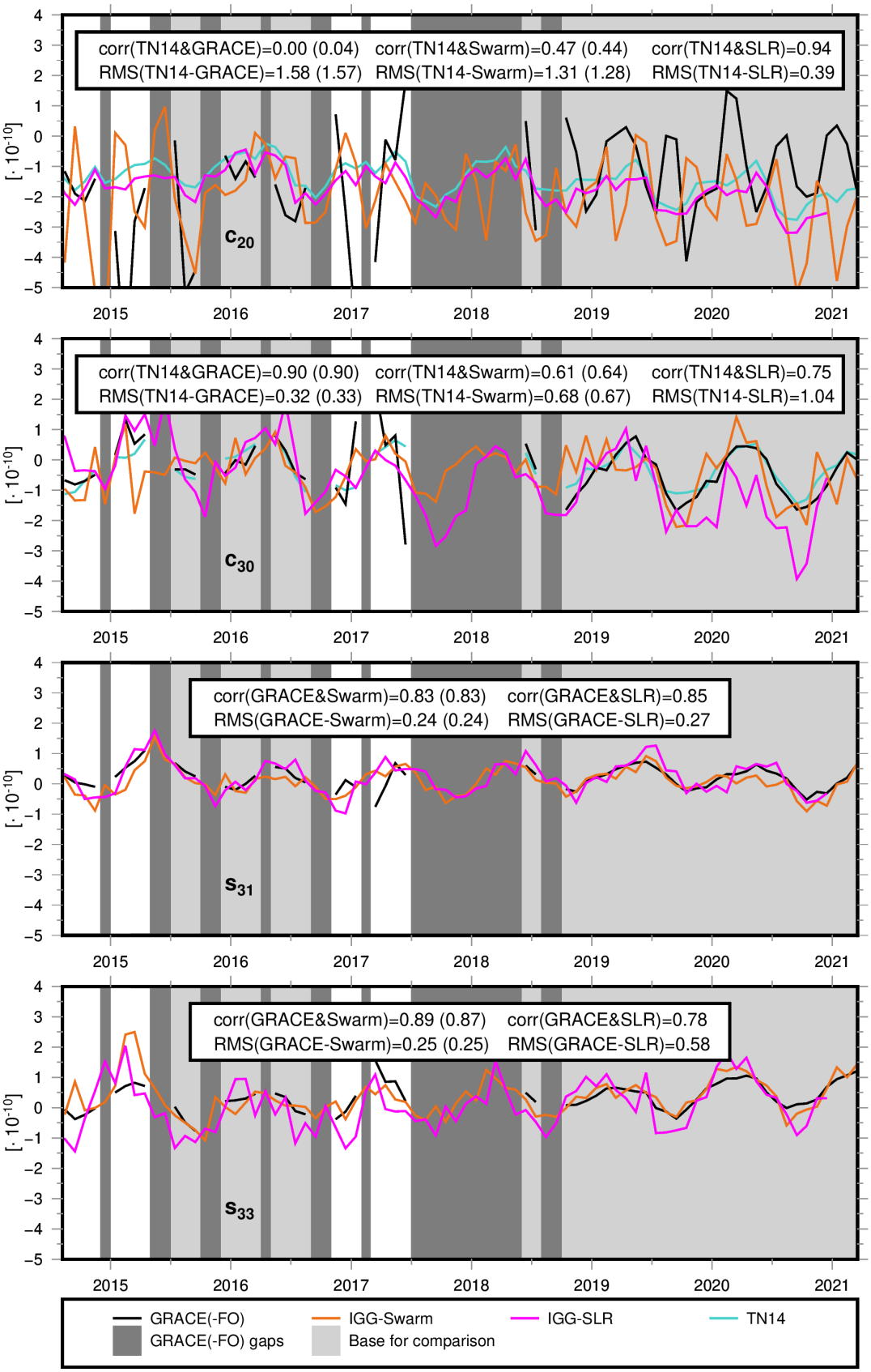

Figure 4.5: Time series of selected lower degree coefficients (c_{20}, c_{30}, s_{31}, s_{33}) from Swarm, GRACE(-FO), and SLR with respect to the static part of the GOCO06s. The TN-14 solution is also shown as a reference. For c_{20}, the TN-14 gaps are filled with the CSR time series for full calender months. Values in brackets are related to the time period of SLR data, which ends in December 2020. RMS values in units of 10^{-10}.

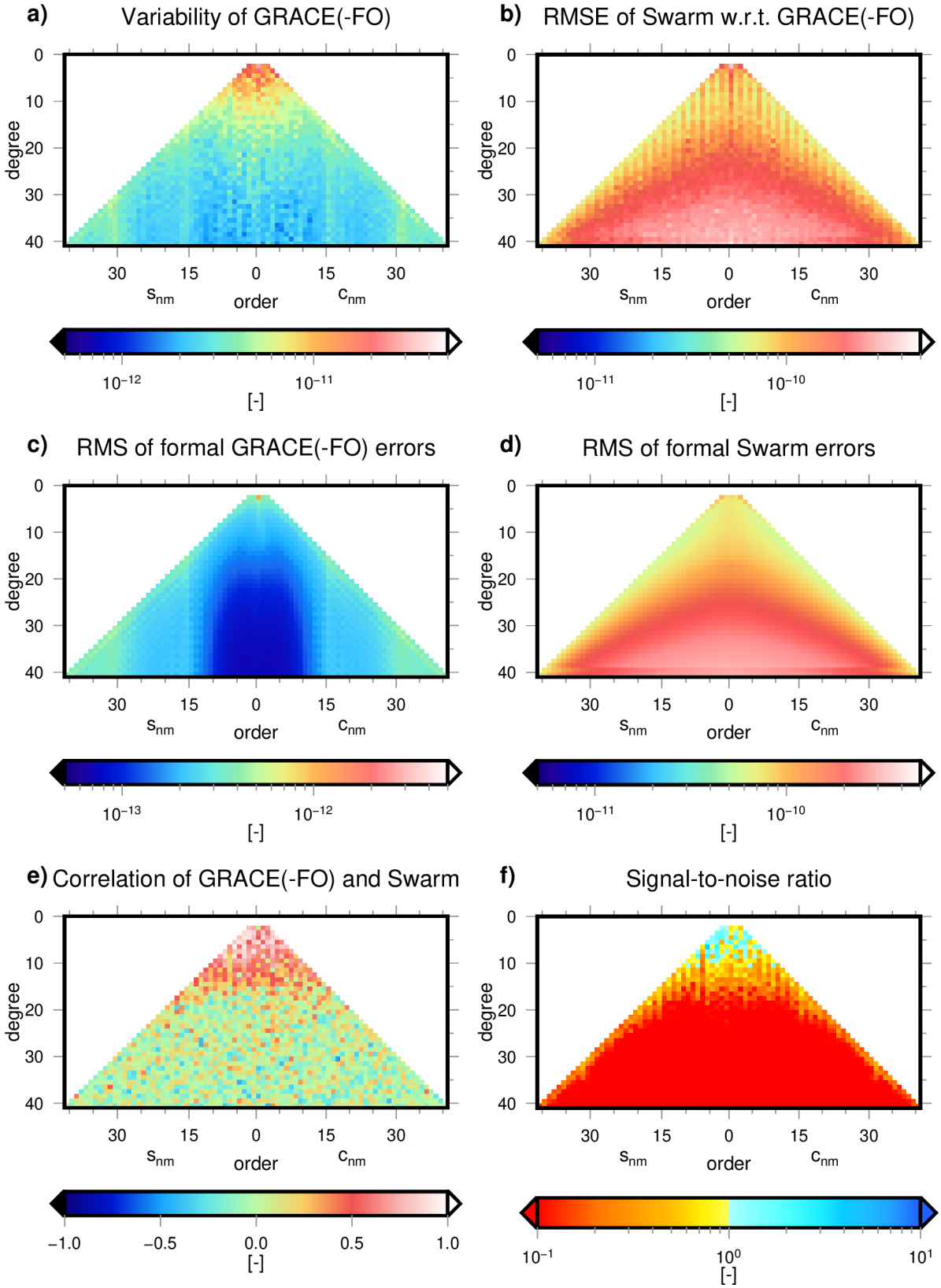

Figure 4.6: SH triangles showing different statistics of GRACE(-FO) and Swarm Stokes' coefficients.

decrease with an increasing degree, which could be expected. Both, mean and RMS are larger than 75 % up to degree 6 and larger than 50 % up to d/o 10. For degrees higher than ∼14, mean and RMS start to diverge, indicating the existence of negative correlations.

As single exceptions could distort the interpretation of mean and RMS of the correlations, another approach is plotted in Figure 4.7 (b). The lines indicate how many coefficients have a correlation of higher than 75 % (and 50 %, 25 %, respectively). Degree 10, for example, is composed of 19 SH coefficients. For each of these 19 coefficients the correlation between Swarm and GRACE(-FO) is computed. 16 coefficients are correlated by more than 25 %, 11 have a correlation of more than 50 % and 2 are correlated by more than 75 %. This amounts to fractions of 0.84, 0.58, and 0.11, corresponding to the values on the y-axis. Only coefficients up to degree 17 have correlations larger than 50 %. This figure once more shows that it is hard to make a clear statement on which degrees can reliably be used. Based on the analyses in Figure 4.6 and Figure 4.7, one should truncate somewhere above degree 10-15, depending on the application.

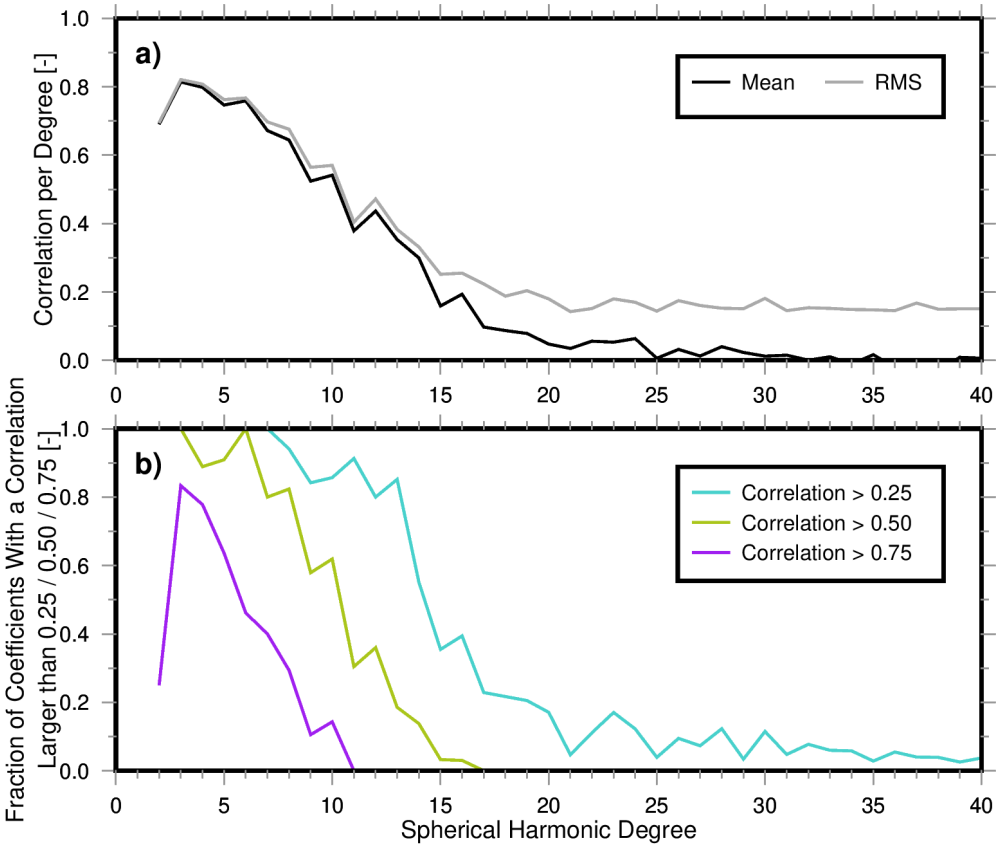

Figure 4.7: Analysis of the correlation between Swarm and GRACE(-FO) per SH degree. Degree c_{20} and c_{30} are excluded, as they are commonly replaced. a) Mean and RMS of the correlation per degree. b) Fraction of coefficients, which have a correlation above 25 % / 50 % / 75 % for each degree. E.g.: there are 6 coefficients of degree 3 (with c_{30} being excluded). For 5 of these coefficients (i.e. 83 %) the correlation between Swarm and GRACE(-FO) is larger than 75 %.

Swarm gravity field models are computed by accumulating the NEQs of Swarm A, B, and C (Section 4.2). The contribution $\mathbf{C}_i$ of each satellite i to the individual SH d/o is computed by

$$\mathbf{C}_i = \mathbf{N}_{ABC}^{-1}\mathbf{N}_i, \tag{4.3.1}$$

where $\mathbf{N}_{ABC}$ is the combined NEQ matrix of Swarm A, B, and C and $\mathbf{N}_i$ denotes the NEQ of a single satellite. Figure 4.8 shows the mean contribution for each SH coefficient. On a first glance, Swarm A and C generally contribute more (around 35 % to 40 %) to the combined gravity field than Swarm B. This can be explained by the lower altitude of A and C (Figure 3.2). However,

Swarm B's contribution to long wavelengths is higher than 1/3. This applies to degrees up to 6 and to sectoral coefficients up to 15. Figure 4.8 illustrates that it is possible to take advantage of the different orbital altitudes for gravity field determination and to obtain individual contributions for each d/o. Another possibility to derive Swarm gravity field models is the combination on solution level. This means that for each of the three solutions one weighting factor is derived. With this method, all coefficients would be treated equally and it would not be possible to exploit the special characteristics as revealed in Figure 4.8.

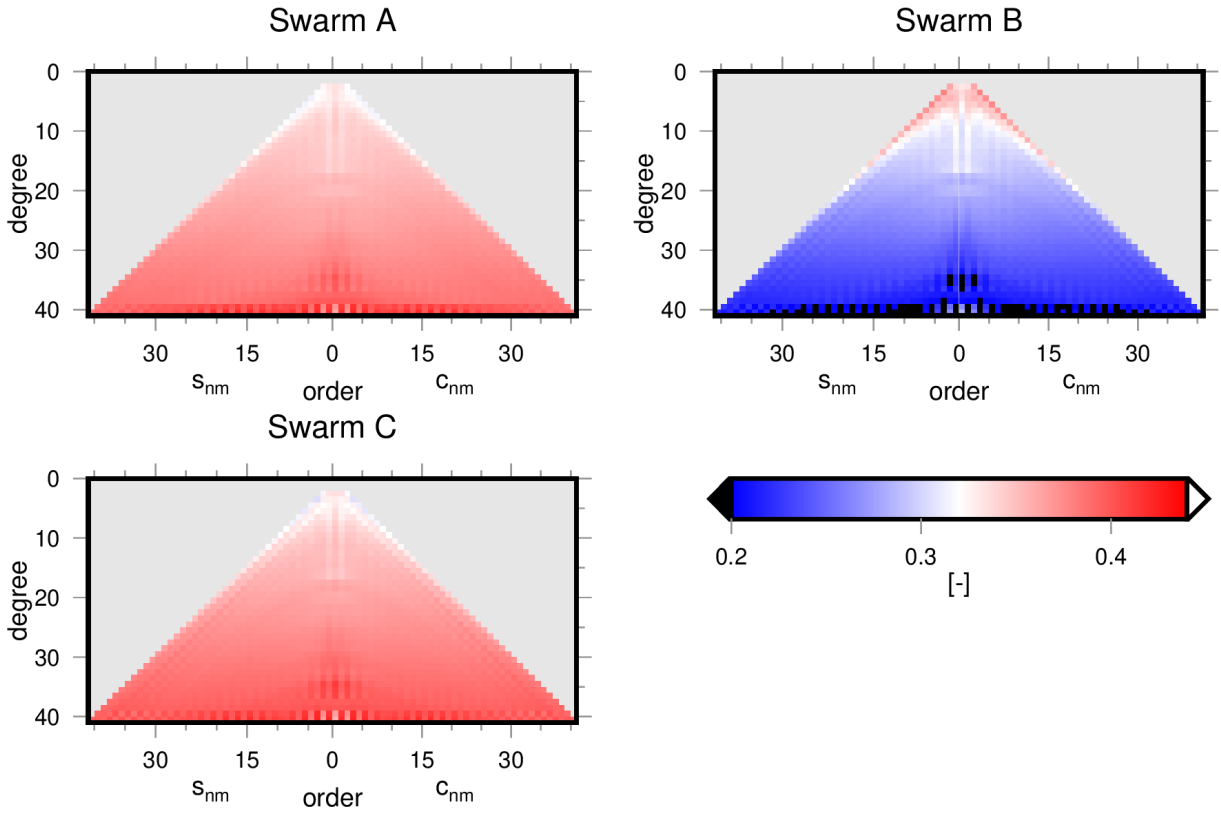

Figure 4.8: Mean contribution of each Swarm satellite to the combined solution.

4.3.3 Degree Amplitudes

The concept of degree amplitudes σ_n, difference degree amplitudes $\Delta\sigma_n$ and error degree amplitudes $\widehat{\sigma}_n$ is explained in Section 4.1.5. For a better understanding, I start by analyzing the GRACE(-FO) degree amplitudes and then move on to Swarm.

Figure 4.9 shows the difference degree amplitudes of the ITSG-Grace2018 gravity field of January 2008 with respect to the static part of GOCO06s and its associated formal errors. According to Kaula (1966), the signal strength of the Earth's gravity field decreases with increasing degree n. One should keep in mind that Figure 4.9 shows the time-variable part of the gravity field (i.e. a monthly solution with respect to a static field), but the degree amplitudes should nevertheless decrease for higher degrees. However, when considering unregularized solutions, such as ITSG-Grace2018, the uncertainties increase for finer structures, which is implied by the error degree amplitudes $\widehat{\sigma}_n$. In simple terms, one could say that the coarse structure of the Earth's gravity field is well-determined, while finer features are subject to larger uncertainties. Hence, one should always carefully decide up to which degree one wants to trust a solution. There are two indicators of a threshold above which one should not trust the solution without further action: (1) the degree at which $\Delta\sigma_n$ rises again, (2) the degree at which $\widehat{\sigma}_n$ is larger than (or in the same order of magnitude as) $\Delta\sigma_n$, which means that the error is larger than the signal. In the example of Figure 4.9 this would be the case for degrees higher than 30 or 40. Usually, one uses smoothing filters to suppress errors in higher degrees, while still benefiting from the smoothed signal (see Figures 5.3 and 5.10). One can also

choose to truncate the expansion at a certain maximum degree (see Figure 5.10).

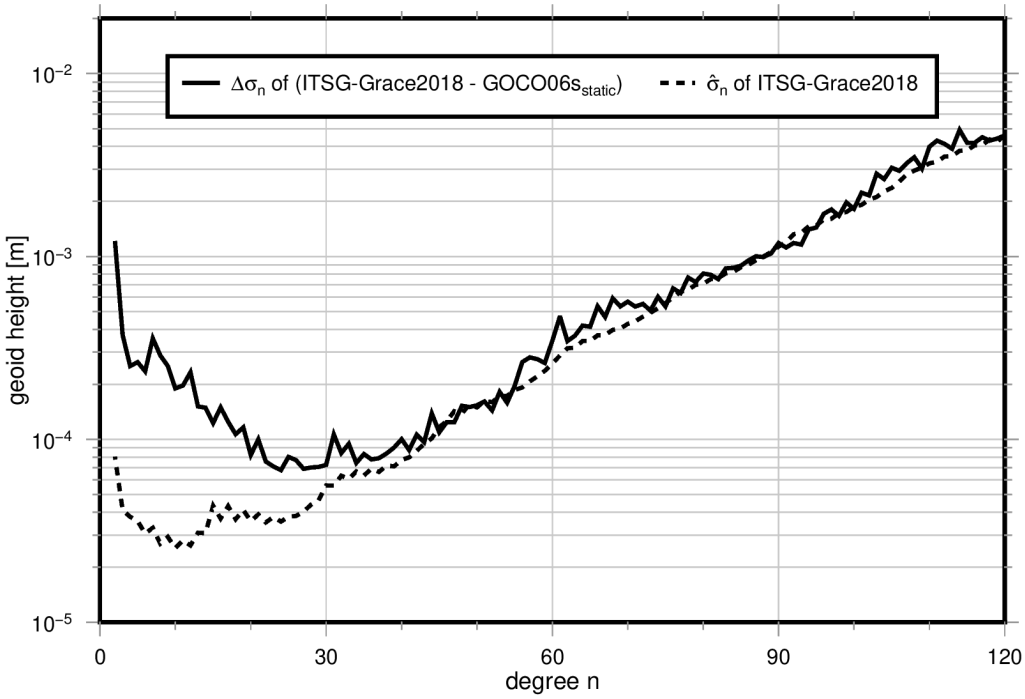

Figure 4.9: Difference degree amplitudes $\Delta\sigma_n$ of ITSG-Grace2018 (January 2008) with respect to the static part of GOCO06s and corresponding error degree amplitudes $\widehat{\sigma}_n$.

Using a representation as in Figure 4.9, only the degree amplitudes for one particular month can be shown. Figure 4.10 depicts the degree amplitudes of the whole GRACE(-FO) time span as colored values in a matrix. Figure 4.10 (a) shows the difference degree amplitudes $\Delta\sigma_n$ of ITSG-Grace2018 with respect to the static part of GOCO06s. For most months, one can see a similar pattern of decreasing $\Delta\sigma_n$ from $n = 2$ to approximately $n = 30$ and increasing $\Delta\sigma_n$ afterwards. Months of inferior quality (see Figure 2.5) are clearly visible and are reflected in larger values than usual. GRACE-FO shows a stable pattern without any peculiarities. Error degree amplitudes $\widehat{\sigma}_n$ are depicted in Figure 4.10 (b). The formal error decreases up to a degree of approximately 10 and gradually increases afterwards. Inferior months show larger error degree amplitudes. Moreover, degree 2 shows larger uncertainties than other low degrees, which can be traced back to corruptions in the GRACE(-FO) c_{20} coefficient (see Section 5.1). Figure 4.10 (c) shows the relation of plot (a) to plot (b) and can be interpreted as a SNR. High SNR values are desirable, as they are linked to a more reliable solution. With increasing degree, the SNR gets worse, which again confirms that high degrees are not reliable in unconstrained and unfiltered solutions. One point that has to be kept in mind is that $\widehat{\sigma}_n$ and $\Delta\sigma_n$ converge for higher degrees (see e.g. Figure 4.9) and even though the SNR might be slightly larger than one, the error can be in the same order of magnitude as the signal. Hence, looking at Figure 4.10 (c), it makes sense to define a threshold at the pink/red border at approximately degree 30 when speaking of the reliability of individual coefficients of a gravity field model. Higher degrees can still contain valuable information, but one should consider the higher noise level and, if necessary, apply smoothing filters (Section 5.1).

A comparison of GRACE-FO and Swarm degree amplitudes up to d/o 40 for July 2019 is presented in Figure 4.11. As it could be expected, the gravity signal (i.e. $\Delta\sigma_n$ with respect to the static part of GOCO06s) of the lower degrees is comparable for GRACE-FO and Swarm, while Swarm is getting more and more unreliable in the higher degrees. In this particular month, Swarm follows the GRACE-FO degree amplitudes well up to degree ∼13. For degrees higher than 14 the two signals start to diverge, while for degrees higher than 25 they are more than one order of magnitude apart. Formal errors of Swarm are larger than those of GRACE-FO, which is due to the missing inter-satellite ranging measurements. However, the Swarm gravity fields are only

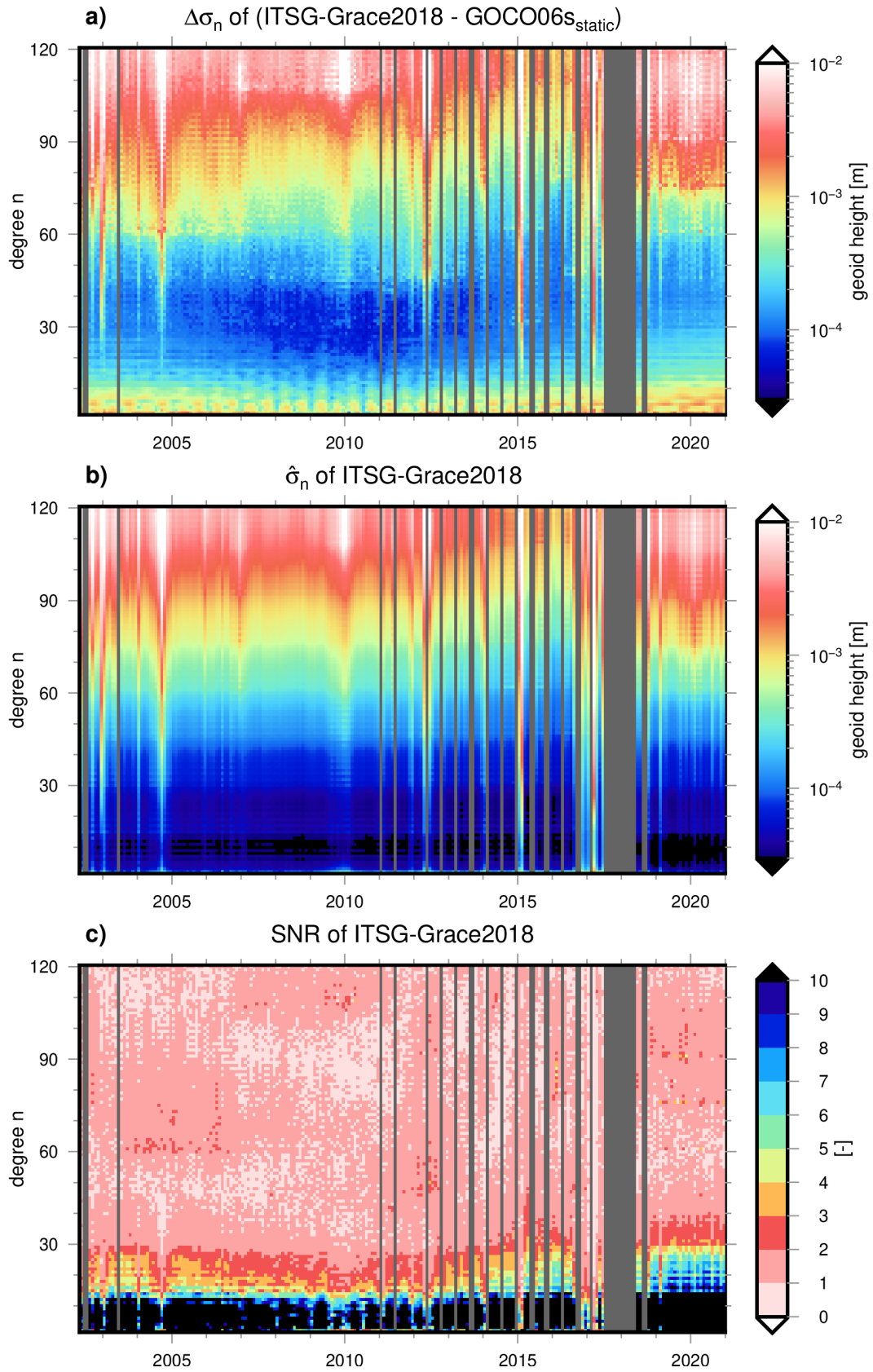

Figure 4.10: a) Difference degree amplitudes $\Delta\sigma_n$ of ITSG-Grace2018 with respect to the static part of GOCO06s. GRACE(-FO) gaps are colored in gray. b) Error degree amplitudes $\widehat{\sigma}_n$ of ITSG-Grace2018. c) SNR ratio, i.e. $\Delta\sigma_n/\widehat{\sigma}_n$

derived from kinematic orbits and the formal errors should be considered with caution, because they strongly depend on the 3x3 epoch-wise covariance matrix from the GPS processing and on the quality of the background models. When both GRACE(-FO) and Swarm time-variable gravity fields are available, one justified assumption is to consider GRACE(-FO) as the truth (Lück et al., 2018). The following exceptions, where GRACE(-FO) cannot be considered as the truth, should be kept in mind: (1) months of inferior quality (see Figure 2.5), (2) the c_{20} coefficient, and (3) degrees with a low SNR (see Figure 4.10 c).

Hence, another way to describe the error of the Swarm gravity fields in terms of degree amplitudes is to compute the difference degree amplitudes of Swarm minus GRACE(-FO). One should keep in mind that $\Delta\sigma_n(GRACE - Swarm) \neq \sigma_n(GRACE) - \sigma_n(Swarm)$ (see Section 4.1.5). $\Delta\sigma_n(GRACE - Swarm)$ can be considered as error and $\Delta\sigma_n(GRACE)$ as signal. $\Delta\sigma_n(GRACE - Swarm)$ is additionally plotted in Figure 4.11 and is smaller than $\sigma_n(GRACE)$ and $\sigma_n(Swarm)$ for the low degrees. For degrees higher than 14, the error is larger than the signal, for this particular month. Degrees higher than 20 are dominated by errors. Yet, in this consideration, only the unfiltered coefficients are compared to each other. Applying postprocessing steps, such as filtering, or the computation of regional averages will additionally reduce the noise.

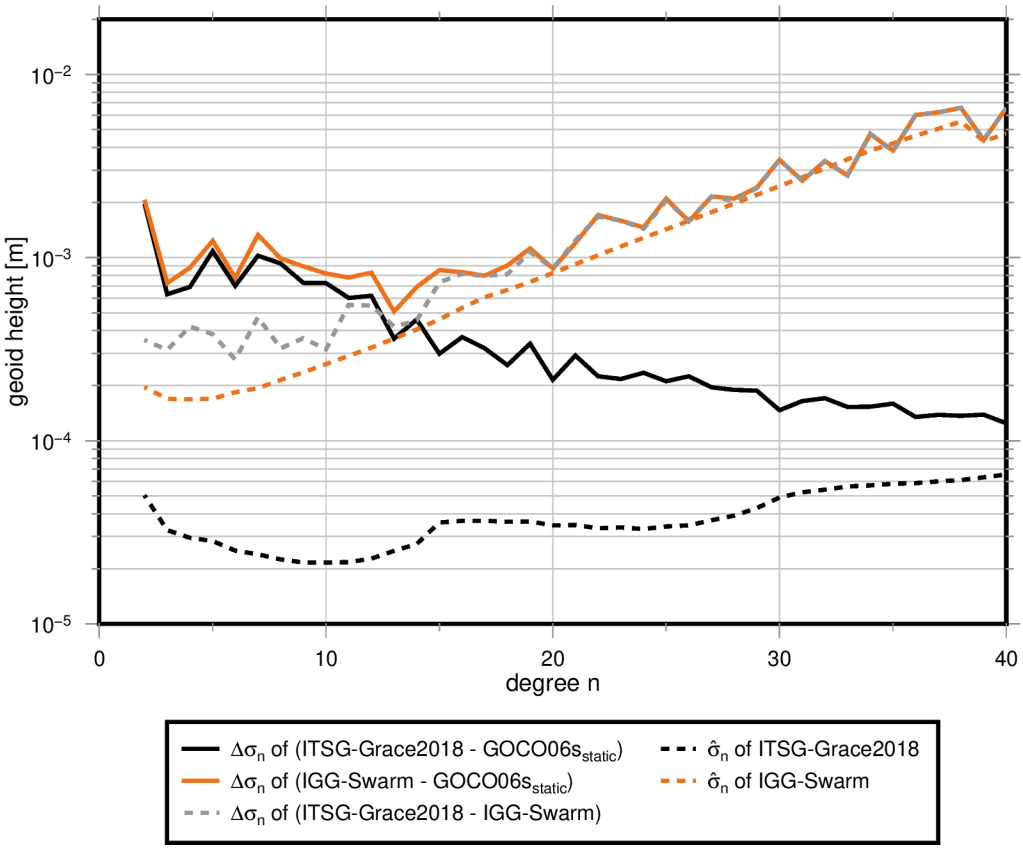

Figure 4.11: Comparison of ITSG-Grace2018 and Swarm degree amplitudes for July 2019. For both missions, the difference degree amplitudes with respect to the static part of the GOCO06s as well as the formal errors are shown. The difference between GRACE-FO and Swarm degree amplitudes is additionally plotted in gray.

In Figure 4.12 the comparison of ITSG-Grace2018 and Swarm degree amplitudes for December 2013 to December 2020 is presented. Figure 4.12 (a) shows what will be considered as "signal" in the following. It is a climatology of the difference degree amplitudes of GRACE(-FO) (Figure 4.10 (a), mind the different scales) with respect to the static part of GOCO06s. The term "climatology" refers to a long-term average of each month, i.e. January will be expressed as the mean of all Januaries in the GRACE(-FO) period. In this way, inferior data of individual months or higher degrees will be smoothed and a more stable estimate is obtained. The difference degree amplitudes

of Swarm with respect to the static field are shown in Figure 4.12 (b). A first comparison of (a) and (b) reveals a similar order of magnitude for the lower degrees, but Swarm is subject to noise, especially in the higher degrees. Furthermore, the Swarm solutions suffer from noise due to the high ionospheric activity in the beginning of the mission (see Section 3.7). The difference degree amplitudes of Swarm with respect to GRACE(-FO) are presented in Figure 4.12 (c). They can be interpreted as "noise", with caution regarding the known GRACE(-FO) issues, as outlined above. Again, higher degrees are subject to larger errors. In Figure 4.12 (d) the SNR is computed from the results of subplots (a) and (c). The signal is larger than the noise for degrees colored in orange. In the beginning of the mission, the SNR is slightly smaller than 1, even for lower degrees. Several receiver updates as well as the decreasing solar activity lead to an improvement of the gravity field models. Starting from May 2015, the Swarm solutions improve considerably. During the last years, the threshold (of SNR larger/smaller than 1) stabilizes around degree 10. However, this does not mean that degrees with $SNR < 1$ should not be used at all, as applying smoothing filters or spatial averages further reduce the noise.

In Figure 4.12 the SNR of different gravity field models derived from tracking data is depicted. Subplot (a) is the same as Figure 4.11 (d) and is shown again for an easier comparison to other models. Figure 4.12 (b) is the SNR of Swarm models that I derived from kinematic orbits of AIUB[2] with the same processing as in Figure 4.12. The SNR is also worse in the beginning of the mission and improves in late 2015. The comparison of Figures (a) and (b) shows that the gravity field models derived from IfG orbits generally show a larger SNR and are thus closer to GRACE(-FO) and more reliable. The SNR of the Level-2 EGF_SHA_2_ product (see Section 3.4) is shown in Figure 4.12 (c). The SNR is generally higher than that of the models derived from AIUB orbits. In the early mission phase until mid-2015, the SNR of the official Level-2 product is comparable to my solution derived from IfG orbits. Then, until 2020, the EGF_SHA_2_ product is inferior, regarding the SNR. In 2020-2021 the solutions are again comparable with stable $SNR > 1$ for degrees lower than 10. In Figure 4.12 (d) the SNR derived by SLR is presented. Degrees 2 and 3 are comparable to those of subplot (a), but the SNR of degree 4 is mostly lower than 1 and thus inferior. The higher degrees seem to be better determined than in any of the Swarm solutions. This could be expected, as degrees larger than 5 are not unconstrained, but are derived from a linear combination of GRACE EOFs (Löcher and Kusche, 2021).

4.3.4 Effect of Different Parameterizations During the Processing

When processing time-variable gravity fields, one can choose numerous different parameterizations. The parameterization of the solution that I investigate closer throughout this thesis is presented in Section 4.1.4. These decisions have been made in order to obtain the best possible gravity field models. However, there is no distinct criteria that defines when a gravity field model is better than another model, especially when a long time series is considered instead of individual months. One solution might deliver good results in one month, but perform worse in the next month. Or a model can be reliable in one area, but contain systematic errors in another region. The solution that I chose as IGG-Swarm gravity field is the one with ocean mass variations most similar to GRACE(-FO) (Lück et al., 2018). The ocean mass time series has the highest SNR and correlation (Figure 5.12) of all investigated solutions. I chose this criteria as sea level change is a current topic of interest in many scientific areas (Section 1.2) and is further investigated in the sea level inversion framework in Chapter 6.

Figure 4.14 shows the SNR of each SH coefficient for a selection of different parameterizations. Subplot (a) refers to the IGG-Swarm solution, as introduced in Section 4.1.4. In (b), only the arc length is changed to 30 min and in (c) 60 min are chosen. The 60 min version looks very similar to IGG-Swarm (45 min), whereas 30 min are inferior. The parameterization of the scaling factor of the non-gravitational forces does, overall, not have a big influence on the solution. In (d), a scaling

[2] ftp://ftp.aiub.unibe.ch/LEO_ORBITS/SWARM (last access: May 13, 2021)

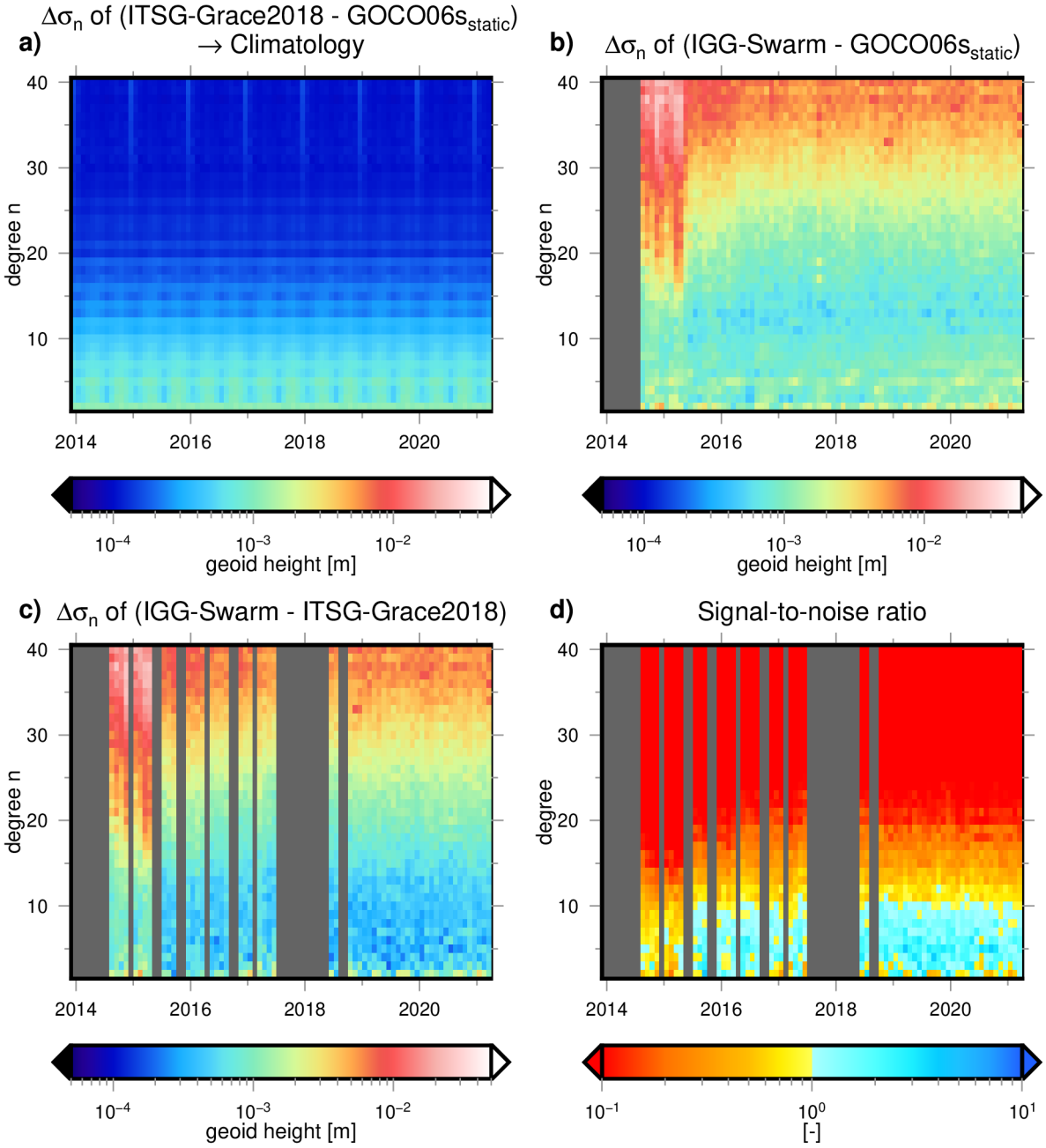

Figure 4.12: Comparison of ITSG-Grace2018 and Swarm degree amplitudes for the whole Swarm period. Missing GRACE(-FO) months are colored in gray. a) Difference degree amplitudes of GRACE(-FO) with respect to the static part of GOCO06s in terms of a climatology. b) Difference degree amplitudes of Swarm with respect to the static part of GOCO06s. c) Difference degree amplitudes of GRACE(-FO) with respect to Swarm ("Noise"). d) Signal-to-noise ratio.

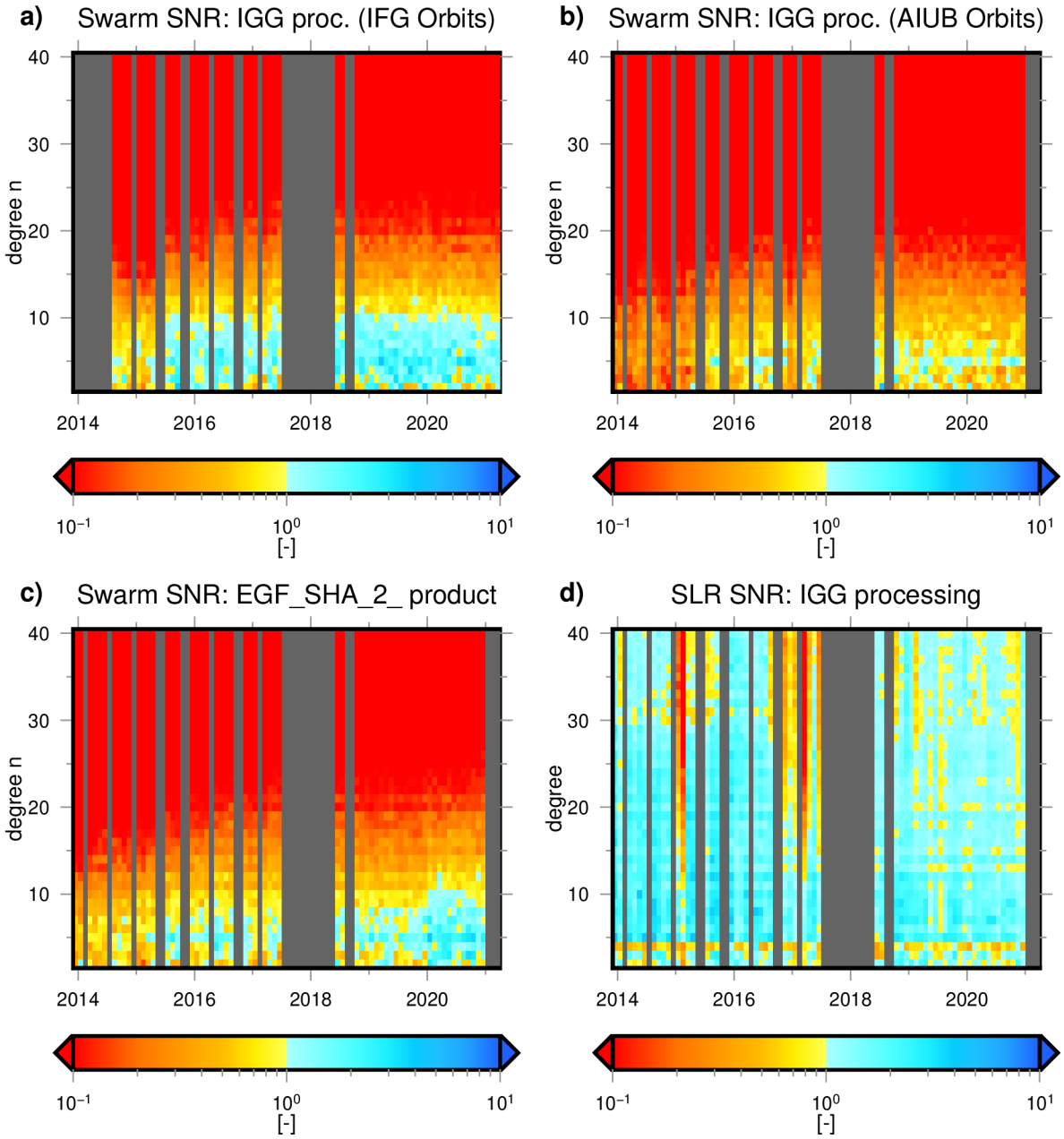

Figure 4.13: SNR of different Swarm and SLR gravity field models. a) IGG-Swarm gravity field model, processed by myself using kinematic orbits from IfG (same as Figure 4.12 d)). b) Swarm gravity field model, processed by myself using kinematic orbits from AIUB. c) Swarm Level 2 EGF_SHA_2_ gravity field model. d) IGG-SLR-HYBRID_S5+4E gravity field model processed by Löcher and Kusche (2021).

factor for both, drag and radiation pressure, is estimated once per 24 h for each direction and in (e) it is estimated once per 48 h. Subfigure (f) shows the SNR when non-gravitational forces are not modeled. Instead, a constant value per arc is estimated in each direction to account for missing accelerometer data. This choice cannot approximate the real non-gravitational accelerations, as one value per 45 min is insufficient. This is visible in the lower degrees, mostly in degree four, and becomes even more apparent when comparing the ocean mass change time series of GRACE(-FO) and Swarm, which will be presented in Section 5.4.2 (Figure 5.12).

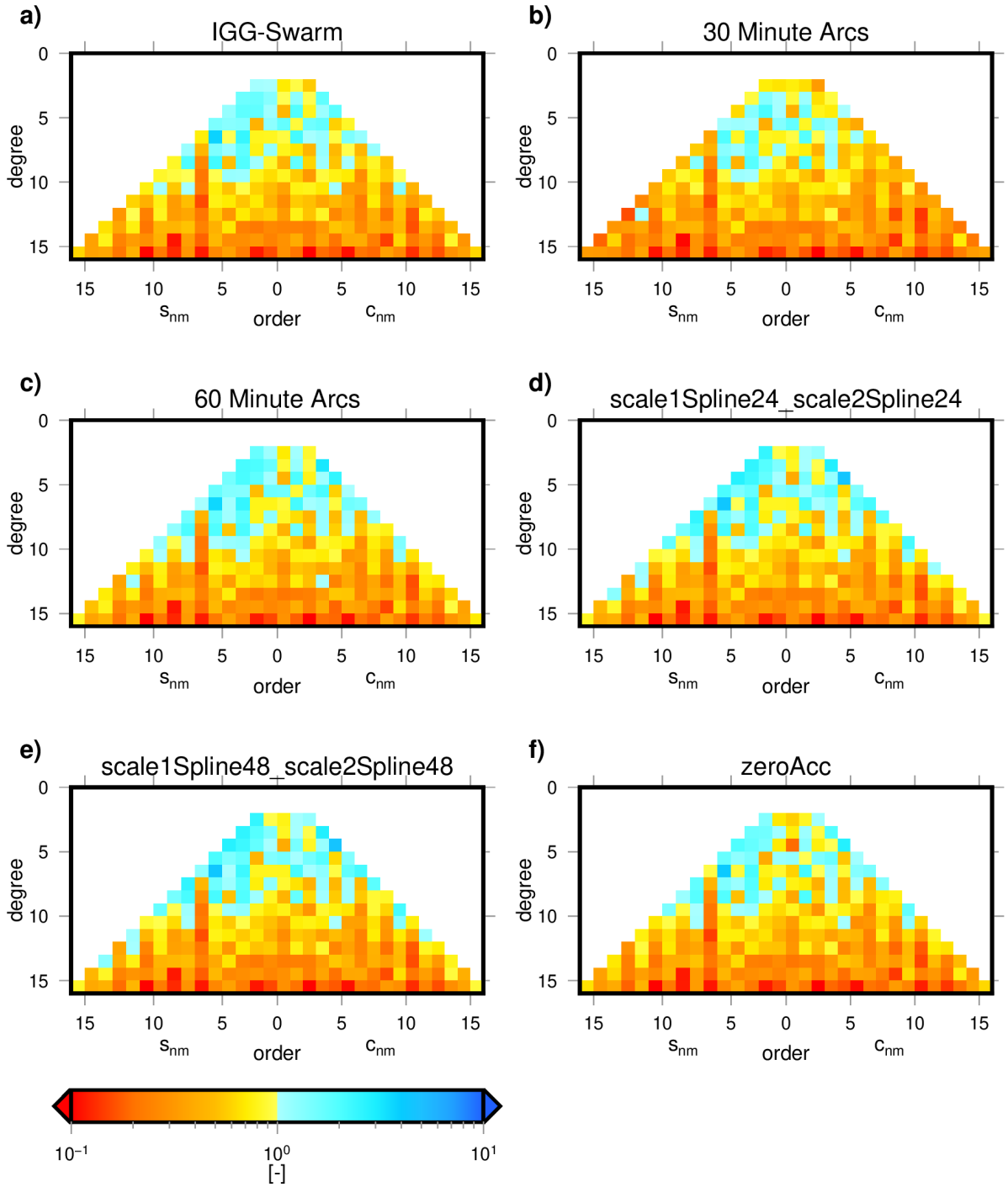

Figure 4.14: Effect of different parameterizations on the SNR of Swarm gravity field models.

Summarized, Swarm is sensitive up to d/o ∼ 10-15. The exact truncation depends on the application and is up to the user. One has to find a compromise between the desired spatial resolution and the noise that increases with increasing d/o. In Lück et al. (2018), we showed that a rea-

sonable choice is to truncate at d/o 12 and to apply a 500 km Gaussian smoothing filter. This is confirmed by de Teixeira da Encarnação et al. (2020) (who apply a slightly stronger smoothing filter). In Richter et al. (2021), we explain how the sensitivity of Swarm can be further exploited by combining the Swarm-only time-variable gravity fields with the dominating spatial modes of mass redistribution obtained from GRACE. In this way, we obtained global RMSE values with respect to GRACE of less than 10 cm EWH up to d/o 40 (compare Figure 5.10).

Chapter 5

Mass Change from Time-Variable Gravity Fields

Mass redistributions within the Earth system cause changes in the Earth's gravity field. Hence, models of the time-variable gravity fields, as derived by satellite missions, offer valuable information on relevant climate-related topics, such as the melting of glaciers and ice sheets, mass-related sea level variations, climate-driven hydrological mass changes, and anthropogenic surface and groundwater retrievals.

Section 5.1 informs about the corrections that should be applied to SH potential coefficients before the conversion to mass change. The conversion of SH coefficients into mass change expressed as EWH is explained in Section 5.2. The theory of computing regional basin averages is outlined in Section 5.3 and results are shown in Section 5.4.

5.1 Corrections to the Potential Coefficients

Degree 1

Degree 1 terms of Stokes' coefficients (i.e. c_{10}, c_{11}, s_{11}) are directly proportional to geocenter motion. Geocenter motion is defined here as the movement of the CoM of the Earth system with respect to the **C**enter **o**f **F**igure (CoF) of the solid Earth (e.g., Ray, 1999). Since both GRACE and GRACE-FO satellites circle the CoM, relative measurements between the satellites, such as the KBR or LRI, are by definition insensitive towards the Earth's crust and thus to any realization of the CoF. The same is true for gravity field determination from Swarm, where the measurements are taken between the GPS satellites and the Swarm spacecraft. For practical applications, such as ocean mass change or terrestrial water storage variations, degree 1 terms are important in order to transform the measurements from the CoM frame to the CoF frame, which is tied to the solid Earth. For example, J. L. Chen et al. (2005) and Meyrath et al. (2017) show that degree 1 coefficients have a significant impact on water storage estimates.

One approach to derive geocenter variations is to estimate degree 1 coefficients from a combination of GRACE(-FO) (degree 2 and higher) and ocean model output, as is done in Swenson et al. (2008), Sun et al. (2016) and Sun et al. (2017). This is also the approach chosen in GRACE TN-13 of the official RL06 GRACE processing. However, it relies heavily on the chosen ocean model which introduces a priori assumptions, i.e. the choice of a different ocean model would result in different degree 1 coefficients. Cheng et al. (2013) use SLR measurements to establish the link between the CoF and CoM, and thus derive degree 1 terms. Another possibility to infer geocenter variations is to utilize IGS GPS observations in a deformation inversion approach, as is presented in e.g. Wu et al. (2002), Blewitt (2003), or Deng et al. (2019). Geocenter motion can also be derived from joint inversion schemes, including e.g. GRACE, GPS, and **O**cean **B**ottom **P**ressure (OBP) data or GRACE and altimetry data, as is shown in Rietbroek (2014).

Figure 5.1 shows degree 1 terms derived from different methods: three TN-13 solutions,

CSR-SLR and IGG-SLR. The IGG-SLR solution is not the one previously mentioned (IGG-SLR-HYBRID_S5+4E), as it does not include degree 1 coefficients. Instead, IGG-SLR is taken from a solution derived purely from SLR (degrees 1 to 5) by my colleague Anno Löcher. The three solutions from CSR, JPL, and GFZ are comparable, as they are computed with the same method. They differ due to the influence of GRACE(-FO), degree 2 and higher, and because the "monthly" solutions do not always strictly cover the exact calender month, such that each processing center can choose which data to include exactly. One problem with the CSR, JPL, and GFZ data sets is that they are not available during GRACE(-FO) gaps (because GRACE(-FO) data of degrees 2 and higher are needed as input). A comparison to the IGG-SLR solution shows large differences. SLR estimates generally have a higher amplitude and include more noise. Additionally, after the GRACE-GRACE-FO gap, there is also a change in the trends. The IGG-SLR time series ends in December 2020. Furthermore, the SLR solution by CSR[1] is shown, which is only available until February 2017, but one can see large differences with respect to the other solutions, especially in c_{10}.

Summarized, the available coefficients that account for geocenter motion differ strongly. Degree 1 can be derived from models, which implicates that the user would need to trust the models or at least be aware of their potential errors. Utilizing SLR measurements to derive geocenter motion provides estimates that are independent from models but are subject to noise. Another possibility would be to combine SLR and model data. One cannot say which solution is closest to reality and wrong estimates would introduce errors in mass change time series. In addition, there is no solution that spans the whole study period until March 2021 without gaps. I decided to refrain from applying geocenter motion corrections completely, since this thesis focuses on the estimation of time-variable gravity fields from Swarm in the CoM frame. For the validation, I will not correct GRACE(-FO) for geocenter motion either, such that mass estimates are computed from degrees 2 and higher. While this does not affect the comparison between Swarm and GRACE(-FO), it should be kept in mind that degree 1 terms generally influence mass change estimates and it is up to the user whether to apply corrections for geocenter motion, depending on the application.

Degree c_{20}

SH degree c_{20}, often referred to as J_2-term ($J_2 = -\sqrt{5} \cdot c_{20}$), represents the flattening of the Earth. Cox and Chao (2002) report a steady decrease of J_2 (i.e. a more spherical shape) due to GIA until around 1998. Then, they find an increase (i.e. flattening of the Earth), which overshadows the effect of mantle rebound. Cheng et al. (2013) attribute this continuing effect to the melting of glaciers and ice sheets as well as atmosphere and ocean mass redistributions. In GRACE gravity field estimates, c_{20} coefficients are corrupted by a ∼161-day period and are usually replaced by estimates from SLR (Cheng and Ries, 2017). For quite a while, the reason for the poor quality of GRACE c_{20} estimates was unclear. There have been assumptions by Seo et al. (2008) and J. L. Chen et al. (2009) that the disturbing signal is related to ocean S2 tidal aliasing errors. A more recent study by Klinger and Mayer-Gürr (2016) suggests that inaccuracies of c_{20} may be related to accelerometer errors and disturbances. Their improved accelerometer calibration parameterization leads to more realistic estimates, when compared to independent SLR data. Cheng and Ries (2017) confirm that the ∼161-day signal is not attributed to aliasing from errors in the S2 tide, but that a temperature-dependent systematic error in the accelerometer data is a more realistic cause.

The common approach in the GRACE RL06 processing is to replace c_{20} coefficients with the value from GRACE TN-14 (Loomis et al., 2020), which is derived from SLR measurements. For the sake of comparability and consistency, I replace c_{20} from both GRACE(-FO) and Swarm time-variable gravity field models with TN-14 values. Time series of c_{20} are discussed in Section 4.3.1.

[1] http://download.csr.utexas.edu/pub/slr/geocenter/ (last access: June 7, 2021)

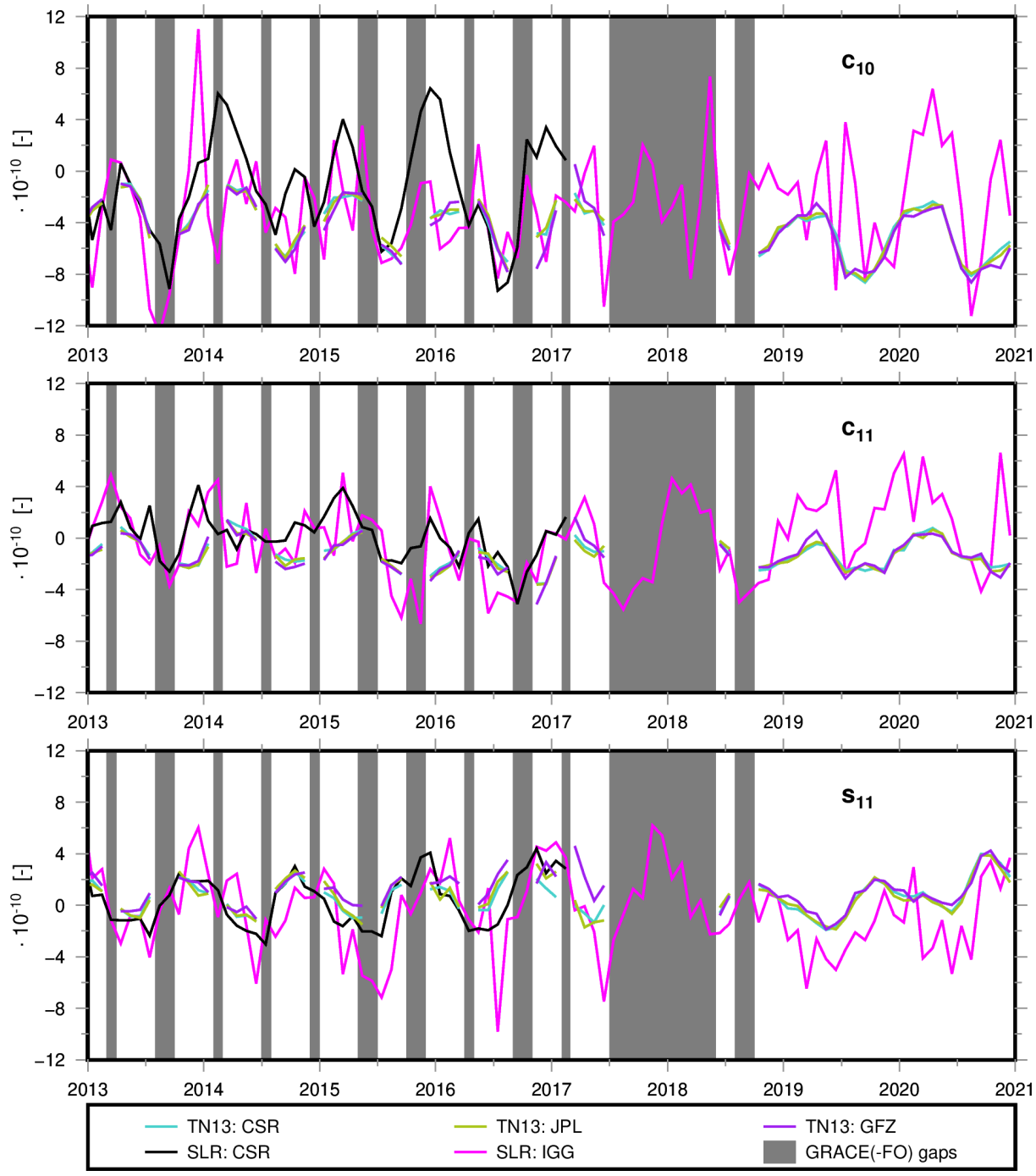

Figure 5.1: Time series of degree 1 Stokes' coefficients. Comparison of TN-13, CSR-SLR, and IGG-SLR.

Degree c_{30}

SH degree c_{30} is related to ice sheet mass changes in the Antarctic. Loomis et al. (2020) report a poor recovery of the c_{30} coefficient from GRACE and GRACE-FO, whenever the satellites are not operating with two fully functional accelerometers. This is the case starting in November 2016, as indicated in Figure 2.5.

GRACE TN-14 (Loomis et al., 2020) offers replacement values from SLR observations starting in 2012 (with the launch of **LA**ser **RE**lativity **S**atellite (LARES)). I use these values to correct GRACE(-FO) and Swarm gravity field models, such that differences in mass changes can be related to the uncorrupted SH coefficients. Time series of c_{30} are discussed in Section 4.3.1.

Glacial Isostatic Adjustment

GIA is the viscoelastic response of the Earth induced by the melting of ice sheets of the last glacial maximum (A et al., 2013; Whitehouse, 2018). During a glacial period, ice mass is concentrated on the Earth's surface. This causes the mantle material under the ice sheet to flow away from that region. After the glacial period, the melting of the ice allows the mantle material to gradually flow back, leading to an uplift of the surface. This delayed adjustment process is still ongoing with rates of > 10 mm/yr in Laurentide, Fennoscandia, and West Antarctica, as can be seen in the GIA model by A et al. (2013) in Figure 5.2.

While mass redistributions caused by GIA are of great interest to the scientific community (e.g., Sella et al., 2007; Lidberg et al., 2010), the GIA signal should be removed for studies of surface mass changes, such as water content changes in hydrological basins, OBP changes or ice sheet mass changes. Furthermore, GIA causes the largest difference between geocentric and relative sea level change. There are several models that can be used to correct for the long-term trend caused by GIA (e.g., the model by A et al. (2013), ICE-6C_C (M5a) (e.g., Argus et al. (2014) and Peltier et al. (2015)), W12a (Whitehouse et al., 2012a; Whitehouse et al., 2012b), and others). In this thesis, I use the 3-D finite element model by A et al. (2013) (see Figure 5.2, where I converted potential change to EWH change in order to correct Swarm mass grids). They use the ICE-5G deglaciation history and the VM2 viscosity profile, both based on Peltier (2004), while the elastic parameters are derived from the **P**reliminary **R**eference **E**arth **M**odel (PREM) (Dziewonski and Anderson, 1981).

The A et al. (2013) GIA model is available in terms of SH coefficients representing the change in potential per year. Thus, it can directly be applied to any set of Stokes' coefficients.

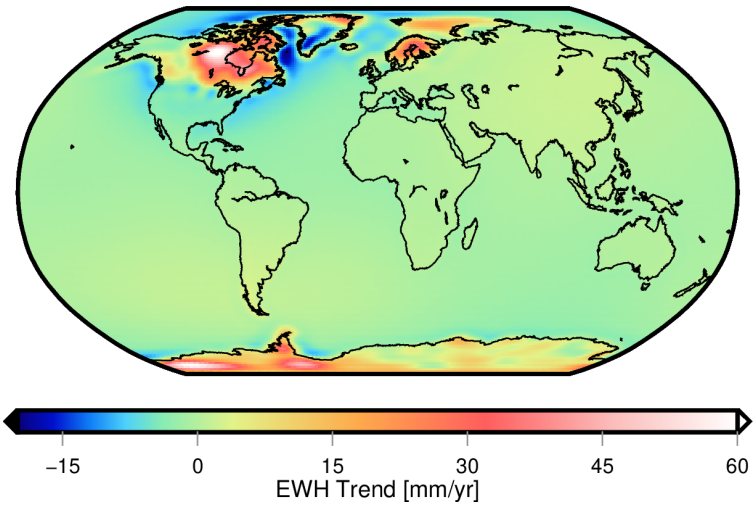

Figure 5.2: GIA model from A et al. (2013), converted here to EWH change in order to correct Swarm mass grids.

Filtering

All gravity field models contain different types of errors (see Figure 4.3 (c) for a visualization of the uncertainty of ITSG-Grace 2018 monthly SH coefficients). Errors can for example be due to instrumental noise or deficiencies in the background models. A prominent pattern in monthly GRACE solutions are the stripes in north-south direction, which are due to correlated errors in the flight-direction and the measurement geometry. For Swarm, a large part of the errors is caused by the noise in GPS observations in combination with the fact that there are no additional inter-satellite measurements. Missing accelerometer data complicates the gravity field estimation further.

The noise in monthly gravity field solutions is commonly reduced by applying smoothing filters. In the spectral domain, a filter matrix $\mathbf{W}$ is multiplied with the SH coefficients to derive smoothed coefficients

$$\mathbf{x}^s = \mathbf{W}\mathbf{x} = \mathbf{W} \begin{pmatrix} c_{nm} \\ s_{nm} \end{pmatrix}, \tag{5.1.1}$$

where vector $\mathbf{x}$ contains the SH coefficients and $\mathbf{x}^s$ contains the smoothed coefficients. A stronger filter reduces more noise. However, one must keep in mind that also the signal is attenuated, leading to leakage effects (Baur et al., 2009). Leakage-out describes that the signal of the investigated area leaks into surrounding areas, while leakage-in describes the signal from surrounding areas that leaks into the area of interest. Hence, one must find a compromise between smoothing the noise and potentially attenuating the signal.

In general, one distinguishes between two kinds of smoothing filters: isotropic and anisotropic filters. For isotropic filters $\mathbf{W}$ becomes a diagonal matrix, which means that the filter is only dependent on the SH degree in the spectral domain and independent of the direction in the spatial domain. The most prominent example is the Gaussian smoothing filter (Jekeli, 1981). Figure 5.3 shows the degree-dependent damping factors of the Gaussian filter for different filter-widths. In the spatial domain, one can think of the filter as a bell-shaped weighting function that reaches 50 % of its maximum value at the chosen filter radius.

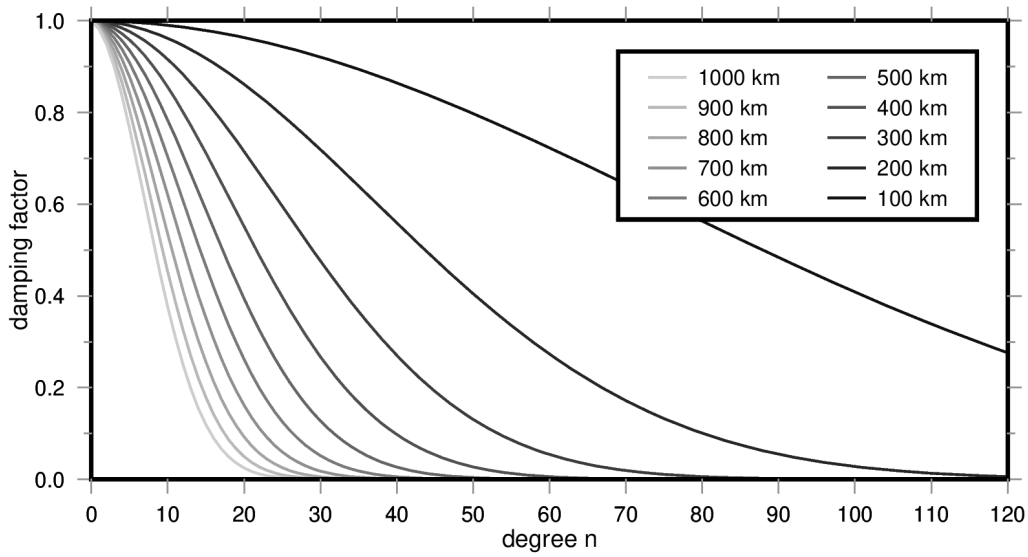

Figure 5.3: Damping factors of the Gaussian filter for different radii. From left to right: 1000 km to 100 km filter radius.

For the processing of GRACE(-FO) gravity field data, anisotropic filters are useful. In the spectral domain, they consider the north-south striping pattern by applying different weights in longitudinal and latitudinal directions. One well-known example is the DDK filter developed by Kusche (2007)

(see also Kusche et al., 2009). In this thesis, I choose the Gaussian filter, as it can be applied to GRACE(-FO) and Swarm gravity field similarly, which is helpful for comparisons. For future investigations, one could think of a smoothing filter especially designed to take care of the noise in Swarm data.

5.2 From Gravity Potential to Equivalent Water Heights

Due to mass redistributions within the Earth system, the Earth's gravity field is continuously changing over time. These time-dependent variations can be expressed through changes of the potential coefficients Δc_{nm} and Δs_{nm} (Wahr et al., 1998)

$$\begin{aligned} \Delta c_{nm} &= c_{nm} - \bar{c}_{nm}, \\ \Delta s_{nm} &= s_{nm} - \bar{s}_{nm}. \end{aligned} \tag{5.2.1}$$

Usually, $\bar{c}_{nm}$ and $\bar{s}_{nm}$ are either the coefficients of a static gravity field, or they are derived as a temporal mean of a (large) number of monthly solutions. While it is possible to compute a gravity field from a given mass distribution, the inverse problem is not uniquely solvable. Different mass redistributions can generate the same gravitational potential. This has to be kept in mind, as data from gravity field satellite missions does not directly provide information on the exact mass distribution inside the Earth.

However, Wahr et al. (1998) show that mass changes can be expressed as density changes that are concentrated in a thin layer at the Earth's surface. This is a valid assumption, as most mass changes are related to movements of water and air around the surface of the Earth. Wahr et al. (1998) define the change in surface density $\Delta\sigma\left[\mathrm{kg/m^2}\right]$ as

$$\Delta\sigma\left(\lambda,\theta\right) = \frac{M}{4\pi R^2}\sum_{n=1}^{\infty}\sum_{m=0}^{n}\frac{(2n+1)}{(1+k'_n)}\left[\Delta c_{nm}C_{nm}\left(\lambda,\theta\right) + \Delta s_{nm}S_{nm}\left(\lambda,\theta\right)\right]. \tag{5.2.2}$$

Apart from the obvious direct gravitational effect caused by surface density changes, an indirect effect from the contribution of the solid Earth deformation caused by the surface density changes also has to be considered. This is achieved by introducing the degree-dependent gravitational load Love Numbers k'_n. Farrell (1972) describes how the load Love numbers can be derived from Earth models.

It is common to convert the surface density changes $\Delta\sigma$ to changes of EWH, as, on short timescales, variations of water storage are the main reason for gravity field changes. Equation (5.2.2) simply has to be divided by the mean density of seawater ($\rho_w = 1025\,\mathrm{kg/m^3}$) to obtain EWH changes

$$\Delta EWH\left(\lambda,\theta\right) = \frac{M}{4\pi R^2\rho_w}\sum_{n=1}^{\infty}\sum_{m=0}^{n}\frac{(2n+1)}{(1+k'_n)}\left[\Delta c_{nm}C_{nm}\left(\lambda,\theta\right) + \Delta s_{nm}S_{nm}\left(\lambda,\theta\right)\right]. \tag{5.2.3}$$

With the above formula, time-variable gravity fields, such as for example from GRACE(-FO), can be represented on a global grid.

5.3 Basin Averages

Frequently discussed questions, such as "How much ice is melting in Greenland?" or "How large are mass changes averaged over the ocean?", can be investigated by computing basin averages for selected regions.

I chose 15 study regions of different size all over the world to visualize, interpret, and validate my results. Figure 5.4 (a) shows the ocean basin, excluding a 300 km buffer zone along the coasts (Section 5.3.2). Total land areas are plotted in Figure 5.4 (b) and the 13 remaining regions are presented in Figure 5.4 (c). Table 5.1 lists the names of the regions and their areas. To cover a

wide area of applications, the regions comprise very large (ocean) and small (Danube) areas, as well as areas with a high signal content (Amazon basin) and low variability (Murray-Darling river basin).

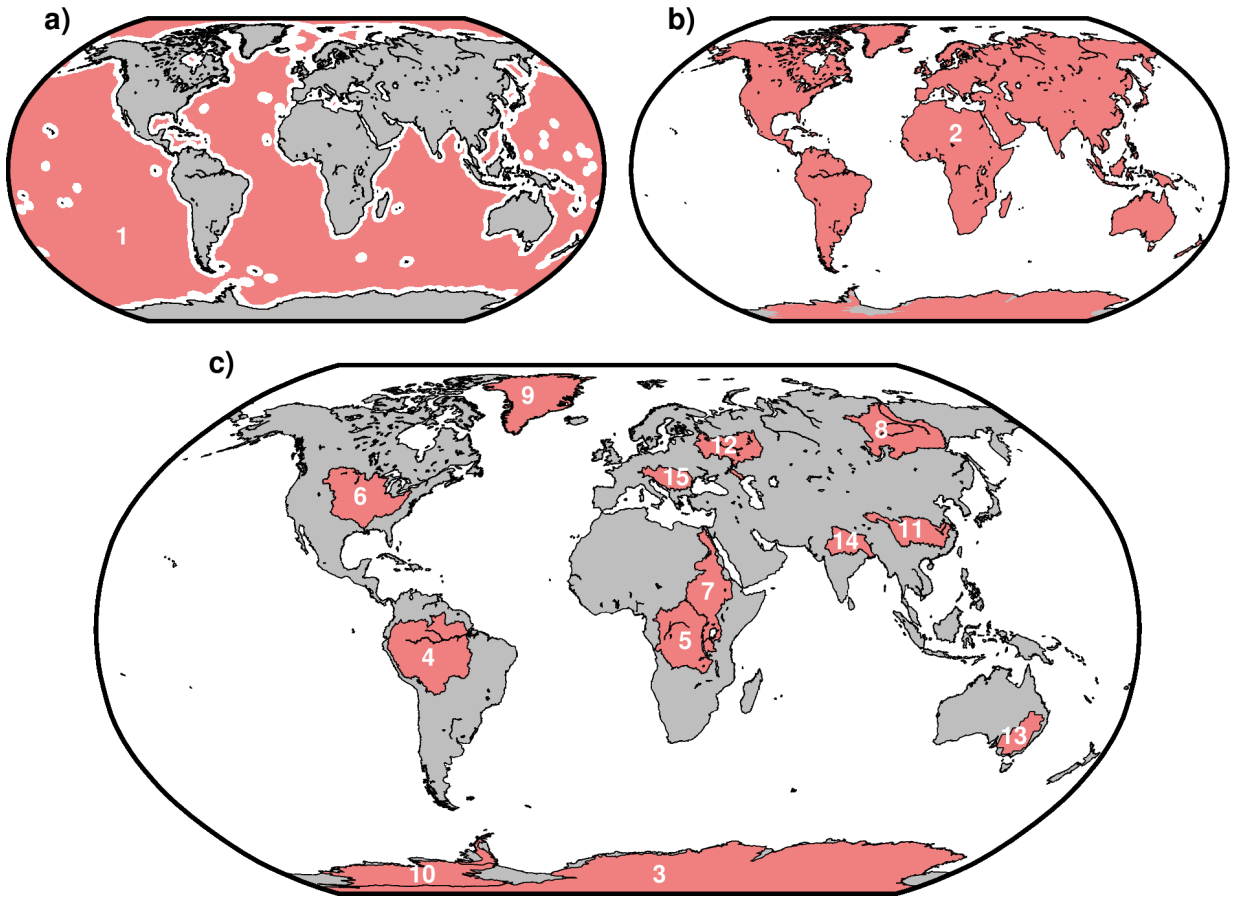

Figure 5.4: Map of 15 selected study regions. a) Ocean mask with 300 km coastal buffer zone. b) Land mask. c) Further regions. The regions are sorted by size and their numbers correspond to those in Table 5.1.

In general, the averaging can be performed either in the spatial domain (i.e. on the basis of gridded EWH) or in the spectral domain. Here, I compute the basin averages in the spectral domain, as will be explained in Section 5.3.1.

The common corrections as described in Section 5.1 have to be considered when deriving mass redistribution in the Earth system. Figure 5.5 gives an overview of the processing steps. These depend on whether one wants to derive basin averages for a general terrestrial basin or for the entire ocean, which is described in the following.

5.3.1 Deriving Mass Changes in Hydrological or Glacial Regions

Swenson and Wahr (2002) describe how spatial averages of EWH can be derived. Their approach is well suited to derive time series of mass change in terrestrial basins, such as hydrological or glacial regions of interest. Before computing the basin averages, the corrections for the lower degrees should be applied, followed by a subtraction of a static reference field. Then, the GIA correction should be added to the SH potential coefficients. After applying these corrections, the actual basin average can be computed, while considering a smoothing filter, if desired.

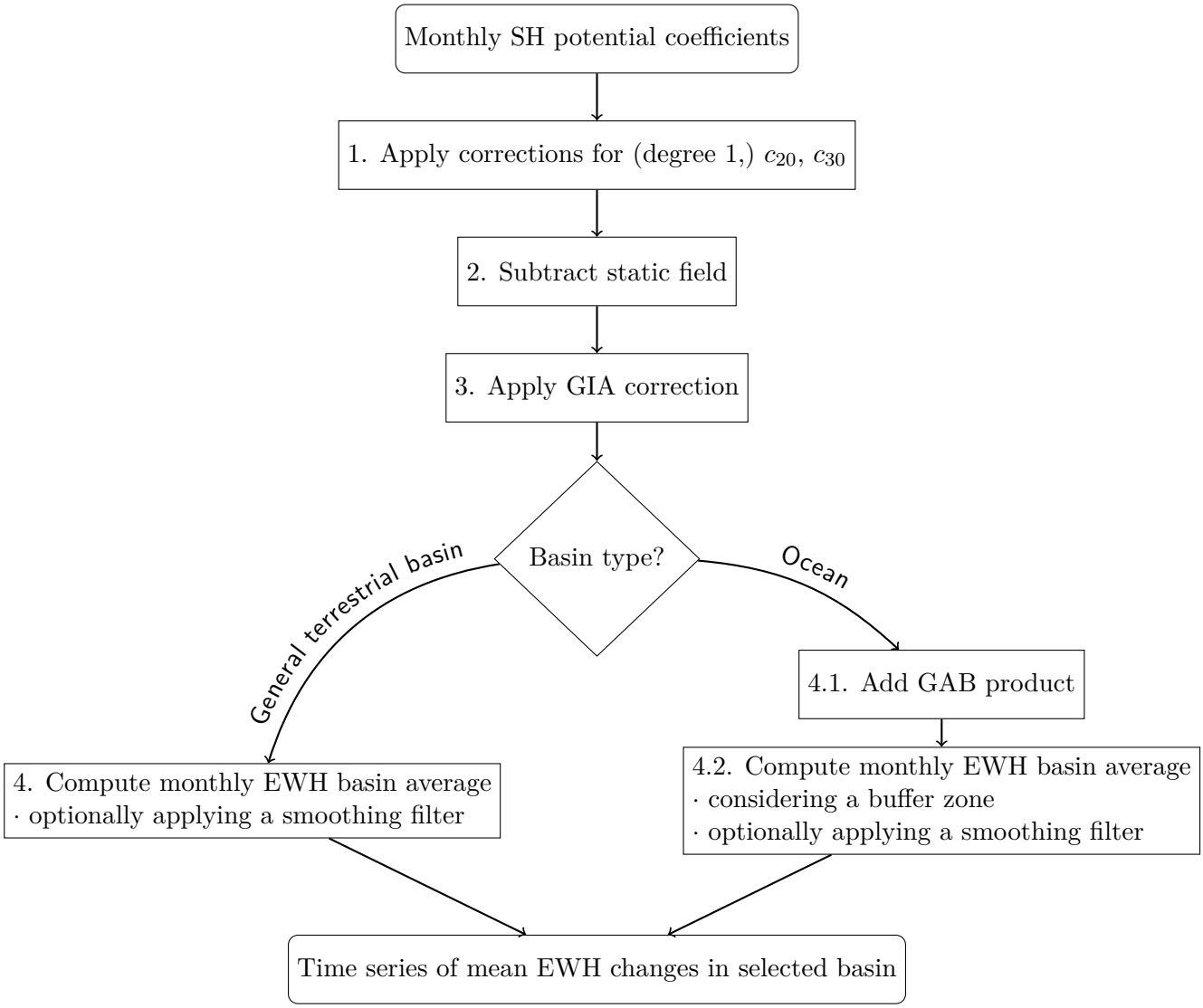

Figure 5.5: Flowchart describing how to derive a time series of EWH changes in a selected basin from monthly SH potential coefficients. Degree 1 coefficients are not considered in this study (Section 5.1).

	Region	Size [10^6 km^2]
1	Ocean (excluding 300 km buffer zone)	217.70
2	Land	147.03
3	East Antarctica	10.07
4	Amazon	5.85
5	Congo	3.72
6	Mississippi	3.15
7	Nile	3.14
8	Lena	2.40
9	West Antarctica + Peninsula	2.02
10	Greenland	2.22
11	Yangtze	1.76
12	Volga	1.41
13	Murray-Darling	1.07
14	Ganges	1.04
15	Danube	0.78

Table 5.1: 15 selected study regions and their size. See Figure 5.4 for the location of the regions.

First, an averaging kernel $\vartheta(\lambda, \theta)$, which describes the shape of the selected basin, has to be defined

$$\vartheta(\lambda, \theta) = \begin{cases} 0 & \text{outside the basin,} \\ 1 & \text{inside the basin.} \end{cases} \tag{5.3.1}$$

In a next step, $\vartheta(\lambda, \theta)$ is expressed through SH coefficients ϑ^c_{nm} and ϑ^s_{nm}

$$\vartheta^c_{nm} = \int_\Omega \vartheta(\lambda, \theta) P_{nm}(\cos(\theta)) \cos(m\lambda)\, d\Omega, \tag{5.3.2}$$

$$\vartheta^s_{nm} = \int_\Omega \vartheta(\lambda, \theta) P_{nm}(\cos(\theta)) \sin(m\lambda)\, d\Omega. \tag{5.3.3}$$

In the above equations, Ω denotes the angular area of the region of interest. Finally, the mean EWH over the region of interest is computed similarly to Equation (5.2.3)

$$\overline{\Delta EWH}_{\text{region}} = \frac{1}{\Omega} \frac{M}{4\pi R^2 \rho_w} \sum_{n=1}^{\infty} \sum_{m=0}^{n} \frac{(2n+1)}{(1+k'_n)} \left[\vartheta^c_{nm} \Delta c_{nm} + \vartheta^s_{nm} \Delta s_{nm}\right]. \tag{5.3.4}$$

By evaluating this equation for each month, a time series of mean EWH for a desired region can be computed. Note that the smoothing filter can either be applied in Equation (5.3.4) directly, or in a previous step (after adding the GIA correction).

5.3.2 Special Characteristics when Deriving Ocean Mass Change

Monitoring ocean mass change is essential for partitioning sea level change, as measured by satellite altimeters, into steric and mass-related parts. In general, global ocean mass variations can be determined similarly to mass changes in any other basin. There are two additional steps that should be applied during the processing: Applying a buffer zone for coastal regions and restoring the AOD1B GAB product (see Figure 5.5).

Ocean mass change from GRACE has been investigated in many studies, e.g. Chambers and Bonin (2012); Johnson and Chambers (2013) or Rietbroek et al. (2016). However, the effect of different processing choices is surprisingly large and trend estimates differ by more than 1 mm/yr. Uebbing et al. (2019) investigated the reason for differences between various studies. A large part of the

discrepancies can be explained by the choice of GIA models and the restoration of the AOD1B product. One should keep in mind that each choice in the processing chain (Figure 5.5) will have an impact on the result and that one should always specify which choices are made and which data sets are used.

Ocean Mask

Mass variations caused by hydrological redistributions or the melting of the ice sheets have a significantly larger amplitude than mass changes within the ocean. Naturally, the spherical harmonic expansion (Equation (5.2.3)) has to be truncated at a certain maximum degree, which will cause signal leakage from the continents into the ocean (e.g., Baur et al., 2009). This effect will be increased when smoothing filters are applied.

Chambers (2009) introduced a buffer zone of 300 km along the coasts to only investigate regions that should not be affected by land-leakage. Such an ocean mask has commonly been used in other studies, for example Johnson and Chambers (2013) or Uebbing et al. (2019). In this thesis, the ocean mask by Uebbing et al. (2019)[2] is applied, whenever results of ocean mass change are shown (Figure 5.4 a).

GAB Product

The AOD1B RL06 product contains non-tidal atmospheric and oceanic mass variations in three-hourly intervals as SH coefficients (Dobslaw et al., 2017a). It is removed as a background model during the gravity field processing to avoid temporal aliasing (Section 4.1.2).

For ocean mass analysis, the GAB product has to be restored, as is depicted in Figure 5.5. The GAB product is defined as the monthly mean of the three-hourly AOD1B RL06 OCN Stokes' coefficients (Dobslaw et al., 2017b). OCN coefficients describe the dynamic ocean contribution to ocean bottom pressure. They are generated from numerical simulations using the **M**ax-**P**lanck-**I**nstitute for Meteorology **O**cean **M**odel (MPIOM) (Jungclaus et al., 2013).

5.4 Results from Swarm and Comparison to GRACE(-FO)

In this section, mass changes from Swarm are analyzed and compared to GRACE(-FO). First, the results are evaluated globally (Section 5.4.1) and then basin averages are considered (Section 5.4.2). If not mentioned otherwise, the following processing steps are performed:

- the parameterization as explained in Section 4.1.4 is chosen to derive IGG-Swarm gravity field models,
- the flowchart in Figure 5.5 is followed (using a 500 km Gaussian filter),
- the gravity field models are truncated at a maximum degree of 12.

5.4.1 Global Results

In theory, one could compare each individual monthly gravity field model of Swarm to GRACE(-FO) (provided that the solution exists). This would however be ineffective and hard to overview. I chose to show one representative month in Section 5.4.1.1 to discuss the spatial resolution. Then I move on to selected quantities, such as trends, seasonal signals, RMS values, RMSEs, and correlations, which effectively represent the whole time period.

[2] https://www.apmg.uni-bonn.de/daten-und-modelle/time_series_of_ocean_mass_change_from_grace (last access: August 1, 2021)

5.4.1.1 Monthly Grids of Equivalent Water Height

By converting GRACE(-FO) and Swarm gravity field models to maps of EWH, it is possible to compare their spatial resolution and to assess regional similarities and differences. I chose to investigate January 2020 in terms of the spatial resolution of GRACE-FO and Swarm in Figure 5.6. It is important to keep in mind that the solution of one particular month does not necessarily reflect the general trends, but is subject to seasonal and possibly extraordinary mass redistributions. Hence, I will discuss the temporal changes at a later point (e.g., Figure 5.7).

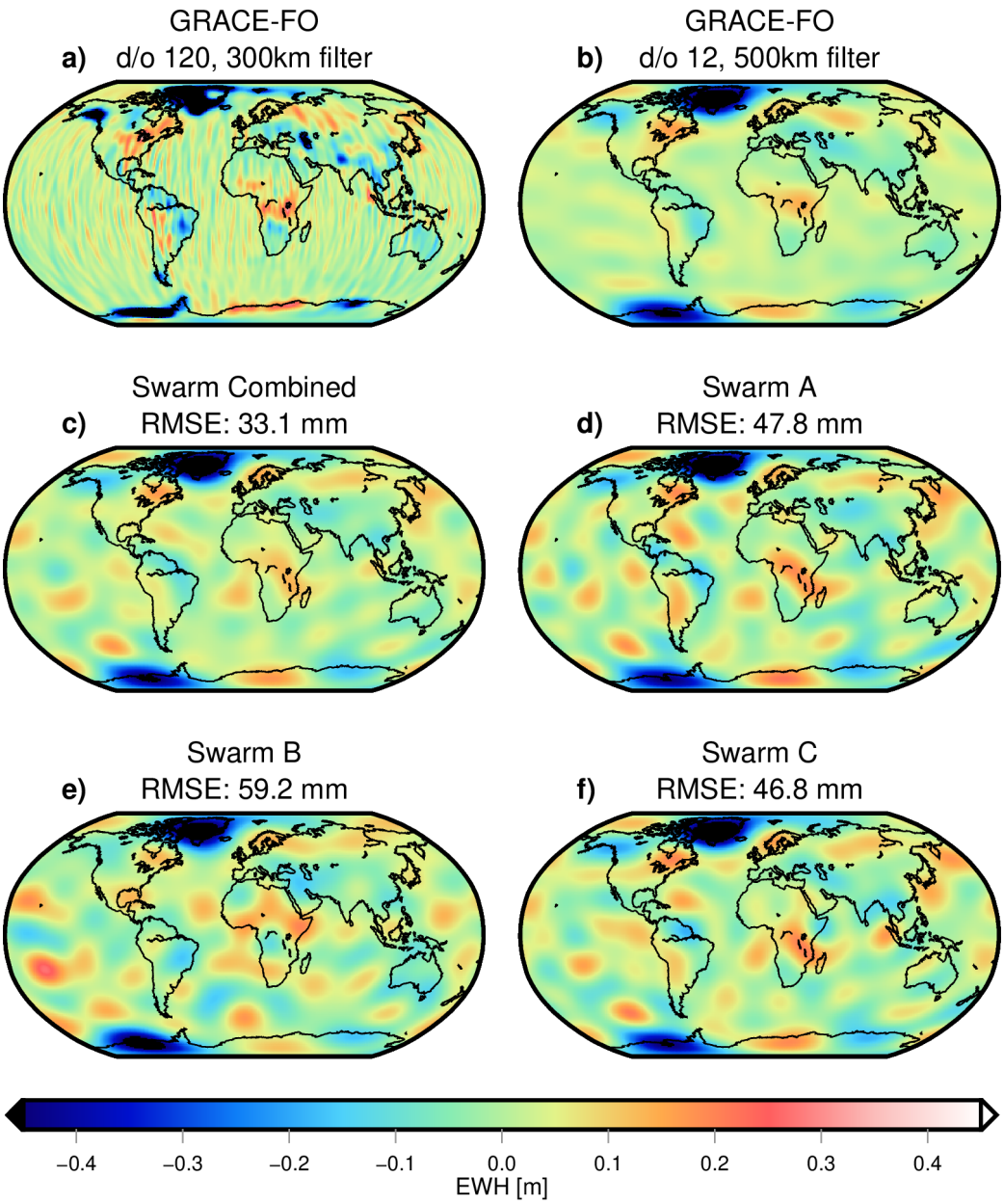

Figure 5.6: Maps of EWH for January 2020 relative to the static part of GOCO06s derived from GRACE-FO and Swarm. a) GRACE-FO with common GRACE processing: d/o 120 and 300 km Gaussian filter. b) GRACE-FO: d/o 12 and 500 km Gaussian filter (i.e. common Swarm resolution). c) Swarm combined: d/o 12 and 500 km Gaussian filter. d)-f) Single-Swarm solutions: d/o 12 and 500 km Gaussian filter. All RMSE values are derived with respect to b).

In Figure 5.6 (a), one can see the result of a common GRACE(-FO) processing choice. The gravity field is evaluated up to d/o 120, while applying a Gaussian filter of 300 km. In this particular month, a large-scale mass loss (compared to the static field) is visible in Greenland and in the

Amundsen Bay (West Antarctica). Furthermore, glaciated regions of Alaska, Wilkes Land (East Antarctica), and the Caspian Sea show negative EWH values. A mass gain is observed in Dronning Maud Land (East Antarctica), parts of Central Africa, and along the East Coast of North America. Apart from mass redistributions, one can clearly see noise in terms of the well-known GRACE(-FO) striping pattern.

If Figure 5.6 (a) would now directly be compared to the Swarm solution, two effects would be mixed up: (1) Different resolutions due to the measurement principle (see Section 3.7) and (2) Swarm and GRACE-FO quality would be compared to each other. In order to separate these effects, it is reasonable to truncate the GRACE-FO gravity field at d/o 12 and apply a 500 km Gaussian filter, which is shown in Figure 5.6 (b) and can be considered as the common Swarm resolution. If not mentioned otherwise, this will be the standard processing for all following investigations. Subfigure (b) can be described as a smoothed version of subfigure (a). The truncation as well as the stronger smoothing eliminated the striping pattern but on the other hand attenuated the signal content in some regions. In West Antarctica, for example, the mass loss leaks into the ocean and details, such as the mass loss in the Caspian Sea, are not visible anymore. However, this figure should be considered as a base for comparison with Swarm, because this is the resolution that can be expected.

Figure 5.6 (c) shows the monthly Swarm time-variable gravity field with the same processing choices as in (b). The solution is derived from a combination of the three satellites on normal equation level. Areas of large-scale mass redistribution are very similar to subfigure (b). Some regions are subject to noise, especially over the ocean, and the global mean RMSE with respect to GRACE-FO is 33.1 mm.

The solutions derived from the individual satellites are presented in Figure 5.6 (d-f). Each solution contains more noise than the combination with global mean RMSE values between 46.8 mm (Swarm C) and 59.2 mm (Swarm B). The inferior performance of Swarm B is due to its higher altitude and is further discussed in Section 4.3.2.

5.4.1.2 Trend and Seasonal Signals

Global maps of trend and seasonal signals can be derived from the time-variable gravity fields. A six-parameter model, consisting of a constant, trend, two annual and two semiannual parameters is fitted to the monthly solutions. The time period as explained in Section 4.2.8 is considered.

Figure 5.7 (a) illustrates the trend derived from GRACE(-FO). The largest mass loss is due to the melting ice in Greenland and is more than 4 cm/yr. Further regions of mass loss are Amundsen Bay and Wilkes Land in Antarctica, Alaska, and south of the Amazon basin. Mass gain can be observed in the Amazon basin and in Central Africa. Accumulating snowfall in Dronning Maud Land has been observed by Velicogna et al. (2020) and can also be identified as a positive trend here. These are the most prominent trends in mass redistribution. For further analysis, e.g. of ocean mass trends, basin averages will be computed and investigated in Section 5.4.2.

In Figure 5.7 (b), the trend derived from Swarm is shown. Swarm can detect large-scale mass trends correctly and generally all statements that were made for subfigure (a) are also true for subfigure (b). Nevertheless, one can locate regions with spurious trends, e.g. in the Pacific Ocean.

Figure 5.7 (c) and (d) show annual signals derived from GRACE(-FO) and Swarm, respectively. Both figures look very similar and Swarm can detect annual variations over land precisely. Large annual signals are concentrated in the tropical regions and are related to seasonal variations in rainfall. Generally, annual variations are larger over land than over the ocean, as they are mainly related to hydrological events. In ocean regions, Swarm overestimates the annual amplitude, when compared to GRACE(-FO).

Semiannual variations derived from GRACE(-FO) are presented in Figure 5.7 (e). The amplitude is generally smaller than that of annual variations. Largest values can be found in the north of

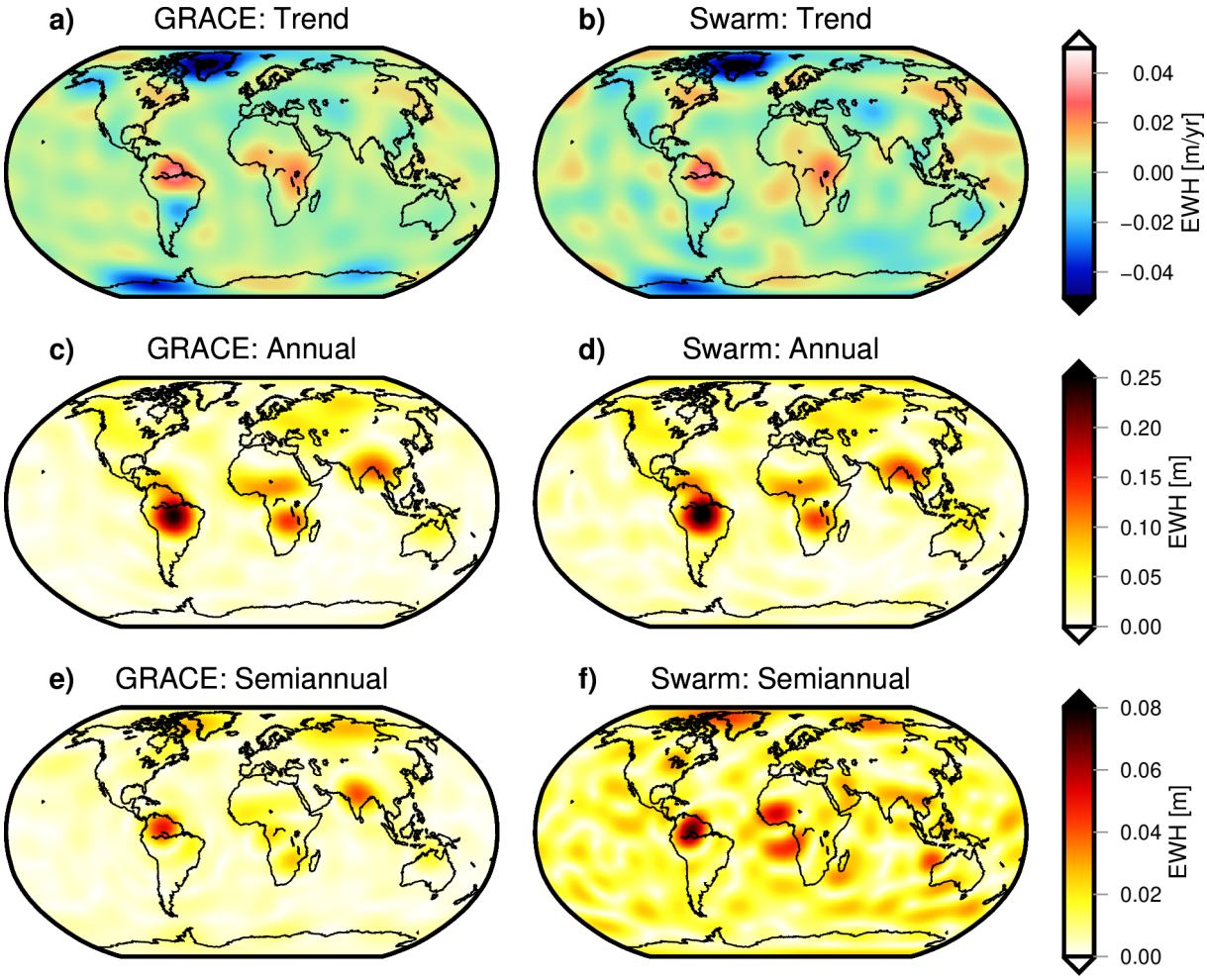

Figure 5.7: Trend, annual, and semiannual signal derived from GRACE(-FO) and Swarm. A six-parameter model (constant, trend, two annual, two semiannual) is fitted to the data. Time frame: July 2015 to March 2021, excluding the GRACE(-FO) gaps and months of inferior quality (see Figure 2.5).

South America and in northern India. Apart from that, semiannual variations are generally larger over land.

Figure 5.7 (f) shows the semiannual signal derived from Swarm data. A large amplitude in northern South America is also detected by Swarm. Other than that, the amplitudes are overall larger than those derived from GRACE(-FO), which can likely be attributed to noise in the Swarm data.

5.4.1.3 Root Mean Square of GRACE(-FO) and Swarm

Figure 5.8 gives an overview of different quantities related to RMS values of GRACE(-FO) and Swarm.

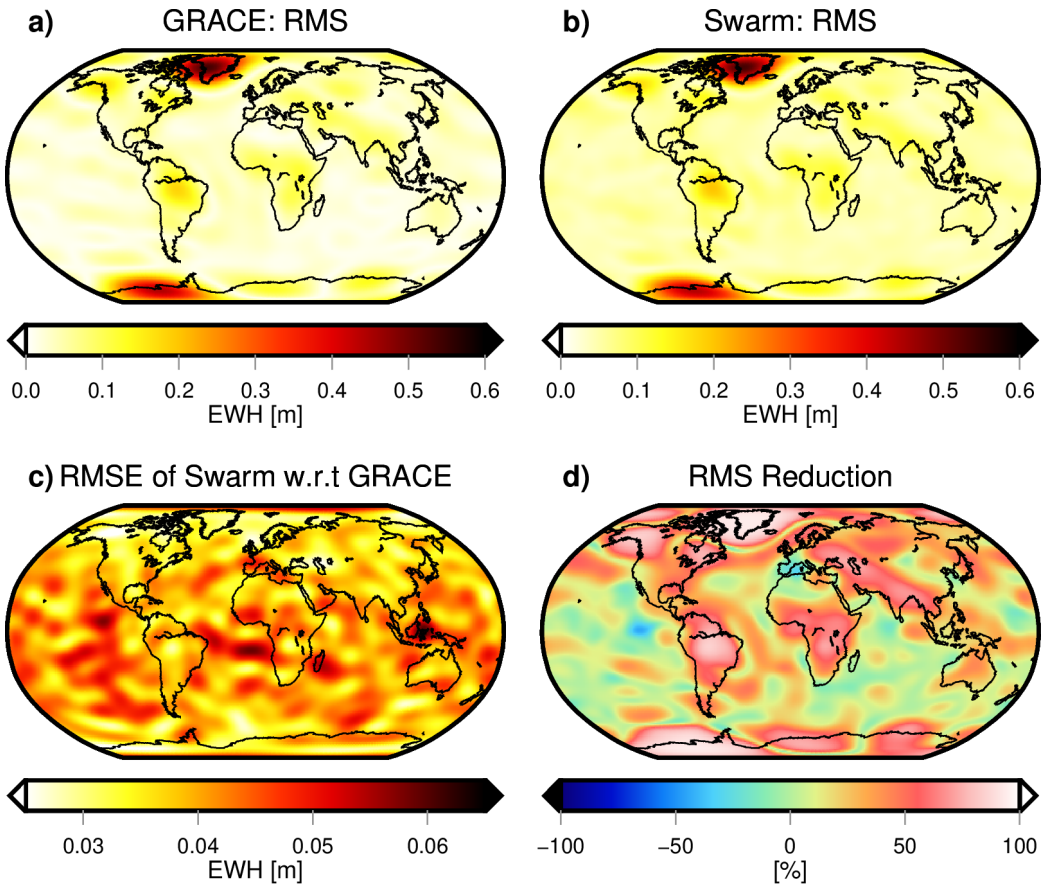

Figure 5.8: Investigation of RMS, RMSE, and RMS reduction of Swarm data with respect to GRACE(-FO). a) RMS of GRACE(-FO) data. b) RMS of Swarm data. c) RMSE of Swarm with respect to GRACE(-FO). d) RMS reduction. Time frame: July 2015 to March 2021, excluding the GRACE(-FO) gaps and months of inferior quality (see Figure 2.5).

RMS maps of GRACE(-FO) and Swarm (Figure 5.8 (a) and (b)) look largely similar. High RMS values can be found in Greenland and West Antarctica and are related to the dominating downwards trend. Due to hydrological variations, regions over land generally have larger values than those over the ocean. In the Swarm map, one can see values of few centimeters all over the globe, which is due to the noise inherent in the monthly time-variable gravity field of Swarm.

The RMSE of Swarm with respect to GRACE(-FO) is presented in Figure 5.8 (c). Assuming that GRACE(-FO) is the truth, the RMSE can be interpreted as the error of Swarm. Values are in the range of a few centimeters, mostly between 3 to 5 cm. There are no specific regions with larger RMSEs, but one could say that they are generally lower over the continents.

Figure 5.8 (d) shows the RMS reduction, which is computed by $(1 - \mathrm{RMSE}/\mathrm{RMS}_{\mathrm{Swarm}}) \cdot 100\%$.

It reveals how much of the RMS of Swarm can be explained by GRACE(-FO). If Swarm and GRACE(-FO) would be identical, the RMS reduction would be 100 % and it is larger than zero, if the RMSE is smaller than $\mathrm{RMS}_{\mathrm{Swarm}}$. In 90.1 % of the Earth's surface, the RMS reduction is positive and in 18.4 % it is even larger than 50 %, revealing a good relation between RMSE and $\mathrm{RMS}_{\mathrm{Swarm}}$ values. Generally, the RMS reduction is higher over land areas, which is due to a higher variability of mass changes and, thus, a better relation between RMSE and $\mathrm{RMS}_{\mathrm{Swarm}}$.

The evolution of RMSE values of Swarm with respect to GRACE(-FO) over time is depicted in Figure 5.9. Three time series are shown: the global mean RMSE, the RMSE over the ocean (excluding a 300 km buffer zone) and the RMSE over land.

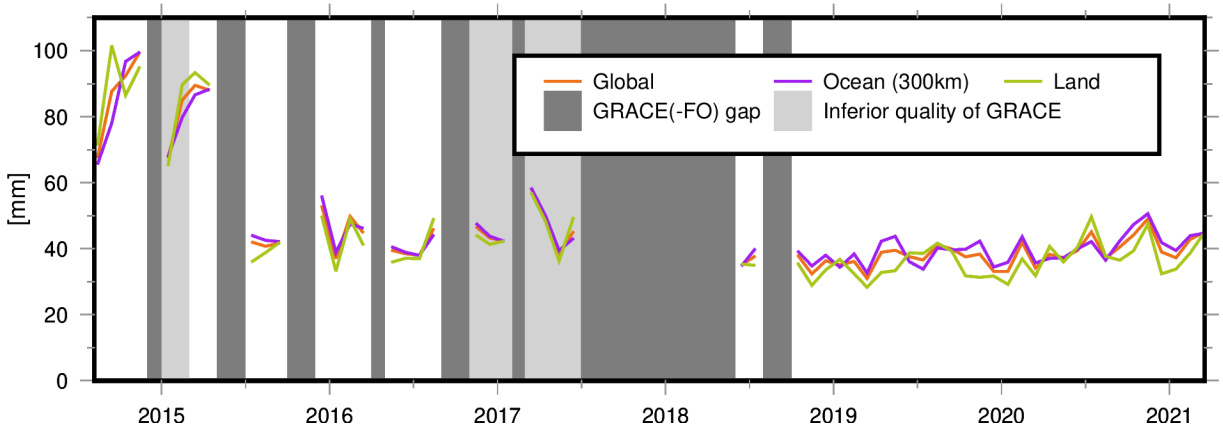

Figure 5.9: Time series of mean (globally, over ocean areas, and over land areas) RMSE of Swarm with respect to GRACE(-FO). GRACE(-FO) gaps are highlighted in dark-gray, while months of inferior quality are marked in light-gray.

The most evident observation is that all RMSE values are high (60 to 100 mm) until mid-2015 and then sharply drop down (30 to 60 mm). This is related to a lower quality of the GPS observations in the beginning of the Swarm mission. The high ionospheric activity led to disturbances and systematic errors in the kinematic orbits and several receiver updates were made in the beginning (see Figure 3.11 and Dahle et al., 2017).

One thing to keep in mind when investigating RMSEs is that the quality of Swarm time-variable gravity fields is assessed with respect to GRACE(-FO), which is considered as the ground-truth. Yet, it is well known that some GRACE months have a lower quality and should be interpreted with caution. They are marked in light-gray and the high RMSE value of March 2017 could be rather due to errors in GRACE than in Swarm.

Generally, the RMSE is lowest over land areas, followed by the global mean and highest over the oceans (with the exception of a few months). Nevertheless, all three time series are only a few mm apart.

Figure 5.10 shows time series of the global mean RMSE of Swarm with respect to GRACE(-FO) for different maximum degrees. Furthermore, the effect of a 500 km Gaussian smoothing filter is investigated. As expected, higher degrees lead to a higher RMSE as the uncertainty of the coefficients gets larger (Figure 4.6). The RMSE is also higher, when no smoothing filter is applied. The range between the individual time series is larger, without filtering, i.e. by applying a smoothing filter, the difference between the time series is not as pronounced. Generally, the RMSE is two to three times higher, for the unfiltered d/o 15 solution, compared to the filtered d/o 10 solution. However, one has to find a compromise between smoothing the noise and retaining as much signal as possible. A reasonable choice for Swarm time-variable gravity fields is to truncate the solutions at d/o 12 and to apply a 500 km Gaussian filter, as was shown in Lück et al. (2018).

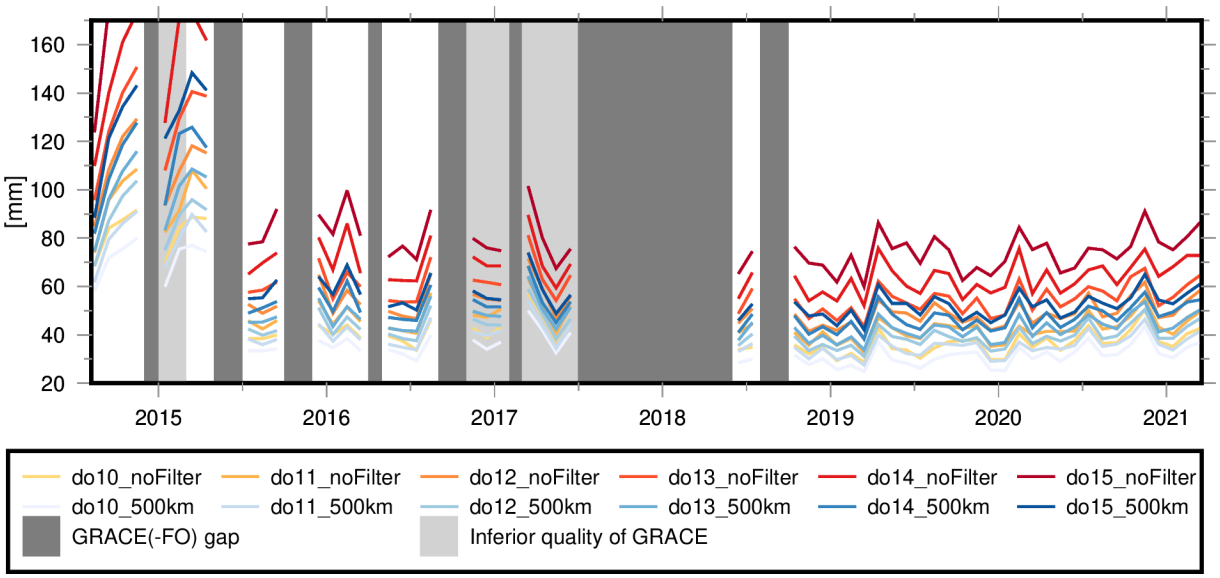

Figure 5.10: Time series of global mean RMSE of Swarm with respect to GRACE(-FO). Comparison of maximum d/os 10 to 15 and 500 km Gaussian filter vs. no filtering. GRACE(-FO) gaps are highlighted in dark-gray, while months of inferior quality are marked in light-gray.

5.4.1.4 Correlation Between GRACE and Swarm

Another possibility to investigate the similarity of GRACE(-FO) and Swarm time-variable gravity field models is to create correlation maps. Figure 5.11 (a) shows the correlation of the full signal. One can observe a high correlation all over the globe and again especially over land areas. Largest values can be found in regions with large trends and annual signals (compare Figure 5.7). 38.2 % of the Earth's surface is correlated by more than 50 %.

An important question is whether Swarm can detect variations apart from the seasonal signals. In Figure 5.11 (b), annual and semiannual signals are removed at each grid point before computing the correlation. Naturally, the correlation is lower than in subfigure (a), but it is still striking that large areas show high correlations even beyond the seasonal variations. Large parts of America are correlated by more than 50 % and other land areas are also highly correlated. Ocean areas show a mixed pattern. Globally, 18.7 % of the Earth's surface is correlated by more than 50 % when seasonal signals are removed.

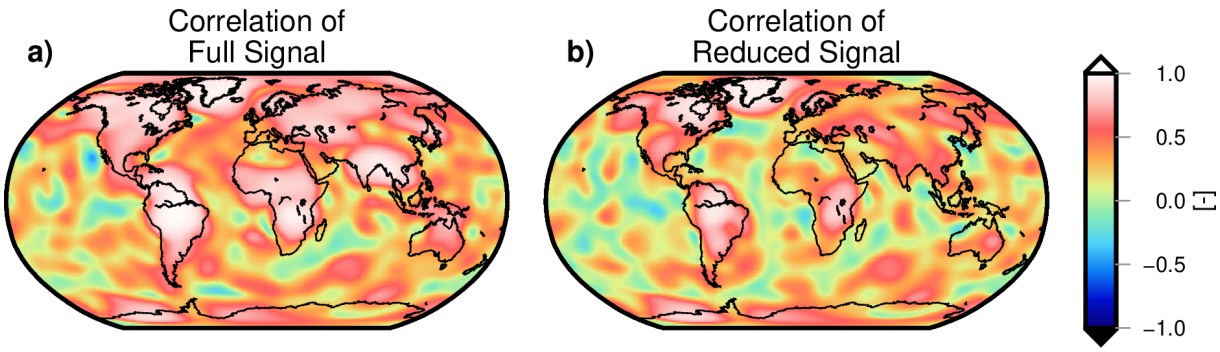

Figure 5.11: Map of the correlation between GRACE(-FO) and Swarm. Time frame: July 2015 to March 2021, excluding the GRACE(-FO) gaps and months of inferior quality (see Figure 2.5). a) Correlation of full GRACE(-FO) and Swarm signals. b) Correlation of reduced GRACE(-FO) and Swarm signals (i.e. annual and semiannual signals of GRACE(-FO) are reduced from GRACE(-FO) and Swarm).

5.4.2 Basin Averages

Time series of basin averages are computed from Swarm and GRACE(-FO) for the 15 selected study regions (Figure 5.4). The processing chain is explained at the beginning of Section 5.4. In Figures 5.12 to 5.16 mass change in five regions is presented. The time series of the remaining regions can be found in Appendix A. The top panel of Figures 5.12 to 5.16 shows the full signal of the mass change time series derived from Swarm and GRACE(-FO). All characteristics (Tables 5.2 and 5.3) are derived from the time period highlighted in light-gray. The bottom figure always shows the time series reduced by the annual and semiannual signal of GRACE(-FO). Furthermore, the trend estimates are plotted and specified. Finally, the RMSE of Swarm with respect to GRACE(-FO) as well as the SNR of Swarm ($\text{std}_{\text{GRACE(-FO)}}/RMSE$) are indicated. For hydrological regions, an additional mass change data set by Humphrey and Gudmundsson (2019)[3] is plotted. Their statistical model uses meteorological forcing as input data and is trained with GRACE(-FO) mascon solutions to reconstruct climate-driven **T**otal **W**ater **S**torage (TWS) change.

Ocean

GRACE(-FO) generally shows an increase in ocean mass from 2013 to 2021 (Figure 5.12). The rate is exceptionally large in the years 2014-2016 (6.4 mm/yr), followed by a slight drop in 2016. From then on, ocean mass increased steadily, but at a lower rate, compared to 2014-2016. The trend derived from GRACE-FO amounts to 1.2 mm/yr.

As described by Uebbing et al. (2019), one should be careful when comparing ocean mass estimates from different studies. Processing choices as well as the considered time period affect the results and can lead to differences in trend estimates of several mm. At the time of writing, there are no studies which consider the GRACE-FO period until March 2021. Hence, I refrain from comparisons to other studies in terms of numbers. The exceptionally strong mass gain in 2014-2016 is however also observed by others (e.g., Löcher and Kusche, 2021).

Swarm estimates of ocean mass change generally agree well with the GRACE(-FO) results. Only in the beginning of 2015, there are larger differences, which could be expected as a consequence of the lower accuracy of Swarm in the early times (Section 3.7). Due to the drop in 2016, the overall trend in the comparison period is small for both Swarm (0.4 mm/yr) and GRACE(-FO) (0.2 mm/yr). The RMSE of Swarm with respect to GRACE(-FO) is 1.9 mm with similar annual amplitudes of 8.5 mm (Swarm) and 7.7 mm (GRACE(-FO)). The semiannual amplitude of GRACE(-FO) is larger (1.1 mm) compared to Swarm (0.5 mm). Swarm has a high SNR of 2.9 and the two time series are strongly correlated by 95.4 %.

In addition to the IGG-Swarm solution, the solution without modeled non-gravitational accelerations is shown (Section 4.3.4). During the processing, a constant value per arc and direction is co-estimated to account for non-gravitational accelerations. The result is clearly inferior to the standard IGG-Swarm solution. The RMSE with respect to GRACE(-FO) increases to 3.6 mm and the SNR consequently worsens (1.7).

When annual and semiannual signals are removed (Figure 5.12, bottom panel), the Swarm and GRACE(-FO) time series still show a similar development. The noise in Swarm can be spotted more easily compared to the representation of the upper panel. The GRACE(-FO) time series has a standard deviation of 1.4 mm, while that of Swarm is 2.3 mm. Still, the correlation of 59.8 % is high.

In the GRACE-GRACE-FO gap, Swarm continues the time series as expected. Based on the Swarm gravity field models, there is no indication of any events that could have led to extraordinary ocean mass changes. A further experiment is to investigate how much the GRACE(-FO) ocean mass trend would change, when Swarm is used as a gap-filler. For this consideration, I compute the

[3] The ensemble mean GSFC_ERA5 data set from https://figshare.com/articles/dataset/GRACE-REC_A_reconstruction_of_climate-driven_water_storage_changes_over_the_last_century/7670849?file=17990393 is used (last access: June 24, 2021)

GRACE(-FO) trend from all available GRACE(-FO) data (including the end-of-life period) from May 2015 to March 2021. The trend amounts to 0.4 mm/yr. When Swarm is used as a gap-filler and the existing GRACE(-FO) data is retained, the trend is still 0.4 mm/yr. This matches the statement that there are no unforeseeable ocean mass change events during the gaps.

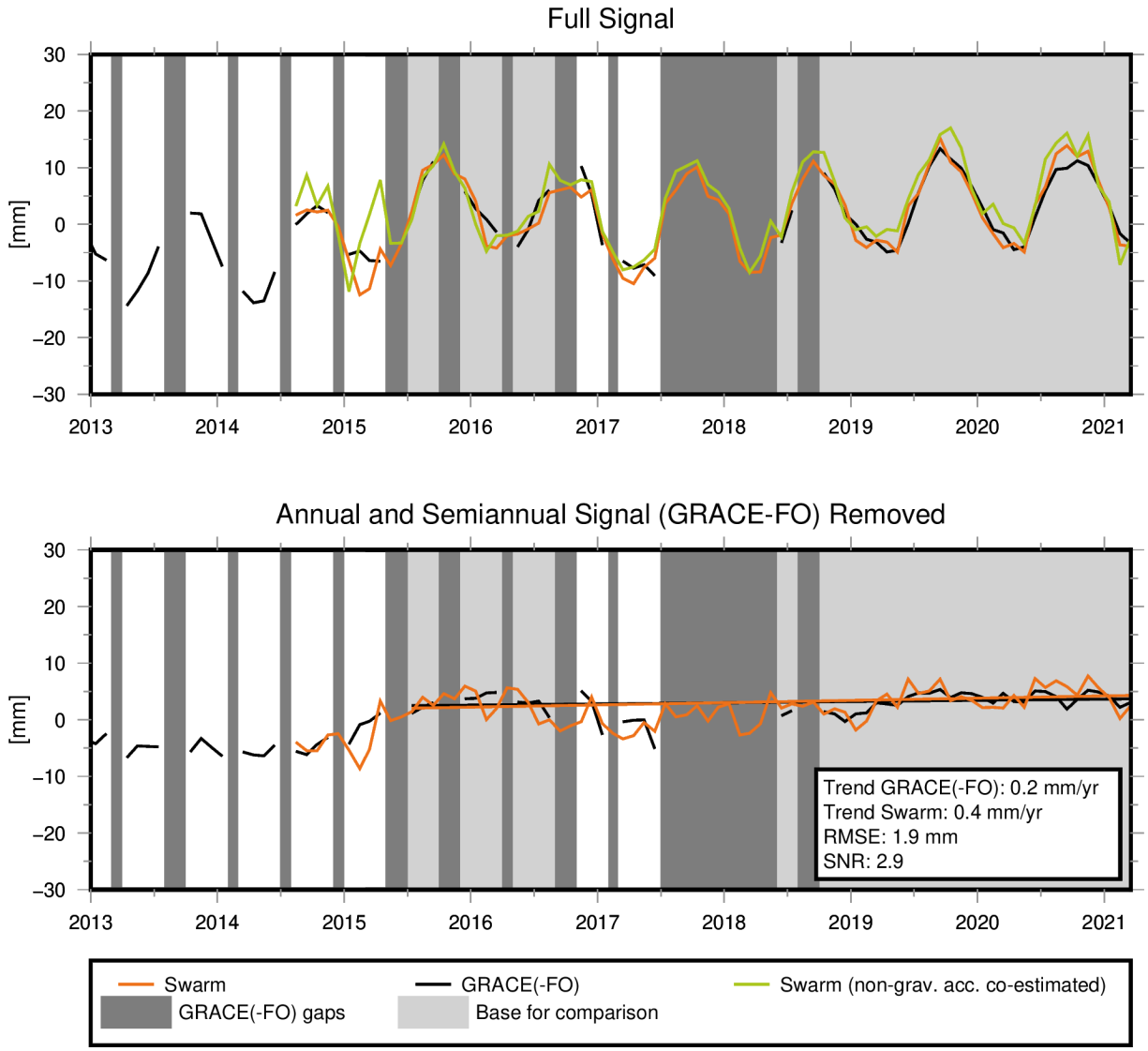

Figure 5.12: Mass change in mm EWH over the ocean (excluding a 300 km buffer zone) from Swarm and GRACE(-FO). In addition to the IGG-Swarm solution (orange), the Swarm solution without modeled non-gravitational accelerations is shown (green). See the beginning of Section 5.4 for processing details. Top panel: Full signal. Bottom panel: Annual and semiannual signals from GRACE(-FO) are removed from both time series. Additionally, the trend is computed from the light-gray time periods and plotted.

Amazon

Due to its large hydrological variations and its size, the Amazon basin is a popular example when comparing GRACE(-FO) mass change to results from gravity field models derived from satellite orbits (e.g., Bezděk et al., 2016; Jäggi et al., 2016; de Teixeira da Encarnação et al., 2020; Löcher and Kusche, 2021). GRACE experiences a large seasonal signal and a slight mass gain from 2013 until mid-2015 (Figure 5.13, top panel). In 2016 there is a clear drop, likely due to a drought caused by an ENSO event in 2016 (Jiménez-Muñoz et al., 2016). In 2017, the EWH rises again and GRACE-FO seems to follow up on GRACE without any extraordinary irregularities.

Swarm is able to reliably observe mass change in the Amazon basin. It almost perfectly determines the ENSO in 2016, which is important when considering Swarm as a gap-filler for the time between GRACE and GRACE-FO (Section 5.4.3). If such an event would have occurred during the gap (or will occur in any future gaps), a simple interpolation from GRACE(-FO) data could not detect such anomalies, whereas Swarm is able to see these irregularities.

The RMSE of Swarm with respect to GRACE(-FO) is 20.7 mm, which is not much, considering the annual amplitudes of 142.5 mm (GRACE(-FO)) and 153.9 mm (Swarm). The SNR of 5.2 is the highest of all study regions. Trends are similar with 14.7 mm/yr for GRACE(-FO) and 13.8 mm/yr for Swarm. The correlation between both time series is extremely high (98.7 %).

When subtracting annual and semiannual signals (Figure 5.13, bottom panel) it becomes evident that Swarm can even reliably detect mass changes beyond those scales. The correlation of the reduced signals is still very high (92.6 %). The reconstruction by Humphrey and Gudmundsson (2019) is similar to the GRACE(-FO) and Swarm time series. Both, Swarm and the reconstruction, close the gap between GRACE and GRACE-FO without any unexpected events.

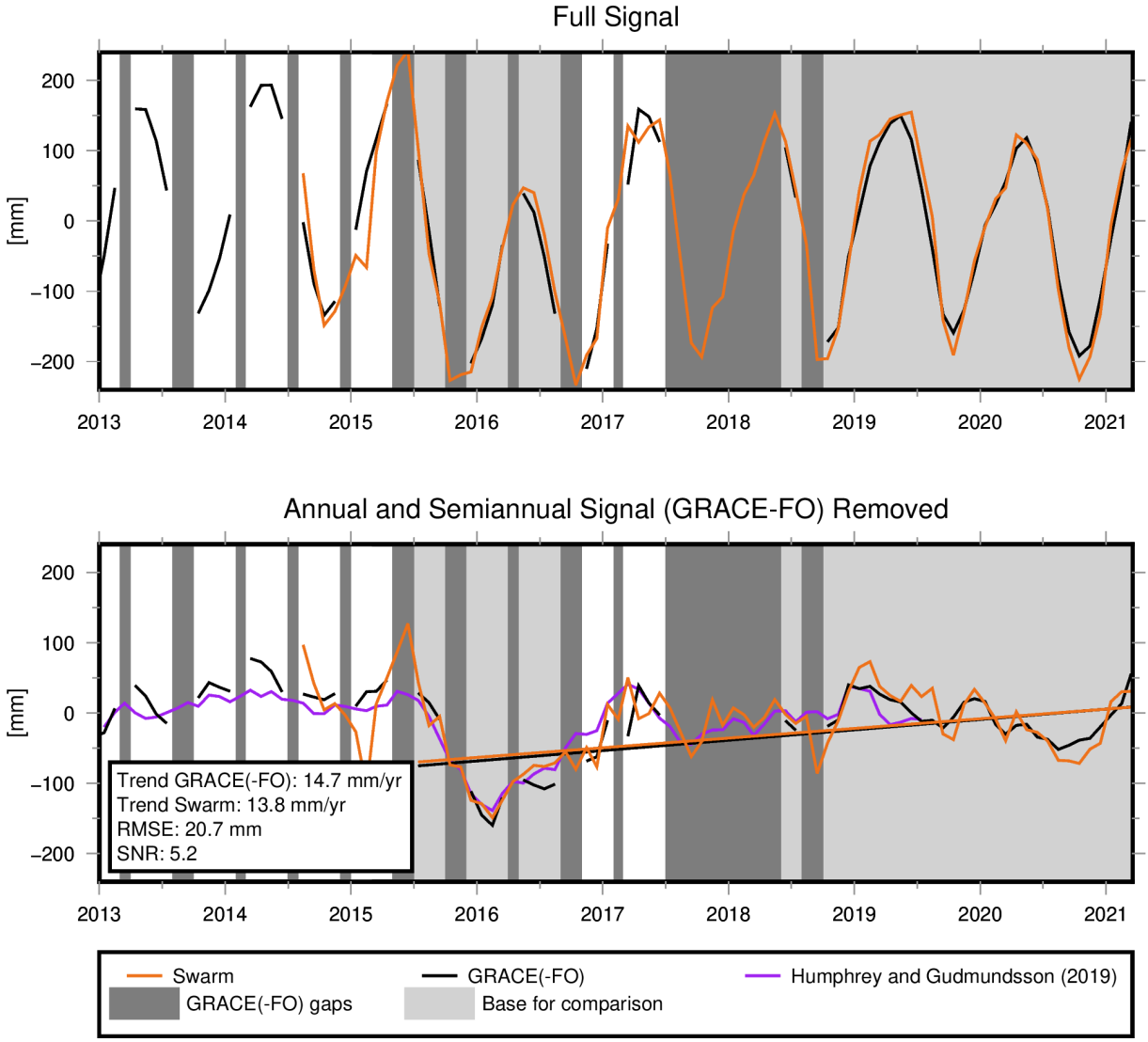

Figure 5.13: Mass change in mm EWH in the Amazon basin from Swarm, GRACE(-FO) and Humphrey and Gudmundsson (2019). See the beginning of Section 5.4 for processing details. Top panel: Full signal. Bottom panel: Annual and semiannual signals from GRACE(-FO) are removed from both time series. Additionally, the trend is computed from the light-gray time periods and plotted.

Greenland

For Greenland, GRACE(-FO) sees a general downwards trend, related to the melting of the ice sheets (Figure 5.14 top panel). In 2017 and 2018 the mass loss seems to decelerate, but this time period only includes 5 months of the GRACE end-of-life period and 5 months of GRACE-FO. The lower mass loss in 2017 and 2018 is also observed by Velicogna et al. (2020) and Sasgen et al. (2020) who could relate this observation to snow-rich winters in eastern Greenland and cold summers in the west. However, in 2019 one can see a rapid mass loss in the GRACE-FO time series due to a hot summer, which is also confirmed by the two previously mentioned studies. After 2019, the melting is comparable to pre-2017 conditions.

Until mid-2015 noise is prominent in the Swarm time series (Section 3.7). In the comparison period, Swarm mass change is close to that derived from GRACE(-FO). Trend estimates are similar with −43.6 mm/yr (equals −99 Gt/yr) for GRACE(-FO) and −44.9 mm/yr (equals −102 Gt/yr) for Swarm. The RMSE of Swarm with respect to GRACE(-FO) is 19.9 mm/yr, resulting in a good SNR of 4.3. The correlation of both time series is 97.5 %. Swarm is able to detect the main characteristics of mass change in Greenland (see previous paragraph) correctly. In the GRACE-GRACE-FO gap, Swarm confirms the hypothesis of a decelerating mass loss, compared to previous years (before 2017) and the year 2019.

The consequence of filling the gap with Swarm can also be investigated by including the gap in the trend estimation. From May 2015 to March 2021, the mass loss observed by GRACE(-FO) is −42.6 mm/yr, including the end-of-life period. When filling the gaps with Swarm, the trend is −39.7 mm/yr. Hence, a small, but continuous decline of the mass loss is observed, regarding the three scenarios (1) end-of-life time and gaps are excluded, (2) only the gaps are excluded, (3) gaps are filled with Swarm data. This observation can be explained by the snow-rich winters and cold summers in 2017 and 2018 (which fall into the end-of-life period and the 11-months gap), as explained above. Hence, it makes sense to consider all available data in order to obtain a realistic trend estimate.

In Figure 5.14 (bottom panel) annual and semiannual signals are subtracted from the Swarm and GRACE(-FO) mass change time series in Greenland. Compared to other regions, the picture does not change too much, because the trend is dominating for d/o 12. The strong mass loss in 2019 becomes even more apparent in both Swarm and GRACE-FO. The correlation of the reduced time series is still extremely high with 97.3 %.

West Antarctica and Antarctic Peninsula

GRACE observes a mass loss over the West Antarctic ice sheet (including the Antarctic Peninsula) until mid-2016, which is followed by a slight mass gain until 2017 (Figure 5.15, top panel). This behavior is also observed by Velicogna et al. (2020). In 2017, GRACE estimates of Antarctic mass change are heavily affected by the degrading quality during the end-of-life period (Section 2.1.4) and should not be trusted. In the GRACE-FO period, the study region is again subject to a mass loss.

When comparing Swarm results to GRACE(-FO) it becomes evident that Swarm follows the GRACE(-FO) time series quite well (except for the time before May 2015 when the quality is lower, as is well known). Swarm detects the overall negative trend in the same order of magnitude as GRACE(-FO) (Swarm: −26.7 mm/yr or −55 Gt/yr, GRACE(-FO): −28.5 mm/yr or −59 Gt/yr). It even sees the stagnation of mass loss in 2016. During the GRACE-GRACE-FO gap, Swarm first observes a slight drop in mid-2016, followed by a mass gain until early 2018. It connects well to GRACE-FO, when the mass decreases again. The annual amplitude for d/o 12 is quite low, but it is the same for both Swarm and GRACE(-FO) (3.8 mm). The RMSE of Swarm with respect to GRACE(-FO) is 20.7 mm, resulting in a SNR of 2.6. The correlation of 92.7 % is very high and hardly changes (92.6 %), when reducing annual and semiannual signals (Figure 5.15, bottom panel). As seasonal signals are rather small, the time series look similar, irrespective of whether

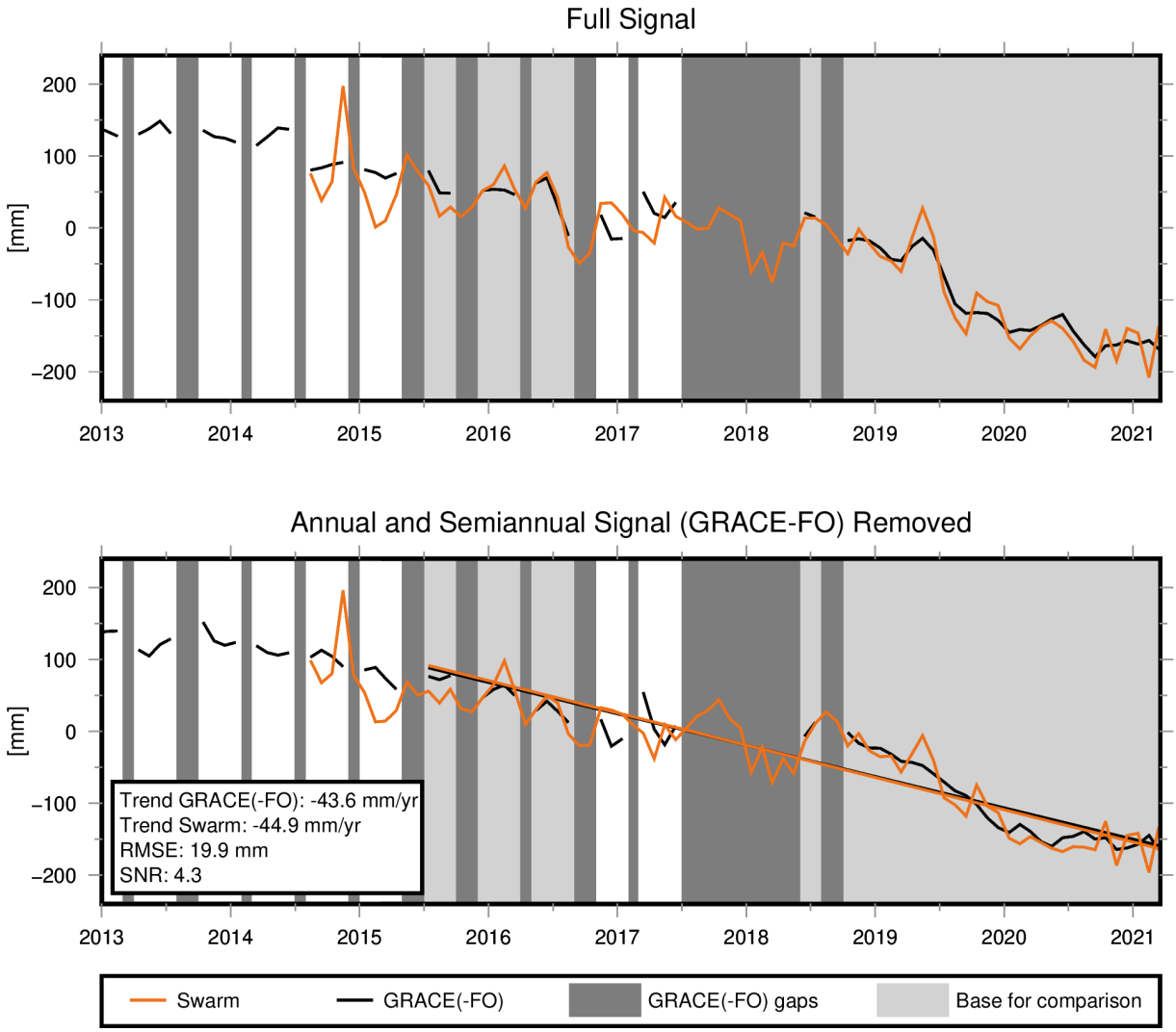

Figure 5.14: Mass change in mm EWH in Greenland from Swarm and GRACE(-FO). See the beginning of Section 5.4 for processing details. Top panel: Full signal. Bottom panel: Annual and semiannual signals from GRACE(-FO) are removed from both time series. Additionally, the trend is computed from the light-gray time periods and plotted.

annual and semiannual signals are removed or not.

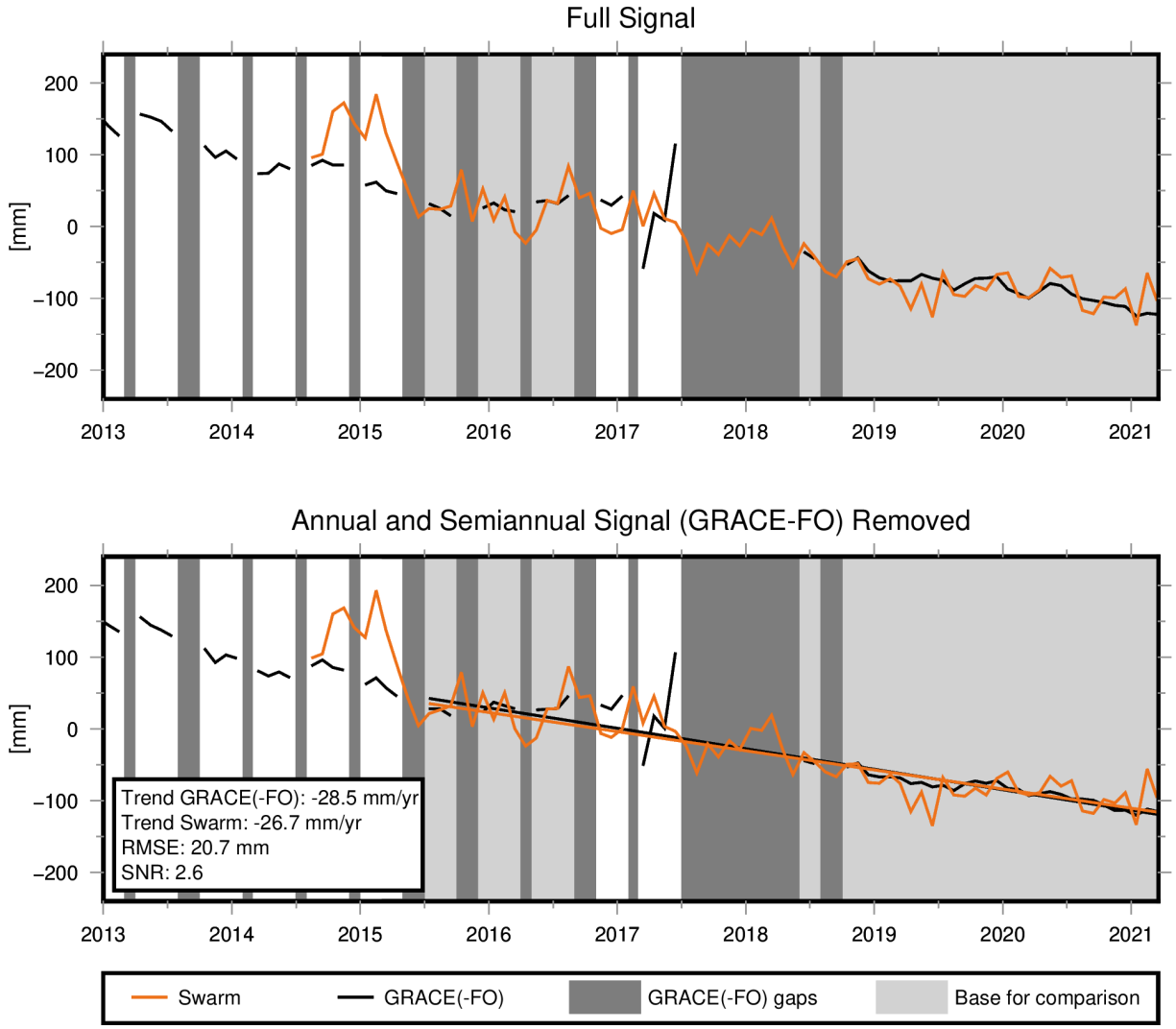

Figure 5.15: Mass change in mm EWH in West Antarctica and the Antarctic Peninsula from Swarm and GRACE(-FO). See the beginning of Section 5.4 for processing details. Top panel: Full signal. Bottom panel: Annual and semiannual signals from GRACE(-FO) are removed from both time series. Additionally, the trend is computed from the light-gray time periods and plotted.

Danube

The Danube basin is, with only about 800 000 km^2, the smallest of all investigated regions. GRACE(-FO) observes a clear annual signal, due to hydrological variations (Figure 5.16, top panel). Furthermore, from 2013-2016 the Danube catchment is subject to a slight mass loss, which stagnates from 2016 until the end of the GRACE lifetime. GRACE-FO provides evidence that the region is getting dryer again.

Swarm also sees the seasonal signal in the Danube basin. However, it underestimates the annual amplitude (Swarm: 28.2 mm, GRACE(-FO): 39.8 mm), while overestimating the semiannual amplitude (Swarm: 20.8 mm, GRACE(-FO): 6.5 mm). Swarm can detect the overall negative trend (Swarm: −4.5 mm/yr, GRACE(-FO): −7.9 mm/yr). The RMSE of 31.3 mm is quite high, leading to a SNR of 1.1. The two time series are correlated by 69.2 %. When the seasonal signals are subtracted (Figure 5.16, bottom panel) the correlation is still moderate (53.1 %). Hence, one can see similarities between Swarm and GRACE(-FO), even beyond the seasonal scales, which is, considering the small size of the catchment, remarkable. The reconstruction by Humphrey

and Gudmundsson (2019) generally overestimates mass change in the considered time period. During the GRACE-GRACE-FO gap, mass change behaves as could have been expected from the previous years. A slight increase can be observed in the second half of 2017, which is detected by both, Swarm and the reconstruction.

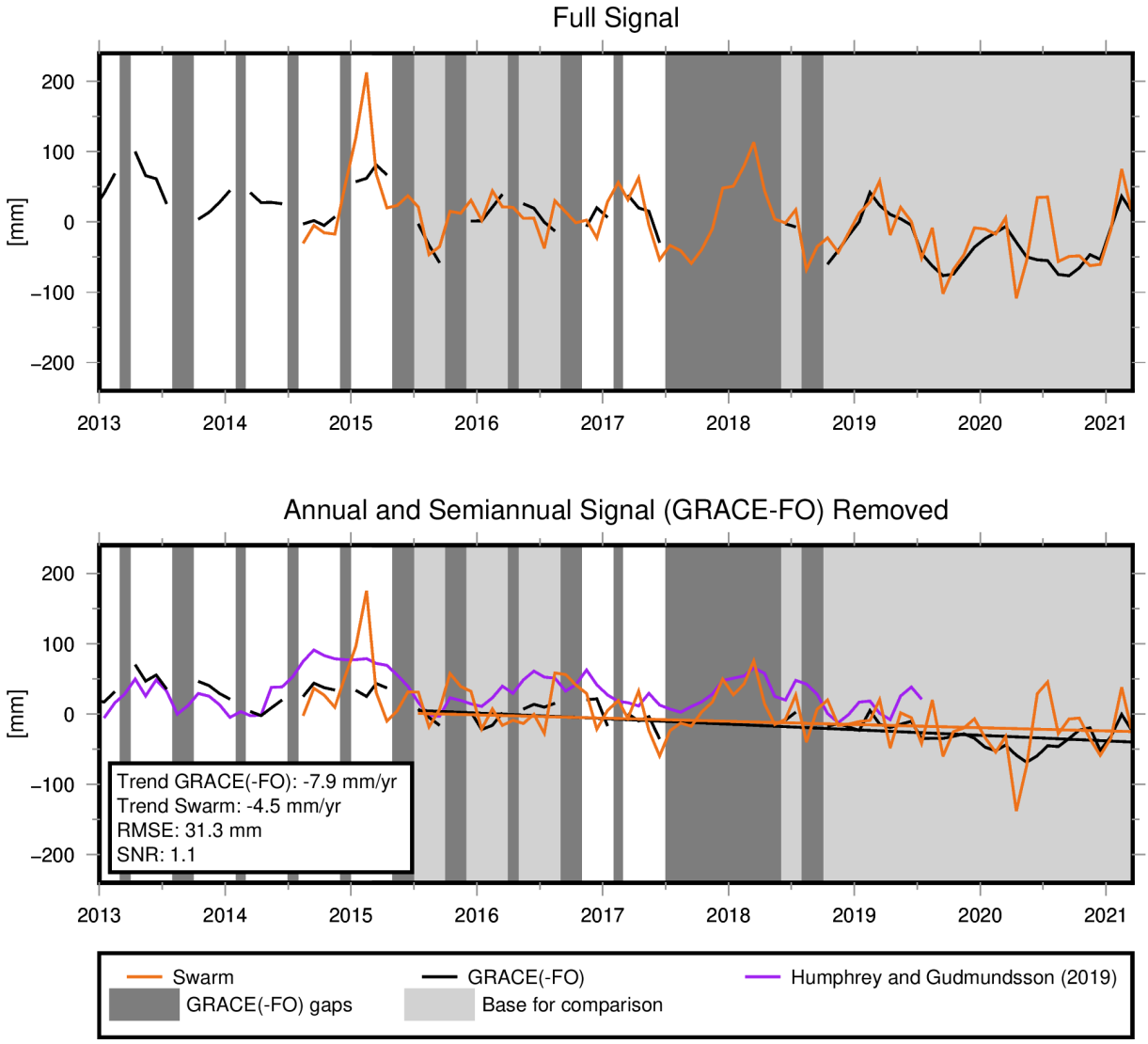

Figure 5.16: Mass change in mm EWH in the Danube basin from Swarm, GRACE(-FO), and Humphrey and Gudmundsson (2019). See the beginning of Section 5.4 for processing details. Top panel: Full signal. Bottom panel: Annual and semiannual signals from GRACE(-FO) are removed from both time series. Additionally, the trend is computed from the light-gray time periods and plotted.

General Observations

In Tables 5.2 and 5.3 some statistical properties for the 15 selected study regions are summarized. The time period that is considered is defined in Section 4.2.8.

Table 5.2 shows the trend, the annual amplitude, and the semiannual amplitude derived from GRACE(-FO) and Swarm. Considering GRACE(-FO) as the truth, Swarm can almost always detect if the mass is increasing or decreasing in a certain region (i.e. the trends have the same sign). This is also confirmed when looking back at the trend maps in Figure 5.7 (a, b). Interestingly, GRACE(-FO) detects a positive trend of 0.2 mm/yr when averaging all land regions, while Swarm sees a negative trend of −0.3 mm/yr. However, these are both very small absolute values with a difference of only 0.5 mm/yr. In the second half of 2020, Swarm underestimates continental mass,

leading to a smaller trend (Figure A.1). When comparing mass change trends for the ocean and land, one should keep in mind that these mass trends do not necessarily compensate each other, as for the ocean, a 300 km buffer zone is applied. The second region with a different arithmetic sign is the Mississippi basin, where Swarm underestimates mass change. Regions with a trend difference of below 1.0 mm/yr are the ocean, total land, Amazon, Lena, Yangtze, and Volga basins. Trends in East Antarctica, Congo, Nile, Greenland, West Antarctica, and Ganges basins are between 1.1 to 3.0 mm/yr and differences are larger than 3.0 mm/yr in the Mississippi, Murray-Darling, and Danube basins.

Annual amplitudes are sometimes overestimated and sometimes underestimated by Swarm, depending on the region. Areas with similar amplitudes (less than 1.0 mm difference) are the ocean (GRACE(-FO): 7.7 mm, Swarm: 8.5 mm), land (GRACE(-FO): 14.6 mm, Swarm: 15.6 mm), West Antarctica (GRACE(-FO): 3.8 mm, Swarm: 3.8 mm), and the Murray-Darling river basin (GRACE(-FO): 11.6 mm, Swarm: 11.1 mm). Differences of more than 10 mm can be found in the Amazon, Congo, Yangtze, and Danube basins. Yet, one should take the absolute amplitude into account when evaluating the differences. In the Amazon basin for example, where hydrological variations are dominant, the amplitude derived by GRACE(-FO) is 142.5 mm. Hence, a difference of 11.4 mm accounts for only 8.0 % of the total value.

In many regions, Swarm overestimates the semiannual amplitude, which was already observed in Figure 5.7 (e, f). When comparing the values of Table 5.2 to those of Figure 5.7 (e, f), it should be mentioned that in areas where noise is dominant in the semiannual signal (e.g., the ocean), periods can be alternating quickly, such that parts of what seems to be semiannual signal in the figure, cancels out when computing basin averages, as in the table. Only in West Antarctica and Greenland, GRACE(-FO) sees a larger semiannual signal than the annual signal, which is confirmed by Swarm. Additionally, for Swarm, the semiannual signal is larger in the Murray-Darling river basin. This is one of the smaller basins and has a very low SNR, as shown later, so Swarm estimates should be handled with caution.

	Region	Trend [mm/yr]		Annual Amp. [mm]		Semiannual Amp. [mm]	
		GRACE	Swarm	GRACE	Swarm	GRACE	Swarm
1	Ocean (excl. 300 km)	0.2	0.4	7.7	8.5	1.1	0.5
2	Land	0.2	-0.3	14.6	15.6	0.5	1.0
3	East Antarctica	-2.2	-1.0	5.9	7.6	4.0	3.0
4	Amazon	14.7	13.8	142.5	153.9	16.9	30.3
5	Congo	13.4	14.8	37.0	48.3	10.6	11.9
6	Mississippi	0.9	-2.7	43.6	50.3	7.4	14.6
7	Nile	10.7	13.5	53.4	51.4	2.2	17.2
8	Lena	5.2	4.9	29.8	26.7	13.3	7.6
9	Greenland	-43.6	-44.9	17.1	21.7	19.5	31.5
10	West Antarctica	-28.5	-26.7	3.8	3.8	6.6	8.0
11	Yangtze	-2.4	-1.7	42.2	28.7	6.9	8.0
12	Volga	-3.4	-4.0	56.0	62.8	7.7	9.5
13	Murray-Darling	-4.4	-10.5	11.6	11.1	2.4	14.4
14	Ganges	3.3	0.6	91.7	95.3	36.8	27.1
15	Danube	-7.9	-4.5	39.8	28.2	6.5	20.8

Table 5.2: Trend, annual, and semiannual amplitudes from GRACE(-FO) and Swarm in the 15 selected study regions (Figure 5.4). The considered time period is defined in Section 4.2.8.

In Table 5.3, standard deviation, RMSE, correlation, and SNR of GRACE(-FO) and Swarm are investigated. The first two columns show the standard deviation of the GRACE(-FO) and Swarm mass change time series. Regions with a high variability (as measured by GRACE(-FO)) are the Amazon basin (107.6 mm), West Antarctica (85.0 mm), Greenland (53.4 mm), and the Congo

basin (49.2 mm). Low variability is present in the ocean (5.4 mm), East Antarctica (7.6 mm), over land regions (10.1 mm), and in the Murray-Darling river basin (15.3 mm). In all investigated regions, the standard deviation computed from Swarm time series is higher than that derived from GRACE(-FO). This is due to the noise inherent in Swarm observations (Section 3.7).

Columns three and four present the standard deviation of the time series reduced by constant, trend, annual, and semiannual signal from GRACE(-FO). Regions with a high interannual signal are the Amazon basin (44.4 mm), Congo (28.8 mm), West Antarctica (25.3 mm), Ganges basin (24.3 mm), and the Mississippi region (22.8 mm). Again, the standard deviation derived from Swarm is always higher than that computed from GRACE(-FO). The best agreement can be found for the ocean (GRACE(-FO): 1.4 mm, Swarm: 2.3 mm) and the largest difference is identified in the Murray-Darling river basin (GRACE(-FO): 9.0 mm, Swarm: 43.3 mm).

The comparison of the standard deviations of the residual signal is similar to analyzing the RMSE of Swarm with respect to GRACE(-FO). Very low RMSE values are found for the ocean and total land (1.9 mm and 3.7 mm, respectively). This might be due to their large size, as noise cancels out when averaging over the whole region. A general relationship between RMSE and size can be detected: the regions in Table 5.3 are sorted by size and the RMSE tends to increase for the smaller regions. Only the Murray-Darling basin exhibits an exceptionally large RMSE of 41.1 mm.

Columns six and seven show the correlation of the full and the reduced signal. High correlations of the full signal can be found throughout almost all investigated regions. For the ocean, total land regions, Amazon, Congo, Greenland, West Antarctica, and Ganges basins the correlation between GRACE(-FO) and Swarm is higher than 90.0 %. The lowest correlations are found in East Antarctica (44.4 %) and the Murray-Darling river basin (51.6 %).

Naturally, the correlations are lower when reducing annual and semiannual variations from the total signal. Even beyond those scales, Swarm can detect mass changes with strong correlations in Greenland (97.3 %), Amazon (92.6 %), West Antarctica (92.6 %), Congo (83.5 %), and Nile basin (72.1 %). Keeping in mind that Swarm is not a dedicated gravity field mission, these are exceptionally good results.

The last column of Table 5.3 presents the SNR of the mass change time series derived from Swarm. The SNR is a measure of how much one should trust the solutions. If it is lower than 1.0, the noise is larger than the signal and one should handle the time series with caution. Generally, there are two factors, leading to a good SNR: (1) a high variability, i.e. a large signal in the time series and (2) low noise, which is often the case for large regions where noise cancels out in the basin average. The highest SNR of 5.2 is achieved for the Amazon basin. Both before-mentioned criteria are fulfilled: the Amazon basin is a region with an exceptionally high seasonal variability due to hydrological mass redistribution, leading to a strong signal. Additionally, it is one of the largest regions investigated in this thesis, which is an advantage when averaging over the basin. Furthermore, high SNR are found in Greenland (4.3), the ocean (2.9), total land regions (2.7), Yangtze basin (2.6), and Ganges basin (2.3). The advantage in the case of ocean and total land is the extremely large region, such that despite a rather low signal, a good SNR is achieved. The Ganges basin should also be highlighted: even though it has a small size of only approximately 1100 km $\times$ 900 km, Swarm is able to detect mass change quite reliably.

	Region	Std. [mm] Full signal		Std. [mm] Residual Signal		RMSE [mm]	Correlation [%] Full Signal	Reduced Signal	SNR
		GRACE	Swarm	GRACE	Swarm				
1	Ocean (excl. 300 km)	5.4	6.1	1.4	2.3	1.9	95.4	59.8	2.9
2	Land	10.1	11.1	2.4	4.1	3.7	95.8	58.7	2.7
3	East Antarctica	7.6	17.7	4.5	17.4	15.9	44.4	40.7	0.5
4	Amazon	107.6	116.8	44.4	49.7	20.7	98.7	92.6	5.2
5	Congo	49.2	60.3	28.8	36.9	26.4	91.1	83.5	1.9
6	Mississippi	37.8	44.0	22.8	28.5	24.2	83.3	56.1	1.6
7	Nile	45.2	53.2	19.4	34.5	28.4	84.4	72.1	1.6
8	Lena	25.8	32.3	7.2	24.8	25.1	73.7	54.7	1.0
9	Greenland	53.4	55.7	9.6	25.3	19.9	97.5	97.3	4.3
10	West Antarctica	85.0	89.1	25.3	32.7	20.7	92.7	92.6	2.6
11	Yangtze	36.6	37.0	18.0	32.6	27.8	72.4	53.4	1.3
12	Volga	41.2	53.8	15.1	32.7	30.6	84.5	50.0	1.3
13	Murray-Darling	15.3	47.2	9.0	43.3	41.1	51.6	49.1	0.4
14	Ganges	71.0	74.8	24.3	34.8	31.5	92.8	60.0	2.3
15	Danube	34.7	41.0	15.8	33.9	31.3	69.2	53.1	1.1

Table 5.3: Statistics of the mass change time series from GRACE(-FO) and Swarm in the 15 selected study regions (Figure 5.4). The denoted values include the standard deviation of the full and residual signal (constant, trend, annual, and semiannual signal from GRACE(-FO) is subtracted from GRACE(-FO) and Swarm), the RMSE of Swarm with respect to GRACE(-FO), the correlation of full and reduced signal as well as the SNR. The considered time period is defined in Section 4.2.8.

5.4.3 Closing Gaps with Swarm

One central question in this thesis is, whether it is possible to maintain a continuous time series of mass change with Swarm, even when dedicated gravity field missions are not available. This issue of course gained special importance due to the 11-months gap between GRACE and GRACE-FO. The following analysis can however be applied to any time before or after GRACE(-FO), as long as kinematic orbits of a LEO satellite mission are available. The key is to find out if it is more reliable to interpolate between existing GRACE(-FO) solutions or to use time-variable gravity fields derived from kinematic orbits as a gap-filler.

As discussed in Richter et al. (2021), one way to find this out is to assume an artificial gap in a time series of basin averaged mass change, even when GRACE(-FO) data is available. The remaining GRACE(-FO) data (excluding the gap) can then be used to estimate a six-parameter model consisting of a constant, a trend, two annual, and two semiannual terms. In a next step, the model is evaluated during the gap and compared to the real GRACE(-FO) data. The RMS of the difference is a measure of how good the model fits the real data. Additionally, the RMS is computed between the difference of GRACE(-FO) and Swarm data during the gap. Generally, the method (i.e. interpolation vs. Swarm) with the lower RMS is the one that fits better.

In Figure 5.17 the above mentioned strategy is evaluated for the 15 study regions. The first 11-month gap is assumed for April 2002 to March 2013 and is then shifted subsequently through the whole GRACE(-FO) time period until April 2020 to March 2021. The RMS of the interpolation vs. real data is plotted for the mid-point of each gap period, i.e. September 2002 to September 2020. The evaluation is only carried out if at least 50 % of the assumed gap is available in reality (at least 6 months for an 11-months gap). The quality of the six-parameter model fit depends on the real mass change during the gap. If mass change is what could be expected from the model (i.e. no inter-annual changes) then the model will probably be a good estimate. In case there is an exceptional mass change, like droughts, floods or ENSO events, the model might not be able to represent this development. In case of a real gap, one of course simply does not know what is

happening in reality. Therefore, the maximum RMS of the artificial-gap-method from 2002-2021 is anticipated as an error for the six-parameter model. The performance of Swarm is independent of the real mass change and the overall quality can be estimated as the mean of all RMSEs of the 11-months gaps. Swarm data before May 2015 is not considered, as the lower quality (Section 3.7) would not be representative for a future gap or the real GRACE-GRACE-FO gap. Summarized, as a rule of thumb, one can say that if

$$\max\left(\mathrm{RMS}\left(\mathrm{GRACE}-\mathrm{Model}\right)\right) > \mathrm{mean}\left(\mathrm{RMS}\left(\mathrm{GRACE}-\mathrm{Swarm}\right)\right), \tag{5.4.1}$$

then Swarm is the better choice to fill a gap. This is the case for all investigated regions. Hence, Swarm should be preferred due to its independence from previous or subsequent existing data.

A closer look at Figure 5.17 allows for further analysis. The RMS of the interpolated model is generally lower over the ocean than for other regions. On the one hand this can be attributed to the generally low signal and on the other hand, the six-parameter model approximates the real mass change well. However, there are two peaks in the RMS time series, which can be related to El Niño and La Niña events. According to Boening et al. (2012), the 2011 La Niña led to a drop of ocean mass of 5 mm EWH or 1800 Gt. The six-parameter model is not able to detect this anomaly. The opposite effect can be observed for El Niño events where a rainfall excess over oceans and rainfall deficit over land is common (Cazenave et al., 2012). This is the case in 2015/2016, where a strong El Niño again led to a high RMS. At this time, Swarm gravity fields are already available and one can see that the artificial gap in 2015/2016 can be closed much better as compared to the six-parameter model (Swarm: RMS: 2.7 mm, six-parameter model: RMS: 5.9 mm). During the GRACE-FO period there are no exceptional deviations from the six-parameter model and both gap-closing methods perform equally. Hence, this means that Swarm should be preferred, because even in quiet times, Swarm can compete against the interpolation method and in times with strong inter-annual change, the interpolation model is clearly inferior.

In the Amazon basin, the 2015/2016 El Niño led to an extraordinary rainfall deficit (Jiménez-Muñoz et al., 2016), as was already observed in Figure 5.13. The six-parameter model is not able to reconstruct this drop, resulting in an RMS of 121 mm. Swarm, on the other hand, is able to detect this anomaly with an RMS of only 21 mm. Even the direct comparison of each gap suggests that Swarm is a better choice to close the gap.

Greenland experienced an extraordinary hot summer in 2012 (Velicogna et al., 2020), resulting in a low performance of the six-parameter model (RMS: 80.6 mm). At this time, Swarm was not launched yet, but based on its current performance, it would have been a better choice to close the gap than the interpolation model (mean RMS: 18.1 mm). A similar situation is present during the start of the GRACE-FO period. Due to two cold summers in 2017 and 2018 snow accumulated in Greenland leading to an RMS of the model of 67.5 mm. Swarm is clearly superior with an RMS of 11.0 mm. Hence, Swarm should be preferred to close gaps, because it is provides independent information and is reliable, even in case of unforeseeable events.

East Antarctica and the Murray-Darling basin are the only two regions with a SNR lower than 1. In these areas, the direct comparison of the RMS for each artificial gap reveals a better performance of the six-parameter model compared to Swarm. However, when following Equation (5.4.1), Swarm should still be preferred as a gap-filler. In the Murray-Darling basin, this is due to the development of the RMS of the model with respect to real GRACE(-FO) data. Generally, the RMS is around 20 mm. In 2010 and 2011, strong rainfall events in the Murray-Darling basin led to an accumulation of mass (Schumacher et al., 2018), which cannot be captured by the six-parameter model and thus lead to a large error (RMS of 61 mm). From what we know of Swarm (mean RMS of 39 mm), it would have been able to detect the rainfall event more reliably than the interpolation of GRACE data.

Summarized, a gap in a mass change time series can be filled with Swarm data with better skills than with an interpolation of GRACE(-FO) data. This statement is based on the assumption that one does not know what happens during the gap and extraordinary mass redistribution, as observed

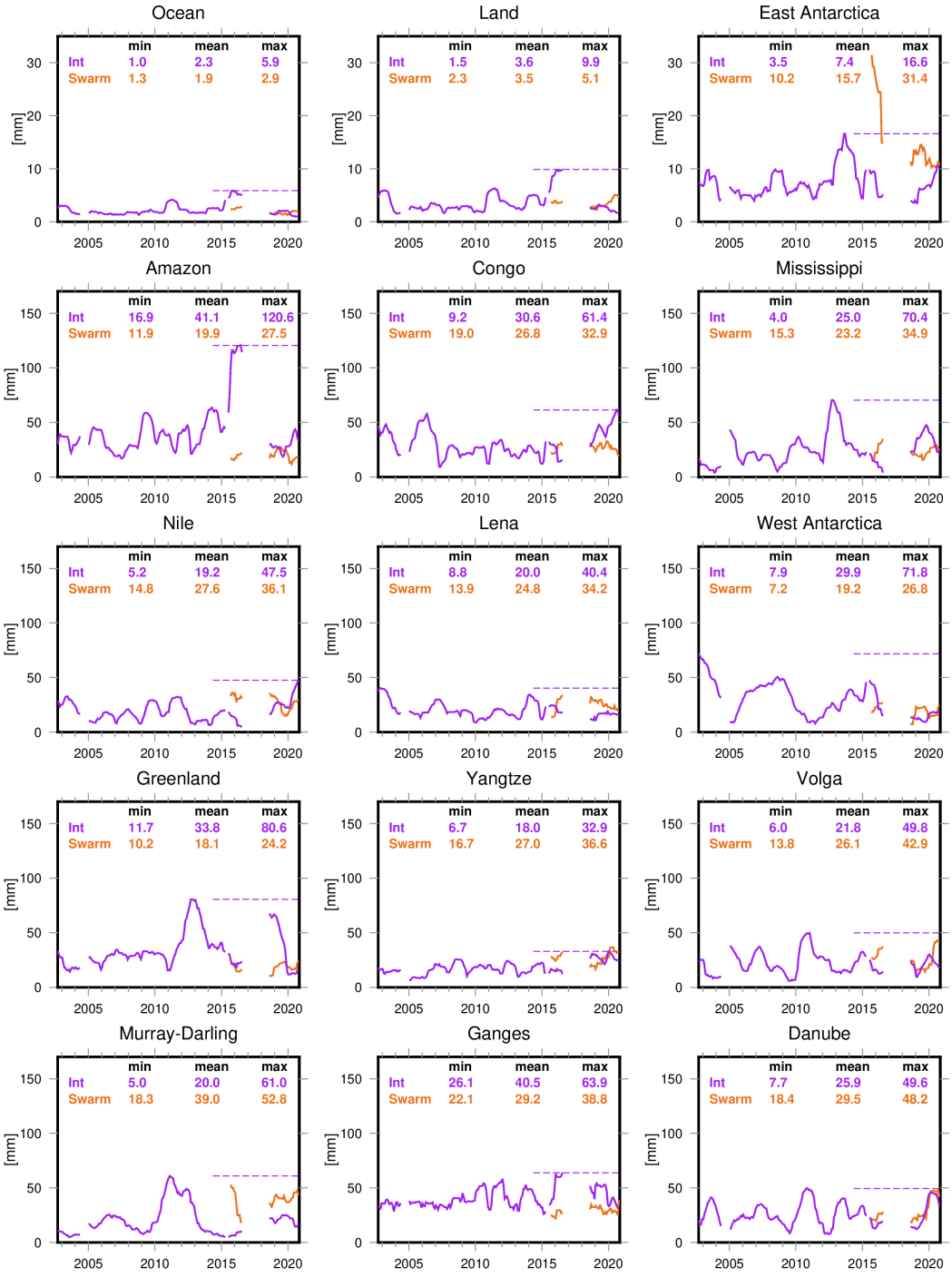

Figure 5.17: Comparison of gap-closing strategies: interpolating GRACE(-FO) vs. Swarm. For the analysis, an artificial 11-month gap is assumed in the GRACE(-FO) mass change time series. It is shifted through the GRACE(-FO) time series and the gap is filled by interpolation of the remaining GRACE(-FO) data (assuming a six-parameter model consisting of constant, trend, annual, and semiannual terms). Furthermore, the gap is filled with Swarm data, starting from May 2015. For each 11-months gap, the RMSE with respect to the real GRACE(-FO) data is computed and plotted for the mid-point of the gap. The maximum RMSE of the interpolation method is indicated with a dotted line for comparisons with Swarm.

in the past, is taken into account. Further analyses show that Swarm even has the potential to fill shorter gaps and should be preferred to a six-parameter interpolation model when unforeseeable mass change cannot be ruled out.

Chapter 6

Sea Level Inversion

Sea level varies due to complex interactions within the Earth system. Nowadays, it is indisputable that global mean sea level is rising. Several studies prove that the rate of sea level rise has been higher than 3 mm/yr during the last decades. The exact value depends on the individual study and the considered time frame (e.g., 3.3 mm/yr from 1994 to 2002 (Cazenave et al., 2014), 3.2 mm/yr from 1993 to 2010 (Church et al., 2013), 3.3 mm/yr from 2003 to 2011 (Cazenave et al., 2014), 3.35 mm/yr from 1993 to 2017 (Ablain et al., 2019)). However, sea level does not rise uniformly, as is investigated in e.g. Slangen et al. (2014) and Jevrejeva et al. (2014). Rietbroek et al. (2016) investigate the time period from April 2002 to June 2014 and find that some regions experience a very strong rise (e.g., 14.7 mm/yr in the Philippines), while others even have a negative trend (e.g., −1.4 mm/yr in the Central Pacific).

The sea level inversion helps to understand complicated processes that lead to sea level change. The original framework has been developed by Roelof Rietbroek at IGG (Rietbroek et al., 2012; Rietbroek, 2014; Rietbroek et al., 2016) and has been further refined and updated during the last years by my colleague Bernd Uebbing (Uebbing et al., 2019). Different from "direct" approaches to partitioning sea level, the inversion framework seeks a least squares fit of both space gravimetric and altimetric data sets without prescribing any data as the "truth".

The basic idea of the sea level inversion is to split sea level change into its different components. This helps to better understand the consequences of the individual contributions, such as the melting of Greenland, Antarctica, and glaciers or hydrological and steric changes. Furthermore, the identification of the main drivers and their current contributions is useful to constrain predicted sea level change.

In previous chapters it was shown that Swarm data can be useful for assessing ocean mass changes. Therefore, in this thesis, I present first efforts of including time-variable gravity fields from Swarm into the inversion framework. In this way, results are obtained, even when no GRACE(-FO) data is available. The challenge is to adapt the program to the lower spatial resolution of Swarm, as will be explained in the course of this chapter.

6.1 Methodology of the Sea Level Inversion

The sea level inversion splits sea level change into individual drivers. If the sea level budget was perfectly closed, the sum of all contributions would equal measurements of total sea level. Closing the budget is a current topic of investigation in many global and regional studies (e.g., Rietbroek et al., 2016; Frederikse et al., 2016; WCRP, 2018).

The basic principle of the sea level inversion is illustrated in Figure 6.1. For each contributor, predefined time-invariant patterns, the so called *fingerprints* (more details concerning the fingerprints in Section 6.1.1) are fitted to observed gravity and altimetry observations.

In a least squares adjustment, the time variability of the patterns is estimated in terms of monthly

scaling factors. While altimetry observes the sum of steric and mass-related changes, GRACE(-FO) and Swarm are only sensitive to mass-driven variations, thus enabling the separation of the two effects. Multiplying all N fingerprints with the estimated corresponding time series results in monthly gridded sea level change. The major part of sea level variations can be represented with this method, such that only small residuals $\mathbf{e}$ remain. $\mathbf{e}$ can be obtained by subtracting the sum of all contributions from total sea level observed by altimetry. If the sea level budget was perfectly closed, the residuals would equal zero.

In order to investigate individual contributions, only a subset of $\overline{N}$ patterns can be multiplied with the corresponding scaling factors and summed up. For example, the influence of hydrological variations could be investigated or the sum of all mass-related contributions.

If not mentioned otherwise, the following explanations are based on Rietbroek (2014).

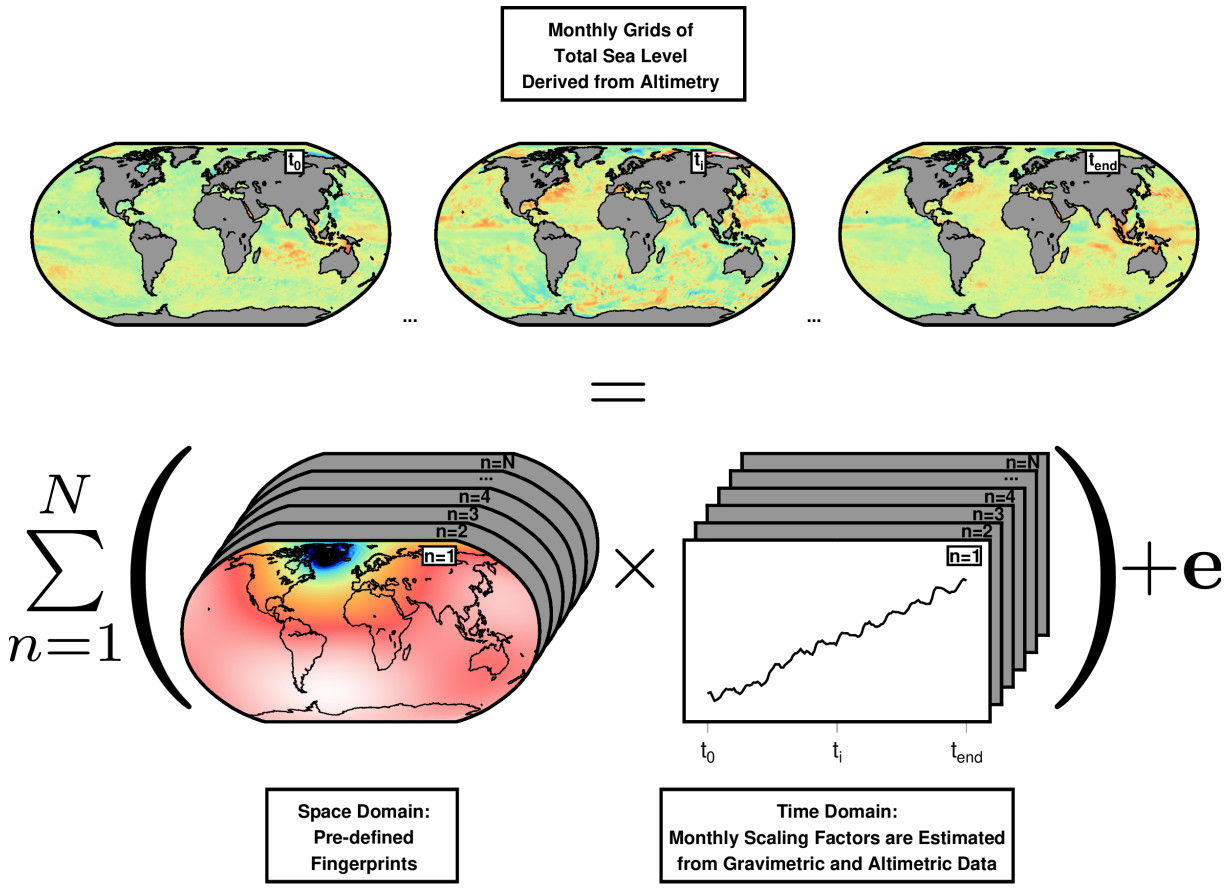

Figure 6.1: Schematic representation of the fingerprint inversion based on Rietbroek (2014). Total sea level change is represented by multiplying time-variable scaling factors to predefined spatial patterns.

6.1.1 Fingerprints

Fingerprints are a set of basis functions or "patterns" in the spatial domain. They represent the change of sea level due to geophysical signals of different origins. Fingerprints are derived from auxiliary data, such as models. The exact definition of the fingerprints used in the current IGG sea level inversion will soon be published in the Ph.D. thesis of Bernd Uebbing and will shortly be described in the following paragraphs. When I refer to the current GRACE(-FO) sea level inversion framework, it will be denoted as GRACE-only$_{\text{allFP}}$. Generally, one can distinguish between mass-related and steric fingerprints.

Mass-Related Fingerprints

Mass-related fingerprints are derived from prescribed surface loads. These are attributed to the melting of Greenland, Antarctica, and glaciers as well as hydrological mass redistribution. Summarized, hydrological fingerprints are derived from a **P**rincipal **C**omponent **A**nalysis (PCA) decomposition of the **W**aterGAP **G**lobal **H**ydrological **M**odel (WGHM) (Döll et al., 2003) and the surface load due to melting ice is considered for individual sub-basins of Greenland and Antarctica, while glaciers are combined to clusters.

However, these fingerprints have been derived for the use of GRACE data. The spatial resolution of Swarm is lower and the considered surface loads are too small to be detected with Swarm. Therefore, the fingerprints are adapted in this thesis: Based on the GRACE-only$_{\text{allFP}}$ inversion results, a set of four fingerprints for Antarctica, Greenland, and land glaciers is derived, respectively. They are computed by fitting a six-parameter model, including constant (C), trend (T), annual (A), and semiannual (S) signals to the GRACE inversion results. The fingerprints and their corresponding scaling factors are shown in Section 6.2. Furthermore, the first 10 EOFs of the WGHM are used, which describe the dominating spatial modes of hydrological mass variation and account for 80 % of the total hydrological variability.

The **S**ea **L**evel **E**quation (SLE) is used to transform the prescribed surface load into corresponding sea level change. It describes the spatial redistribution of sea level due to mass variations within the Earth system (Farrell and Clark, 1976). One example would be the melting of the Greenland ice sheet: Melting ice is not distributed uniformly over the whole ocean. Instead, sea level drops close to the coast of Greenland and rises further away from it. This is due to the reduced gravitational pull of the ice mass (as parts of it are melting), such that less water accumulates close to the attracting mass. Secondly, relative sea level drops in the vicinity of the ice mass loss, as the continents experience an uplift when ice is melting and flowing into the ocean. Hence, each mass distribution on Earth can be related to a specific pattern of sea level change with the help of the SLE. In its most basic form, it reads

$$S(\lambda,\theta,t) = T(\lambda,\theta,t) - H(\lambda,\theta,t), \tag{6.1.1}$$

where S denotes the relative sea level change. It can be computed by subtracting the continental surface load H from the total surface load T (both expressed in m EWH). The detailed version of the SLE is given by

$$\begin{aligned} S(\lambda,\theta,t) =& O(\lambda,\theta) \int_{\Omega} G_{N-U}(\alpha-\alpha') \left[S(\lambda',\theta',t) + H(\lambda',\theta',t)\right] d\omega' \\ &+ \frac{\Lambda_{N-U}(S,H,\lambda,\theta)}{g} + \frac{\Delta\phi}{g}. \end{aligned} \tag{6.1.2}$$

To compute sea level change at a specific location (λ,θ) at time t, two effects are considered in the integral: (1) the influence of a continental surface load (H) at position (λ',θ') on sea level change as well as (2) the influence of self-gravitating oceans (S) at position (λ',θ'). The integral is computed over the whole sphere Ω. The total surface load is convolved with Green's function ($G_{N-U}(\alpha-\alpha')$), which describes the influence of a point mass at location (λ',θ') on sea level change at (λ,θ) (i.e. at spherical distance $(\alpha-\alpha')$). The Green's function accounts for the elastic deformation of the Earth (Farrell, 1972). The ocean function $O(\lambda,\theta)$

$$O(\lambda,\theta) = \begin{cases} 1 & \text{over the ocean,} \\ 0 & \text{over land} \end{cases} \tag{6.1.3}$$

ensures that only ocean regions are considered.

Surface load changes induce changes in the Earth's moment of inertia tensor. The resulting centrifugal effect is considered by the term including Λ_{N-U}. The potential difference with respect to

the geoid is $\Delta\phi$. Hence, the last term $\left(\frac{\Delta\phi}{g}\right)$ ensures mass conservation (where g denotes the mean gravitational potential of the Earth) and the sea surface can be considered as an equipotential surface, even after the change of surface load. It is important to understand that mass-related fingerprints computed in this way will account only for the "passive" response of the ocean to the modified gravitational pull and elastic loading; i.e. dynamic variations due to e.g. freshwater inflow (which modifies current systems) are not accounted for and will show up in the residual.

Steric Fingerprints

Steric fingerprints are derived from gridded **O**cean **Re**A**n**alysis **S**ystem (ORAS)5 model data. The model is decomposed into EOFs using PCA. Here, I use the 20 dominant patterns. They describe the main spatial modes of thermosteric and halosteric sea level variability and account for about 70 % of the total steric signal.

Investigated Sets of Fingerprints

In this thesis, I present first experiments of including Swarm data into the sea level inversion framework with different sets of fingerprints. In all inversion runs, altimetry data and either GRACE(-FO), Swarm or both are used. The following scenarios will be considered:

- **allFP**: All fingerprints of the current GRACE-only$_{\text{allFP}}$ sea level inversion
- **merged**: the Greenland and Antarctica fingerprints of the GRACE-only$_{\text{allFP}}$ are merged into one fingerprint, each; glaciers are combined to 18 clusters
- **Ctas**: Only the constant parameter of a six-parameter model is used for glacier, Greenland, and Antarctica fingerprints
- **CTas**: Constant and trend parameters of a six-parameter model are used for glacier, Greenland, and Antarctica fingerprints
- **CTAS**: Constant, trend, annual, and semiannual parameters of a six-parameter model are used for glacier, Greenland, and Antarctica fingerprints

In all versions, except for "allFP", 10 WGHM fingerprints and 20 steric fingerprints are used. The GRACE-only$_{\text{allFP}}$ sea level inversion is used as a reference, when investigating different experiments.

6.1.2 Observation Equations

In the current GRACE-only$_{\text{allFP}}$ version of the sea level inversion framework, gravimetric and altimetric data is used as input. Hence, there are two types of observation equations. The first one is related to the mass-driven components of sea level change (Equation (6.1.4)) and the second one is related to total sea level change (Equation (6.1.7)). Observation equations are built separately for each month.

Gravimetric Observation Equations

Monthly time-variable gravity fields serve as observations for the gravimetric part of the sea level inversion. In the current GRACE-only$_{\text{allFP}}$ inversion framework, the complete ITSG-Grace2018 normal equation systems up to d/o 120 (April 2002 to December 2020) are used as input. In this work, the IGG-Swarm monthly normal equation systems up to d/o 40 (Chapter 4) are included additionally.

Equation (6.1.4) presents the observation equation related to the mass-driven components of sea

level change

$$\begin{pmatrix} \Delta c_{20} \\ \Delta c_{21} \\ \Delta s_{21} \\ \vdots \\ \Delta s_{n_{max}n_{max}} \end{pmatrix} = \mathbf{A}\mathbf{x}_{mass} + \mathbf{e}. \tag{6.1.4}$$

On the left side, the changes of the Stokes' coefficients (with respect to a mean field) serve as (pseudo-)observations. The design matrix $\mathbf{A}$ contains the mass-related fingerprints expressed in terms of Stokes coefficients in its columns. The NEQ system is transformed into the solution space defined by the fingerprints

$$\begin{aligned} \overline{\mathbf{N}} &= \mathbf{A}^T\mathbf{N}\mathbf{A}, \\ \overline{\mathbf{n}} &= \mathbf{A}^T\mathbf{n}, \\ \overline{\mathbf{e}^T\mathbf{P}\mathbf{e}} &= \mathbf{e}^T\mathbf{P}\mathbf{e}. \end{aligned} \tag{6.1.5}$$

In the above equation, $\mathbf{N}$ and $\mathbf{n}$ denote the original normal equation system from GRACE(-FO) or Swarm. After the transformation, one scaling factor for each mass-related fingerprint is estimated, which is contained in the vector $\mathbf{x}_{mass}$. Finally, $\mathbf{e}$ denotes the residuals and the system can be solved by

$$\hat{\mathbf{x}}_{mass} = \overline{\mathbf{N}}^{-1}\overline{\mathbf{n}}. \tag{6.1.6}$$

Altimetric Observation Equations

Satellite altimeters measure the distance to the sea surface and thus deliver the sea surface height with respect to a reference ellipsoid (Section 2.4). Originally, the fingerprint inversion used Jason-1 and Jason-2 along-track data. As, meanwhile, GRACE-FO and IGG-Swarm data is available, altimetry data now also includes Jason-3. 1 Hz along-track data from the **R**adar **A**ltimeter **D**atabase **S**ystem (RADS) (Scharroo et al., 2013) is used to compute sea level anomalies Δh_i (i.e. sea surface height with respect to a mean sea surface).

The observation equation for altimetry data is constructed as follows:

$$\begin{pmatrix} \Delta h_1 \\ \Delta h_2 \\ \vdots \\ \Delta h_M \end{pmatrix} = \mathbf{Y}\mathbf{C}\mathbf{x}_{mass} + \mathbf{K}\mathbf{D}\mathbf{x}_{ster} + \mathbf{e}. \tag{6.1.7}$$

The unknowns are the mass-related ($\mathbf{x}_{mass}$) and steric ($\mathbf{x}_{ster}$) scaling factors for the corresponding predefined fingerprints. Matrices $\mathbf{C}$ and $\mathbf{D}$ contain the fingerprints expressed in terms of geocentric sea level. $\mathbf{Y}$ and $\mathbf{K}$ map the patterns onto the altimeter tracks.

6.2 Results of the Sea Level Inversion

In the following, Swarm inversion results will be discussed and compared to the current GRACE-only$_{\text{allFP}}$ inversion. If not stated otherwise, the Swarm-only$_{\text{CTas}}$ solution is chosen. Figures 6.4 to 6.6 show the reason for this choice.

Fingerprints and Corresponding Scaling Factors

Figure 6.2 presents the CTas fingerprints related to the melting of Glaciers, Greenland, and Antarctica, together with their corresponding scaling factors. The left column shows fingerprints, which need to be multiplied by scaling factor 1 (black) and the middle column shows sea level change,

which is multiplied by scaling factor 2 (orange). One can clearly see how the melting of ice contributes to global mean sea level rise. Moreover, the patterns show how sea level drops close to the actual loss of surface load, e.g. in Greenland and rises further away from it. Scaling factor 2 shows a dominant trend which could be expected, because the corresponding fingerprint was derived from the trend parameter (of a six-parameter model) of the GRACE-only$_{\text{allFP}}$ inversion results (Section 6.1.1). In addition to a linear trend, annual signals are visible, which are most prominent for land glaciers, followed by Greenland.

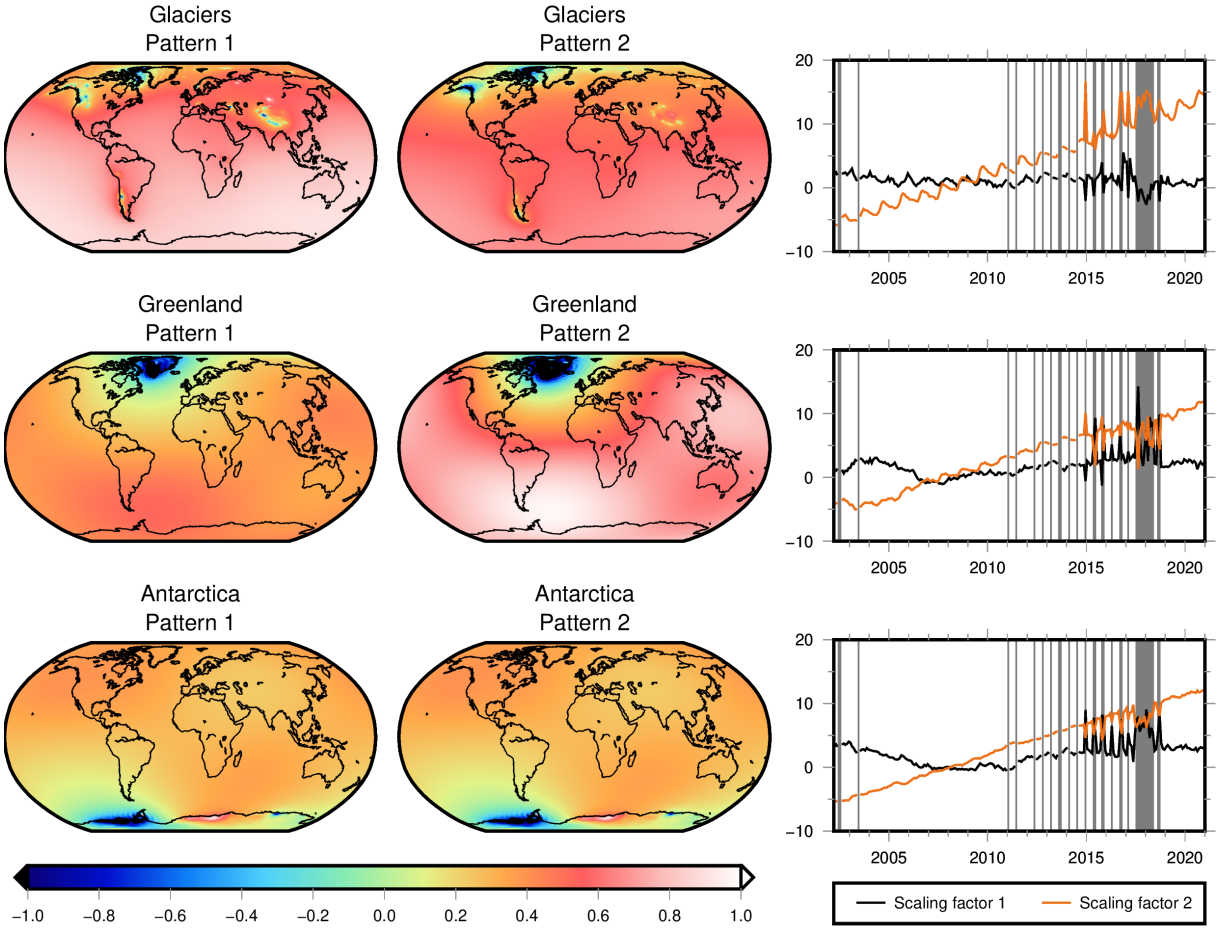

Figure 6.2: CTas fingerprints for land glaciers, Greenland, and Antarctica and their corresponding scaling factors. GRACE(-FO) gaps are highlighted in gray.

Comparing Mass-Related Sea Level Change from Inversion Results to the Direct Method

Figure 6.3 compares mass-related sea level change from different approaches. GRACE-only$_{\text{allFP}}$ and Swarm-only$_{\text{CTas}}$ are derived from the inversion. Swarm$_{\text{direct}}$ is computed from the IGG-Swarm gravity fields according to Section 5.4.2. It should be noted that Figure 6.3 only serves as a rough comparison, as two effects might lead to differences: (1) degree 1 is not included in the direct method, while the inverse approach solves implicitly for degree 1, as it is included in the fingerprints. (2) The 300 km buffer zone is only needed in the direct method to prevent land-ocean leakage effects.

While GRACE-only$_{\text{allFP}}$ is not available during GRACE(-FO) gaps, the other two solutions are continuously available, starting in August 2014. Generally, the direct method confirms the inversion results. It is closer to the GRACE-only$_{\text{allFP}}$ sea level inversion, especially during the GRACE-FO period, where Swarm-only$_{\text{CTas}}$ slightly underestimates mass-related sea level change. This underestimation during GRACE-FO times might be a result of the chosen fingerprints, which are currently derived from the GRACE period. The two peaks in the GRACE-only$_{\text{allFP}}$ in late 2016

and late 2019 are not reproduced by the other two methods. Thus, they are probably due to the lower quality of GRACE during its end-of-lifetime and GRACE-FO in its early months.

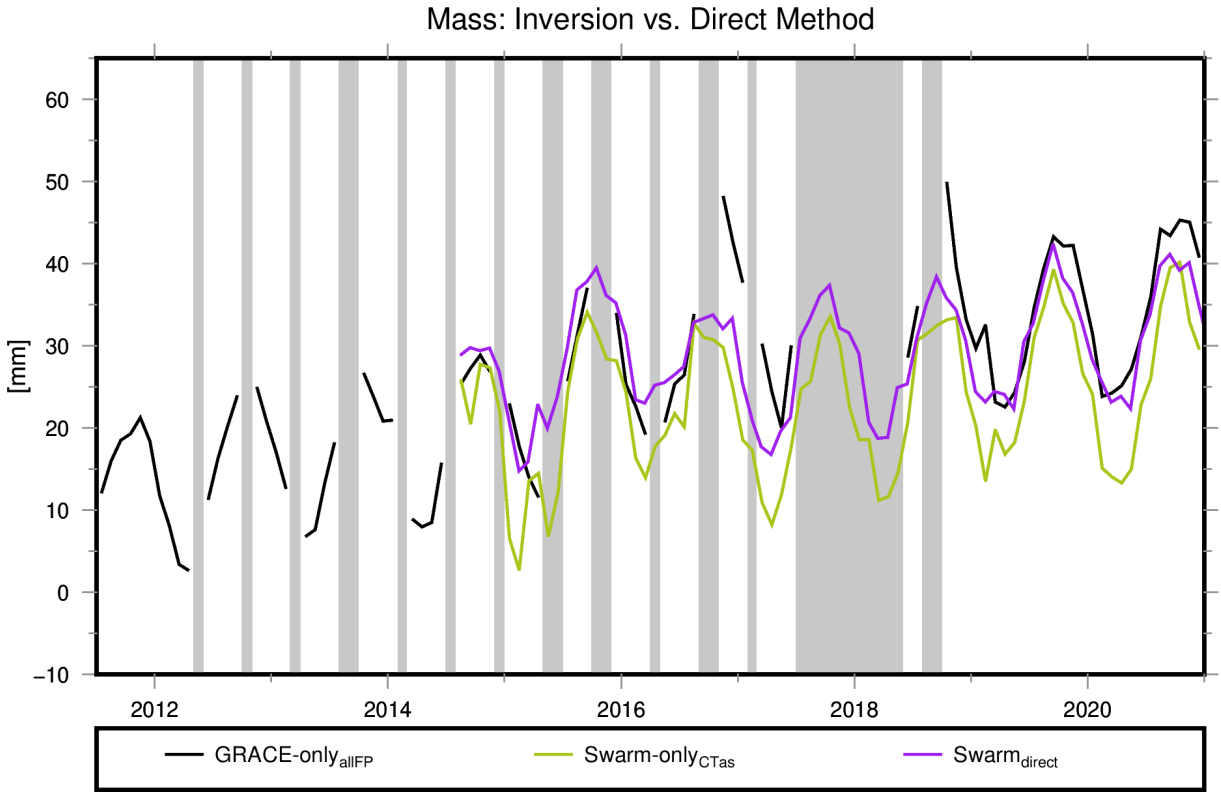

Figure 6.3: Comparing mass-related sea level change from the inversion and direct methods. GRACE(-FO) gaps are highlighted in gray.

Investigating Different Sets of Fingerprints in Terms of Global Mean Contributions to Sea Level Change

Figure 6.4 shows the contribution of the melting of the Greenland ice sheet to sea level change. Different parameterizations are investigated. As already explained, GRACE-only$_{allFP}$ can be considered as the ground-truth. It is obvious that Swarm-only$_{allFP}$ does not deliver reliable results. The fingerprints need to be adapted to the spatial resolution of Swarm and thus, their number should be reduced. The first choice was to merge Antarctic and Greenland fingerprints to obtain one fingerprint for each of them. Here, the combined GRACE+Swarm$_{merged}$ inversion result is shown. It seems that reasonable results are achieved during the GRACE(-FO) gaps, i.e. when Swarm is the only gravimetric mission. However, when GRACE(-FO) is available the time series shows large offsets. Later, it will be clear that GRACE+Swarm$_{merged}$ should not be trusted in general; the reason will be explained in the next paragraphs, when investigating Antarctic contributions.

Hence, the CTAS approach was developed in order to incorporate spatial patterns as determined by fitting a six-parameter model (constant, trend, annual, and semiannual parameters) to the much more reliable GRACE mission. In a first step, only constant and trend fingerprints (CTas) were used in a GRACE(-FO)-only inversion. During the GRACE period (starting from April 2002, which is not shown here) the resulting GRACE-only$_{CTas}$ time series is very close to the GRACE-only$_{allFP}$ sea level inversion and trends are reproduced well. This encourages further investigations as a reduced number of fingerprints seems to be able to describe sea level change due to the melting of the Greenland ice sheet well. In the GRACE-FO period, there is a slight offset between GRACE-only$_{allFP}$ and GRACE-only$_{CTas}$. This might be related to the fact that the CTas fingerprints are derived from GRACE data, such that mass redistribution from GRACE-FO can possibly not be fully represented by the spatial patterns. Swarm-only results from Ctas (only constant parameter of the

six-parameter model is utilized), CTas (constant and trend parameters of the six-parameter model are utilized) and CTAS (all parameters of the six-parameter model are utilized) fingerprints are similar. They are a bit more noisy, when compared to the GRACE-only$_{\text{CTas}}$ inversion, which could be expected. Still, they close the gap between the GRACE and GRACE-FO mission well.

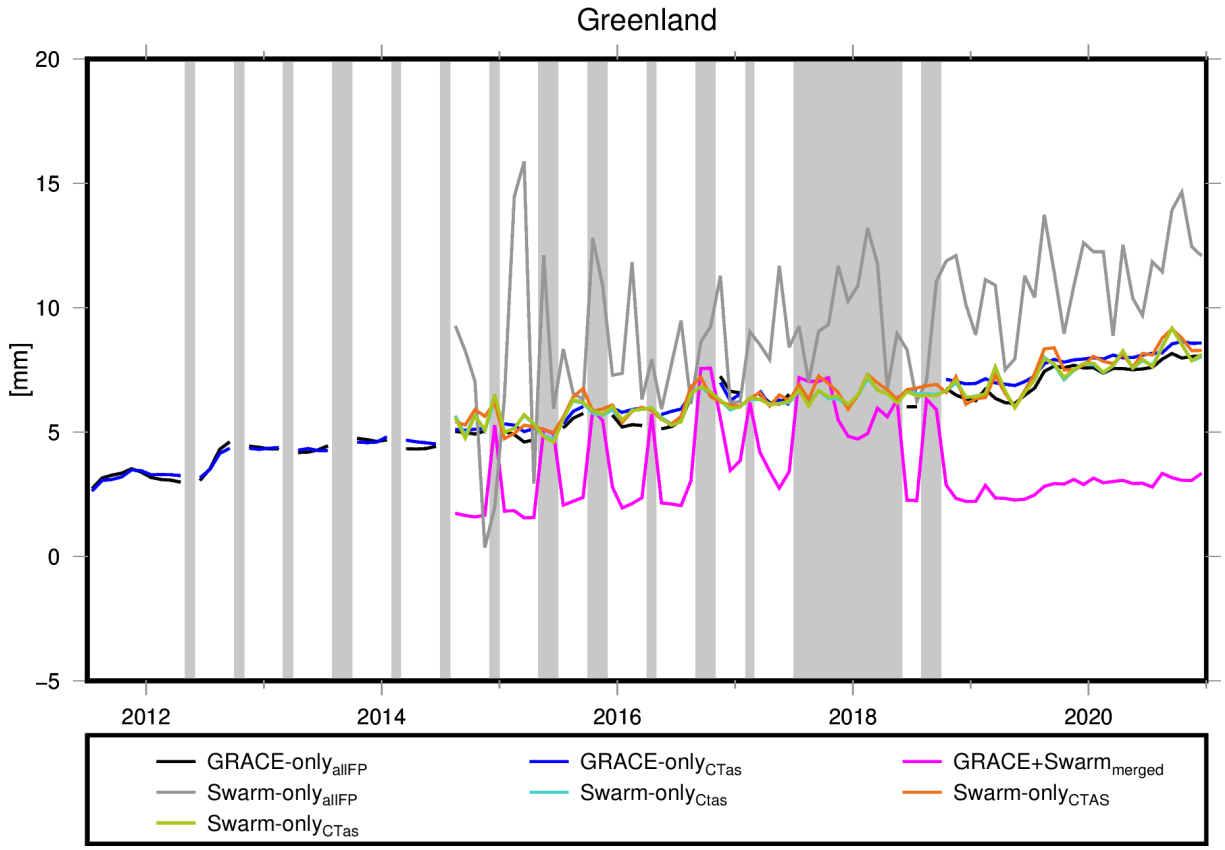

Figure 6.4: The contribution of the melting of the Greenland ice sheet to global mean sea level. Investigation of different parameterizations of the sea level inversion. GRACE(-FO) gaps are highlighted in gray.

The contribution of the Antarctic ice sheet to global mean sea level change is shown in Figure 6.5. Many observations concerning the results of Greenland are also true in Antarctica and I will only point out the main differences in the following. While GRACE+Swarm$_{\text{merged}}$ delivered reasonable results in Figure 6.4, when only Swarm was available, the solution is generally poor for Antarctic contributions, especially during the GRACE(-FO) gaps. CTAS shows large deviations to the GRACE-only$_{\text{allFP}}$ sea level inversion and is close to Swarm-only$_{\text{allFP}}$, indicating that too many fingerprints are used. CTas is the closest Swarm result, when compared to the GRACE-only$_{\text{allFP}}$ version, while Ctas shows a slight offset.

In Figure 6.6 the hydrological contribution to sea level change is investigated. A pronounced annual signal is detected by all investigated solutions. GRACE-only$_{\text{CTas}}$ is again very close to GRACE-only$_{\text{allFP}}$, but slightly underestimates hydrological contributions during the GRACE-FO period. In contrast, all Swarm-only solutions underestimate the hydrological contribution, when compared to GRACE-only$_{\text{allFP}}$. The reason for this behavior is still unclear and should be further investigated in future studies. It does not seem to be a general problem concerning the fingerprints, as both GRACE-only solutions perform well. It rather seems to be related to the generally lower quality of the Swarm time-variable gravity fields. When comparing the different Swarm-only solutions, considering constant and trend parameters in the fingerprints again leads to results closest to the GRACE-only$_{\text{allFP}}$ version. Hence, CTas is the version that will be investigated closer in the following.

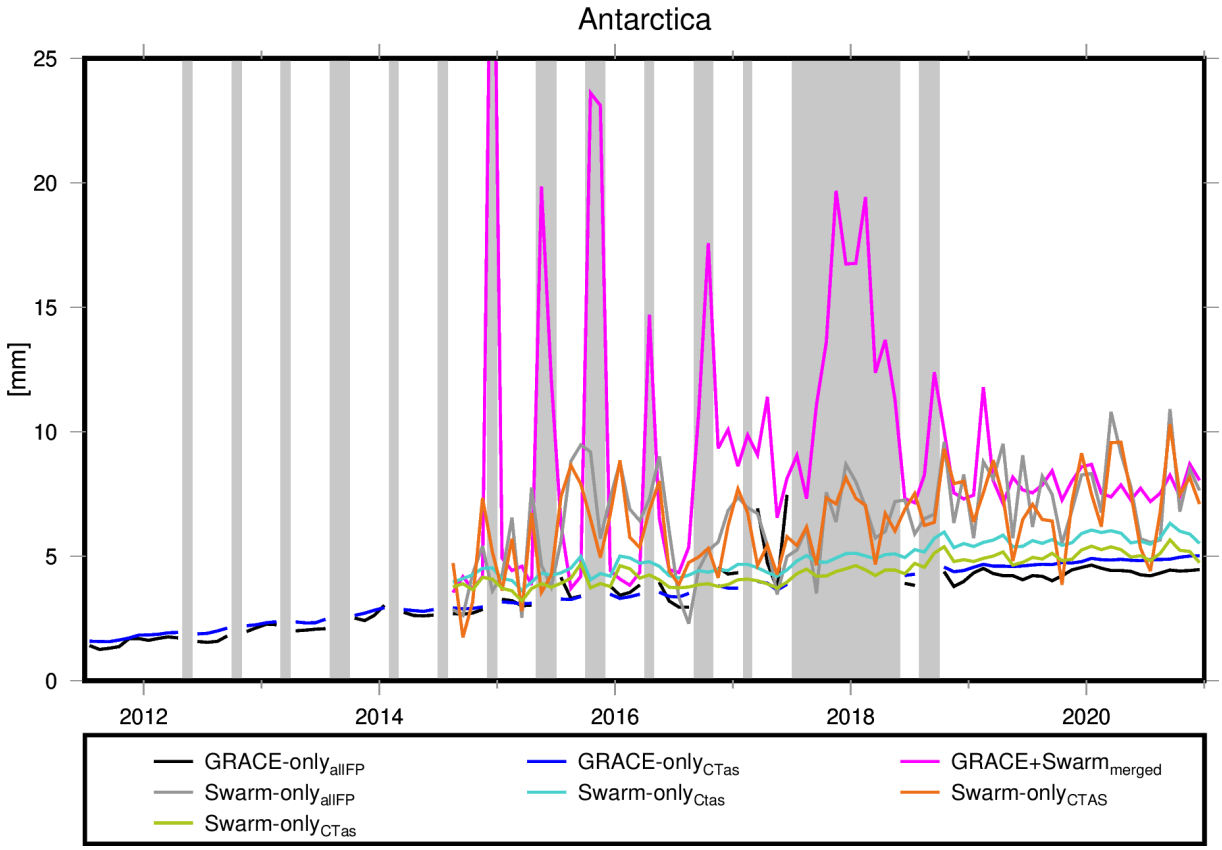

Figure 6.5: The contribution of the melting of the Antarctic ice sheet to global mean sea level. Investigation of different parameterizations of the sea level inversion. GRACE(-FO) gaps are highlighted in gray.

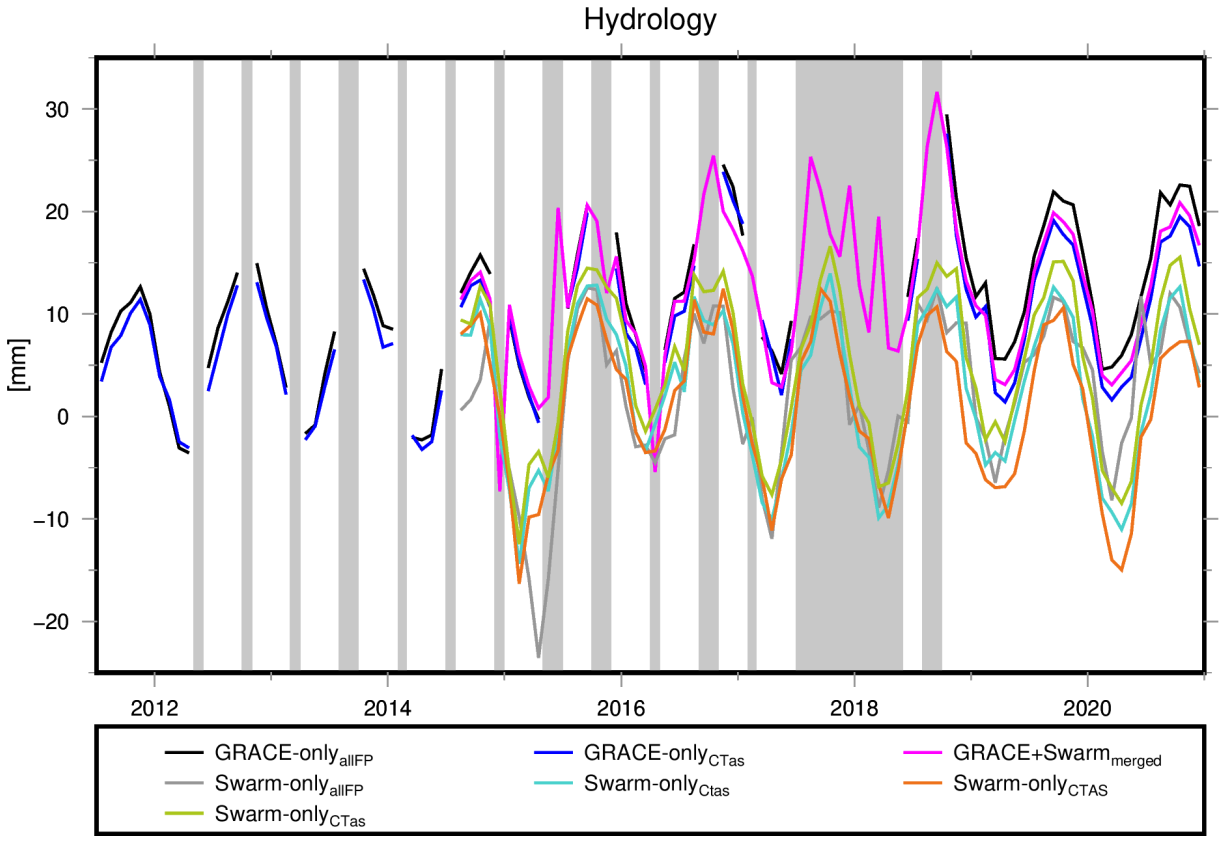

Figure 6.6: The contribution of hydrological mass redistribution to global mean sea level. Investigation of different parameterizations of the sea level inversion. GRACE(-FO) gaps are highlighted in gray.

Sea Level Budget from the CTas Fingerprints

In Figure 6.7 the individual contributions to sea level change derived from the CTas solution (constant and trend parameter of the six-parameter GRACE model are utilized) are presented and Table 6.1 shows the corresponding trends. GRACE, GRACE-FO, and Swarm are used as gravimetric input. Due to the lower quality of its gravity field solutions, Swarm does not have a significant influence on the combined solution, when GRACE or GRACE-FO are available. Hence, the combined solution is essentially almost equal to the GRACE-only solution and the gaps are filled with the Swarm-only results.

During the GRACE period, the CTas solution provides a trend of 2.9 mm/yr of total global mean sea level rise (subplot (a)). When GRACE-FO and Swarm are included in the analysis, the trend amounts to 3.0 mm/yr, indicating a stronger sea level rise during the past years. The drop in 2017/2018 is due to the hydrological contributions, which are underestimated by the Swarm-only solution during the GRACE-GRACE-FO gap.

Figure 6.7 (a) additionally shows the partitioning into mass-related and steric sea level change. Generally, mass-related change has a larger amplitude than steric change. In the beginning, both contributed mostly equally to sea level change. Over time, mass contributions experienced a stronger acceleration, such that their influence is larger by now. From the total investigating period, the trends amount to 1.9 mm/yr mass-related sea level rise and 1.0 mm/yr for steric changes. Again, the drop in 2017/2018 in the mass change time series is due to the underestimation of hydrological contributions by Swarm-only. When excluding Swarm data from the trend computation, the mass-related trend is slightly larger and amounts to 2.0 mm/yr.

Figure 6.7 (b) splits mass-related sea level change further into individual drivers. Hydrological mass redistributions have by far the largest amplitude. The melting of Greenland and land glaciers results in the largest trends of 0.6 mm/yr, each. Antarctica has a smaller trend of 0.4 mm/yr, followed by hydrology (0.3 mm/yr). Except for hydrology, the GRACE-GRACE-FO gap is closed well, which is also confirmed by the trend values in Table 6.1.

	GRACE	GRACE + GRACE-FO	GRACE + Swarm + GRACE-FO
Antarctica	0.3	0.4	0.4
Greenland	0.6	0.6	0.6
Glaciers	0.6	0.6	0.6
Hydrology	0.3	0.4	0.3
Mass	1.9	2.0	1.9
Steric	1.0	1.0	1.1
Total	2.9	3.0	3.0

Table 6.1: Trends [mm/yr] of individual sea level contributors of the CTas inversion solution. Three different time periods are considered: (1) GRACE period, ignoring the gaps, (2) GRACE and GRACE-FO period, ignoring the gaps, and (3) all available GRACE, GRACE-FO, and Swarm solutions (i.e. the gaps are filled with Swarm, starting in 2014).

Spatial Patterns of Sea Level Change

In Figure 6.8 total, steric, and mass related sea level trends are derived from different methods. All months between July 2015 and December 2020 have been considered in the analysis (except for subplot (h), where data is missing during the gaps of GRACE(-FO)). Figure 6.8 (a) and (b) show trends of total sea level change from the inversion with CTas fingerprints. In (a), GRACE, GRACE-FO and Swarm are combined, while in (b), the Swarm-only solution is presented. Both figures show similarities in wide areas. In most areas, sea level is rising. A pronounced pattern

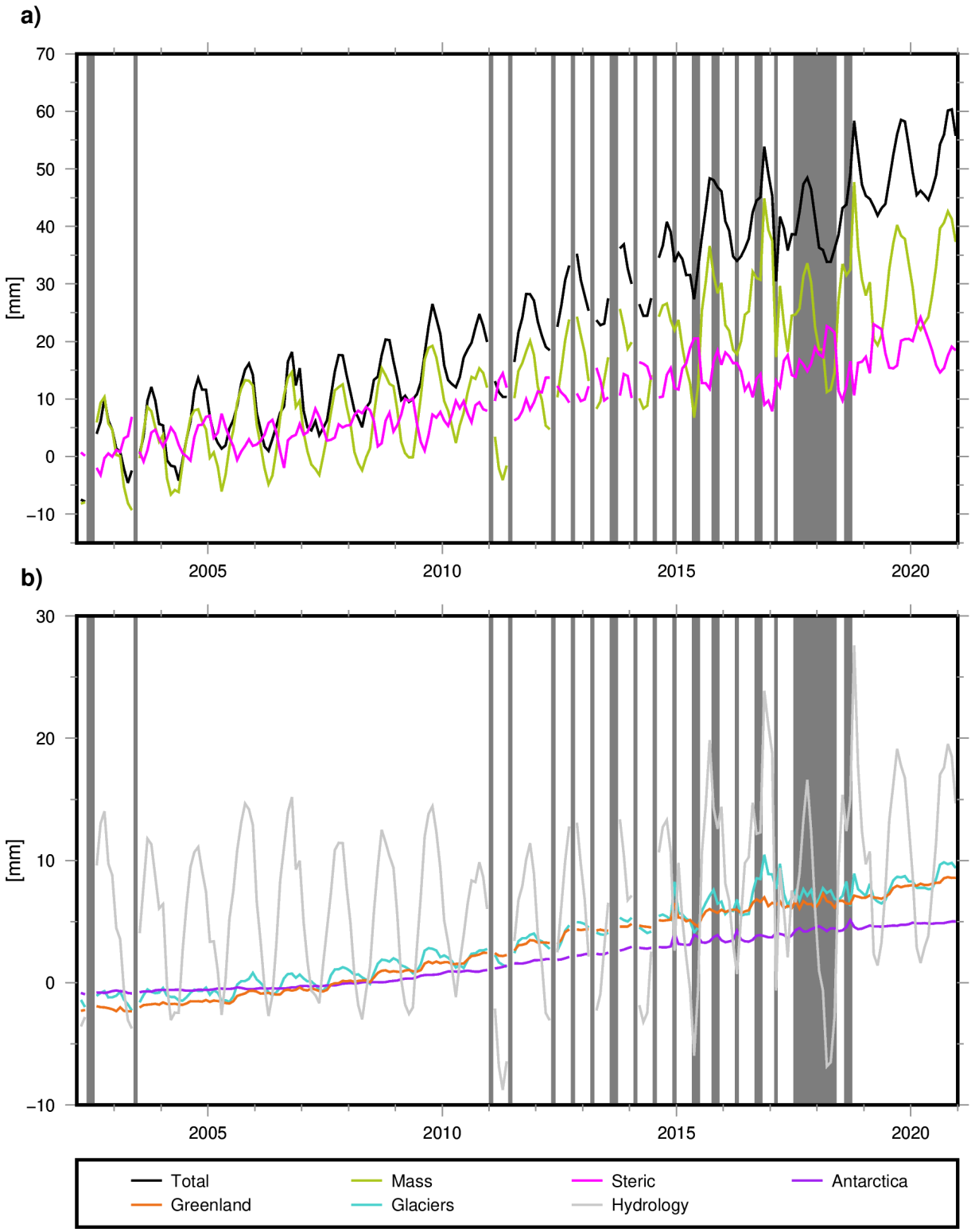

Figure 6.7: Components of total global mean sea level change as derived from the CTas inversion from altimetry, GRACE, GRACE-FO, and Swarm. a) Total, mass-related, and steric change. b) Individual drivers of mass-related sea level change. GRACE(-FO) gaps are highlighted in gray.

related to ENSO is visible in the Pacific Ocean. Differences can be detected in the northeast of Scandinavia and in parts of the Southern Ocean, where the Swarm-only inversion shows negative trends, while the combined solution points to a sea level rise. The reasons for the differences can be investigated in the remaining subplots.

In Figure 6.8 (c) and (d) only the steric part of the CTas solution is considered, again for the combined and the Swarm-only solution, respectively. Both maps look almost identical, because the altimetric observations and steric patterns are the same in the two versions. Mass-related trends are presented in subplots (e) to (h). The combined CTas solution (e), the Swarm-only CTas solution (f), and the combined solution with all current fingerprints (g) all show a mass accumulation in the Southern Ocean. (e) can be described as a smoothed version of (g), which is due to the reduced number of spatial patterns in combination with the same input data. (f) shows some differences due to the exclusive use of Swarm time-variable gravity fields, as for example strong mass loss north of West Antarctica. Figure 6.8 (h) shows the mass-related sea level trends derived from the direct method using GRACE(-FO) up to d/o 60 (compare Figure 5.7 (a), with a lower resolution). The direct method has a lower resolution, when compared to the inversion with all current fingerprints. This could be expected, as the inversion results are a linear combination of higher-resolution spatial patterns. One of the main differences is that the direct solution detects a mass loss in large parts of the Arctic Ocean and the northeastern Atlantic Ocean, where other methods see a mass gain.

Summarized, the ongoing work shows that it is possible to include Swarm time-variable gravity fields into the sea level inversion framework. Results can be obtained, even when GRACE(-FO) is not available. The Swarm-only$_{\mathrm{CTas}}$ version (with fingerprints derived from constant and trend parameters of a six-parameter model fitted to GRACE inversion results) is close to the current GRACE-only$_{\mathrm{allFP}}$ inversion result when investigating global mean sea level change. However, contributions from hydrology are underestimated by Swarm-only and thus distort total mass estimates. This problem could be investigated in future studies for an overall improvement of Swarm inversion results (Section 7.2). The integration of Swarm into the sea level inversion framework will facilitate future experiments of additionally including time-variable gravity fields derived from SLR data.

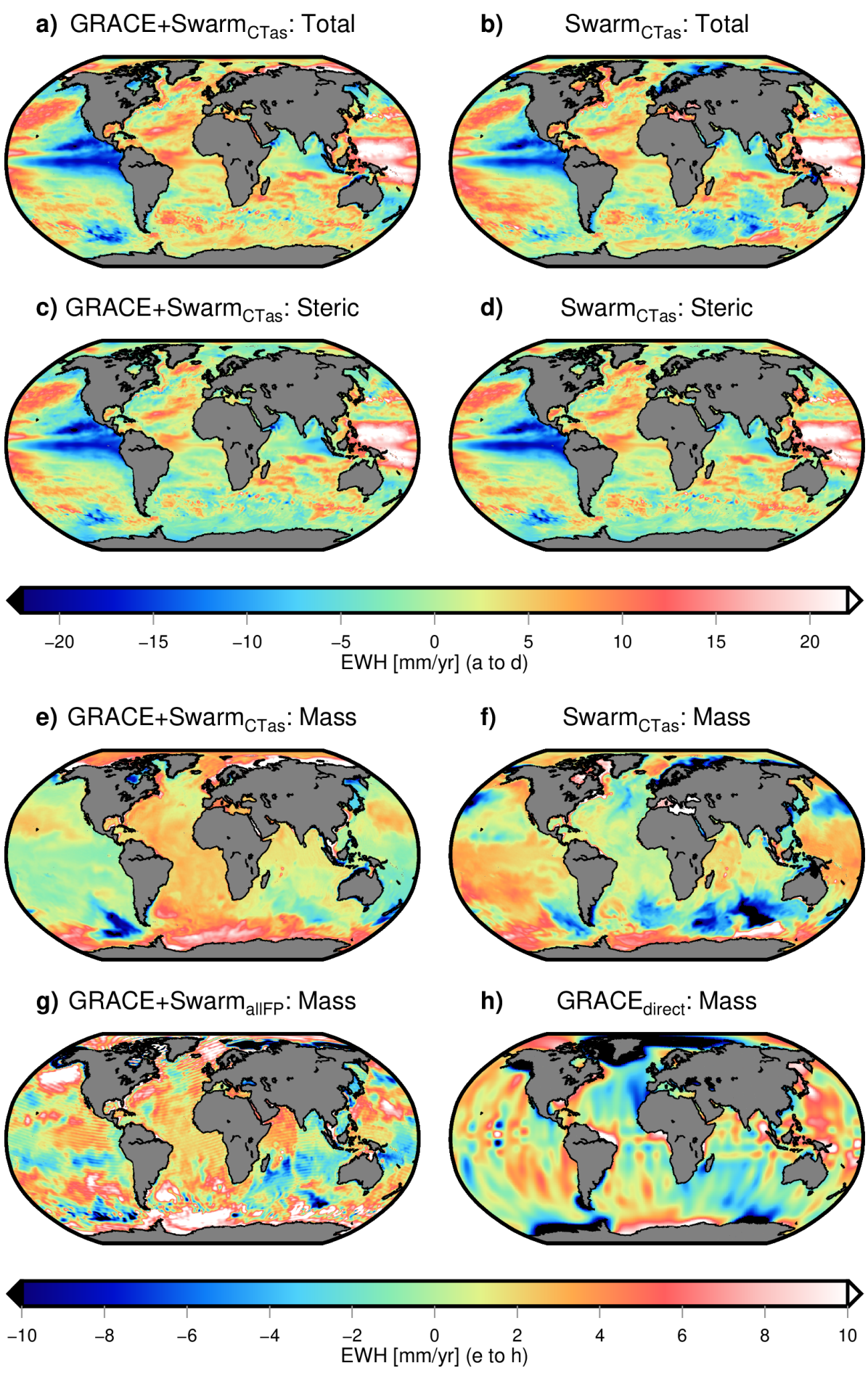

Figure 6.8: Total, steric, and mass-related sea level trends [mm/yr] derived from different methods. Time period: July 2015 to December 2020.

Chapter 7

Conclusions and Outlook

7.1 Conclusions

This thesis' aim was to derive time-variable gravity fields and corresponding large-scale mass change from data of the Swarm mission. The challenge is that Swarm has not been planned as a dedicated gravity field mission. While the main instrument of GRACE(-FO), the KBR system, provides precise inter-satellite measurements, the Swarm satellites only follow the principle of hl-SST. Thus, the quality of the Swarm gravity fields is restricted by the precision of the kinematic orbits. Moreover, the accelerometers on-board the satellites suffer from various errors and noise, such that most of the data cannot be used in gravity field retrieval.

In this work, I used the integral equation approach with short arcs to derive monthly time-variable gravity fields and large-scale mass redistribution from Swarm data. I investigated different parameterizations and assessed the quality of the results by comparing them to the more accurate GRACE(-FO) data during the overlap period. It was shown that Swarm is able to detect the long-wavelength part of the Earth's time-variable gravity field and can be used to fill the gap between GRACE and GRACE-FO.

As accelerometer data from Swarm cannot be used for gravity field retrieval (calibrated data only exists for Swarm C, along-track), I modeled aerodynamic accelerations, SRP, and ERP. When compared to the calibrated ACCCCAL_2_ product, the correlations were higher than 75 % for 80 % of the data. Modeled non-gravitational accelerations were introduced in the processing and treated in the same way as accelerometer data.

A large part of the unfiltered SH coefficients up to d/o 10 were correlated by more than 70 %, when compared to GRACE(-FO). The SNR of the individual Swarm SH coefficients was larger than one for the lower degrees. An analysis of the degree amplitudes confirmed these findings. Degree amplitudes from Swarm and GRACE(-FO) were comparable for degrees up to 10. Somewhere between degree 10-15 (depending on the investigated month) they started to diverge, as noise in the Swarm models becomes larger. Until May 2015, the lower performance of Swarm due to ionospheric disturbances could be identified well in the results.

A comparison of different Swarm gravity field products showed that the current IGG Swarm solution provides the best results. I additionally computed time-variable gravity fields from kinematic orbits of AIUB and found that they have a lower quality than those derived from IfG orbits. Furthermore, I compared my results to the official ESA EGF_SHA_2_ product, which is a combination of individual gravity models from different groups. The SNR of the individual SH degrees of this solution was lower compared to my results from July 2015 to December 2019. In the remaining time period, the quality was comparable to IGG results.

When converting the SH coefficients to gridded EWH, the results proved that Swarm is able to globally detect the major trends and annual signals that are observed by GRACE(-FO). The RMS reduction was positive for more than 90 % of the Earth's surface. The global RMSE with respect

to GRACE(-FO) was between 30 mm and 60 mm from July 2015 to March 2021. Swarm enabled the detection of global mean ocean mass change with an RMSE of 1.9 mm. Co-estimating non-gravitational accelerations instead of modeling them would downgrade the RMSE to 3.6 mm. Basin averages have been computed for areas as small as the Danube basin and showed that Swarm can determine trends and seasonal signals correctly in most regions. Moreover, the SNR was higher than one in all investigated regions except for East Antarctica and the Murray-Darling river basin. Generally, basin averages provide best results, when either the region is large and/or there is a high signal.

I showed that it is more reliable to fill the 11-months gap with data from the Swarm mission than to interpolate between existing GRACE and GRACE-FO data. It would not be possible to reconstruct extraordinary mass redistribution, like ENSO events, from GRACE(-FO) during a gap. Swarm is able to actually observe these changes, as the analysis revealed.

Preliminary results showed that it is possible to include Swarm in the sea level inversion framework. In this way, sea level could be split into individual components, even when GRACE(-FO) data is not available. Spatial patterns needed to be adapted, such that they matched the Swarm resolution. Hydrological contributions were found to be underestimated by Swarm, which should be investigated further.

7.2 Outlook

GNSS receivers are a common instrument on scientific satellite missions. Additionally, more and more commercial satellites are equipped with GNSS receivers. While Swarm can only track GPS signals, more recent missions are additionally able to process data from Galileo, GLONASS and BeiDou. The growing number of observations increases the interest in gravity field retrieval from hl-SST. This is especially important when no dedicated gravity field mission is available, but can also serve as an additional source of information. Hence, I provide ideas for future studies to improve the results of this thesis even further.

Extend Studies into the Past or Future, Using Additional LEO Satellite Missions

In this thesis, Swarm is used to derive time-variable gravity fields and large-scale mass redistribution from kinematic orbits in order to fill the gaps during the GRACE(-FO) record. The results are validated by comparing to GRACE and GRACE-FO data in the overlapping period. Additionally, Swarm serves as a demonstrator and the approach can easily be transferred to any other LEO satellite mission, as long as the kinematic orbits are available from GNSS measurements. Accelerometer data would be desirable, but this work has shown that it is not strictly necessary. The elaborate modeling technique of the non-gravitational accelerations provides a valuable alternative in case measurements are not available, yet this will depend e.g. on the shape and orbit of the satellite.

It would be of great interest to a large scientific community to obtain a long and consistent time series of mass redistribution in the Earth system, extending the GRACE(-FO) period. Swarm demonstrated that the gap can successfully be closed, but collecting data from as many satellite missions as possible might even improve the results from hl-SST. In this way, the time before GRACE could be investigated by evaluating CHAMP data. However, the CHAMP mission was launched only about two years prior to GRACE and kinematic orbits are not available in the beginning (due to the sparse network of IGS ground stations and consequently missing receiver clock corrections). If one is interested to look further into the past, one would need to extend and modify the approach, such that SLR or **D**oppler **O**rbitography and **R**adiopositioning **I**ntegrated by **S**atellite (DORIS) measurements could be processed. Continuing the time series in the future will most likely not cause any problems, because today's LEO satellite missions are equipped with up-to-date GNSS receivers.

Investigate the Swarm Constellation in More Detail

I computed monthly time-variable gravity fields by accumulating the NEQs of the three satellites. What has not been investigated further is a possible relation of the gravity field solutions with respect to the satellite constellation. As explained in Section 3.2, the constellation of the three Swarm satellites changes over time. This opens up opportunities to investigate the quality of the gravity fields with respect to different orbital parameters and the varying constellation of the three spacecraft. One could analyze the added value of additional satellites by comparing single-satellite solutions to solutions with two or three satellites. It would be interesting to compute and evaluate the orbit residuals. Additionally, analyzing the variance-covariance matrices of the solutions could reveal possible correlations between the parameters. These kinds of investigation could help to plan future satellite missions.

Kinematic baselines between the Swarm satellites can be computed to see whether they have an added value for gravity field recovery. Baselines can usually be detected with a higher accuracy compared to the kinematic positions, as common errors cancel out. X. Guo and Zhao (2019) derive two types of time-variable gravity fields from GRACE: one is derived from kinematic orbits of both satellites and the other is derived from kinematic orbits of GRACE-A and additionally the kinematic baseline between the satellites. Including the baseline reduces the noise in the gravity field solutions significantly, especially beyond d/o 10. De Teixeira da Encarnação et al. (2020) adapted the idea and included baselines in the Swarm gravity field retrieval. They could not find an added value. Still it might be worth it to investigate the approach further, especially in the context of steadily improving orbit products and non-gravitational acceleration modeling.

Study Ionospheric Processes

In the beginning of the Swarm mission, the ionosphere was highly active. This is reflected in the quality of the kinematic orbits and thus in the quality of the time-variable gravity fields. It would certainly be beneficial to bring expertise regarding ionospheric processes, orbit determination and gravity field retrieval together to study interactions between those topics. Right now, we are in the beginning of solar cycle 25 and ionospheric disturbances will become stronger during the next few years. Hence, a better understanding of ionospheric activity and its consequences for gravity field retrieval is becoming more and more important.

Calibrate Swarm Accelerometers and Study the Thermospheric Density

In this work, non-gravitational accelerations are modeled in order to be used in gravity field retrieval. First assessments showed a good agreement with calibrated or modeled data from other groups. In the process of gravity field retrieval, bias and scaling factors for aerodynamic accelerations and radiation pressure are co-estimated. These factors are a byproduct of the gravity field estimation and were, so far, not investigated further. They might be beneficial for studies of the thermosphere and its density.

It would be interesting to compare ACCCCAL_2_ data not only to the modeled non-gravitational accelerations, but also to modeled time series which are calibrated with the parameters derived in the gravity field processing. This could give a first estimate whether or not the calibration parameters are realistic. An evaluation of scale factor and bias might be helpful in studies regarding the quality of the NRLMSIS 2.0 model. Thermospheric density models might need to be calibrated themselves, which could depend on the solar activity. The calibration values from Swarm span a solar maximum and minimum, such that both extremes can be investigated. Moreover, calibration parameters related to radiation pressure can be evaluated and could be beneficial for future work in this context.

Moreover, Swarm C gravity fields could be investigated separately. One could use the calibrated along-track data of the ACCCCAL_2_ product instead of the modeled data in the process of gravity field retrieval. By comparing the quality of the resulting gravity fields (i.e. with respect

to GRACE(-FO)) it might be possible to determine if the modeled values or the ACCCCAL_2_ product is closer to the true non-gravitational accelerations.

Lastly, the modeling approach could easily be adapted for the use with GRACE(-FO). During the end-of-life period, the accelerometer of GRACE-B failed and also GRACE-D's accelerometer is not working correctly. Efforts are made to transplant data from one satellite to the other or to model non-gravitational accelerations. It would be interesting to share experience with the GRACE(-FO) community and see if the IGG modeling approach could help to improve GRACE(-FO) accelerometer data.

Investigate Alternative Approaches of Gravity Field Retrieval

In this thesis, the integral equation approach has been applied to derive time-variable gravity fields and mass redistribution from Swarm data. The advantages of using short arcs were mentioned in Section 4.1.3 and the parameterization has been tuned in order to achieve the best results. Other approaches, as mentioned at the beginning of Section 4.1 have not been investigated. In a mathematical sense, they are equivalent and should deliver comparable results, but it might still be worth it to investigate them closer.

The approaches of our former studies (Lück et al., 2018; Richter et al., 2021) could be updated with more recent and improved kinematic orbits from IfG, which would surely be beneficial for the retrieval of gravity fields. In Richter et al. (2021), we combined Swarm temporal gravity field models with the dominating spatial modes derived from GRACE. In Lück et al. (2018), we presented a solution where we estimated a six-parameter model for each spherical harmonic coefficient. This solution offers a possibility to estimate stable long-term mass change. It would be interesting to update the solution with recent Swarm data and the improved kinematic orbits IfG. A disadvantage of this approach is that it cannot resolve fast mass redistributions or acceleration signals. One could think of a Kalman filter approach comparable to Didova et al. (2016), where the trend of each SH coefficient might change over time. This would allow to better capture rapid changes.

Löcher and Kusche (2021) developed a hybrid approach for recovering high-resolution time-variable gravity fields from SLR. They compute EOFs from GRACE data in terms of SHs, which are then used as base functions in the gravity field retrieval. Additionally, the low degrees can be estimated separately in order to achieve more flexibility. First investigations have shown that the approach can easily be transferred to Swarm data and it would be interesting to investigate this in more detail.

Improve the Sea Level Inversion Framework Regarding the Use of Swarm data

Including Swarm into the sea level inversion framework showed promising results. By comparing the Swarm solution with CTas fingerprints to the current GRACE(-FO) inversion results, one could see similar global mean contributions of each driver. Only hydrological mass redistribution was generally underestimated, which also led to differences when assessing the sum of all mass contributions. This might be caused by the fact that WGHM data has a higher spatial resolution, which cannot be resolved by Swarm. This problem should definitely be investigated further. One should set up additional experiments with different sets of fingerprints. For example, one could think of alternative patterns or investigate the influence of a different number of hydrological fingerprints.

Right now, the fingerprints are time-invariant and monthly scaling factors are estimated for each of them. However, one could imagine that large-scale patterns of mass variability might change over time. Hence, it could be reasonable to allow a certain time-variability of prescribed patterns and let them evolve over time. Integrating Swarm into the inversion framework facilitates including time-variable gravity fields from SLR, which will generally work in the same way. This might help to improve the solutions, especially during times of GRACE(-FO) gaps. Additionally, Argo data could be included, such that also the steric part of sea level change is observed separately.

Appendix A

Time Series

Land

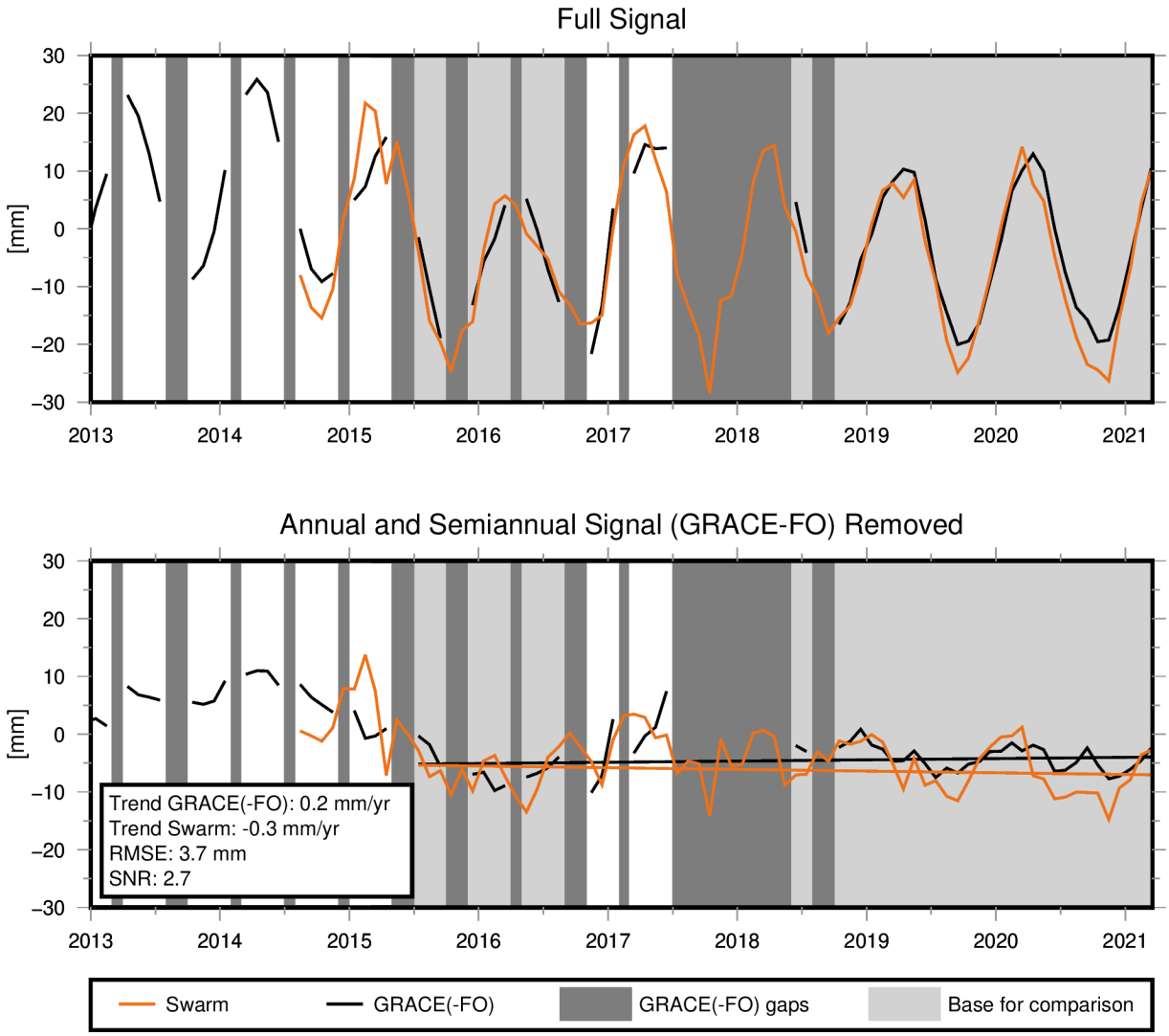

Figure A.1: Mass change in mm EWH over land areas from Swarm, GRACE(-FO), and Humphrey and Gudmundsson (2019). See the beginning of Section 5.4 for processing details. Top panel: Full signal. Bottom panel: Annual and semiannual signal from GRACE(-FO) are removed from both time series. Additionally, the trend is computed from the light-gray time periods and plotted.

East Antarctica

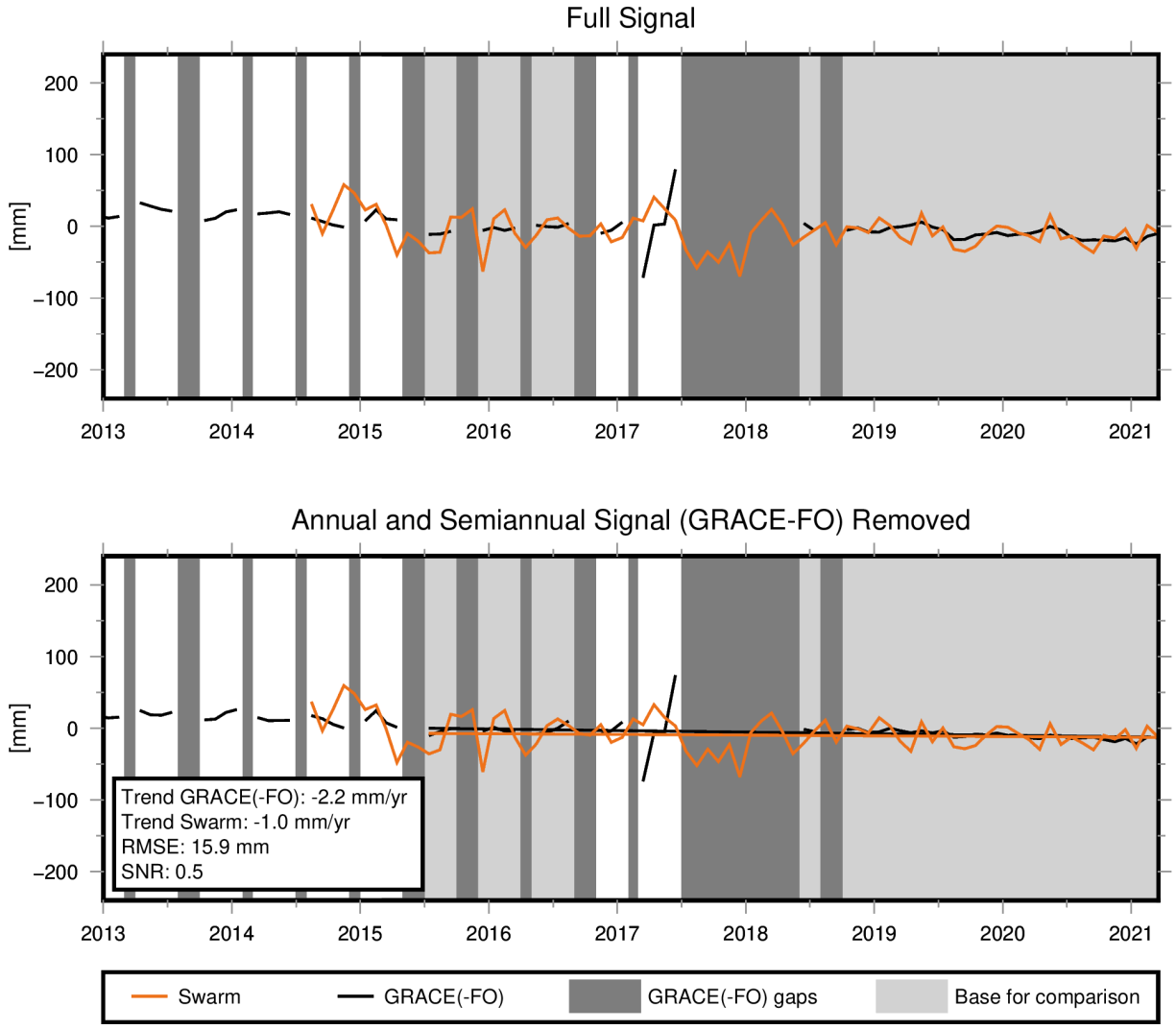

Figure A.2: Mass change in mm EWH in East Antarctica from Swarm and GRACE(-FO). See the beginning of Section 5.4 for processing details. Top panel: Full signal. Bottom panel: Annual and semiannual signal from GRACE(-FO) are removed from both time series. Additionally, the trend is computed from the light-gray time periods and plotted.

Congo

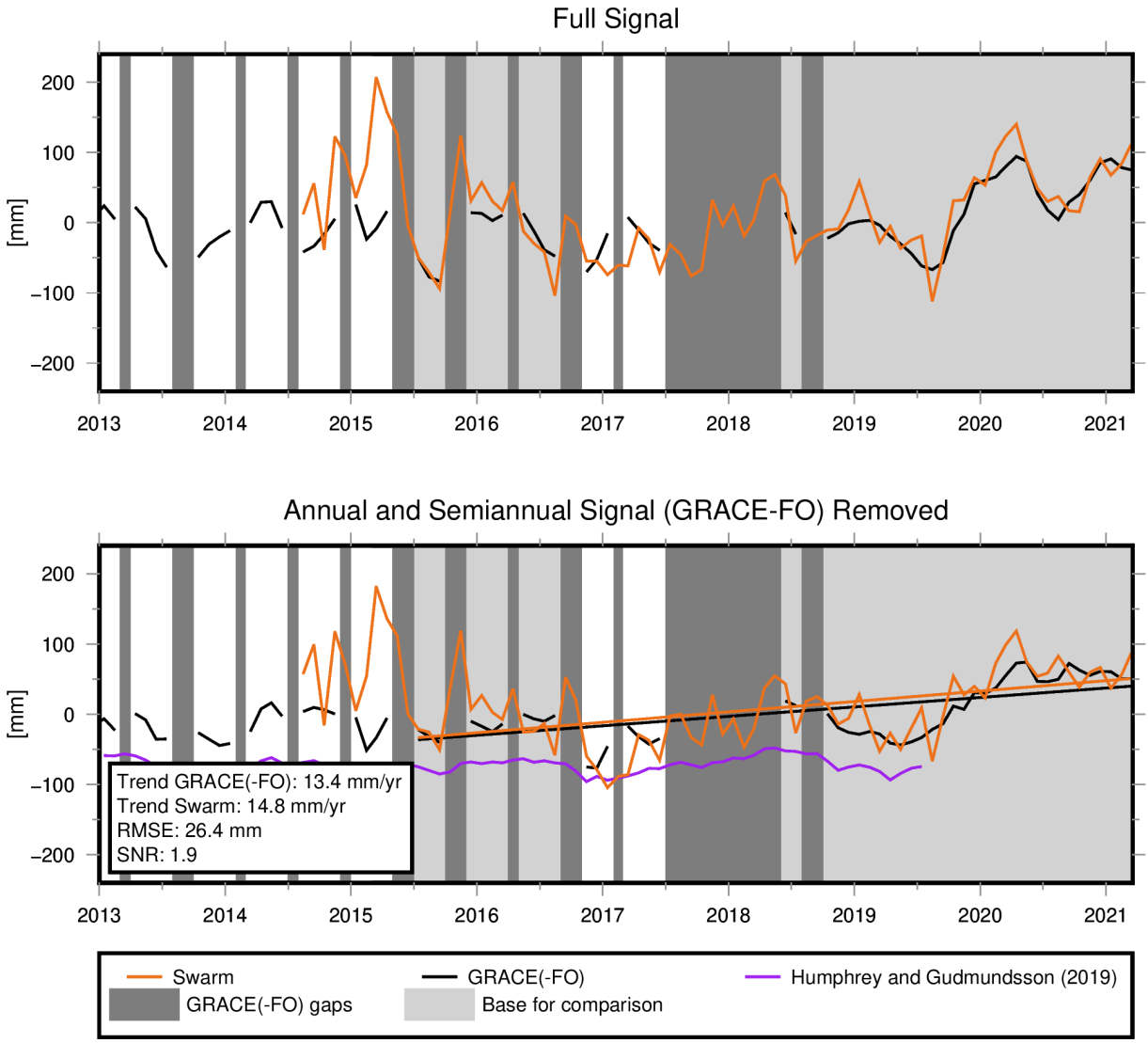

Figure A.3: Mass change in mm EWH in the Congo basin from Swarm, GRACE(-FO), and Humphrey and Gudmundsson (2019). See the beginning of Section 5.4 for processing details. Top panel: Full signal. Bottom panel: Annual and semiannual signal from GRACE(-FO) are removed from both time series. Additionally, the trend is computed from the light-gray time periods and plotted.

Mississippi

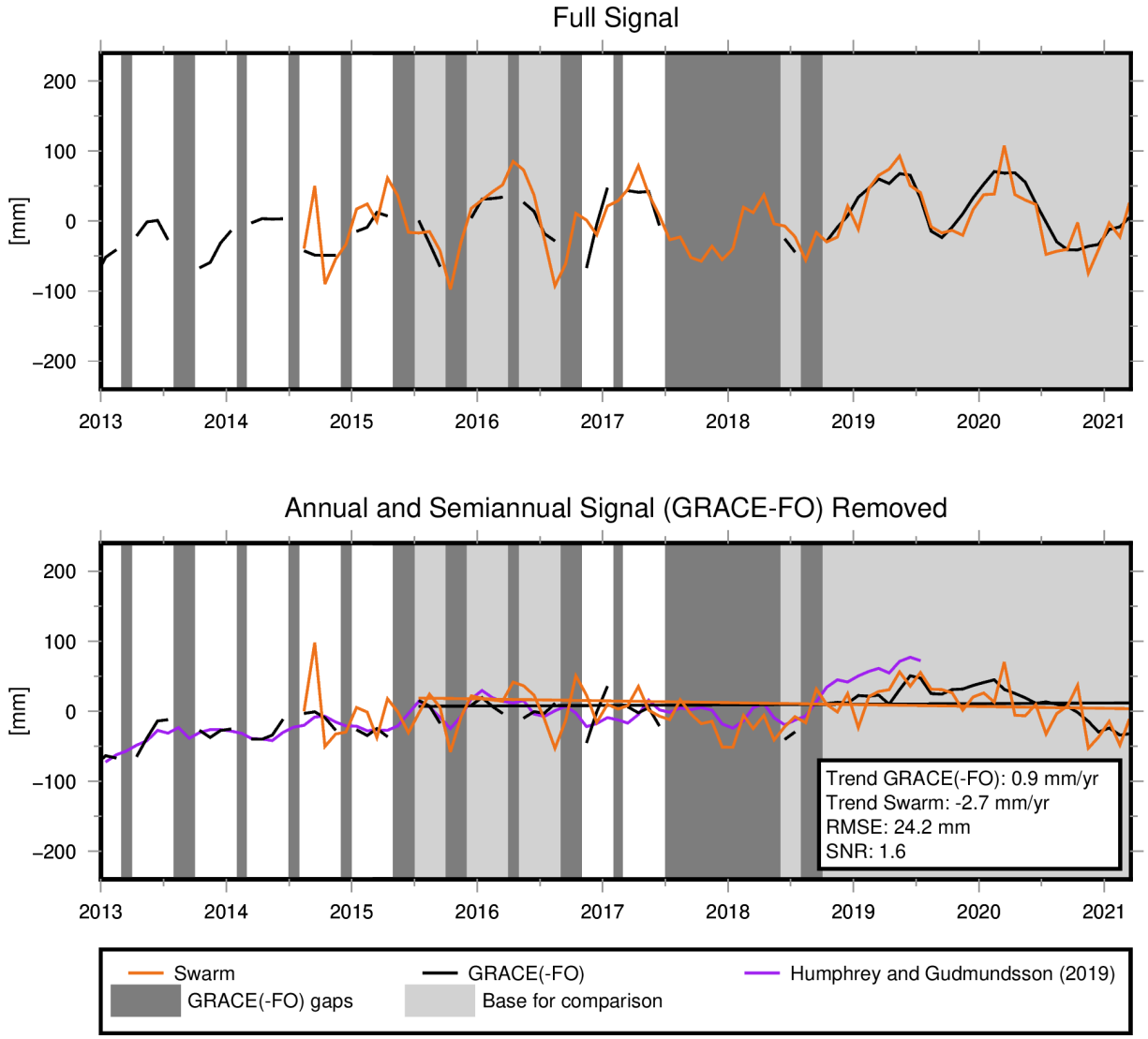

Figure A.4: Mass change in mm EWH in the Mississippi basin from Swarm, GRACE(-FO), and Humphrey and Gudmundsson (2019). See the beginning of Section 5.4 for processing details. Top panel: Full signal. Bottom panel: Annual and semiannual signal from GRACE(-FO) are removed from both time series. Additionally, the trend is computed from the light-gray time periods and plotted.

Nile

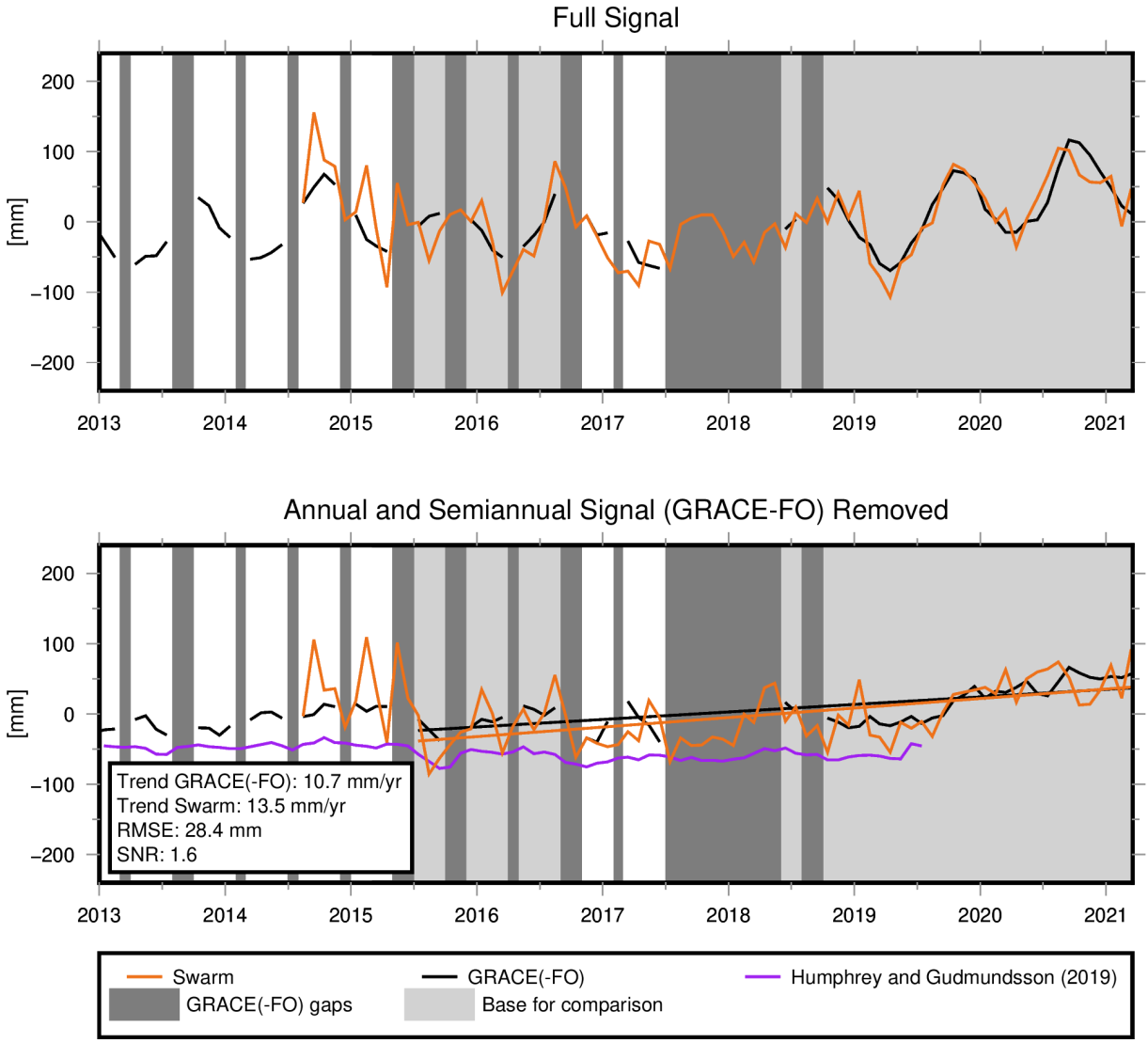

Figure A.5: Mass change in mm EWH in the Nile basin from Swarm, GRACE(-FO), and Humphrey and Gudmundsson (2019). See the beginning of Section 5.4 for processing details. Top panel: Full signal. Bottom panel: Annual and semiannual signal from GRACE(-FO) are removed from both time series. Additionally, the trend is computed from the light-gray time periods and plotted.

Lena

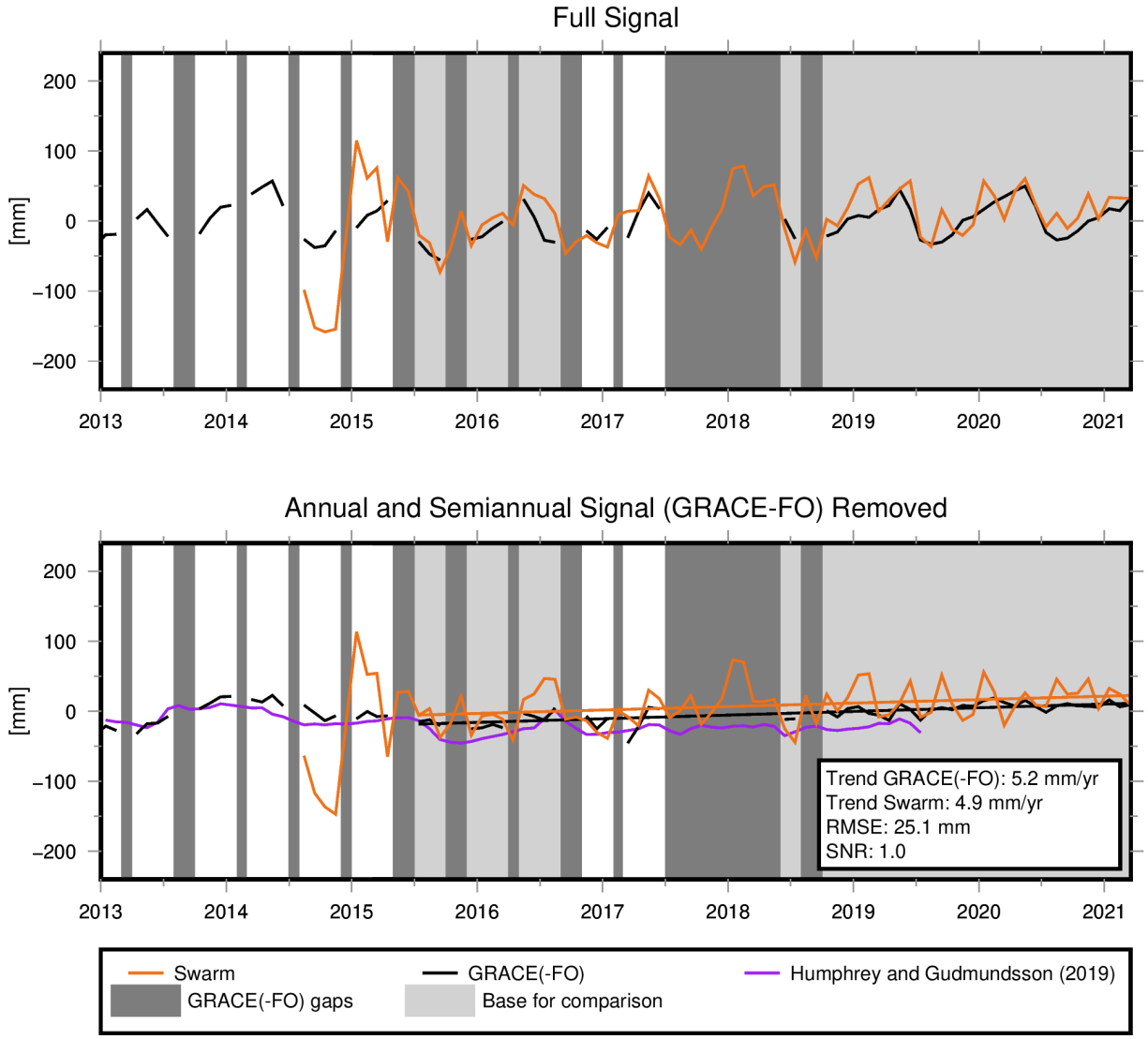

Figure A.6: Mass change in mm EWH in the Lena basin from Swarm, GRACE(-FO), and Humphrey and Gudmundsson (2019). See the beginning of Section 5.4 for processing details. Top panel: Full signal. Bottom panel: Annual and semiannual signal from GRACE(-FO) are removed from both time series. Additionally, the trend is computed from the light-gray time periods and plotted.

Yangtze

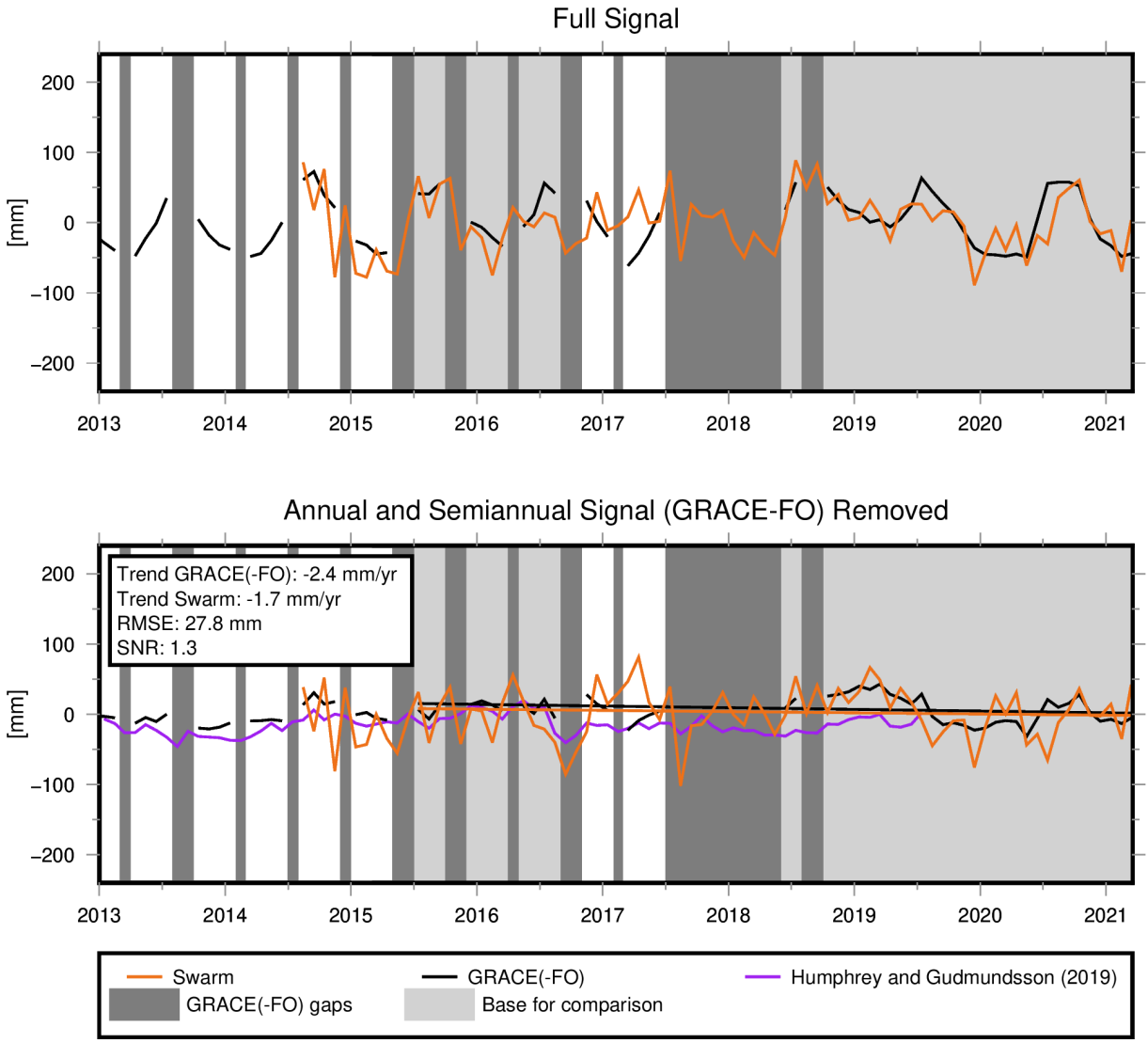

Figure A.7: Mass change in mm EWH in the Yangtze basin from Swarm, GRACE(-FO), and Humphrey and Gudmundsson (2019). See the beginning of Section 5.4 for processing details. Top panel: Full signal. Bottom panel: Annual and semiannual signal from GRACE(-FO) are removed from both time series. Additionally, the trend is computed from the light-gray time periods and plotted.

Volga

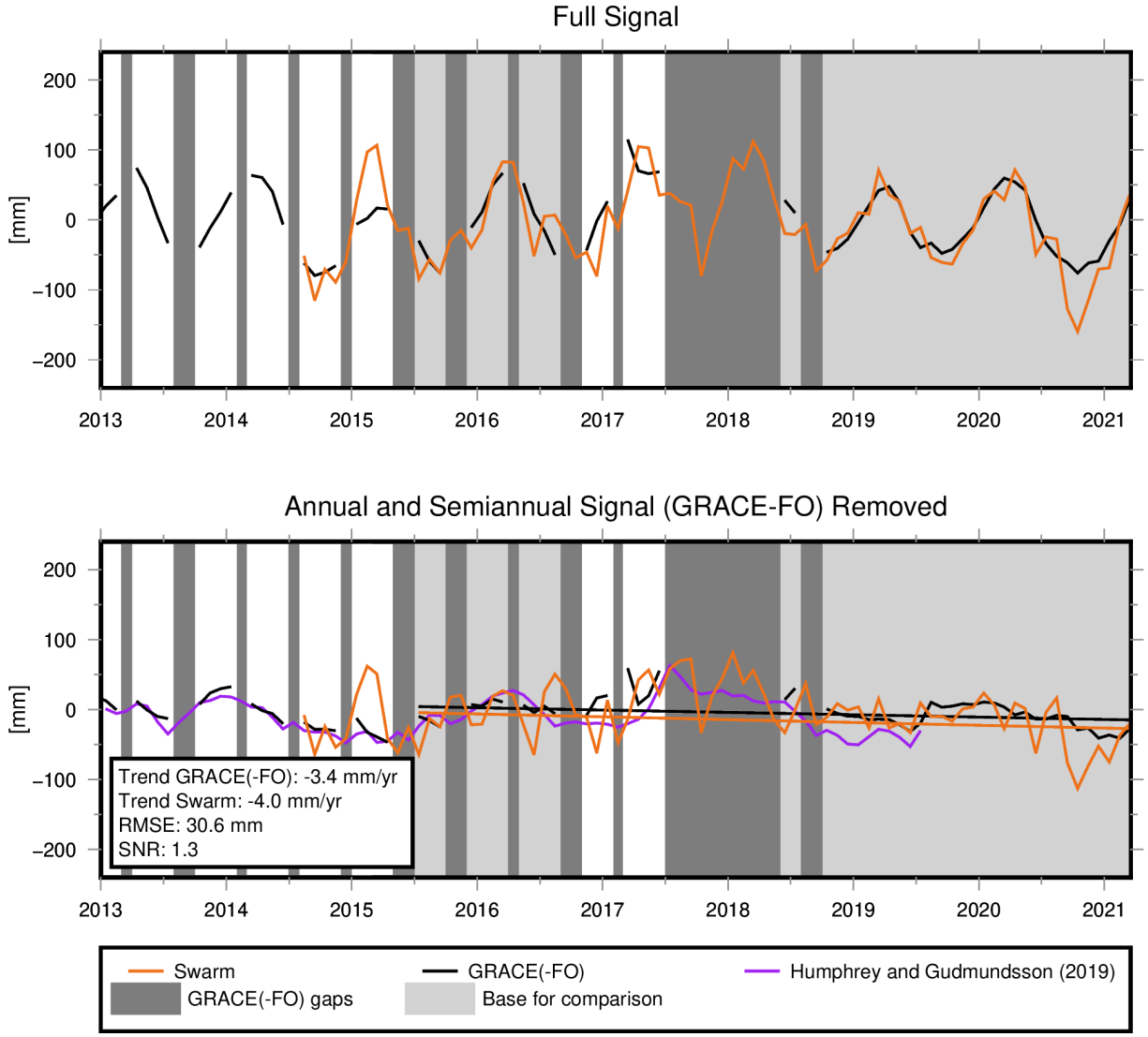

Figure A.8: Mass change in mm EWH in the Volga basin from Swarm, GRACE(-FO), and Humphrey and Gudmundsson (2019). See the beginning of Section 5.4 for processing details. Top panel: Full signal. Bottom panel: Annual and semiannual signal from GRACE(-FO) are removed from both time series. Additionally, the trend is computed from the light-gray time periods and plotted.

Murray-Darling

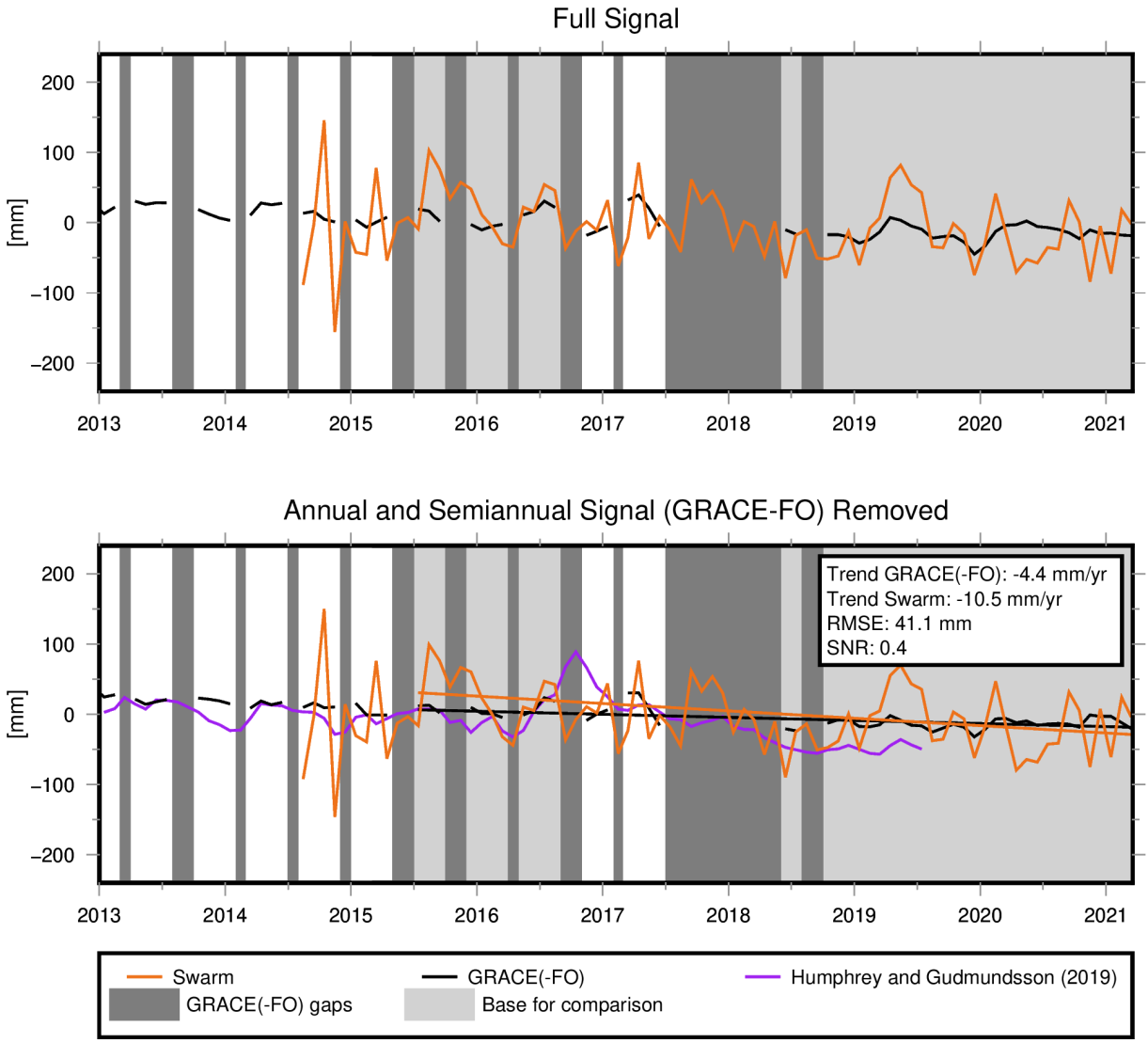

Figure A.9: Mass change in mm EWH in the Murray-Darling basin from Swarm, GRACE(-FO), and Humphrey and Gudmundsson (2019). See the beginning of Section 5.4 for processing details. Top panel: Full signal. Bottom panel: Annual and semiannual signal from GRACE(-FO) are removed from both time series. Additionally, the trend is computed from the light-gray time periods and plotted.

Ganges

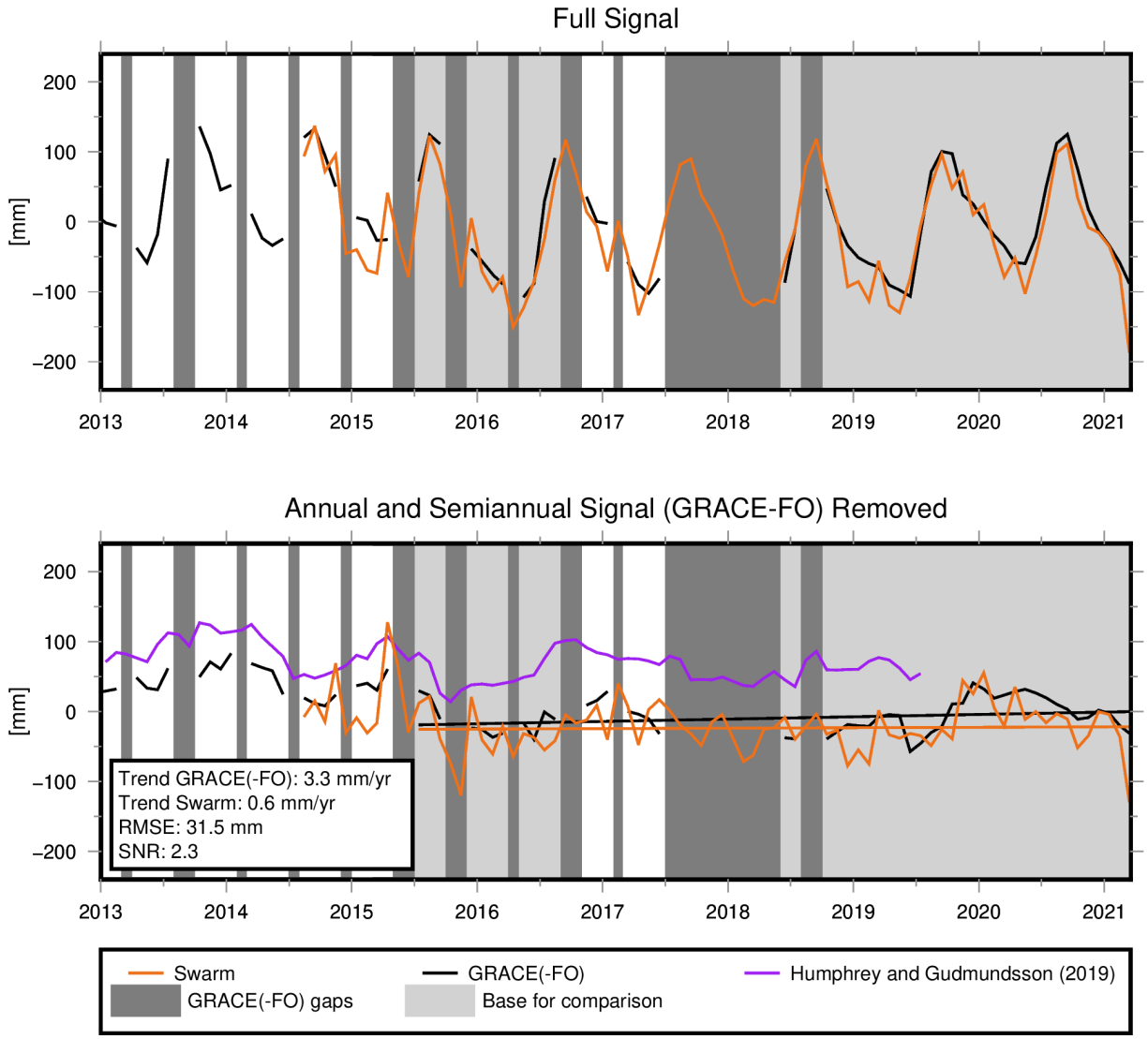

Figure A.10: Mass change in mm EWH in the Ganges basin from Swarm, GRACE(-FO), and Humphrey and Gudmundsson (2019). See the beginning of Section 5.4 for processing details. Top panel: Full signal. Bottom panel: Annual and semiannual signal from GRACE(-FO) are removed from both time series. Additionally, the trend is computed from the light-gray time periods and plotted.

Appendix B

Glossary

$\mathbf{A}$	Design matrix	51, 55, 56, 58, 109
A	Area $[m^2]$	34, 35
A_{ref}	Reference area of a satellite panel $[m^2]$	34
AU	Astronomical unit (mean distance between Earth and Sun) $[m]$	34
$\mathbf{a}$	Vector of non-gravitational accelerations $[ms^{-2}]$	34, 35
a	Semi-major axis (e.g., of a satellite's orbit) [°]	24
α_k	Angle between the connection line of the satellite to a surface element and the element's normal vector $[rad]$	35
$\mathbf{B}$	Matrix with observation times (corresponding to boundary values in $\mathbf{b}$)	50, 51, 58
$\mathbf{b}$	Vector containing boundary values	50, 51, 58
$\mathbf{C}$	Matrix containing the contributions of a single satellite to a combined solution or	64
$\mathbf{C}$	Matrix containing the mass-related fingerprints in its columns	109
C_{aero}	Coefficient accounting for aerodynamic (drag and lift) accelerations [−]	34
$C_{D,i,j}$	Drag coefficient [−]	34
$C_{L,i,j}$	Lift coefficient [−]	34
C_{nm}	Cosine surface spherical harmonics of degree n and order m [−]	46, 80
$\mathbf{c}^{\odot}_{R_{LW}}$	Radiation pressure coefficients for incoming photons of the Sun (longwave) [−]	34, 35
$\mathbf{c}^{\oplus}_{R_{LW,k}}$	Radiation pressure coefficients for incoming radiation of the Earth (longwave) [−]	35
$\mathbf{c}^{\odot}_{R_{SW}}$	Radiation pressure coefficients for incoming photons of the Sun (shortwave) [−]	34, 35
$\mathbf{c}^{\oplus}_{R_{SW,k}}$	Radiation pressure coefficients for incoming radiation of the Earth (shortwave) [−]	35
c	Speed of light $[ms^{-1}]$	35
c_{nm}	Fully normalized Stokes cosine coefficients of degree n and order m [−]	46, 51, 52, 79, 80, 83
$\mathbf{D}$	Matrix used in a preprocessing step in the gravity field retrieval process or	57
$\mathbf{D}$	Matrix containing the steric fingerprints in its columns	109
dm	Mass element $[kg]$	46
$\Delta\omega_k$	$1° \times 1°$ surface element in the FoV of a satellite $[m^2]$	35

EWH	Equivalent water height $[m]$	80, 83
$\mathbf{e}$	Noise in a Gauss-Markoff model	50, 51, 55–58, 106, 109
$\mathbf{F}$	Force $[kgms^{-2}]$	45, 49
$F_{LW,k}$	TOA longwave flux $[Wm^{-2}]$	35
$F_{SW,k}$	TOA shortwave flux $[Wm^{-2}]$	35
$\mathbf{f}$	Force w.r.t. a unity mass element $[ms^{-2}]$	49, 50
G	Newton's gravitational constant $[m^3kgs^{-2}]$ or	45, 46
G	Green's function	107
GM	Standard gravitational parameter $[m^3s^{-2}]$	46
$\mathbf{g}$	Gravitational field strength $[ms^{-2}]$	45
g	Mean gravitational acceleration of the Earth $[ms^{-2}]$	107, 108
γ	Angle between the normal vector of a satellite panel and the incoming radiation $[rad]$	34, 35
H	Continental surface load $[m$ EWH$]$	107
$\mathbf{h}$	Second part of the integral equation (Equation (4.1.14))	50, 51, 58
h	Along-track corrected altimeter measurements $[m]$	109
i	Inclination (e.g., of a satellite's orbit) [°]	22, 24
$\mathbf{K}$	Matrix which maps the steric fingerprints to the locations of the altimeter measurements	109
K	Integral kernel	49, 50
k'_n	Love number of degree n $[-]$	80, 83
$\mathbf{l}$	Vector of observations	50, 51, 55, 56, 58
l	Distance between two points $[m]$	45, 46
$\mathbf{\Lambda}$	Diagonal matrix	57
Λ	Centrifugal potential $[m^2s^{-2}]$	107
λ	Longitude angle [° or rad]	34, 46, 80, 83, 107
M	Earth's mass $[kg]$	45, 80, 83
m	Mass $[kg]$ or	34, 35, 45, 49
m	Spherical harmonic order $[-]$	46, 52, 80, 83
$\mathbf{N}$	Normal equation matrix	56, 58, 64, 109
N	Geoid height (above a reference ellipsoid) $[m]$	107

$\mathbf{n}$	Normal equation vector	56, 58, 109
n	Spherical harmonic degree [−]	46, 47, 51, 52, 65, 80, 83
ν	Shadow function, which indicates if a satellite is in sunlight or in shadow [−]	34
$O(\lambda, \theta)$	Ocean function (0 over ocean, 1 over land) [-]	107
Ω	Right ascension of the ascending node (e.g., of a satellite's orbit) [°] or	22, 24
Ω	Angular area of a region of interest $[rad^2]$	83, 107
$\mathbf{P}$	Weight matrix in a least square adjustment	55, 56, 58, 109
$\bar{P}_{nm}$	Fully normalized associated Legendre function of degree n and order m [−]	46, 83
P_{1AU}	Solar radiation pressure at 1 AU $[Nm^{-2}]$	34
ϕ	Gravitational potential $[m^2s^{-2}]$	107, 108
ψ	Full-wavelength resolution of a spherical harmonic expansion $[km]$	47
$\mathbf{Q}$	Orthogonal matrix	57
$\mathbf{R}$	Upper triangular matrix	58
R	Mean Earth radius $[m]$	46, 47, 52, 80, 83
$R_{LW,k}$	Factor which considers the angular dependence of the Earth's radiation (long-wave) [−]	35
$R_{SW,k}$	Factor which considers the angular dependence of the Earth's radiation (short-wave) [−]	35
$\mathbf{r}$	3-dimensional vector to the origin of an Earth-fixed coordinate system $[m]$	31, 45, 46, 49, 50
$\dot{\mathbf{r}}$	3-dimensional velocity vector w.r.t to an Earth-fixed coordinate system $[ms^{-1}]$	49
$\ddot{\mathbf{r}}$	3-dimensional acceleration vector w.r.t. to an Earth-fixed coordinate system $[ms^{-2}]$	49
r	Distance to the origin of an Earth-fixed coordinate system $[m]$ or	46
r	Redundancy [−]	57
$r_{\odot,sat}$	Distance between Sun and satellite $[m]$	34
$r_{sat,k}$	Distance between a surface Element k the Earth's surface and the satellite $[m]$	35
ρ	Density $[kgm^{-3}]$	34
ρ_w	Average density of sea water $[kgm^{-3}]$	80, 83
$\mathbf{S}$	Covariance function	57
S	Relative sea level change [m EWH]	107
S_{nm}	Sine surface spherical harmonics of degree n and order m [−]	46, 80
s_{nm}	Fully normalized Stokes sine coefficients of degree n and order m [−]	46, 51, 52, 79, 80, 83
$\mathbf{\Sigma}_{3x3}(t_i)$	3x3 covariance matrix of epoch t_i	57
$\mathbf{\Sigma_{ll}}$	Covariance matrix of observations	55–58
σ	Standard deviation or	55–57

σ	Surface density $[kgm^{-2}]$	80
$\hat{\sigma}$	Formal error (e.g., of SH coefficients of degree amplitudes)	52, 53, 65–67
σ_n	Degree amplitudes $[m]$	52, 53, 65–68
T	Time period, e.g. duration of one orbit arc $[s]$ or	50
T	Total surface load $[m$ EWH$]$	107
t	Time in general, see individual explanations for more detail	34, 49, 50, 107
τ	Normalized time variable $[-]$	49, 50
θ	Co-latitude angle [° or rad]	46, 80, 83, 107
ϑ^c_{nm}	Cosine spherical harmonic coefficients that describe $\vartheta(\lambda,\theta)$ [-]	83
ϑ^s_{nm}	Sine spherical harmonic coefficients that describe $\vartheta(\lambda,\theta)$ [-]	83
$\vartheta(\lambda,\theta)$	Function that describes the shape of a basin (either 0 or 1) [-]	83
U	Radial deformation of the Earth $[m]$	107
$\hat{\mathbf{u}}_D$	Unit vector of velocity in drag direction $[ms^{-1}]$	34
$\hat{\mathbf{u}}_{L,i}$	Unit vector of velocity in lift direction $[ms^{-1}]$	34
V	Earth's gravitational potential $[m^2s^{-2}]$	45, 46
$\mathbf{v}_r$	Vector of relative velocity $[ms^{-1}]$	34
$\hat{\mathbf{v}}_r$	Unit vector of relative velocity $[ms^{-1}]$	34
$\mathbf{W}$	Matrix containing filtering coefficients	79
$\mathbf{x}$	Vector of unknown parameters	51, 55, 56, 58, 79, 109
$\mathbf{Y}$	Matrix which maps the mass-related fingerprints to the locations of the altimeter measurements	109
Y_n	Surface spherical harmonics of degree n $[-]$	46

Appendix C

Acronyms

AIUB	Astronomical Institute of the University of Bern (**A**stronomisches **I**nstitut der **U**niversität **B**ern) 11, 32, 40, 44, 69, 71, 119
AOD1B	**A**tmosphere and **O**cean **D**e-aliasing Level-**1B** 48, 83, 84
ASI	Italian Space Agency (**A**genzia **S**peziale **I**taliana) 15
ASM	**A**bsolute **S**calar **M**agnetometer 25
ASU	Astronomical Institute of the Czech Academy of Sciences (**AS**tronomický **U**stav) 40, 45
AU	**A**stronomical **U**nit 34
BLUE	**B**est **L**inear **U**nbiased **E**stimator 56
CASSIOPE	**CA**scade **S**mall**S**at and **IO**nospheric **P**olar **E**xplorer 20
CDC	**C**ompact **D**etector **C**oil 25
CEA-LETI	Alternative Energies and Atomic Energy Commission - Research Institute for Electronics and Information Technologies (**C**ommissariat à l'**É**nergie **A**tomique et aux énergies alternatives - **L**aboratoire d'**É**lectronique et de **T**echnologie de l'**I**nformation) 25
CERES	**C**louds and the **E**arth's **R**adiant **E**nergy **S**ystem 35
CHAMP	**CHA**llenging **M**inisatellite **P**ayload 1, 4, 7, 21, 33, 39, 43, 44, 49, 120
CHU	**C**amera **H**ead **U**nit 26
CNES	National Centre for Space Studies (**C**entre **N**ational d'**É**tudes **S**patiales) 15, 17, 25
CODE	**C**enter for **O**rbit **D**etermination in **E**urope 29
CoF	**C**enter **o**f **F**igure 75
CoG	**C**enter **o**f **G**ravity 9, 27, 29
CoM	**C**enter **o**f **M**ass 29, 30, 75, 76
CSA	**C**anadian **S**pace **A**gency 20
CSC	**C**ompact **S**pherical **C**oil 25
CSR	**C**enter for **S**pace **R**esearch 9, 11, 12, 44, 62, 76, 77
d/o	**d**egree and **o**rder 12, 21, 30, 51, 55, 60, 61, 64–66, 72, 73, 85, 86, 89, 90, 94, 108, 116, 119, 121
DLR	German Aerospace Center (**D**eutsches Zentrum für **L**uft- und **R**aumfahrt e.V.) 7, 8, 11
DORIS	**D**oppler **O**rbitography and **R**adiopositioning **I**ntegrated by **S**atellite 120
DTU	Technical University of Denmark (**D**anmarks **T**ekniske **U**niversitet) 9, 25

e-POP	**E**nhanced **P**olar **O**utflow **P**robe 20
EarthCARE	**Earth** **C**louds **A**erosols and **R**adiation **E**xplorer 19, 20
EDAC	**E**rror **D**etection **A**nd **C**orrection 27, 33
EFI	**E**lectric **F**ield **I**nstrument 25, 26
EGS	**E**xperimental **G**eodetic **S**atellite 15
EIGEN	**E**uropean **I**mproved **G**ravity model of the **E**arth by **N**ew techniques 19
ENSO	**E**l **N**iño **S**outhern **O**scillation 4, 92, 93, 100, 116, 120
EOF	**E**mpirical **O**rthogonal **F**unction 16, 69, 107, 108, 122
ERP	**E**arth **R**adiation **P**ressure 9, 27, 34–37, 47, 51, 119
ERS-1	**E**uropean **R**emote **S**ensing 1 16
ESA	**E**uropean **S**pace **A**gency xxv, 1, 3, 5, 13, 19, 20, 25, 27, 32, 33, 119
ESRIN	**E**uropean **S**pace **R**esearch **IN**stitute 27
ESSP	**E**arth **S**ystem **S**cience **P**athfinder 8
EUMETSAT	**EU**ropean Organization for the Exploitation of **MET**eorological **SAT**ellites 17
EWH	**E**quivalent **W**ater **H**eight i–x, 5, 11, 73, 75, 78, 80–83, 85, 86, 92, 93, 95–97, 101, 107, 119
FLEX	**FL**uorescence **EX**plorer 19, 20
FORUM	**F**ar-infrared **O**utgoing **R**adiation **U**nderstanding and **M**onitoring 19, 20
FoV	**F**ield **o**f **V**iew 26, 35, 40
FTP	**F**ile **T**ransfer **P**rotocol 28
GEOS-3	**G**eodynamics **E**xperimental **O**cean **S**atellite **3** 16
GFZ	German Research Centre for Geosciences (Deutsches **G**eo**F**orschungs**Z**entrum) 8, 9, 11, 12, 26, 44, 48, 76
GGM	**G**RACE **G**ravity **M**odel 19
GIA	**G**lacial **I**sostatic **A**djustment 1, 3, 11, 43, 76, 78, 81, 83, 84
GLONASS	**GLO**bal **NA**vigation **S**atellite **S**ystem (**GLO**balnaja **NA**wigazionnaja **S**putnikowaja **S**istema) 30, 120
GMT	**G**eneric **M**apping **T**ools 55
GNSS	**G**lobal **N**avigation **S**atellite **S**ystem 1, 2, 4, 30, 43, 44, 55, 120
GOCE	**G**ravity Field and Steady-State **O**cean **C**irculation **E**xplorer 1, 7, 19, 20, 27, 43–45, 47, 49
GOCO	**G**ravity **O**bservation **CO**mbination 19, 47, 52–54, 59, 62, 65–68, 70, 85
GPS	**G**lobal **P**ositioning **S**ystem 2, 7, 9, 16, 26–33, 40, 45, 50, 68, 75, 79, 89, 120
GPSR	**G**lobal **P**ositioning **S**ystem **R**eceiver 25, 26, 28, 30, 32, 40, 41
GRACE	**G**ravity **R**ecovery **A**nd **C**limate **E**xperiment 1–5, 7–9, 11, 12, 15, 16, 22, 32, 33, 39, 40, 43–45, 47, 49, 51, 52, 59, 69, 73, 75, 76, 78, 79, 83, 85, 89, 91–94, 96, 97, 100, 101, 107, 110–112, 114–116, 119–122
GRACE(-FO)	**G**ravity **R**ecovery **A**nd **C**limate **E**xperiment (**F**ollow-**O**n) i–x, 1–5, 7, 11–13, 22, 27, 33, 39, 40, 43, 44, 47, 51, 59–70, 72, 75, 76, 78–80, 84–102, 105, 106, 108–116, 119, 120, 122
GRACE-FO	**G**ravity **R**ecovery **A**nd **C**limate **E**xperiment **F**ollow-**O**n 1–5, 7–9, 11, 12, 32, 33, 39, 40, 59, 66, 68, 75, 76, 78, 85, 86, 91–94, 96, 97, 100, 101, 109–112, 114, 115, 119, 120
GROOPS	**G**ravity **R**ecovery **O**bject **O**riented **P**rogramming **S**ystem 43, 55
GRS80	**G**eodetic **R**eference **S**ystem 1980 9, 23

GSFC **G**oddard **S**pace **F**light **C**enter 60

hl-SST **h**igh-**l**ow **S**atellite-to-**S**atellite **T**racking 2, 9, 43, 44, 119, 120

IAG **I**nternational **A**ssociation of **G**eodesy 49
ICESat **I**ce, **C**loud and Land **E**levation **Sat**ellite 3
ICGEM **I**nternational **C**entre for **G**lobal **E**arth **M**odels 30, 59
IERS **I**nternational **E**arth **R**otation **S**ervice 29, 47, 48
IfE Institute of Geodesy (**I**nstitut **f**ür **E**rdmessung) 32
IfG Institute of Geodesy (**I**nstitut **f**ür **G**eodäsie) 11, 12, 32, 38, 40, 44, 55, 56, 59, 69, 71, 119, 122
IGG Institute of Geodesy and Geoinformation (**I**nstitut für **G**eodäsie und **G**eoinformation) 4, 5, 30, 34, 38, 40, 51, 55, 60, 61, 69, 71, 76, 77, 84, 91, 92, 105, 106, 108–110, 119, 122
IGS **I**nternational **G**NSS **S**ervice 29, 75, 120
ILRS **I**nternational **L**aser **R**anging **S**ervice 14
IPCC **I**ntergovernmental **P**anel on **C**limate **C**hange 2, 3
ITRF **I**nternational **T**errestrial **R**eference **F**rame 15, 28, 29
ITSG **I**nstitute of **T**heoretical Geodesy and **S**atellite **G**eodesy 11, 12, 52–54, 60, 65–68, 70, 79, 108

JAXA **J**apan **A**erospace E**X**ploration **A**gency 15
JPL **J**et **P**ropulsion **L**aboratory 8, 9, 11, 12, 44, 48, 76

KBR **K**-**B**and **R**anging 1, 9, 11, 12, 39, 44, 45, 59, 75, 119

L0 **L**evel-**0** 11
L1A **L**evel-**1A** 11
L1B **L**evel-**1B** 11, 12, 26, 33, 56
L2 **L**evel-**2** 11, 32, 38
L3 **L**evel-**3** 11
LAGEOS **LA**ser **GEO**dynamics **S**atellite 15
LARES **LA**ser **RE**lativity **S**atellite 78
LEO **L**ow **E**arth **O**rbit 2, 4, 22, 27, 30, 31, 34, 40, 43, 47, 100, 120
ll-SST low-**l**ow **S**atellite-to-**S**atellite **T**racking 9, 43, 44
LP **L**iving **P**lanet 19
LP **L**angmuir **P**robe 26
LRI **L**aser **R**anging **I**nterferometer 8, 9, 11, 75
LRR **L**aser **R**etro-**R**eflector 9, 14, 26
LSA **L**east **S**quares **A**djustment 55, 57, 59
LTAN **L**ocal **T**ime of the **A**scending **N**ode 38, 39

MPIOM **M**ax-**P**lanck-**I**nstitute for Meteorology **O**cean **M**odel 84

NASA **N**ational **A**eronautics and **S**pace **A**dministration 7–9, 14, 15, 17, 60
NEQ **N**ormal **EQ**uation 12, 55–59, 64, 109, 121
NOAA **N**ational **O**ceanic and **A**tmospheric **A**dministration 17
NRLMSIS **N**aval **R**esearch **L**aboratory **M**ass **S**pectrometer **I**ncoherent **S**catter radar 4, 34, 37, 38, 121

OBP **O**cean **B**ottom **P**ressure 75, 78
ONERA French national aerospace research centre (**O**ffice **N**ational d'**É**tudes et de **R**echerches **A**érospatiales) 9, 27
ORAS **O**cean **Re**A**n**alysis **S**ystem 108
OSU **O**hio **S**tate **U**niversity 40, 44

PCA **P**rincipal **C**omponent **A**nalysis 107, 108
PDGS **P**ayload **D**ata **G**round **S**egment 27, 29
POD **P**recise **O**rbit **D**etermination 4, 5, 16, 20, 26, 29–33, 40, 43, 50
PREM **P**reliminary **R**eference **E**arth **M**odel 78

RAAN **R**ight **A**scension of the **A**scending **N**ode 22, 24
RADS **R**adar **A**ltimeter **D**atabase **S**ystem 109
RDC **R**aw **D**ata **C**enter 11
RINEX **R**eceiver **IN**dependent **EX**change Format 28
RL **Re**L**ease** 12, 48, 75, 76, 84
RMS **R**oot **M**ean **S**quare 59–62, 64, 84, 88, 89, 100, 101, 119
RMSE **R**oot **M**ean **S**quare **E**rror 59–61, 73, 84–86, 88–91, 93, 94, 96, 98–102, 119, 120
RUAG Joint Stock Defense Company (**R**üstungs**U**nternehmen-**A**ktien**G**esellschaft) 26

SAC-C Scientific Application Satellite-C (**S**atélite de **A**plicaciones **C**ientíficas-**C**) 21
SAR **S**ynthetic **A**perture **R**adar 20
SDS **S**cience **D**ata **S**ystem 11
SH **S**pherical **H**armonic 3, 5, 11, 12, 15, 16, 30, 40, 46, 48, 51, 52, 54, 60, 61, 63, 64, 69, 75, 76, 78, 79, 81–84, 119, 122
SII **S**uprathermal **I**on **I**mager 26
SLE **S**ea **L**evel **E**quation 107
SLR **S**atellite **L**aser **R**anging 5, 7, 14–16, 26, 27, 44, 47, 60–62, 69, 71, 75–78, 116, 120, 122
SMOS **S**oil **M**oisture and **O**cean **S**alinity 19, 20
SNR **S**ignal-to-**N**oise **R**atio 61, 66–69, 71, 72, 91, 93, 94, 96, 98–101, 119, 120
SPC **S**cientific **P**rocessing **C**entre 27–29
SRP **S**olar **R**adiation **P**ressure 9, 27, 34–37, 47, 51, 119
SSL **S**pace **S**ystems **L**oral 8
SST **S**atellite-to-**S**atellite **T**racking 8, 9, 43
STR **S**tar **TR**acker 24–26

TN **T**echnical **N**ote 60, 62, 75–78
TOA **T**op **O**f the **A**tmosphere 35
TUD Delft University of Technology (**T**echnische **U**niversiteit **D**elft) 32
TWS **T**otal **W**ater **S**torage 91
TWSA **T**otal **W**ater **S**torage **A**nomaly 3

UTC **C**oordinated **U**niversal **T**ime 28–30
UTCSR **U**niversity of **T**exas at Austin, **C**enter for **S**pace **R**esearch 8

VCE **V**ariance **C**omponent **E**stimation 47, 49, 57

VFM **V**ector **F**ield **M**agnetometer 25
VTEC **V**ertical **T**otal **E**lectron **C**ontent 40, 41
VZLU Aerospace Research Centre (**V**ýzkumný a **Z**kušební **L**etecký **Ú**stav) 27

WCRP **W**orld **C**limate **R**esearch **P**rogramme 2
WGHM **W**aterGAP **G**lobal **H**ydrological **M**odel 107, 108, 122

List of Figures

List of Tables

Bibliography

A, G., J. Wahr, and S. Zhong. "Computations of the viscoelastic response of a 3-D compressible Earth to surface loading: an application to Glacial Isostatic Adjustment in Antarctica and Canada". In: *Geophysical Journal International* 192.2 (2013), pp. 557–572. DOI: 10.1093/gji/ggs030.

Abich, K., C. Bogan, C. Braxmaier, K. Danzmann, M. Dehne, M. Gohlke, A. Görth, G. Heinzel, M. Herding, C. Mahrdt, V. Müller, K. Nicklaus, J. Sanjuan, D. Schütze, B. Sheard, G. Stede, and K. Voss. "GRACE-Follow On Laser Ranging Interferometer: German contribution". In: *Journal of Physics: Conference Series* 610 (2015), p. 012010. DOI: 10.1088/1742-6596/610/1/012010.

Abich, K. et al. "In-Orbit Performance of the GRACE Follow-on Laser Ranging Interferometer". In: *Phys. Rev. Lett.* 123 (3 2019), p. 031101. DOI: 10.1103/PhysRevLett.123.031101.

Ablain, M., B. Meyssignac, L. Zawadzki, R. Jugier, A. Ribes, A. Cazenave, and N. Picot. "Uncertainty in Satellite estimate of Global Mean Sea Level changes, trend and acceleration". In: *Earth System Science Data Discussions* 11.3 (2019), pp. 1–26. DOI: 10.5194/essd-2019-10.

Altamimi, Z., P. Rebischung, L. Métivier, and X. Collilieux. "ITRF2014: A new release of the International Terrestrial Reference Frame modeling nonlinear station motions". In: *Journal of Geophysical Research: Solid Earth* 121.8 (2016), pp. 6109–6131. DOI: https://doi.org/10.1002/2016JB013098.

Andersen, O. B. and R. Scharroo. "Range and Geophysical Corrections in Coastal Regions: And Implications for Mean Sea Surface Determination". In: *Coastal Altimetry*. Ed. by Stefano Vignudelli, Andrey G. Kostianoy, Paolo Cipollini, and Jérôme Benveniste. Berlin, Heidelberg: Springer Berlin Heidelberg, 2011, pp. 103–145. ISBN: 978-3-642-12796-0. DOI: 10.1007/978-3-642-12796-0_5.

Appleby, G., J. Rodríguez, and Z. Altamimi. "Assessment of the accuracy of global geodetic satellite laser ranging observations and estimated impact on ITRF scale: estimation of systematic errors in LAGEOS observations 1993–2014". In: *Journal of Geodesy* 90 (2016), pp. 1371–1388. DOI: 10.1007/s00190-016-0929-2.

Argus, D. F., W. R. Peltier, R. Drummond, and A. W. Moore. "The Antarctica component of postglacial rebound model ICE-6G_C (VM5a) based on GPS positioning, exposure age dating of ice thicknesses, and relative sea level histories". In: *Geophysical Journal International* 198.1 (2014), pp. 537–563. ISSN: 0956-540X. DOI: 10.1093/gji/ggu140.

Bandikova, T., C. McCullough, G. L. Kruizinga, H. Save, and B. Christophe. "GRACE accelerometer data transplant". In: *Advances in Space Research* 64.3 (2019), pp. 623–644. ISSN: 0273-1177. DOI: https://doi.org/10.1016/j.asr.2019.05.021.

Barre, H., B. Duesmann, and Y. Kerr. "SMOS: The mission and the system". In: *Geoscience and Remote Sensing, IEEE Transactions on* 46 (2008), pp. 587–593. DOI: 10.1109/TGRS.2008.916264.

Baur, O., H. Bock, E. Höck, A. Jäggi, S. Krauss, T. Mayer-Gürr, T. Reubelt, C. Siemes, and N. Zehentner. "Comparison of GOCE-GPS gravity fields derived by different approaches". In: *Journal of Geodesy* 88 (2014), pp. 959–973. DOI: 10.1007/s00190-014-0736-6.

Baur, O., M. Kuhn, and W. E. Featherstone. "GRACE-derived ice-mass variations over Greenland by accounting for leakage effects". In: *Journal of Geophysical Research: Solid Earth* 114.B6 (2009). DOI: https://doi.org/10.1029/2008JB006239.

Behzadpour, S., T. Mayer-Gürr, J. Flury, B. Klinger, and S. Goswami. "Multiresolution wavelet analysis applied to GRACE range-rate residuals". In: *Geoscientific Instrumentation, Methods and Data Systems* 8.2 (2019), pp. 197–207. DOI: 10.5194/gi-8-197-2019.

Behzadpour, S., T. Mayer-Gürr, and S. Krauss. "GRACE Follow-On Accelerometer Data Recovery". In: *Journal of Geophysical Research: Solid Earth* 126.5 (2021). e2020JB021297 2020JB021297, e2020JB021297. DOI: 10.1029/2020JB021297.

Benveniste, J. et al. "Requirements for a Coastal Hazards Observing System". In: *Frontiers in Marine Science* 6 (2019), p. 348. ISSN: 2296-7745. DOI: 10.3389/fmars.2019.00348.

Bettadpur, S. *Gravity Recovery and Climate Experiment - Level-2 Gravity Field Product User Handbook*. Tech. rep. GRACE 327-734 (CSR-GR-03-01, Rev. 4.0). Center for Space Research, The University of Texas at Austin, 2018.

Bettadpur, S. *Gravity Recovery and Climate Experiment - Product Specification Document*. Tech. rep. GRACE 327-720 (CSR-GR-03-02, Rev. 4.6). Center for Space Research, The University of Texas at Austin, 2012.

Bettadpur, S. *Recommendation for a-priori Bias & Scale Parameters for Level-1B ACC Data*. Tech. rep. GRACE TN-02, Version 2. Center for Space Research, The University of Texas at Austin, 2009.

Bettadpur, S. and C. McCullough. *The Classical Variational Approach*. Ed. by M. Naeimi and J. Flury. Cham, Switzerland: Springer International Publishing, 2017, pp. 81–95. ISBN: 978-3-319-49940-6. DOI: 10.1007/978-3-319-49941-3_3.

Beutler, G. *Methods of Celestial Mechanics - Volume II: Application to Planetary System, Geodynamics and Satellite Geodesy*. Berlin, Heidelberg: Springer-Verlag, 2005. ISBN: 978-3-540-40750-8. DOI: 10.1007/b137725.

Beutler, G., A. Jäggi, U. Hugentobler, and L. Mervart. "Efficient satellite orbit modelling using pseudo-stochastic parameters". In: *Journal of Geodesy* 80 (2006), pp. 353–372. DOI: 10.1007/s00190-006-0072-6.

Beutler, G., A. Jäggi, L. Mervart, and U. Meyer. "The celestial mechanics approach: Theoretical foundations". In: *Journal of Geodesy* 84 (2010), pp. 605–624. DOI: 10.1007/s00190-010-0401-7.

Bezděk, A. "Calibration of accelerometers aboard GRACE satellites by comparison with POD-based nongravitational accelerations". In: *Journal of Geodynamics* 50.5 (2010), pp. 410–423. ISSN: 0264-3707. DOI: https://doi.org/10.1016/j.jog.2010.05.001.

Bezděk, A., J. Sebera, and J. Klokočník. "Calibration of Swarm accelerometer data by GPS positioning and linear temperature correction". In: *Advances in Space Research* 62.2 (2018), pp. 317–325. ISSN: 0273-1177. DOI: https://doi.org/10.1016/j.asr.2018.04.041.

Bezděk, A., J. Sebera, and J. Klokočník. "Validation of Swarm accelerometer data by modelled nongravitational forces". In: *Advances in Space Research* 59.1 (2017), pp. 2512–2521. ISSN: 1572-9672. DOI: 10.1016/j.asr.2017.02.037.

Bezděk, A., J. Sebera, J. Teixeira da Encarnação, and J. Klokočník. "Time-variable gravity fields derived from GPS tracking of Swarm". In: *Geophysical Journal International* 205.3 (2016), pp. 1665–1669. DOI: 10.1093/gji/ggw094.

Biancale, R., G. Balmino, J.-M. Lemoine, J.-C. Marty, B. Moynot, F. Barlier, P. Exertier, O. Laurain, P. Gegout, P. Schwintzer, C. Reigber, A. Bode, R. König, F.-H. Massmann, J.-C. Raimondo, R. Schmidt, and S. Yuan Zhu. "A new global Earth's gravity field model from satellite orbit perturbations: GRIM5-S1". In: *Geophysical Research Letters* 27.22 (2000), pp. 3611–3614. DOI: https://doi.org/10.1029/2000GL011721.

Bianco, G., R. Devoti, M. Fermi, V. Luceri, P. Rutigliano, and C. Sciarretta. "Estimation of low degree geopotential coefficients using SLR data". In: *Planetary and Space Science* 46.11 (1998). Second Italian Meeting on Celestial Mechanics, pp. 1633–1638. ISSN: 0032-0633. DOI: https://doi.org/10.1016/S0032-0633(97)00215-8.

Bjerhammar, A. "On the energy integral for satellites1". In: *Tellus* 21.1 (1969), pp. 1–9. DOI: 10.1111/j.2153-3490.1969.tb00412.x.

Blewitt, G. "Self-consistency in reference frames, geocenter definition, and surface loading of the solid Earth". In: *Journal of Geophysical Research: Solid Earth* 108.B2 (2003). DOI: https://doi.org/10.1029/2002JB002082.

Bloxham, J., S. Zatman, and M. Dumberry. "The Origin of Geomagnetic Jerks". In: *Nature* 420 (2002), pp. 65–8. DOI: 10.1038/nature01134.

Boening, C., J. K. Willis, F. W. Landerer, R. S. Nerem, and J. Fasullo. "The 2011 La Niña: So strong, the oceans fell". In: *Geophysical Research Letters* 39.19 (2012). DOI: https://doi.org/10.1029/2012GL053055.

Boergens, E., A. Güntner, H. Dobslaw, and C. Dahle. "Quantifying the Central European Droughts in 2018 and 2019 With GRACE Follow-On". In: *Geophysical Research Letters* 47.14 (2020). e2020GL087285 10.1029/2020GL087285, e2020GL087285. DOI: https://doi.org/10.1029/2020GL087285.

Bruinsma, S., A. Jäggi, and N.]Sánchez-Ortiz. "Semi-empirical thermosphere model evaluation at low altitude with GOCE densities". In: *Journal of Space Weather and Space Climate* 7 (2017), A4. DOI: 10.1051/swsc/2017003.

Carrère, L., F. Lyard, M. Cancet, A. Guillot, and N. Picot. "FES 2014, a new tidal model - Validation results and perspectives for improvements". In: *Proceedings of the ESA Living Planet Symposium 2016, Prague, Czech Republic* (2016).

Case, K., G. Kruizinga, and S.-C. Wu. *GRACE Level 1B Data ProductUser Handbook*. Tech. rep. JPL D-22027. Jet Propulsion Laboratory, California Institute of Technology, 2010.

Cazenave, A., N. Champollion, F. Paul, and J. Benveniste. *Integrative Study of the Mean Sea Level and Its Components*. Vol. 58. Space Sciences Series of ISSI. 2017. ISBN: 978-3-319-56489-0. DOI: 10.1007/978-3-319-56490-6.

Cazenave, A. and S. Daillet. "Lunar tidal acceleration from Earth satellite orbit analyses". In: *Journal of Geophysical Research: Solid Earth* 86.B3 (1981), pp. 1659–1663. DOI: https://doi.org/10.1029/JB086iB03p01659.

Cazenave, A., H.-B. Dieng, B. Meyssignac, K. Schuckmann, B. Decharme, and E. Berthier. "The rate of sea-level rise". In: *Nature Climate Change* 4 (2014), pp. 358–361. DOI: 10.1038/nclimate2159.

Cazenave, A., O. Henry, S. Munier, T. Delcroix, A. L. Gordon, B. Meyssignac, W. Llovel, H. Palanisamy, and M. Becker. "Estimating ENSO Influence on the Global Mean Sea Level, 1993–2010". In: *Marine Geodesy* 35.sup1 (2012), pp. 82–97. DOI: 10.1080/01490419.2012.718209.

Chambers, D. P. "Calculating trends from GRACE in the presence of large changes in continental ice storage and ocean mass". In: *Geophysical Journal International* 176.2 (2009), pp. 415–419. ISSN: 0956-540X. DOI: 10.1111/j.1365-246X.2008.04012.x.

Chambers, D. P. and J. A. Bonin. "Evaluation of Release-05 GRACE time-variable gravity coefficients over the ocean". In: *Ocean Science* 8.5 (2012), pp. 859–868. DOI: 10.5194/os-8-859-2012.

Chambers, D. P., A. Cazenave, N. Champollion, H.-B. Dieng, W. Llovel, R. Forsberg, K. Schuckmann, and Y. Wada. "Evaluation of the Global Mean Sea Level Budget Between 1993 and 2014". In: *Surveys in Geophysics* 38 (2017), pp. 309–327. DOI: 10.1007/s10712-016-9381-3.

Chelton, D. B., E. J. Walsh, and J. L. MacArthur. "Pulse Compression and Sea Level Tracking in Satellite Altimetry". In: *Journal of Atmospheric and Oceanic Technology* 6.3 (1989), pp. 407–438. DOI: 10.1175/1520-0426(1989)006<0407:PCASLT>2.0.CO;2.

Chen, J. L., M. Rodell, C. R. Wilson, and J. S. Famiglietti. "Low degree spherical harmonic influences on Gravity Recovery and Climate Experiment (GRACE) water storage estimates". In: *Geophysical Research Letters* 32.14 (2005). DOI: 10.1029/2005GL022964.

Chen, J. L., C. R. Wilson, and K.-W. Seo. "S_2 tide aliasing in GRACE time-variable gravity solutions". In: *Journal of Geodesy* 83 (2009), pp. 679–687. DOI: 10.1007/s00190-008-0282-1.

Chen, J., B. Tapley, H. Save, M. E. Tamisiea, S. Bettadpur, and J. C. Ries. "Quantification of Ocean Mass Change Using Gravity Recovery and Climate Experiment, Satellite Altimeter, and

Argo Floats Observations". In: *Journal of Geophysical Research: Solid Earth* 123.11 (2018), pp. 10, 212–10, 225. DOI: 10.1029/2018JB016095.

Chen, Q., Y. Shen, W. Chen, O. Francis, X. Zhang, Q. Chen, W. Li, and T. Chen. "An Optimized Short-Arc Approach: Methodology and Application to Develop Refined Time Series of Tongji-Grace2018 GRACE Monthly Solutions". In: *Journal of Geophysical Research: Solid Earth* 124.6 (2019), pp. 6010–6038. DOI: https://doi.org/10.1029/2018JB016596.

Chen, Q., Y. Shen, O. Francis, W. Chen, X. Zhang, and H. Hsu. "Tongji-Grace02s and Tongji-Grace02k: High-Precision Static GRACE-Only Global Earth's Gravity Field Models Derived by Refined Data Processing Strategies". In: *Journal of Geophysical Research: Solid Earth* 123.7 (2018), pp. 6111–6137. DOI: https://doi.org/10.1029/2018JB015641.

Cheng, M. and J. C. Ries. "The unexpected signal in GRACE estimates of C_{20}". In: *Journal of Geodesy* 91 (2017). DOI: 10.1007/s00190-016-0995-5.

Cheng, M., C. K. Shum, and B. D. Tapley. "Determination of long-term changes in the Earth's gravity field from satellite laser ranging observations". In: *Journal of Geophysical Research: Solid Earth* 102.B10 (1997), pp. 22377–22390. DOI: https://doi.org/10.1029/97JB01740.

Cheng, M., B. D. Tapley, and J. C. Ries. "Deceleration in the Earth's oblateness". In: *Journal of Geophysical Research: Solid Earth* 118.2 (2013), pp. 740–747. DOI: 10.1002/jgrb.50058.

Cheng, M., B. D. Tapley, and J. C. Ries. *Geocenter Variations from Analysis of SLR Data*. Ed. by Z. Altamimi and X. Collilieux. Vol. 138. Berlin, Heidelberg: Springer-Verlag, 2013, pp. 19–25. ISBN: 978-3-642-32998-2. DOI: https://doi.org/10.1007/978-3-642-32998-2_4.

Cherniak, I., I. Zakharenkova, and S. Sokolovsky. "Multi-Instrumental Observation of Storm-Induced Ionospheric Plasma Bubbles at Equatorial and Middle Latitudes". In: *Journal of Geophysical Research: Space Physics* 124.3 (2019), pp. 1491–1508. DOI: 10.1029/2018JA026309.

Church, J. A., P. U. Clark, A. Cazenave, J. M. Gregory, S. Jevrejeva, A. Levermann, M. A. Merrifield, G. A. Milne, R. S. Nerem, P. D. Nunn, A. J. Payne, W. T. Pfeffer, D. Stammer, and A. S. Unnikrishnan. "Sea Level Change". In: *Climate Change 2013: The Physical Science Basis. Contribution of Working Group I to the Fifth Assessment Report of the Intergovernmental Panel on Climate Change*. Ed. by T. F. Stocker, D. Qin, G.-K. Plattner, M. Tignor, S. K. Allen, J. Boschung, A. Nauels, Y. Xia, V. Bex, and P. M. Midgley. Cambridge, United Kingdom and New York, NY, USA: Cambridge University Press, 2013. Chap. 13, pp. 1137–1216. ISBN: ISBN 978-1-107-66182-0. DOI: 10.1017/CBO9781107415324.026.

Cooley, S. S. and F. W. Landerer. *Gravity Recovery and Climate Experiment Follow-On - Level-3 Data Product User Handbook*. Tech. rep. GRACE D-103133. Jet Propulsion Laboratory, California Institute of Technology, 2020.

Cox, C. M. and B. F. Chao. "Detection of a Large-Scale Mass Redistribution in the Terrestrial System Since 1998". In: *Science* 297.5582 (2002), pp. 831–833. ISSN: 0036-8075. DOI: 10.1126/science.1072188.

Crétaux, J.-F., K. Nielsen, F. Frappart, F. Papa, S. Calmant, and J. Benveniste. "Hydrological Applications of Satellite AltimetryRivers, Lakes, Man-Made Reservoirs, Inundated Areas". In: *Satellite Altimetry over Oceans and Land Surfaces (1st ed.)* Ed. by D. Stammer and A. Cazenave. London, UK: Taylor & Francis Inc, 2017, pp. 459–504. ISBN: 9781315151779. DOI: 10.1201/9781315151779-14.

Dahle, C., D. Arnold, and A. Jäggi. "Impact of tracking loop settings of the Swarm GPS receiver on gravity field recovery". In: *Advances in Space Research* 59.12 (2017). DOI: 10.1016/j.asr.2017.03.003.

Dahle, C., F. Flechtner, M. Murböck, G. Michalak, H. Neumayer, O. Abrykosov, A. Reinhold, and R. König. *Gravity Recovery and Climate Experiment Follow-On - GFZ Level-2 Processing Standards Document for Level-2 Product Release 06*. Tech. rep. GRACE-FO D-103919, Rev. 1.0. GFZ German Research Centre for Geosciences, Potsdam, 2019.

Dahle, C., M. Murböck, F. Flechtner, H. Dobslaw, G. Michalak, K. Neumayer, O. Abrykosov, A. Reinhold, R. König, R. Sulzbach, and C. Foerste. "The GFZ GRACE RL06 Monthly Gravity Field Time Series: Processing Details and Quality Assessment". In: *Remote Sensing* 11 (2019), p. 2116. DOI: 10.3390/rs11182116.

de Teixeira da Encarnação, J., P. N. A. M. Visser, D. Arnold, A. Bezděk, E. Doornbos, M. Ellmer, J. Guo, J. van den IJssel, E. Iorfida, A. Jäggi, J. Klokocník, S. Krauss, X. Mao, T. Mayer-Gürr, U. Meyer, J. Sebera, C. K. Shum, C. Zhang, Y. Zhang, and C. Dahle. "Description of the multi-approach gravity field models from Swarm GPS data". In: *Earth System Science Data* 12.2 (2020), pp. 1385–1417. DOI: 10.5194/essd-12-1385-2020.

Deng, L., Z. Li, N. Wei, Y. Ma, and H. Chen. "GPS-derived geocenter motion from the IGS second reprocessing campaign". In: *Earth, Planets and Space* 71 (2019). DOI: 10.1186/s40623-019-1054-2.

Desai, S. D. "Observing the pole tide with satellite altimetry". In: *Journal of Geophysical Research: Oceans* 107.C11 (2002), pp. 7-1-7-13. DOI: 10.1029/2001JC001224.

Didova, O., B. Gunter, R. Riva, R. Klees, and L. Roese-Koerner. "An approach for estimating time-variable rates from geodetic time series". In: *Journal of Geodesy* 90.11 (2016), pp. 1207–1221.

Ditmar, P., V. Kuznetsov, A. van Eck van der Sluijs, E. Schrama, and R. Klees. "'DEOS_CHAMP-01C_70': a model of the Earth's gravity field computed from accelerations of the CHAMP satellite". In: *Journal of Geodesy* 79.10-11 (2006), pp. 586–601. DOI: 10.1007/s00190-005-0008-6.

Ditmar, P. and A. van Eck van der Sluijs. "A technique for modeling the Earth's gravity field on the basis of satellite accelerations". In: *Journal of Geodesy* 78.1-2 (2004), pp. 12–33.

Dobslaw, H., I. Bergmann-Wolf, R. Dill, L. Poropat, and F. Flechtner. *Gravity Recovery and Climate Experiment - Product Description Document for AOD1B Release 06*. Tech. rep. GRACE 327-750, Rev. 6.1. Geoforschungszentrum Potsdam, 2017.

Dobslaw, H., I. Bergmann-Wolf, R. Dill, L. Poropat, M. Thomas, C. Dahle, S. Esselborn, R. König, and F. Flechtner. "A new high-resolution model of non-tidal atmosphere and ocean mass variability for de-aliasing of satellite gravity observations: AOD1B RL06". In: *Geophysical Journal International* 211.1 (2017), pp. 263–269. ISSN: 0956-540X. DOI: 10.1093/gji/ggx302.

Doelling, D. R., M. Sun, L. T. Nguyen, M. L. Nordeen, C. O. Haney, D. F. Keyes, and P. E. Mlynczak. "Advances in Geostationary-Derived Longwave Fluxes for the CERES Synoptic (SYN1deg) Product". In: *Journal of Atmospheric and Oceanic Technology* 33.3 (2016), pp. 503–521. DOI: 10.1175/JTECH-D-15-0147.1.

Döll, P., F. Kaspar, and B. Lehner. "A global hydrological model for deriving water availability indicators: Model tuning and validation". In: *Journal of Hydrology* 270 (2003), pp. 105–134. DOI: 10.1016/S0022-1694(02)00283-4.

Döll, P., H. Müller Schmied, C. Schuh, F. T. Portmann, and A. Eicker. "Global-scale assessment of groundwater depletion and related groundwater abstractions: Combining hydrological modeling with information from well observations and GRACE satellites". In: *Water Resources Research* 50.7 (2014), pp. 5698–5720. DOI: https://doi.org/10.1002/2014WR015595.

Doornbos, E. *Thermospheric Density and Wind Determination from Satellite Dynamics*. Berlin, Heidelberg: Springer-Verlag, 2012. ISBN: 9783642251290. DOI: 10.1007/978-3-642-25129-0.

Drinkwater, M. R., R. Floberghagen, R. Haagmans, D. Muzi, and A. Popescu. "GOCE: ESA's First Earth Explorer Core Mission". In: *Earth Gravity Field from Space — From Sensors to Earth Sciences: Proceedings of an ISSI Workshop 11–15 March 2002, Bern, Switzerland*. Ed. by G. Beutler, M. R. Drinkwater, R. Rummel, and R. Von Steiger. Dordrecht: Springer Netherlands, 2003, pp. 419–432. ISBN: 978-94-017-1333-7. DOI: 10.1007/978-94-017-1333-7_36.

Dziewonski, A. M. and D. L. Anderson. "Preliminary reference Earth model". In: *Physics of the Earth and Planetary Interiors* 25.4 (1981), pp. 297–356. ISSN: 0031-9201. DOI: https://doi.org/10.1016/0031-9201(81)90046-7.

Ebbing, J., P. Haas, F. Pappa, W. Szwillus, and J. Bouman. "Earth tectonics as seen by GOCE - Enhanced satellite gravity gradient imaging". In: *Scientific Reports* 8 (2018). DOI: 10.1038/s41598-018-34733-9.

Eicker, A. "Gravity Field Refinement by Radial Basis Functions from In-situ Satellite Data". Dissertation. Bonn, Germany: Universität Bonn, 2008.

Emmert, J. T., D. P. Drob, J. M. Picone, D. E. Siskind, M. Jones Jr., M. G. Mlynczak, P. F. Bernath, X. Chu, E. Doornbos, B. Funke, L. P. Goncharenko, M. E. Hervig, M. J. Schwartz, P. E. Sheese, F. Vargas, B. P. Williams, and T. Yuan. "NRLMSIS 2.0: A Whole-Atmosphere Empirical Model of Temperature and Neutral Species Densities". In: *Earth and Space Science* 8.3 (2021). e2020EA001321 2020EA001321, e2020EA001321. DOI: https://doi.org/10.1029/2020EA001321.

Farrell, W. E. "Deformation of the Earth by surface loads". In: *Reviews of Geophysics* 10.3 (1972), pp. 761–797. DOI: 10.1029/RG010i003p00761.

Farrell, W. E. and J. A. Clark. "On Postglacial Sea Level". In: *Geophysical Journal of the Royal Astronomical Society* 46.3 (1976), pp. 647–667. DOI: https://doi.org/10.1111/j.1365-246X.1976.tb01252.x.

Fedosov, V. and R. Peřestý. "Measurement of Microaccelerations on Board of the LEO Spacecraft". In: *IFAC Proceedings Volumes* 44.1 (2011). 18th IFAC World Congress, pp. 1883–1888. ISSN: 1474-6670. DOI: https://doi.org/10.3182/20110828-6-IT-1002.01873.

Finlay, C., N. Olsen, S. Kotsiaros, N. Gillet, and L. Tøffner-Clausen. "Recent geomagnetic secular variation from Swarm and ground observatories as estimated in the CHAOS-6 geomagnetic field model". In: *Earth, Planets and Space* 68 (2016). DOI: 10.1186/s40623-016-0486-1.

Flury, J., S. Bettadpur, and B. D. Tapley. "Precise accelerometry onboard the GRACE gravity field satellite mission". In: *Advances in Space Research* 42 (2008), pp. 1414–1423. DOI: 10.1016/j.asr.2008.05.004.

Foerste, C., S. Bruinsma, O. Abrykosov, J.-M. Lemoine, J. C. Marty, F. Flechtner, G. Balmino, F. Barthelmes, and R. Biancale. *EIGEN-6C4 The latest combined global gravity field model including GOCE data up to degree and order 2190 of GFZ Potsdam and GRGS Toulouse*. GFZ Data Services. 2014. DOI: 10.5880/icgem.2015.1.

Földváry, L., D. Švehla, C. Gerlach, M. Wermuth, T. Gruber, R. Rummel, M. Rothacher, B. Frommknecht, T. Peters, and P. Steigenberger. "Gravity Model TUM-2Sp Based on the Energy Balance Approach and Kinematic CHAMP Orbits". In: *Earth Observation with CHAMP: Results from Three Years in Orbit*. Ed. by C. Reigber, H. Lühr, P. Schwintzer, and J. Wickert. Berlin, Heidelberg: Springer Berlin Heidelberg, 2005, pp. 13–18. ISBN: 978-3-540-26800-0. DOI: 10.1007/3-540-26800-6_2.

Folkner, W. M., J. G. Williams, and D. H. Boggs. *The Planetary and Lunar Ephemeris DE 421*. Tech. rep. Jet Propulsion Laboratory, 2009.

Frederikse, T., R. Riva, M. Kleinherenbrink, Y. Wada, M. van den Broeke, and B. Marzeion. "Closing the sea level budget on a regional scale: Trends and variability on the Northwestern European continental shelf". In: *Geophysical Research Letters* 43.20 (2016), pp. 10, 864–10, 872. DOI: https://doi.org/10.1002/2016GL070750.

Friis-Christensen, E., H. Lühr, and G. Hulot. "Swarm: A constellation to study the Earth's magnetic field". In: *Earth, Planets, and Space* 58 (2006), pp. 351–358. DOI: 10.1186/BF03351933.

Friis-Christensen, E., H. Lühr, D. Knudsen, and R. Haagmans. "Swarm – An Earth Observation Mission investigating Geospace". In: *Advances in Space Research* 41.1 (2008), pp. 210–216. ISSN: 0273-1177. DOI: https://doi.org/10.1016/j.asr.2006.10.008.

Gardner, A. S., G. Moholdt, J. G. Cogley, B. Wouters, A. A. Arendt, J. Wahr, E. Berthier, R. Hock, W. T. Pfeffer, G. Kaser, S. R. M. Ligtenberg, T. Bolch, M. J. Sharp, J. O. Hagen, M. R. van den Broeke, and F. Paul. "A Reconciled Estimate of Glacier Contributions to Sea Level Rise: 2003 to 2009". In: *Science* 340.6134 (2013), pp. 852–857. ISSN: 0036-8075. DOI: 10.1126/science.1234532.

Gerdener, H., O. Engels, and J. Kusche. "A framework for deriving drought indicators from the Gravity Recovery and Climate Experiment (GRACE)". In: *Hydrology and Earth System Sciences* 24.1 (2020), pp. 227–248. DOI: 10.5194/hess-24-227-2020.

Gerlach, h., L. Földvary, D. Švehla, T. Gruber, M. Wermuth, N. Sneeuw, B. Frommknecht, H. Oberndorfer, T. Peters, M. Rothacher, R. Rummel, and P. Steigenberger. "A CHAMP-only gravity field model from kinematic orbits using the energy integral". In: *Geophysical Research Letters* 30.20 (2003). DOI: 10.1029/2003GL018025.

Gould, J., D. Roemmich, S. Wijffels, H. Freeland, M. Ignaszewsky, X. Jianping, S. Pouliquen, Y. Desaubies, U. Send, K. Radhakrishnan, K. Takeuchi, K. Kim, M. Danchenkov, P. Sutton, B. King, B. Owens, and S Riser. "Argo profiling floats bring new era of in situ ocean observations". In: *Eos, Transactions American Geophysical Union* 85.19 (2004), pp. 185–191. DOI: https://doi.org/10.1029/2004EO190002.

Gouweleeuw, B. T., A. Kvas, C. Gruber, A. K. Gain, T. Mayer-Gürr, F. Flechtner, and A. Güntner. "Daily GRACE gravity field solutions track major flood events in the Ganges–Brahmaputra Delta". In: *Hydrology and Earth System Sciences* 22.5 (2018), pp. 2867–2880. DOI: 10.5194/hess-22-2867-2018.

Gruber, C., D. Tsoulis, and N. Sneeuw. "Champ Accelerometer Calibration by Means of the Equation of Motion and an a-priori Gravity Model". In: *Zeitschrift fuer Vermessungswesen* 130 (2005), pp. 92–98.

Guo, J.-Y., K. Shang, C. Jekeli, and C. K. Shum. "On the energy integral formulation of gravitational potential differences from satellite-to-satellite tracking". In: *Celestial Mechanics and Dynamical Astronomy* 121 (2015), pp. 415–429. DOI: 10.1007/s10569-015-9610-y.

Guo, X. and Q. Zhao. "A New Approach to Earth's Gravity Field Modeling Using GPS-Derived Kinematic Orbits and Baselines". In: *Remote Sensing* 11.14 (2019). ISSN: 2072-4292. DOI: 10.3390/rs11141728.

Gurtner, W. and L. Estey. *RINEX - The Receiver Independent Exchange Format Version 3.00*. Tech. rep. Bern, Switzerland: Astronomical Institute, University of Bern, 2007.

Han, S.-C., C. Jekeli, and C. K. Shum. "Efficient gravity field recovery using in situ disturbing potential observables from CHAMP". In: *Geophysical Research Letters* 29.16 (2002), pp. 36-1-36-4. DOI: 10.1029/2002GL015180.

Han, S.-C., C. K. Shum, and C. Jekeli. "Precise estimation of in situ geopotential differences from GRACE low-low satellite-to-satellite tracking and accelerometer data". In: *Journal of Geophysical Research: Solid Earth* 111.B4 (2006). DOI: 10.1029/2005JB003719.

He, M., B. D. Tapley, and R. J. Eanes. "Earth Rotation Parameters Deduced From Starlette Laser Ranging". In: *Science in China Series A-Mathematics, Physics, Astronomy & Technological Science* 25.10 (1982), pp. 1090–1098. DOI: 10.1360/ya1982-25-10-1090.

Herceg, M., P. S. Jørgensen, and J. L. Jørgensen. "Characterization and compensation of thermoelastic instability of SWARM optical bench on micro Advanced Stellar Compass attitude observations". In: *Acta Astronautica* 137 (2017), pp. 205–213. ISSN: 0094-5765. DOI: https://doi.org/10.1016/j.actaastro.2017.04.018.

Hofmann-Wellenhof, B. and H. Moritz. "Physical Geodesy". In: (2006). DOI: 10.1007/978-3-211-33545-1.

Holme, R. "Electromagnetic core-mantle coupling:: III. Laterally varying mantle conductance". In: *Physics of the Earth and Planetary Interiors* 117 (2000), pp. 329–344. DOI: 10.1016/S0031-9201(99)00105-3.

Holme, R. and O. de Viron. "Geomagnetic jerks and a high-resolution length-of-day profile for core studies". In: *Geophysical Journal International* 160.2 (2005), pp. 435–439. ISSN: 0956-540X. DOI: 10.1111/j.1365-246X.2004.02510.x.

Hulot, G., P. Vigneron, J.-M. Léger, I. Fratter, N. Olsen, T. Jager, F. Bertrand, L. Brocco, O. Sirol, X. Lalanne, A. Boness, and V. Cattin. "Swarm's absolute magnetometer experimental vector mode, an innovative capability for space magnetometry". In: *Geophysical Research Letters* 42.5 (2015), pp. 1352–1359. DOI: 10.1002/2014GL062700.

Humphrey, V. and L. Gudmundsson. "GRACE-REC: a reconstruction of climate-driven water storage changes over the last century". In: *Earth System Science Data* 11.3 (2019), pp. 1153–1170. DOI: 10.5194/essd-11-1153-2019.

IAG. "Resolutions of the XVIII General Assembly of the International Association of Geodesy". In: *Bulletin Géodésique* 58.3 (1984), pp. 309–323. DOI: 10.1007/BF02519005.

Jäggi, A. and D. Arnold. "Precise Orbit Determination". In: *Global Gravity Field Modeling from Satellite-to-Satellite Tracking Data, Lecture Notes in Earth System Sciences*. Ed. by M. Naeimi

and J. Flury. Cham, Switzerland: Springer International Publishing, 2017, pp. 35–80. ISBN: 978-3-319-49940-6. DOI: 10.1007/978-3-319-49941-3_2.

Jäggi, A., H. Bock, L. Prange, U. Meyer, and G. Beutler. "GPS-only gravity field recovery with GOCE, CHAMP, and GRACE". In: *Advances in Space Research* 47.6 (2011), pp. 1020–1028. ISSN: 0273-1177. DOI: https://doi.org/10.1016/j.asr.2010.11.008.

Jäggi, A., C. Dahle, D. Arnold, H. Bock, U. Meyer, G. Beutler, and J. van den IJssel. "Swarm kinematic orbits and gravity fields from 18 months of GPS data". In: *Advances in Space Research* 57.1 (2016), pp. 218–233. DOI: 10.1016/j.asr.2015.10.035.

Jäggi, A., U. Hugentobler, and G. Beutler. "Pseudo-Stochastic Orbit Modeling Techniques for Low-Earth Orbiters". In: *Journal of Geodesy* 80 (2006), pp. 47–60. DOI: 10.1007/s00190-006-0029-9.

Jault, D. "Electromagnetic and topographic coupling, and LOD variations". In: *Earth's Core and Lower Mantle. Series: The Fluid Mechanics of Astrophysics and Geophysics*. Ed. by K. Zhang, A. M. Soward, and C. A. Jones. London, UK: CRC Press, 2003, pp. 56–76. ISBN: 978-0-415-30936-3. DOI: 10.1201/9780203207611.ch3.

Jekeli, C. *Alternative Methods to Smooth the Earth's Gravity Field*. Tech. rep. 327. Columbus, Ohio, USA: Ohio State University, 1981.

Jekeli, C. "The determination of gravitational potential differences from satellite-to-satellite tracking". In: *Celestial Mechanics and Dynamical Astronomy* 75 (1999), pp. 85–101. DOI: 10.1023/A:1008313405488.

Jevrejeva, S., J. C. Moore, A. Grinsted, A. P. Matthews, and G. Spada. "Trends and acceleration in global and regional sea levels since 1807". In: *Global and Planetary Change* 113 (2014), pp. 11–22. ISSN: 0921-8181. DOI: https://doi.org/10.1016/j.gloplacha.2013.12.004.

Jiménez-Muñoz, J. C., C. Mattar, J. Barichivich, A. Santamaría-Artigas, K. Takahashi, Y. Malhi, J. A. Sobrino, and G. van der Schrier. "Record-breaking warming and extreme drought in the Amazon rainforest during the course of El Niño 2015–2016". In: *Scientific Reports* 6 (2016). DOI: 10.1038/srep33130.

Johannessen, J., G. Balmino, C. Provost, R. Rummel, R. Sabadini, H. Sünkel, C. C. Tscherning, P. N. A. M. Visser, P. Woodworth, C. Hughes, P. Legrand, N. Sneeuw, F. Perosanz, M. Aguirre-Martinez, H. Rebhan, and M. Drinkwater. "The European Gravity Field and Steady-State Ocean Circulation Explorer Satellite Mission Its Impact on Geophysics". In: *Surveys in Geophysics* 24 (2003), pp. 339–386. DOI: 10.1023/B:GEOP.0000004264.04667.5e.

Johannessen, O. M., E. Augenstein, F. Becker, B. Carli, A. Holligsworth, M. Jacob, A. Korosov, G. Konecny, J.-P. Malingreau, G. Mègie, J.-F. Minister, H. Rott, and R. Rummel. *The Science and Research Elements of ESA's Living Planet Programme*. Tech. rep. European Space Agency, 1998.

Johnson, G. C. and D. P. Chambers. "Ocean bottom pressure seasonal cycles and decadal trends from GRACE Release-05: Ocean circulation implications". In: *Journal of Geophysical Research: Oceans* 118.9 (2013), pp. 4228–4240. DOI: https://doi.org/10.1002/jgrc.20307.

Jungclaus, J. H., N. Fischer, H. Haak, K. Lohmann, J. Marotzke, D. Matei, U. Mikolajewicz, D. Notz, and J. S. von Storch. "Characteristics of the ocean simulations in the Max Planck Institute Ocean Model (MPIOM) the ocean component of the MPI-Earth system model". In: *Journal of Advances in Modeling Earth Systems* 5.2 (2013), pp. 422–446. DOI: https://doi.org/10.1002/jame.20023.

Kaula, W. M. *Theory of Satellite Geodesy: Applications of Satellites to Geodesy*. Dover Publishing Company, reprint, 1966.

Kervalishvili, G. *Swarm Level 2 Processing System - Product specification for L2 Products and Auxiliary Products*. Tech. rep. SW-DS-DTU-GS-0001-Rev:2Y. Potsdam, Germany: British Geological Survey, National Space Institute – DTU Space, Delft Institute of Earth Observation and Space Systems, Helmholtz Centre Potsdam - German Research Centre for Geosciences, Eidgenössische Technische Hochschule Zürich, Institut de Physique du Globe de Paris, 2019.

Klinger, B. "A contribution to GRACE time-variable gravity field recovery: Improved Level-1B data pre-processing methodologies". Dissertation. Graz, Austria: Graz University of Technology, 2018.

Klinger, B. and T. Mayer-Gürr. "The role of accelerometer data calibration within GRACE gravity field recovery: Results from ITSG-Grace2016". In: *Advances in Space Research* 58.9 (2016), pp. 1597–1609. DOI: 10.1016/j.asr.2016.08.007.

Knudsen, D. J., J. K. Burchill, S. C. Buchert, A. I. Eriksson, R. Gill, J.-E. Wahlund, L. Åhlen, M. Smith, and B. Moffat. "Thermal ion imagers and Langmuir probes in the Swarm electric field instruments". In: *Journal of Geophysical Research: Space Physics* 122.2 (2017), pp. 2655–2673. DOI: 10.1002/2016JA022571.

Koch, K.-R. *Parameter Estimation and Hypothesis Testing in Linear Models*. 2nd ed. Berlin, Heidelberg: Springer-Verlag, 1999. ISBN: 978-3-540-65257-1.

Koch, K.-R. and J. Kusche. "Regularization of geopotential determination from satellite data by variance components". In: *Journal of Geodesy* 76.5 (2002), pp. 259–268. DOI: 10.1007/s00190-002-0245-x.

Kornfeld, R. P., B. W. Arnold, M. A. Gross, N. T. Dahya, W. M. Klipstein, P. F. Gath, and S. Bettadpur. "GRACE-FO: The Gravity Recovery and Climate Experiment Follow-On Mission". In: *Journal of Spacecraft and Rockets* 56.3 (2019), pp. 931–951. DOI: 10.2514/1.A34326.

Kusche, J. "Approximate decorrelation and non-isotropic smoothing of time-variable GRACE-type gravity field models". In: *Journal of Geodesy* 81.11 (2007), pp. 733–749. DOI: 10.1007/s00190-007-0143-3.

Kusche, J. and J. Loon. "Statistical Assessment of CHAMP Data and Models Using the Energy Balance Approach". In: *Earth Observation with CHAMP Results from Three Years in Orbit*. Ed. by C. Reigber, H. Lühr, P. Schwintzer, and J. Wickert. Berlin, Heidelberg: Springer-Verlag, 2005, pp. 133–138. ISBN: 978-3-540-22804-2. DOI: 10.1007/3-540-26800-6_21.

Kusche, J., R. Schmidt, S. Petrovic, and R. Rietbroek. "Decorrelated GRACE time-variable gravity solutions by GFZ, and their validation using a hydrological model". In: *Journal of Geodesy* 83.10 (2009), pp. 903–913. DOI: 10.1007/s00190-009-0308-3.

Kuvshinov, A., T. Sabaka, and N. Olsen. "3-D electromagnetic induction studies using the Swarm constellation: Mapping conductivity anomalies in the Earth's mantle". In: *Earth Planets Space* 58 (2006), pp. 417–427. DOI: 10.1186/BF03351938.

Kvas, A., S. Behzadpour, M. Ellmer, B. Klinger, S. Strasser, N. Zehentner, and T. Mayer-Gürr. "ITSG-Grace2018: Overview and Evaluation of a New GRACE-Only Gravity Field Time Series". In: *Journal of Geophysical Research: Solid Earth* 124.8 (2019), pp. 9332–9344. DOI: 10.1029/2019JB017415.

Kvas, A., J. M. Brockmann, S. Krauss, T. Schubert, T. Gruber, U. Meyer, T. Mayer-Gürr, W.-D. Schuh, A. Jäggi, and R. Pail. "GOCO06s – a satellite-only global gravity field model". In: *Earth System Science Data* 13.1 (2021), pp. 99–118. DOI: 10.5194/essd-13-99-2021.

Kvas, A. and T. Mayer-Gürr. "GRACE gravity field recovery with background model uncertainties". In: *Journal of Geodesy* 93 (2019), pp. 2543–2552. DOI: 10.1007/s00190-019-01314-1.

Kvas, A., T. Mayer-Gürr, S. Krauss, J. M. Brockmann, T. Schubert, W.-D. Schuh, R. Pail, T. Gruber, A. Jäggi, and U. Meyer. *The satellite-only gravity field model GOCO06s*. 2019. DOI: 10.13140/RG.2.2.14101.99047.

Landerer, F. W. et al. "Extending the Global Mass Change Data Record: GRACE Follow-On Instrument and Science Data Performance". In: *Geophysical Research Letters* 47.12 (2020), e2020GL088306. DOI: https://doi.org/10.1029/2020GL088306.

Laundal, K. M., C. C. Finlay, N. Olsen, and J. P. Reistad. "Solar Wind and Seasonal Influence on Ionospheric Currents From Swarm and CHAMP Measurements". In: *Journal of Geophysical Research: Space Physics* 123.5 (2018), pp. 4402–4429. DOI: 10.1029/2018JA025387.

Le Huy, M., M. Mandea, J.-L. Le Mouël, and A. Pais. "Time evolution of the fluid flow at the top of the core. Geomagnetic jerks". In: *Earth, Planets and Space* 52.3 (2000), pp. 163–173. ISSN: 1880-5981. DOI: 10.1186/BF03351625.

Leger, J.-M., T. Jager, F. Bertrand, G. Hulot, L. Brocco, P. Vigneron, X. Lalanne, A. Chulliat, and I. Fratter. "In-flight performance of the Absolute Scalar Magnetometer vector mode on board the Swarm satellites". In: *Earth, Planets and Space* 67 (2015). DOI: 10.1186/s40623-015-0231-1.

Lerch, F. J., S. M. Klosko, G. B. Patel, and C. A. Wagner. "A gravity model for crustal dynamics (GEM-L2)". In: *Journal of Geophysical Research: Solid Earth* 90.B11 (1985), pp. 9301–9311. DOI: https://doi.org/10.1029/JB090iB11p09301.

Lesur, V., S. Macmillan, and A. Thomson. "Deriving main field and secular variation models from synthetic Swarm satellite and observatory data". In: *Earth, Planets and Space* 58.4 (2006), pp. 409–416. DOI: 10.1186/BF03351937.

Lidberg, M., J. M. Johansson, and G. A. Scherneck H.-G.and Milne. "Recent results based on continuous GPS observations of the GIA process in Fennoscandia from BIFROST". In: *Journal of Geodynamics* 50.1 (2010), pp. 8–18. ISSN: 0264-3707. DOI: https://doi.org/10.1016/j.jog.2009.11.010.

Liebe, C. C. "Accuracy Performance of Star Trackers - A Tutorial". In: *IEEE Transactions on Aerospace and Electronic Systems* 38 (2002), pp. 587–599. DOI: 10.1109/TAES.2002.1008988.

Llovel, W., J. Willis, F. W. Landerer, and I. Fukumori. "Deep-ocean contribution to sea level and energy budget not detectable over the past decade". In: *Nature Clim. Change* 4 (2014), pp. 1031–1035. DOI: 10.1038/nclimate2387.

Löcher, A. "Möglichkeiten der Nutzung kinematischer Satellitenbahnen zur Bestimmung des Gravitationsfeldes der Erde". Dissertation. Bonn, Germany: Universität Bonn, 2010.

Löcher, A. and J. Kusche. "A hybrid approach for recovering high-resolution temporal gravity fields from satellite laser ranging". In: *Journal of Geodesy* 95.6 (2021). DOI: 10.1007/s00190-020-01460-x.

Loeb, N. G., W. Su, D. R. Doelling, T. Wong, P. Minnis, S. Thomas, and W. F. Miller. "5.03 - Earth's Top-of-Atmosphere Radiation Budget". In: *Comprehensive Remote Sensing*. Ed. by Shunlin Liang. Oxford: Elsevier, 2018, pp. 67–84. ISBN: 978-0-12-803221-3. DOI: https://doi.org/10.1016/B978-0-12-409548-9.10367-7.

Loomis, B. D., K. E. Rachlin, D. N. Wiese, F. W. Landerer, and S. B. Luthcke. "Replacing GRACE/GRACE-FO With Satellite Laser Ranging: Impacts on Antarctic Ice Sheet Mass Change". In: *Geophysical Research Letters* 47.3 (2020). e2019GL085488 10.1029/2019GL085488, e2019GL085488. DOI: https://doi.org/10.1029/2019GL085488.

Lück, C., J. Kusche, R. Rietbroek, and A. Löcher. "Time-variable gravity fields and ocean mass change from 37 months of kinematic Swarm orbits". In: *Solid Earth* 9.2 (2018), pp. 323–339. DOI: 10.5194/se-9-323-2018.

Mandea, M., E. Bellanger, and J.-L. Le Mouël. "A geomagnetic jerk for the end of the 20th century?" In: *Earth and Planetary Science Letters* 183.3 (2000), pp. 369–373. ISSN: 0012-821X. DOI: https://doi.org/10.1016/S0012-821X(00)00284-3.

Manoj, C., A. Kuvshinov, S. Maus, and H. Lühr. "Ocean circulation generated magnetic signals". In: *Earth, Planets and Space* 58 (2006), pp. 429–437.

Maus, S., H. Lühr, and M. Purucker. "Simulation of the high-degree lithospheric field recovery for the Swarm constellation of satellites". In: *Earth, Planets and Space* 58.4 (2006), pp. 397–407. ISSN: 1880-5981. DOI: 10.1186/BF03351936.

Maus, S., M. Rother, K. Hemant, C. Stolle, H. Lühr, A. Kuvshinov, and N. Olsen. "Earth's lithospheric magnetic field determined to spherical harmonic degree 90 from CHAMP satellite measurements". In: *Geophysical Journal International* 164.2 (2006), pp. 319–330. ISSN: 0956-540X. DOI: 10.1111/j.1365-246X.2005.02833.x.

Mayer-Gürr, T. "Gravitationsfeldbestimmung aus der Analyse kurzer Bahnbögen am Beispiel der Satellitenmissionen CHAMP und GRACE". Dissertation. Bonn, Germany: Universität Bonn, 2006.

Mayer-Gürr, T., S. Behzadpour, A. Eicker, M. Ellmer, B. Koch, S. Krauss, C. Pock, D. Rieser, S. Strasser, B. Süsser-Rechberger, N. Zehentner, and A. Kvas. "GROOPS: A software toolkit for gravity field recovery and GNSS processing". In: *Computers & Geosciences* (2021), p. 104864. ISSN: 0098-3004. DOI: 10.1016/j.cageo.2021.104864.

Mayer-Gürr, T., S. Behzadpour, M. Ellmer, A. Kvas, B. Klinger, S. Strasser, and N. Zehentner. *ITSG-Grace2018 - Monthly, Daily and Static Gravity Field Solutions from GRACE. GFZ Data Services.* 2018. DOI: 10.5880/ICGEM.2018.003.

McCullough, C., N. Harvey, H. Save, and T. Bandikova. *Description of Calibrated GRACE-FO Accelerometer Data Products (ACT) - Level-1 Product Version 04.* Tech. rep. JPL D-103863. Jet Propulsion Laboratory, California Institute of Technology, 2019.

Merson, R. H. and D. King-Hele. "Use of Artificial Satellites to Explore the Earth's Gravitational Field: Results from Sputnik 2 (1957β)". In: *Nature* 182 (1958), pp. 640–641.

Meyer, U., A. Jäggi, Y. Jean, and G. Beutler. "AIUB-RL02: an improved time-series of monthly gravity fields from GRACE data". In: *Geophysical Journal International* 205.2 (2016), pp. 1196–1207. ISSN: 0956-540X. DOI: 10.1093/gji/ggw081.

Meyer, U., K. Sośnica, D. Arnold, C. Dahle, D. Thaller, R. Dach, and A. Jäggi. "SLR, GRACE and swarm gravity field determination and combination". In: *Remote Sensing* 11 (2019), p. 956. DOI: 10.3390/rs11080956.

Meyrath, T., T. van Dam, X. Collilieux, and P. Rebischung. "Seasonal low-degree changes in terrestrial water mass load from global GNSS measurements". In: *Journal of Geodesy* 91 (2017). DOI: 10.1007/s00190-017-1028-8.

Moe, K. and M. M. Moe. "Gas–surface interactions and satellite drag coefficients". In: *Planetary and Space Science* 53.8 (2005), pp. 793–801. ISSN: 0032-0633. DOI: https://doi.org/10.1016/j.pss.2005.03.005.

Montenbruck, O., S. Hackel, J. van den IJssel, and D. Arnold. "Reduced dynamic and kinematic precise orbit determination for the Swarm mission from 4 years of GPS tracking". In: *GPS Solutions* 22.3 (2018), p. 79. ISSN: 1521-1886. DOI: 10.1007/s10291-018-0746-6.

Montenbruck, O., A. Hauschild, R. B. Langley, and C. Siemes. "CASSIOPE orbit and attitude determination using commercial off-the-shelf GPS receivers". In: *GPS Solutions* 23 (2019). DOI: 10.1007/s10291-019-0907-2.

Moretto, T., S. Vennerstrøm, N. Olsen, L. Rastatter, and J. Raeder. "Using global magnetospheric models for simulation and interpretation of Swarm external field measurements". English. In: *Earth, Planets and Space* 58.4 (2006), pp. 439–449. ISSN: 1343-8832.

Nicholls, R. J. and A. Cazenave. "Sea-Level Rise and Its Impact on Coastal Zones". In: *Science* 328.5985 (2010), pp. 1517–1520. ISSN: 0036-8075. DOI: 10.1126/science.1185782.

Nielsen, J. B. *Swarm Level 1b Processor Algorithms.* Tech. rep. SW-RS-DSC-SY-0002, Issue 6.11. Denmark: National Space Institute Technical University of Denmark, 2019.

Nielsen, J. B. *Swarm Level 1b Product Definition.* Tech. rep. SW-RS-DSC-SY-0007, Issue 5.23. Denmark: National Space Institute Technical University of Denmark, 2019.

Niemeier, W. *Ausgleichungsrechnung.* Reprint 2020. Berlin: De Gruyter, 2002. ISBN: 9783110140804. DOI: doi:10.1515/9783110887259.

O'Keefe, J. A. "An application of Jacobi's integral to the motion of an earth satellite". In: *The Astronomical Journal* 62.1252 (1957), pp. 265–266. DOI: 10.1086/107530.

Olsen, N., R. Haagmans, T. J. Sabaka, A. Kuvshinov, S. Maus, M. E. Purucker, M. Rother, V. Lesur, and M. Mandea. "The Swarm End-to-End mission simulator study: A demonstration of separating the various contributions to Earth's magnetic field using synthetic data". In: *Earth, Planets and Space* 58.4 (2006), pp. 359–370. ISSN: 1880-5981. DOI: 10.1186/BF03351934.

Olsen, N., C. Stolle, R. Floberghagen, G. Hulot, and A. Kuvshinov. "Special issue "Swarm science results after 2 years in space"". In: *Earth, Planets and Space* 68 (2016), p. 172. DOI: 10.1186/s40623-016-0546-6.

Pais, M. A. and G. Hulot. "Length of day decade variations, torsional oscillations and inner core superrotation: Evidence from recovered core surface zonal flows". In: *Physics of the Earth and Planetary Interiors* 118 (2000), p. 291. DOI: 10.1016/S0031-9201(99)00161-2.

PDGS Team. *Swarm Users - Data Access Manual.* Tech. rep. SWAM-GSEG-EOPG-MA-14-0032, Issue 1, Revision 8. European Space Agency, 2018.

Pearlman, M., D. Arnold, M. Davis, F. Barlier, R. Biancale, V. Vasiliev, I. Ciufolini, A. Paolozzi, E. C. Pavlis, K. Sośnica, and M. Bloßfeld. "Laser geodetic satellites: a high-accuracy scientific tool". In: *Journal of Geodesy* 93.11 (2019), pp. 2181–2194. DOI: 10.1007/s00190-019-01228-y.

Peltier, W. R. "Global glacial isostasy and the surface of the ice-age Earth: the ICE-5G (VM2) model and GRACE". In: *Annual Review of Earth and Planetary Sciences* 20 (2004), pp. 111–49. DOI: 10.1146/annurev.earth.32.082503.144359.

Peltier, W. R., D. F. Argus, and R. Drummond. "Space geodesy constrains ice age terminal deglaciation: The global ICE-6G_C (VM5a) model". In: *Journal of Geophysical Research: Solid Earth* 120.1 (2015), pp. 450–487. DOI: 10.1002/2014JB011176.

Peterseim, N., J. Flury, and A. Schlicht. "Magnetic torquer induced disturbing signals within GRACE accelerometer data". In: *Advances in Space Research* 49.9 (2012), pp. 1388–1394. ISSN: 0273-1177. DOI: https://doi.org/10.1016/j.asr.2012.02.013.

Petit, G. and B. Luzum. *IERS Conventions (2010). (IERS Technical Note No. 36)*. Tech. rep. Frankfurt am Main: International Earth Rotation and Reference Systems Service, 2010.

Ramillien, G., R. Biancale, S. Gratton, X. Vasseur, and S. Bourgogne. "GRACE-derived surface water mass anomalies by energy integral approach: Application to continental hydrology". In: *Journal of Geodesy* 85 (2011), pp. 313–328. DOI: 10.1007/s00190-010-0438-7.

Ray, J. *IERS Analysis Campaign to Investigate Motions of the Geocenter*. Tech. rep. 25. Paris: Central Bureau of IERS - Observatoire de Paris, 1999.

Reager, J. T., B. Thomas, and J. Famiglietti. "River basin flood potential inferred using GRACE gravity observations at several months lead time". In: *Nature Geoscience* 7 (2014), pp. 588–592. DOI: 10.1038/ngeo2203.

Reigber, C. "Gravity field recovery from satellite tracking data". In: *Theory of Satellite Geodesy and Gravity Field Determination*. Ed. by S. Sansò and R. Rummel. Berlin, Heidelberg: Springer-Verlag, 1989, pp. 197–234. ISBN: 978-3-540-51528-9. DOI: https://doi.org/10.1007/BFb0010552.

Reigber, C. *Zur Bestimmung des Gravitationsfeldes der Erde aus Satellitenbeobachtungen*. Tech. rep. 137. Mitteilungen aus dem Institut für Astronomische und Physikalische Geodäsie, Nr. 63. Verlag der Bayerischen Akademie der Wissenschaften, 1969.

Reigber, C., G. Balmino, H. Müller, W. Bosch, and B. Moynot. "GRIM gravity model improvement using LAGEOS (GRIM3-L1)". In: *Journal of Geophysical Research: Solid Earth* 90.B11 (1985), pp. 9285–9299. DOI: https://doi.org/10.1029/JB090iB11p09285.

Reigber, C., H. Lühr, L. Grunwaldt, C. Förste, R. König, H. Massmann, and C. Falck. "CHAMP Mission 5 Years in Orbit". In: *Observation of the Earth System from Space*. Ed. by J. Flury, R. Rummel, C. Reigber, M. Rothacher, G. Boedecker, and U. Schreiber. Berlin, Heidelberg: Springer-Verlag, 2006, pp. 3–15. ISBN: 978-3-540-29522-8. DOI: 10.1007/3-540-29522-4_1.

Ren, L. and S. Schön. "PPP-based Swarm kinematic orbit determination". In: 36.5 (2018), pp. 1227–1241. DOI: 10.5194/angeo-36-1227-2018.

Reubelt, T. "Harmonische Gravitationsfeldanalyse aus GPS-vermessenen kinematischen Bahnen niedrig fliegender Satelliten vom Typ CHAMP, GRACE und GOCE mit einem hoch auflösenden Beschleunigungsansatz". Dissertation. Stuttgart, Germany: Universität Stuttgart, 2009.

Reubelt, T., G. Austen, and E. Grafarend. "Harmonic analysis of the Earth's gravitational field by means of semi-continuous ephemeris of a low Earth orbiting (LEO) GPS-tracked satellite—case study CHAMP". In: *Journal of Geodesy* 77 (2003), pp. 257–278. DOI: 10.1007/s00190-003-0322-9.

Richter, H. M. P., C. Lück, A. Klos, M. G. Sideris, E. Rangelova, and J. Kusche. "Reconstructing GRACE-type time-variable gravity from the Swarm satellites". In: *Nature Scientific Reports* 11 (1 2021), pp. 2045–2322. DOI: 10.1038/s41598-020-80752-w.

Ries, J. C., S. Bettadpur, R. Eanes, Z. Kang, U. Ko, C. McCullough, P. Nagel, N. Pie, S. Poole, T. Richter, H. Save, and B. D. Tapley. *The Combined Gravity Model GGM05C*. GFZ Data Services. 2016. DOI: 10.5880/icgem.2016.002.

Rietbroek, R. "Retrieval of Sea Level and Surface Loading Variations from Geodetic Observations and Model Simulations: an Integrated Approach". Dissertation. Bonn, Germany: Universität Bonn, 2014.

Rietbroek, R., S.-E. Brunnabend, J. Kusche, and J. Schröter. "Resolving sea level contributions by identifying fingerprints in time-variable gravity and altimetry". In: *Journal of Geodynamics* 59-60 (2012). Mass Transport and Mass Distribution in the System Earth, pp. 72–81. ISSN: 0264-3707. DOI: https://doi.org/10.1016/j.jog.2011.06.007.

Rietbroek, R., S.-E. Brunnabend, J. Kusche, J. Schröter, and C. Dahle. "Revisiting the contemporary sea-level budget on global and regional scales". In: *Proceedings of the National Academy of Sciences* 113.6 (2016), pp. 1504–1509. DOI: 10.1073/pnas.1519132113.

Riley, J. D., M. M. Bennett, and E. McCormick. "Numerical integration of variational equations". In: *Mathematics of Computation* 21 (1967), pp. 12–17. DOI: 10.1090/S0025-5718-1967-0228186-1.

Ritter, P. and H. Lühr. "Curl-B technique applied to Swarm constellation for determining field-aligned currents". In: *Earth, Planets, and Space* 58 (2006). DOI: 10.1186/BF03351942.

Rodell, M., J. Famiglietti, D. N. Wiese, J. T. Reager, H. Beaudoing, F. W. Landerer, and M.-H. Lo. "Emerging trends in global freshwater availability". In: *Nature* 557 (2018), pp. 651–659. DOI: 10.1038/s41586-018-0123-1.

Rubincam, D. P. "Postglacial rebound observed by lageos and the effective viscosity of the lower mantle". In: *Journal of Geophysical Research: Solid Earth* 89.B2 (1984), pp. 1077–1087. DOI: https://doi.org/10.1029/JB089iB02p01077.

Rummel, R., W. Yi, and C. Stummer. "GOCE gravitational gradiometry". In: *Journal of Geodesy* 85.11 (2011), pp. 777–790. DOI: 10.1007/s00190-011-0500-0.

Sabaka, T. J. and N. Olsen. "Enhancing comprehensive inversions using the Swarm constellation". In: *Earth Planets Space* 58 (2006), pp. 371–395. DOI: 10.1186/BF03351935.

Sabaka, T. J., N. Olsen, and M. E. Purucker. "Extending comprehensive models of the Earth's magnetic field with Ørsted and CHAMP data". In: *Geophysical Journal International* 159.2 (2004), pp. 521–547. ISSN: 0956-540X. DOI: 10.1111/j.1365-246X.2004.02421.x.

Sasgen, I., B. Wouters, A. Gardner, M. King, M. Tedesco, F. W. Landerer, C. Dahle, H. Save, and X. Fettweis. "Return to rapid ice loss in Greenland and record loss in 2019 detected by the GRACE-FO satellites". In: *Communications Earth & Environment* 1 (2020). DOI: 10.1038/s43247-020-0010-1.

Save, H. *Gravity Recovery and Climate Experiment Follow-On - CSR Level-2 Processing Standards Document For Level-2 Product Release 06*. Tech. rep. CSR GRFO-19-01(GRACE-FOD-103920, V1.1). Center for Space Research, The University of Texas at Austin, 2019.

Save, H., S. Bettadpur, and B. D. Tapley. "Single Accelerometer Gravity Solutions for GRACE". In: *AGU Fall Meeting Abstracts (pp. G13A-0026)* (2006).

Scanlon, B. R., Z. Zhang, A. Rateb, A. Sun, D. N. Wiese, H. Save, H. Beaudoing, M. H. Lo, H. Müller-Schmied, P. Döll, R. van Beek, S. Swenson, D. Lawrence, M. Croteau, and R. C. Reedy. "Tracking Seasonal Fluctuations in Land Water Storage Using Global Models and GRACE Satellites". In: *Geophysical Research Letters* 46.10 (2019), pp. 5254–5264. DOI: 10.1029/2018GL081836.

Schall, J. "Optimization of point grids in regional satellite gravity analysis using a Bayesian approach". Dissertation. Bonn, Germany: Universität Bonn, 2020.

Scharroo, R., E. Leuliette, J. Lillibridge, D. Byrne, M. Naeije, and G. Mitchum. "RADS: Consistent multi-mission products". In: 2013, p. 69.

Schneider, M. "A general method of orbit determination". Dissertation. Farnborough, England: Ministry of Technology, 1968.

Schreiter, L., D. Arnold, V. Sterken, and A. Jäggi. "Mitigation of ionospheric signatures in Swarm GPS gravity field estimation using weighting strategies". In: *Annales Geophysicae* 37.1 (2019), pp. 111–127. DOI: 10.5194/angeo-37-111-2019.

Schumacher, M., E. Forootan, A. I. J. M. van Dijk, H. Müller Schmied, R. S. Crosbie, J. Kusche, and P. Döll. "Improving drought simulations within the Murray-Darling Basin by combined

calibration/assimilation of GRACE data into the WaterGAP Global Hydrology Model". In: *Remote Sensing of Environment* 204 (2018), pp. 212–228. ISSN: 0034-4257. DOI: https://doi.org/10.1016/j.rse.2017.10.029.

Sella, G. F., S. Stein, T. H. Dixon, M. Craymer, T. S. James, S. Mazzotti, and R. K. Dokka. "Observation of glacial isostatic adjustment in "stable" North America with GPS". In: *Geophysical Research Letters* 34.2 (2007). DOI: 10.1029/2006GL027081.

Sentman, L. H. *Free Molecule Flow Theory and Its Application to the Determination of Aerodynamic Forces*. LMSC-448514. Lockheed Missiles & Space Company, a division of Lockheed Aircraft Corporation, 1961.

Seo, K.-W., C. R. Wilson, S. C. Han, and D. E. Waliser. "Gravity Recovery and Climate Experiment (GRACE) alias error from ocean tides". In: *Journal of Geophysical Research: Solid Earth* 113.B3 (2008). DOI: 10.1029/2006JB004747.

Shang, K., J. Guo, C. K. Shum, C. Dai, and J. Luo. "GRACE time-variable gravity field recovery using an improved energy balance approach". In: *Geophysical Journal International* 203.3 (2015), pp. 1773–1786. ISSN: 0956-540X. DOI: 10.1093/gji/ggv392.

Shepherd, A., E. Ivins, E. Rignot, B. Smith, M. R. van den Broeke, P. Whitehouse, K. Briggs, I. Joughin, G. Krinner, S. Nowicki, A. Payne, T. Scambos, N.-J. Schlegel, G. A, C. Agosta, A. Ahlstrøm, G. Babonis, V. Barletta, A. Blazquez, and B. Wouters. "Mass balance of the Antarctic Ice Sheet from 1992 to 2017". In: *Nature* 558 (2018), pp. 219–222. DOI: 10.1038/s41586-018-0179-y.

Shepherd, A., E. Ivins, E. Rignot, B. Smith, M. van den Broeke, I. Velicogna, P. Whitehouse, K. Briggs, I. Joughin, G. Krinner, S. Nowicki, A. Payne, T. Scambos, N.-J. Schlegel, G. A, C. Agosta, A. Ahlstrøm, G. Babonis, V. Barletta, and J. Wuite. "Mass balance of the Greenland Ice Sheet from 1992 to 2018". In: *Nature* 579 (2020), pp. 233–239. DOI: 10.1038/s41586-019-1855-2.

Siemes, C. *Swarm SPC to PDGS Interface Control Document*. Tech. rep. ESA-EOPG-MOM-IF-17, Issue 1.1. European Space Agency, 2019.

Siemes, C., J. de Teixeira da Encarnação, E. Doornbos, J. van den IJssel, J. Kraus, R. Pereštý, L. Grunwaldt, G. Apelbaum, J. Flury, and P. E. Holmdahl Olsen. "Swarm accelerometer data processing from raw accelerations to thermospheric neutral densities". In: *Earth, Planets, and Space* 68, 92 (2016), p. 92. DOI: 10.1186/s40623-016-0474-5.

Slangen, A. B. A., R. S. W. van de Wal, Y. Wada, and L. L. A. Vermeersen. "Comparing tide gauge observations to regional patterns of sea-level change (1961-2003)". In: *Earth System Dynamics* 5.1 (2014), pp. 243–255. DOI: 10.5194/esd-5-243-2014.

Stoffelen, A., J. Pailleux, E. Källén, J. M. Vaughan, L. Isaksen, P. Flamant, W. Wergen, E. Andersson, H. Schyberg, A. Culoma, R. Meynart, M. Endemann, and P. Ingmann. "The Atmospheric Dynamics Mission for Global Wind Field Measurement". In: *Bulletin of the American Meteorological Society* 86.1 (2005), pp. 73–88. ISSN: 0003-0007. DOI: 10.1175/BAMS-86-1-73.

Sun, Y., P. Ditmar, and R. Riva. "Statistically optimal estimation of degree-1 and C20 coefficients based on GRACE data and an ocean bottom pressure model". In: *Geophysical Journal International* 210.3 (2017), pp. 1305–1322. ISSN: 0956-540X. DOI: 10.1093/gji/ggx241.

Sun, Y., R. Riccardo, and D. Pavel. "Optimizing estimates of annual variations and trends in geocenter motion and J2 from a combination of GRACE data and geophysical models". In: *Journal of Geophysical Research: Solid Earth* 121.11 (2016), pp. 8352–8370. DOI: 10.1002/2016JB013073.

Švehla, D. and M. Rothacher. "Kinematic and reduced-dynamic precise orbit determination of low earth orbiters". In: *Advances in Geosciences* 1 (2003), pp. 47–56. DOI: 10.5194/adgeo-1-47-2003.

Swatschina, P. *Dynamic and Reduced-dynamic Precise Orbit Determination of Satellites in Low Earth Orbits*. Geowissenschaftliche Mitteilungen 89. Department of Geodesy and Geoinformation of the Vienna University of Technology, 2012.

Swenson, S., D. Chambers, and J. Wahr. "Estimating geocenter variations from a combination of GRACE and ocean model output". In: *Journal of Geophysical Research: Solid Earth* 113.B8 (2008). DOI: 10.1029/2007JB005338.

Swenson, S. and J. Wahr. "Methods for inferring regional surface-mass anomalies from Gravity Recovery and Climate Experiment (GRACE) measurements of time-variable gravity". In: *Journal of Geophysical Research: Solid Earth* 107.B9 (2002), ETG 3-1-ETG 3-13. DOI: https://doi.org/10.1029/2001JB000576.

Tapley, B. D., S. Bettadpur, M. Watkins, and C. Reigber. "The gravity recovery and climate experiment: Mission overview and early results". In: *Geophysical Research Letters* 31.9 (2004). DOI: 10.1029/2004GL019920.

Tapley, B. D., F. Flechtner, M. Watkins, and S. Bettadpur. *GRACE mission: status and prospects.* presented at: GRACE Science Team Meeting 2015, Austin, Texas. 2015.

Tapley, B. D., B. E. Schutz, and R. J. Eanes. "Satellite laser ranging and its applications". In: *Celestial Mechanics* 37.3 (1985), pp. 247–261. DOI: 10.1007/BF02285050.

Tapley, B. D., B. E. Schutz, and R. J. Eanes. "Station coordinates, baselines, and Earth rotation from LAGEOS laser ranging: 1976–1984". In: *Journal of Geophysical Research: Solid Earth* 90.B11 (1985), pp. 9235–9248. DOI: https://doi.org/10.1029/JB090iB11p09235.

Tapley, B. D., M. Watkins, F. Flechtner, C. Reigber, S. Bettadpur, M. Rodell, I. Sasgen, J. Famiglietti, F. W. Landerer, D. Chambers, J.T. Reager, A. Gardner, H. Save, E. Ivins, S. Swenson, C. Boening, C. Dahle, D. N. Wiese, H. Dobslaw, and I. Velicogna. "Contributions of GRACE to understanding climate change". In: *Nature Climate Change* 5 (2019). DOI: 10.1038/s41558-019-0456-2.

Thébault, E., P. Vigneron, B. Langlais, and G. Hulot. "A Swarm lithospheric magnetic field model to SH degree 80". In: *Earth, Planets and Space* 68 (2016). DOI: 10.1186/s40623-016-0510-5.

Tilling, R. L., A. Ridout, and A. Shepherd. "Estimating Arctic sea ice thickness and volume using CryoSat-2 radar altimeter data". In: *Advances in Space Research* 62.6 (2018). The CryoSat Satellite Altimetry Mission: Eight Years of Scientific Exploitation, pp. 1203–1225. ISSN: 0273-1177. DOI: https://doi.org/10.1016/j.asr.2017.10.051.

Tøffner-Clausen, L., V. Lesur, N. Olsen, and C. Finlay. "In-flight scalar calibration and characterisation of the Swarm magnetometry package". In: *Earth, Planets and Space* 68.129 (2016). DOI: 10.1186/s40623-016-0501-6.

Touboul, P., E. Willemenot, B. Foulon, and V. Josselin. "Accelerometers for CHAMP, GRACE and GOCE space missions: synergy and evolution". In: *Bollettino Di Geofisica Teorica Ed Applicata* 40 (1999), pp. 321–327.

Uebbing, B., J. Kusche, and E. Forootan. "Waveform Retracking for Improving Level Estimations From TOPEX/Poseidon, Jason-1, and Jason-2 Altimetry Observations Over African Lakes". In: *IEEE Transactions on Geoscience and Remote Sensing* 53.4 (2015), pp. 2211–2224. DOI: 10.1109/TGRS.2014.2357893.

Uebbing, B., J. Kusche, R. Rietbroek, and F. W. Landerer. "Processing Choices Affect Ocean Mass Estimates From GRACE". In: *Journal of Geophysical Research: Oceans* 124.2 (2019), pp. 1029–1044. DOI: 10.1029/2018JC014341.

van den IJssel, J., J. de Teixeira da Encarnação, E. Doornbos, and P. N. A. M. Visser. "Precise science orbits for the Swarm satellite constellation". In: *Advances in Space Research* 56.6 (2015), pp. 1042–1055. DOI: 10.1016/j.asr.2015.06.002.

van den IJssel, J., E. Doornbos, E. Iorfida, G. March, C. Siemes, and O. Montenbruck. "Thermosphere densities derived from Swarm GPS observations". In: *Advances in Space Research* 65.7 (2020), pp. 1758–1771. DOI: 10.1016/j.asr.2020.01.004.

van den IJssel, J., B. Forte, and O. Montenbruck. "Impact of Swarm GPS receiver updates on POD performance". In: *Earth, Planets and Space* 68.1 (2016), p. 85. ISSN: 1880-5981. DOI: 10.1186/s40623-016-0459-4.

van Gelderen, M. and R. Koop. "The use of degree variances in satellite gradiometry". In: *Journal of Geodesy* 71 (1997), pp. 337–343. DOI: 10.1007/s001900050101.

Velicogna, I., Y. Mohajerani, G. A, F. W. Landerer, J. Mouginot, B. Noel, E. Rignot, T. Sutterley, M. van den Broeke, M. van Wessem, and D. N. Wiese. "Continuity of Ice Sheet Mass Loss in Greenland and Antarctica From the GRACE and GRACE Follow-On Missions". In: *Geophysical Research Letters* 47.8 (2020), e2020GL087291. DOI: https://doi.org/10.1029/2020GL087291.

Vennerstrom, S., T. Moretto, L. Rastaetter, and J. Raeder. "Modeling and analysis of solar wind generated contributions to the near-Earth magnetic field". In: *Earth Planets and Space* 58 (2006), pp. 451–461. DOI: 10.1186/BF03351941.

Vichare, G., N. Thomas, K. Shiokawa, A. Bhaskar, and A. K. Sinha. "Spatial Gradients in Geomagnetic Storm Time Currents Observed by Swarm Multispacecraft Mission". In: *Journal of Geophysical Research: Space Physics* 124.2 (2019), pp. 982–995. DOI: 10.1029/2018JA025692.

Vielberg, K., E. Forootan, C. Lück, A. Löcher, J. Kusche, and K. Börger. "Comparison of accelerometer data calibration methods used in thermospheric neutral density estimation". In: *Annales Geophysicae* 36.3 (2018), pp. 761–779. DOI: 10.5194/angeo-36-761-2018.

Vielberg, K. and J. Kusche. "Extended forward and inverse modeling of radiation pressure accelerations for LEO satellites". In: *Journal of Geodesy* 94.43 (2020). DOI: 10.1007/s00190-020-01368-6.

Visser, P. N. A. M., E. Doornbos, J. van den IJssel, and J. Teixeira da Encarnação. "Thermospheric density and wind retrieval from Swarm observations". In: *Earth, Planets and Space* 65.11 (2013), pp. 1319–1331. ISSN: 1343-8832. DOI: 10.5047/eps.2013.08.003.

Wahr, J., M. Molenaar, and F. Bryan. "Time variability of the Earth's gravity field: Hydrological and oceanic effects and their possible detection using GRACE". In: *Journal of Geophysical Research: Solid Earth* 103.B12 (1998), pp. 30205–30229. DOI: 10.1029/98JB02844.

WCRP, Global Sea Level Budget Group. "Global sea-level budget 1993–present". In: *Earth System Science Data* 10.3 (2018), pp. 1551–1590. DOI: 10.5194/essd-10-1551-2018.

Weigelt, M. "The Acceleration Approach". In: *Global Gravity Field Modeling from Satellite-to-Satellite Tracking Data, Lecture Notes in Earth System Sciences*. Ed. by M. Naeimi and J. Flury. Cham, Switzerland: Springer International Publishing, 2017, pp. 97–126. ISBN: 978-3-319-49940-6. DOI: 0.1007/978-3-319-49941-3_4.

Weigelt, M. and N. Sneeuw. "Numerical Velocity Determination and Calibration Methods for CHAMP Using the Energy Balance Approach". In: *Gravity, Geoid and Space Missions. International Association of Geodesy Symposia*. Ed. by C. Jekeli, L. Bastos, and J. Fernandes. Vol. 129. Berlin, Heidelberg: Springer-Verlag, 2005, pp. 54–59. DOI: 10.1007/3-540-26932-0_10.

Wen, H. Y., G. Kruizinga, M. Paik, F. W. Landerer, W. Bertiger, C. Sakumura, T. Bandikova, and C. McCullogh. *Gravity Recovery and Climate Experiment Follow-On - Level-1 Data Product User Handbook*. Tech. rep. JPL D-56935 (URS270772). Jet Propulsion Laboratory, California Institute of Technology, 2019.

Wessel, P., J. F. Luis, L. Uieda, R. Scharroo, F. Wobbe, W. H. F. Smith, and D. Tian. "The Generic Mapping Tools Version 6". In: *Geochemistry, Geophysics, Geosystems* 20.11 (2019), pp. 5556–5564. DOI: https://doi.org/10.1029/2019GC008515.

Whitehouse, P. L. "Glacial isostatic adjustment modelling: Historical perspectives, recent advances, and future directions". In: *Earth Surface Dynamics* 6 (2018), pp. 401–429. DOI: 10.5194/esurf-6-401-2018.

Whitehouse, P. L., M. J. Bentley, and A. M. Le Brocq. "A deglacial model for Antarctica: geological constraints and glaciological modelling as a basis for a new model of Antarctic glacial isostatic adjustment". In: *Quaternary Science Reviews* 32 (2012), pp. 1–24. ISSN: 0277-3791. DOI: https://doi.org/10.1016/j.quascirev.2011.11.016.

Whitehouse, P. L., M. J. Bentley, G. A. Milne, M. A. King, and I. D. Thomas. "A new glacial isostatic adjustment model for Antarctica: calibrated and tested using observations of relative sea-level change and present-day uplift rates". In: *Geophysical Journal International* 190.3 (2012), pp. 1464–1482. ISSN: 0956-540X. DOI: 10.1111/j.1365-246X.2012.05557.x.

Williamson, R. G. and J. G. Marsh. "Starlette geodynamics: The Earth's tidal response". In: *Journal of Geophysical Research: Solid Earth* 90.B11 (1985), pp. 9346–9352. DOI: 10.1029/JB090iB11p09346.

Wingham, D. J., C. R. Francis, S. Baker, C. Bouzinac, D. Brockley, R. Cullen, de Chateau-Thierry P., S. W. Laxon, U. Mallow, C. Mavrocordatos, L. Phalippou, G. Ratier, L. Rey, F. Rostan, P. Viau, and D. W. Wallis. "CryoSat: A mission to determine the fluctuations in Earth's land and marine ice fields". In: *Advances in Space Research* 37.4 (2006). Natural Hazards and Oceanographic Processes from Satellite Data, pp. 841–871. ISSN: 0273-1177. DOI: https://doi.org/10.1016/j.asr.2005.07.027.

Wouters, B., D. Chambers, and E. J. O. Schrama. "GRACE observes small-scale mass loss in Greenland". In: *Geophysical Research Letters* 35.20 (2008). DOI: 10.1029/2008GL034816.

Wu, X., D. F. Argus, M. B. Heflin, E. R. Ivins, and F. H. Webb. "Site distribution and aliasing effects in the inversion for load coefficients and geocenter motion from GPS data". In: *Geophysical Research Letters* 29 (2002), pp. 63-1-63-4.

Yau, A. W. and H. G. James. "CASSIOPE Enhanced Polar Outflow Probe (e-POP) Mission Overview". In: *Space Science Reviews* 189 (2015). DOI: 10.1007/s11214-015-0135-1.

Yuan, D.-N. *Gravity Recovery and Climate Experiment Follow-On - JPL Level-2 Processing Standards Document For Level-2 Product Release 06*. Tech. rep. JPL D-103921 (V. 1.0). Jet Propulsion Laboratory, California Institute of Technology, 2019.

Yuan, D.-N. *Gravity Recovery and Climate Experiment Follow-On - Level-2 Gravity Field Product User Handbook*. Tech. rep. JPL D-103922 (Rev 1.1). Jet Propulsion Laboratory, California Institute of Technology, 2019.

Zakharenkova, I., I. Cherniak, and A. Krankowski. "Features of Storm-Induced Ionospheric Irregularities From Ground-Based and Spaceborne GPS Observations During the 2015 St. Patrick's Day Storm". In: *Journal of Geophysical Research: Space Physics* 124.12 (2019), pp. 10728–10748. DOI: 10.1029/2019JA026782.

Zangerl, F., F. Griesauer, M. Sust, O. Montenbruck, S. Buchert, and A. Garcia. "SWARM GPS Precise Orbit Determination Receiver Initial In-Orbit Performance Evaluation". In: vol. 2. Tampa, Florida, 2014, pp. 1459–1468.

Zatman, S. A. and J. Bloxham. "Torsional oscillations and the magnetic field within the Earth's core". In: *Nature* 388 (1997), pp. 760–763.

Zehentner, N. and T. Mayer-Gürr. "Precise orbit determination based on raw GPS measurements". In: *Journal of Geodesy* 90.3 (2016), pp. 275–286. ISSN: 1432-1394. DOI: 10.1007/s00190-015-0872-7.

Zeng, Y. Y., J. Y. Guo, K. Shang, C. K. Shum, and J. H. Yu. "On the formulation of gravitational potential difference between the GRACE satellites based on energy integral in Earth fixed frame". In: *Geophysical Journal International* 202.3 (2015), pp. 1792–1804. ISSN: 0956-540X. DOI: 10.1093/gji/ggv248.